UNIVERZITA PALACKÉHO OLOMOUC
Přírodovědecká fakulta
Společná laboratoř optiky UP a FzÚ AV ČR

Simulace pro vývoj detektoru času průletu vysokoenergetických částic pro projekt ATLAS/AFP

Habilitační Práce

2024

Mgr. Libor Nožka, Ph.D.

Poděkování

Tato práce by nevznikla bez všech spolupracovníků zapojených do vývoje detektoru AFP. Vedle zahraničních kolegů a tuzemských pracovníků z MFF UK v Praze (dr. T. Sýkora) a FEL ZČÚ v Plzni (skupina okolo doc. V. Georgieva) bych chtěl vyzdvihnout spolupracovníky v rámci Společné laboratoře optiky PřF UP a FzÚ Akademie věd ČR. Jedná se především o prof. Miroslava Hrabovského, dr. Petra Schovánka, dr. Jiřího Kvitu, dr. Karla Černého, dr. Tomáše Komárka a Vladimíra Urbáška. Zvláštní poděkování patří také všem pracovníkům zdejší optické dílny.

Rovněž děkuji své rodině za veškerou podporu a pomoc, kterou mě zahrnují.

V Olomouci, dne 25. září 2024. ....

Mgr. Libor Nožka, Ph.D.

Obsah

Kapitola 1

Úvod

Tato práce vznikla na základě zapojení pracoviště Společné laboratoře optiky Univerzity Palackého v Olomouci a Fyzikálního ústavu Akademie věd České republiky (dále jen SLO) v projektu ATLAS v laboratořích CERN, který je jedním ze čtyř základních experimentů vybudovaných na Velkém hadronovém srážeči (LHC) [1]. V roce 2007 vznikla na SLO skupina, která se začlenila do kolaborace projektu ALFA [2]. Tento detektor se až do roku 2023 nacházel v dopředné oblasti centrálního detektoru ATLAS a jeho cílem bylo měřit luminozitu (intenzitu) protonového svazku LHC. V rámci tohoto projektu se skupina věnovala především modelování geometrie a fyzikální analýze za použití dat vzešlých z kombinace výstupu z detektoru ATLAS a ALFA [3, 4, 5].

V roce 2011 jsme jako skupina plynule přešli na vývoj detektoru AFP, který je do jisté míry nástupcem detektoru ALFA. Zprvu jsme se opět věnovali především softwarovým záležitostem v oblasti modelování detektoru. Postupně se těžiště naší práce posunulo do hardwarové části. Protože se pracoviště SLO specializuje na výrobu optických prvků, stali jsme se zodpovědnými za vývoj a výrobu optické části jednoho z dílčích detektorů AFP, detektoru času průletu odchýlených protonů ze srážek v centrální části detektoru ATLAS, zkráceně detektoru ToF (z angl. Time-of-Flight). Postupně jsme také převzali zodpovědnost za vývoj a výrobu části elektroniky pro vyčítání signálu z detektoru ToF a optimalizaci samotného fotodetektoru (fotonásobiče), která byla realizována v součinnosti s výrobcem, společností Photonis, Inc. (USA). Ve všech zmíněných aspektech naší práce jsme uplatnili moderní metody modelování, pomocí kterých jsme úspěšně směřovali cestu vývoje detektoru ToF. Modelování se tímto stalo nepostradatelnou součástí jeho vývoje. Tato práce byla vytvořena na základech několika článků uvedených v plném znění v části C na konci textu. Ty tvoří pouze část ze všech publikací, které vznikly během vývoje detektoru. Seznam těch publikací o detektoru ToF, na kterých je autor této práce veden jako spoluautor, je uveden v Příloze B.

V následující kapitole bude krátce představen projekt AFP včetně detailnějšího popisu detektoru ToF. Hardwarové části detektoru bylo v minulosti věnováno dostatek publikací, na které se tato kapitola odkazuje. Problematika modelování si zaslouží ucelenější popis a další kapitoly, které jsou těžištěm této práce, se věnují nejdůležitějším aspektům této části vývoje. Fyzikální simulace popisující fyzikální motivaci pro vznik projektu AFP nejsou součástí této práce, a jsou krátce zmíněny v rámci představení projektu v následující kapitole s odkazy na bližší informace.

Kapitola 2

Projekt AFP

2.1 Fyzikální motivace

Projekt AFP (z angl. ATLAS Forward Proton) spadá do dopředné oblasti detektoru ATLAS v laboratořích CERN. Fyzikální motivace je detailně uvedena v [6]. AFP byl navržen pro detekci difrakčních událostí při srážkách dvou protonů v interakčním bodě P1 urychlovače LHC. Schématicky je situace znázorněna na Obrázku 2.1. Centrální detektor (v tomto případě ATLAS) je umístěn v okolí interakčního bodu (IP) urychlovače LHC. Dopředná oblast detektoru je v případě velkých detektorů ATLAS a CMS na urychlovači LHC dlouhá přibližně 250 m na obě strany od IP. V této oblasti se na odchozí trubici urychlovače instalují dopředné detektory. Mezi základní charakteristiky centrálních detektorů je úhlová viditelnost produktů srážek, tj. úhel rozptylu θ, pod kterým lze aktivní částí detektoru ještě zachytit trajektorii odchozí částice. V částicové fyzice se, spíše než úhel odchýlení, používá odvozená veličina pseudorapidity definovaná jako $\eta = -\ln[\tan(\theta/2)]$, kde θ je úhel odchýlení od původního směru, tj. od osy svazku. Hodnota $\eta = 0$ odpovídá úhlu 90° od osy svazku a $\eta = \infty$ odpovídá nulovému odklonu od svazku. Pro detektor ATLAS je nejvyšší hodnota psudorapidity rovna $\eta_{max} = 4.9$ [7]. Vyšší hodnoty pseudorapidity lze v tomto případě měřit pouze dopřednými detektory.

Vysokoenergetické proton-protonové interakční procesy lze rozdělit do skupin podle Obrázku 2.2. Při, obecně hadronových, srážkách na energetických škálách odpovídajících velikostem hadronů (1 fm) je coulombická interakce upozaděna a do popředí se dostávají

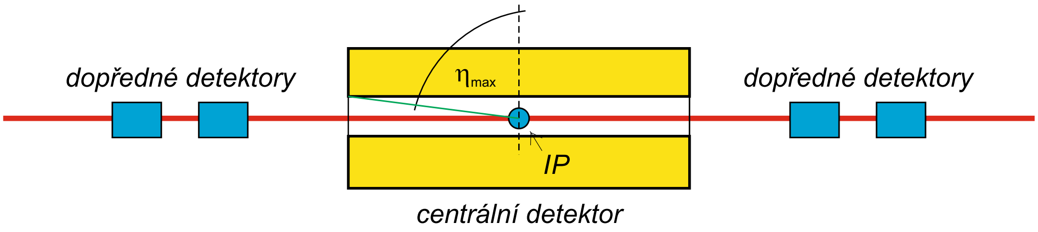

Obrázek 2.1: Schéma umístění centrálního detektoru v okolí interakčního bodu (IP) urychlovače s dopřednými detektory.

procesy spojené s elektroslabou a silnou interakcí, které lze popsat moderními metodami kvantové chromodynamiky (QCD). Při těchto interakcích dochází obecně ke změnám čtyřhybností zúčastněných částic, popřípadě k jejich excitaci a rozpadu na fragmenty, které hadronizují v nové částice. Ze zákonů zachování plyne, že součet čtyřhybností produktů srážky je roven součtu čtyřhybností vstupujících částic. Například podle procesu na Obrázku 2.2a platí $p_1 + p_2 = p_3 + p_4$ apod. Kinematika těchto reakcí se popisuje pomocí Mandelstamových proměnných (invariantů):

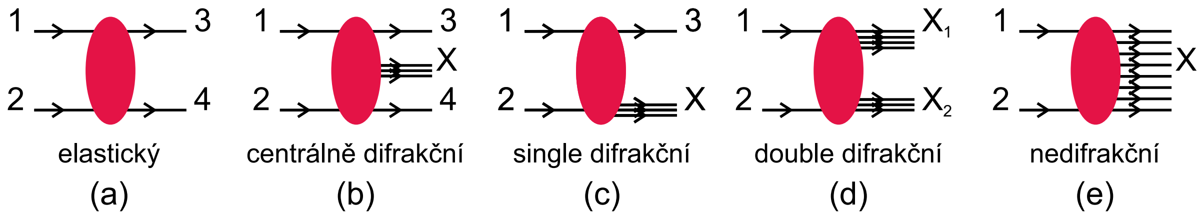

Obrázek 2.2: Typy vysokoenergetických proton-protonových srážek. První čtyři se řadí mezi měkké procesy a poslední mezi tvrdé procesy.

$$\begin{aligned} s &= (p_1 + p_2)^2 = (p_3 + p_4)^2 \\ t &= (p_1 - p_3)^2 = (p_2 - p_4)^2 \\ u &= (p_1 - p_4)^2 = (p_2 + p_3)^2 \end{aligned} \tag{2.1}$$

Veličina s je kvadrát celkové energie v těžišti systému srážky a t je kvadrát přenosu hybnosti. Při dostatečně nízkých energiích interagujících částic dochází pouze k jejich rozptylu (ve které však není coulombická interakce dominantní), Obrázek 2.2a. Nedochází při ní výměně kvantových čísel, protože oba původní protony po interakci přežijí a jsou jen nepatrně odkloněny od svých původních trajektorií, a to v řádu mikroradiánů. Související změna veličiny t je v řádu stovek MeV^2 [8] a závislost diferenciálního účinného průřezu těchto interakcí na t exponenciálně klesá, tj. $d\sigma/dt \sim \exp(|t|)$.

Vzhledem k takto nízkým přenosům momentu hybnosti nelze pro popis těchto inerakcí použít poruchovou QCD. Místo toho se používá od 60. let 20. století Reggeho teorie [9], která je založena na kvantově-mechanickém přístupu s operátorem matice přechodu (tzv. matice S). Matematický způsob řešení odpovídajících vlnových rovnic je založeno na rozšíření čtyřhybností do komplexní roviny a integraci přes tzv. Reggeho křivky v komplexní rovině. Reggeho teorie zavedla novou abstraktní částici zvanou *pomeron*, která má charakter částice vakua (s příslušnými kvantovými čísly). Pomocí této částice byl dobře popsán účinný průřez těchto rozptylových procesů a to i pro vyšší energie, kde účinný průřez vykazuje lokální minima. Tento charakter rozptylu je podobný difrakci známé v optice, proto jsou tyto procesy obecně označeny jako difrakční procesy.

S rostoucí energií částic může docházet k uvolnění energie dostatečné ke vzniku nových částic v centrálním systému (s nízkou dopřednou složkou hybnosti), Obrázek 2.2b. Tento proces se označuje jako centrální difrakce (CD) a obsahuje tedy jednak elastickou složku (s vyšším přenosem hybnosti t oproti čistě elastickému rozptylu) a také neelastickou složku, kterou lze popsat poruchovou QCD. Protože oba protony prochází interakcí beze změn svých kvantových čísel, vysvětluje se proces přenosu energie z protonů pomerony (výměna kvantových čísel vakua). Při stále se zvyšujících energiích mohou nastat procesy, při kterých dochází k excitaci jednoho z protonů nebo obou protonů, která způsobí jejich rozpad (fragmentaci), Obrázek 2.2c a 2.2d. Tyto srážky se označují single difrakční (SD) resp. double difrakční (DD). Fragmenty rozpadajících se protonů si zachovávají dopředný směr trajektorie, a nejsou tedy detekované centrálním detektorem. Přeživší produkty se však zřídkakdy dostanou do některého z dopředných detektorů, což v případě srážky typu DD znamená, že je téměř neměřitelná. Difrakční procesy popsané Obrázky 2.2a-d spadají do tzv. měkkých procesů, ve kterých se uplatňuje Reggeho teorie. Poslední typ srážky na Obrázku 2.2e je spojen s velkým přenosem hybnosti nad 1 GeV^2. Při těchto srážkách dochází k disociaci obou vstupujících částic a k výměně jejich kvantových čísel za vzniku produktů z jejich fragmentů procesem hadronizace. Nedifrakční procesy představují hlavní oblast zájmu experimentu ATLAS.

Pro centrální difrakční proces a procesy spojené s disociací protonů (tj. SD, a DD) je typický vznik mezer ve směrech trajektorií odchozích částic, tj. mezer v pseudorapiditě. Například, v případě single difrakce je celková invariantní hmota M vzniklých fragmentů X rovna:

$$M^2 = (p_1 + p_2 - p_3)^2 \ , \tag{2.2}$$

Mezera v pseudorapiditě $\Delta\eta$ úzce koreluje s invariantní hmotností s invariantní hmotou [10]:

$$\Delta\eta \sim \ln \frac{M^2}{s} \ . \tag{2.3}$$

Fyzikální motivace pro konstrukci detektoru AFP vyplývá z podstaty difrakčních procesů, a tím je jejich měření na vysokých hodnotách pseudorapidity, která je mimo dosah centrálního detektoru ATLAS. Zahrnuje tedy měkké procesy s nižším přenosem čtyřhybnosti. Jedná se především o procesy spojené se single difrakcí a centrální difrakcí [6]. Vzhledem k tomu, že SD srážky jsou relativně běžnou součástí interakcí v interakčním bodě (přibližně 10% z celkového účinného průřezu), je snadné zaměnit dva odchozí protony ze dvou různých difrakčních událostí. Proto se od počátku projektu AFP počítalo i s detektorem času průletu těchto částic, aby bylo možné párovat protony zachycené na obou stranách dopředné oblasti ze stejné interakce. Podrobný rozbor možností detektorů ToF pro použití v dopředné fyzice lze najít v [11]. Příkladem fyzikální analýzy za použití informací s ToF je detekce axionu-podobných částic (ALP, zangl. Axion-Like Particles) [12].

2.2 Konstrukce detektoru

Poloha detektorů AFP je schématicky naznačena na Obrázku 2.3. Po obou stranách A (z ang. Anticlockwise) a C (z ang. Clockwise) centrálního detektoru se na odchozích trubicích nachází po dvou detektorech AFP a to přibližně 205 m a 217 m od interakčního bodu P1, konkrétně mezi kvadrupólovými magnety Q5 a Q6. Ze schématu je také vidět, že předchozí detektory ALFA se nacházely za magnety Q6. Na každé straně jsou nainstalovány dvě stanice. Ta bližší k P1 se označuje NEAR a vzdálenější FAR. Podle strany dopředné oblasti jsou pak stanice označeny jako A-FAR, A-NEAR, C-NEAR a C-FAR. Vlastní detektory jsou umístěny v Římských hrncích, které jsou dlouhodobě osvědčenou

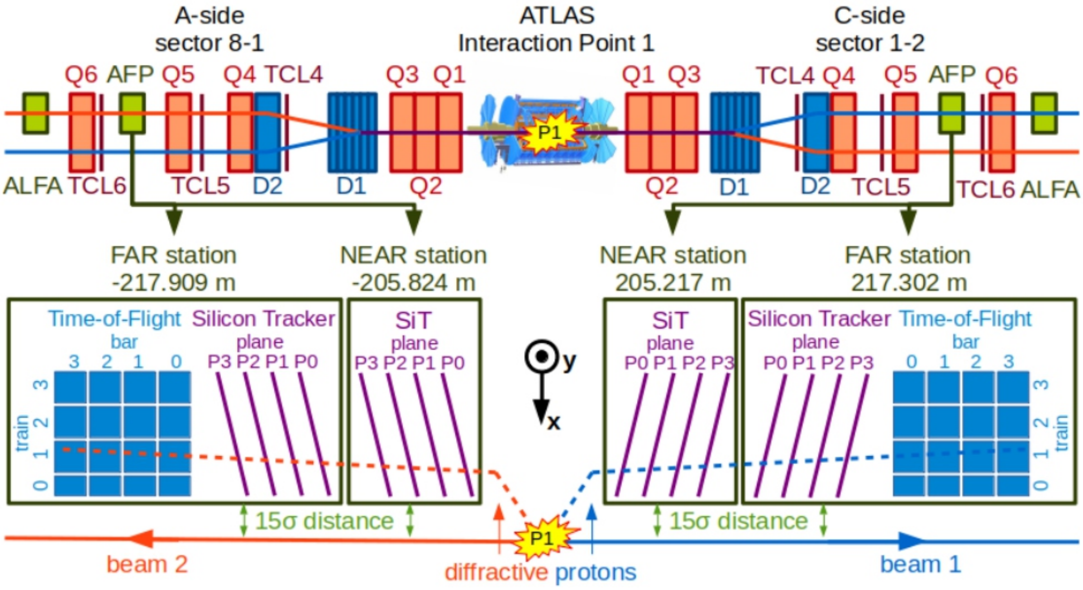

Obrázek 2.3: Schéma rozmístění detektorů ALFA a AFP v dopředné oblasti detektoru ATLAS. Vzdálenosti jsou vůči interakčnímu bodu P1. Dipólové magnety jsou označeny modře a kvadrupólové magnety červeně.

konstrukcí dopředných detektorů, Obrázek 2.4. Římské hrnce jsou ke stanici připevněny na pohyblivém ústrojí, takže je možné dálkově precizně vysouvat hrnec s detektory do měřící polohy směrem ke svazku nebo jej oddálit do parkovací polohy. V hrncích se rotačními vývěvami udržuje vakuum v rozmezí 100 Pa - 1 kPa, aby se snížil tlak na strany hrnce přiléhající ke svazku v trubici LHC, kde je vysoké vakuum $10^{-8} - 10^{-9}$ Pa [13] [1]. Nevýhodou Římských hrnců je omezený prostor pro detektory, které mají takto k dispozici objem ve formě válce o průměru 130 mm a výšce 135 mm. Důležitým prvkem konstrukčního řešení pro AFP je oddělení fotonásobiče od prostoru s nízkým vakuem (tedy v podstatě mimo hrnec) válcovým tubusem, aby nedocházelo k nechtěným výbojům kvůli napájecímu vysokému napětí, Obrázek 2.4a. Pro vzdálené ověřování funkčnosti fotonásobiče jsou přes tubus vedena čtyři optická vlákna z optického pulzru [14].

---

[1] Uvedené rozmezí je platné v oblastech experimentů pro snížení signálového pozadí, v ostatních částech je tlak přibližně 10^{-4} Pa [13].

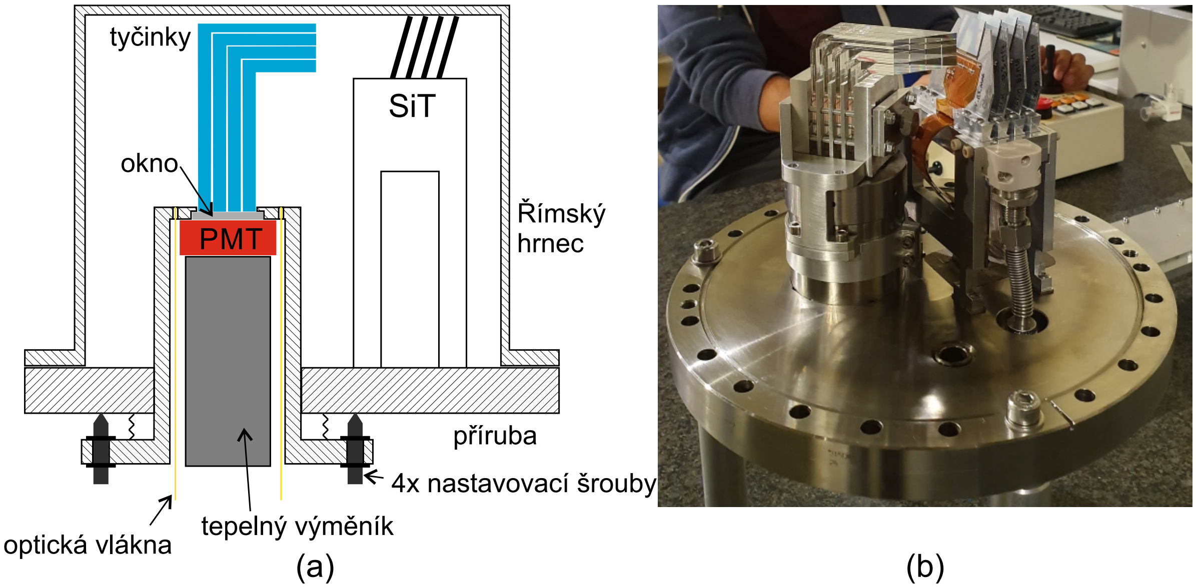

(a) (b)

Obrázek 2.4: Detektor AFP: (a) schématické umístění v Římském hrnci, (b) pohled na sestavu na přírubě hrnce s oddělaným krytem.

2.2.1 Křemíkové detektory

Primárními měřícími prvky AFP jsou křemíkové trasovací detektory (SiT), které se nacházejí ve všech stanicích AFP, Obrázek 2.5. Jejich úkolem je měření trajektorie a hybnosti protonů odchýlených vlivem srážek v interakčním bodě. Jsou tvořeny radiačně odolnými křemíkovými 3D senzory o velikosti snímací plochy 20×20 mm^2 s pixely o velikosti 50×250 μm^2 [15]. Vyčítání probíhá přes čip FEI4, který je osvědčeným prvkem schopným pracovat ve vysokém taktu přicházejících dat při vysoké radiační zátěži [16]. V rámci jedné stanice tvoří jednotlivé senzory čtveřici skloněnou o úhel 13° kvůli zvýšení citlivosti jeho odezvy a prostorového rozlišení, které je $2,8$ μm ve směru od svazku [15].

2.2.2 Detektory času průletu částic

Detektory času průletu odchýlených protonů jsou umístěny pouze ve vzdálených stanicích. Pracují na principu tvorby Čerenkovského záření, které je detekované pixelovým mikrokanálkovým fotonásobičem. Časové rozlišení detektorů ToF je přibližně 20 ps [17]. Citlivá optická část detektorů ToF je tvořena maticí 4×4 optických tyčinek z křemenného skla

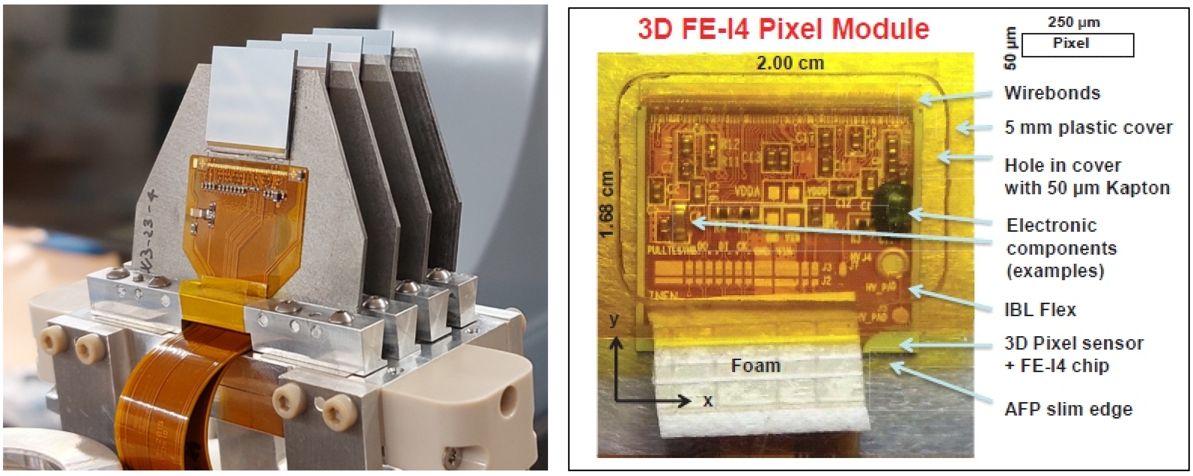

(a) (b)

Obrázek 2.5: Křemíkový detektor AFP: (a) detailní pohled na skupinu čtyř vrstev detektoru, (b) pohled na vyčítací čip FE-I4 [15].

(SK-1300 společnosti O'Hara) ve tvaru písmene 'L', Obrázek 2.6. Návrh a výroba celé této optické části proběhla na pracovišti SLO.

Optická část detektoru ToF byla navržena tak, že měřená částice prochází jednou čtveřicí tyčinek. Tyto řady (čtveřice) se označují výrazem *train* a jednotlivé řady se označují jako T1 (nejblíže ose svazku protonů), T2, T3, a T4. Tyčinky v každé řadě se označují písmeny A (první v pořadí ve směru svazku), B, C, a D. Na tomto základě se jednotlivé tyčinky označují 1A, 1B, apod. až 4D. Vnější rozměry této optické sestavy jsou 73,3 mm na výšku (ve směru od příruby), 65,5 mm na šířku, a 25,2 mm na hloubku. Celá sestava tyčinek je pootočena o úhel 48°, aby významná část Čerenkovova záření byla svedena po nejkratší dráze do fotonásobiče, viz Obrázek 2.6b. Rozměry tyčinek pro první prototyp jsou zveřejněny v [18]. Každá tyčinka slouží zároveň jako vyzařovač Čerenkovova záření (radiátor) a jeho světlovod do fotonásobiče. V místě zalomení tyčinek se nachází seříznutí o úhel 45° a na vzniklé ploše seříznutí je nanesena zrcadlová plocha z hliníku [18]. Komplikovaný tvar tyčinek je dán omezeným prostorem uvnitř Římského hrnce a snahou oddálit fotonásobič od svazku kvůli vysoké radiaci. Bližší informace ke geometrii tyčinek jsou podány v kapitole 5.

V první verzi detektoru, byly tyčinky vyráběny tak, že jednotlivá ramena tyčinky se vyráběla zvlášť a v místě spoje byly slepeny lepidlem s vysokou propustností v ultrafialové oblasti spektra (Epotek 305 [19]). Použití lepidla mělo negativní vliv na odezvu (propustnost) tyčinek. Přítomnost lepidla odfiltrovala část světelných pulzů pod 230 nm, tedy v oblasti, kde se nachází značná část vytvořeného Čerenkovova záření. Zvýšená radiace nadále zvyšovala absorpci lepidla - více podrobností je uvedeno níže v následující části. Lepením obou ramen navíc docházelo k odchylkám od požadovaného výsledného tvaru tyčinky, což se projevilo tím, že tyčinky nebyly precizně zarovnané vůči ostatním. Tento nedostatek byl spíše kosmetické povahy, na účinnost detektoru to mělo nepatrný vliv. Postupně byla technologie výroby tyčinek na našem pracovišti změněna tak, že bylo možné vyrábět tyčinky z jednoho kusu. Tím se odstranily všechny uvedené nedostatky. Především propustnost se zvýšila až o 60 % [20], což umožnilo zvýšit účinnost detekce a časové rozlišení.

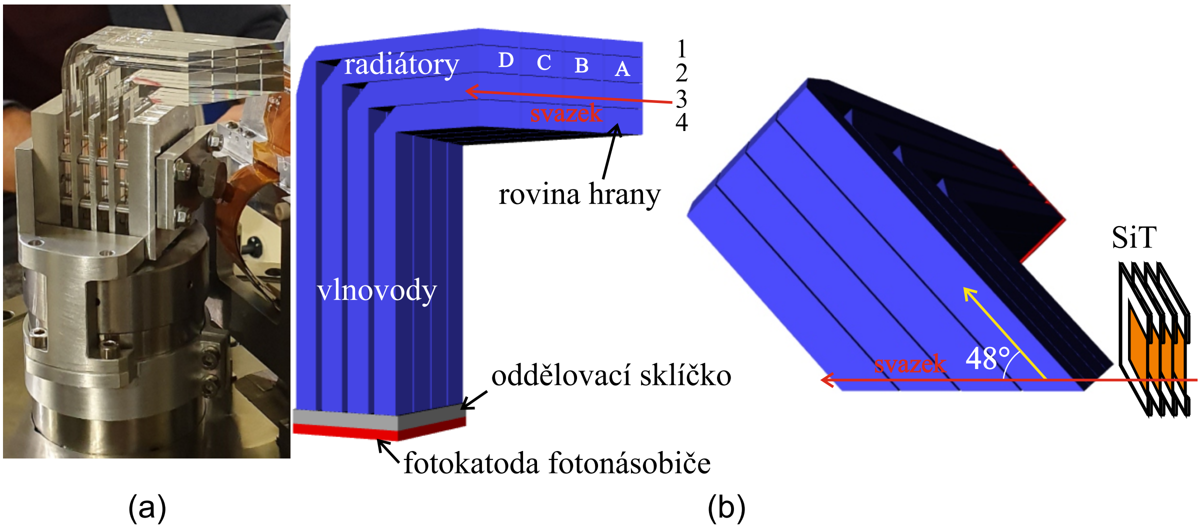

Obrázek 2.6: Detektor ToF: (a) pohled na nainstalovanou optickou část, (b) geometrické schéma, převzato z [17].

Geometrie tyčinek je nastavena tak, aby každá z nich vyvedla optický signál na jeden z 16-ti pixelů (kanálů) mikrokanálkového fotonásobiče miniPLANACON XPM85112 společnosti Photonis [21], Obrázek 2.7a. Základní parametry tohoto fotonásobiče jsou uvedeny v Tabulce 2.1 a kvantová účinnost jeho fotokatody je na Obrázku 2.7b. Její hodnoty jsou známe od 200 nm, ale očekává se, že je nenulová až do 160 nm (přibližná dolní mez citlivosti bialkalického materiálu fotokatody). Pro potřeby simulací byl tedy nakonec zvolen pracovní rozsah fotonásobiče 160 – 650 nm, přičemž v rozmezí 160 – 200 nm byla kvantová účinnost považována za konstantní s hodnotou na vlnové délce 200 nm. Během vývoje detektoru ToF jsme aktivně zasáhli do elektronické části fotonásobiče ve snaze optimalizovat jeho odezvu pro potřeby našeho detektoru [22]. Podrobnější informace o těchto změnách jsou uvedeny v kapitole 7 v rámci popisu modelování odezvy fotonásobiče.

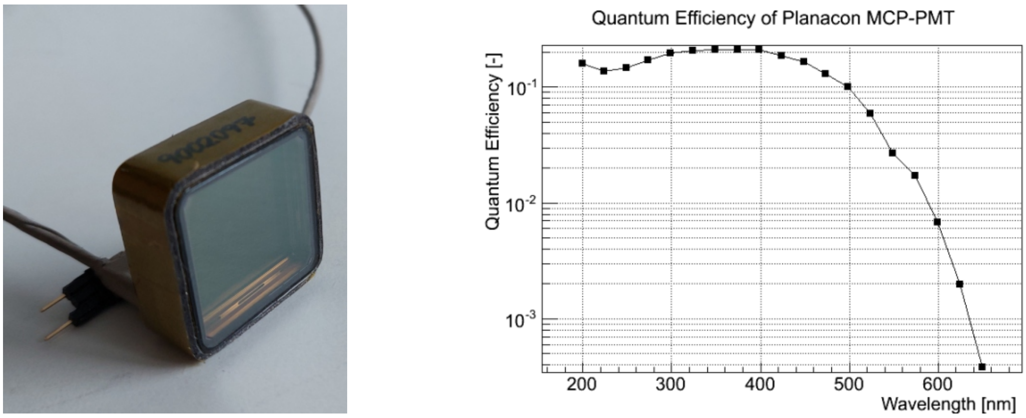

(a) (b)

Obrázek 2.7: (a) Mikrokanálkový fotonásobič miniPLANACON XPM85112 společnosti Photonis, (b) kvantová účinnost fotonásobiče (převzato z [18]).

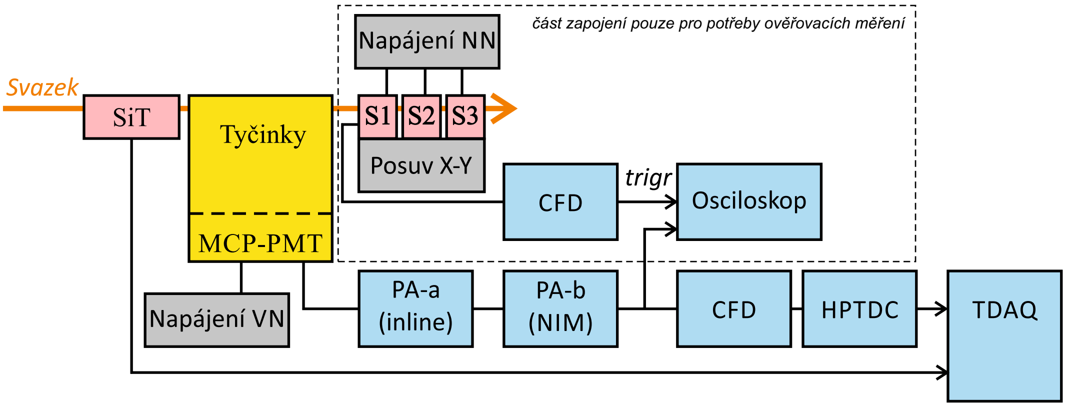

Obrázek 2.8: Zjednodušené schéma měřícího řetězce detektoru ToF v AFP.

Obecné zjednodušené schéma zapojení detektoru ToF do měřícího řetězce je ukázáno na Obrázku 2.8. Měřená částice po výstupu z trekru SiT prochází jednou z řad tyčinek de-

Tabulka 2.1: Parametry mikrokanálkového fotonásobiče miniPLANACON XPM85112 společnosti Photonis [21].

Parametr	**Hodnota/Popis**
Materiál vstupního okénka	syntetické křemenné sklo
Materiál fotokatody	Bialkali
Struktura MCP	2 vrstvy, 10 μm póry, L:D=60:1
Struktura anody	4×4, velikost pixelu $5,8 \times 5,8$ $\mathtt{mm}^2$, rozteč 6,4 mm
Aktivní plocha	25×25 $\mathtt{mm}^2$
Prostorová uniformita	max 2:1, typicky $< 1.5 : 1$
Čas náběhu pulzu	0,5 ns
Šířka pulzu	0,7 ns
TTS	max. 50 ps, typicky < 35 ps
Kolekční účinnost	0,6

tektoru ToF. V případě ověřovacích měření prochází částice trojicí referenčních detektorů ze SiPM s příčným aktivním průřezem 3×3 mm^2 [23]. První z nich, $S1$, se používal jako trigr událostí pro detektor ToF. Pomocí řízeného posuvného stolku se vybíraly jednotlivé zájmové oblasti tyčinek.

Signál vytvořený tyčinkami a registrovaný fotonásobičem je dále zesílen dvěma stupni předzesilovačů PA-a a PA-b. Jednotkou CFD (z angl. Constant Fraction Discriminator) je dále převeden na logický pulz s náběžnou hranou, jejíž časová značka je následně určena jednotkou HPTDC (z angl. High Precision Time-to-Digital Converter) a zpracována systémem TDAQ (z angl. Tigger and Data AQuisition). Pro měření na ověřovacích svazcích byl nejčastěji měřen výstup z PA-b, trigrovaný detektorem $S1$. V případě integračních testech s použitím obou detektorů SiT a ToF bylo použito synchronizovaného sběru dat z obou detektorů.

Tabulka 2.2: Očekávané dávky ozáření a toků částic v blízkosti urychlovače při luminozitě 100 fb^{-1}. Převzato z [6].

Vzdálenost od svazku	**5 mm**	**5 cm**	**70 cm**
Tok protonů	$< 5 \times 10^{15} cm^{-2}$	$5 \times 10^{12} cm^{-2}$	$1 \times 10^{11} cm^{-2}$
Ekvivalentní tok neutronů	$< 3 \times 10^{15} cm^{-2}$	$3 \times 10^{12} cm^{-2}$	$5 \times 10^{10} cm^{-2}$
Dávka	< 700 kGy	200 Gy	50 Gy

2.3 Radiační odolnost detektorů AFP

Vzhledem k faktu, že se citlivé měřící části detektoru přibližují na vzdálenost pouze několika málo milimetrů od osy svazku (tvořené nevychýlenými protony), je úroveň radiace velmi vysoká [6]. Bližší hodnoty očekávaných dávek a toků částic na celkovou luminozitu (intenzitu) svazku 100 fb^{-1} jsou uvedeny v Tabulce 2.2. Uvedená luminozita 100 fb^{-1} odpovídá celkové luminozitě svazku LHC v roce 2017.

Radiační odolnost křemíkových senzorů byla v minulosti úspěšně ověřena [24] a senzory se používají i v pixelovém subdetektoru IBL centrálního detektoru ATLAS [25]. Co se týče detektoru ToF, radiační odolnost a životnost fotonásobičů XPM85112 byla měřena různými skupinami v minulosti [26, 27]. Odolnost tyčinek i lepidla jsme proměřovali ve spolupráci Ústavem jaderné fyziky Akademie věd v Řeži, která k tomuto účelu poskytnula protonový svazek o energii 30 MeV na zdejším cyklotronu [28]. K tomuto účelu jsme použili kruhové vzorky o tloušťce 2 mm, některé z nich byly slepeny proměřovaným lepidlem (v tomto případě byla celková tloušťka skla tedy 4 mm). Vliv radiace byl sledován podle poklesu propustnosti vzorků vlivem degradace skla a lepidla. Výsledky jsou znázorněny na Obrázku 2.9. Odtud je zřejmé, že část tyčinek, která je velmi blízko svazku (tyčinky v Trainu 1), kde je celková roční dávka nad 700 kGy, trpí výrazným poklesem propustnosti. Avšak již následující řady, které jsou vystaveny řádově nižší dávce (přibližně 20 kGy), nevykazují významný pokles propustnosti. Degradace lepidla je oproti tomu znatelná, viz Obrázek 2.9b. Při dávce 20 kGy dochází ke znatelnému poklesu propustnosti o 30% v okolí vlnové délky 280 nm. Při započtení spektrální odezvy fotonásobiče a spektrálního rozložení Čerenkovova záření (obojí viz následující kapitola), byl celkový pokles po ročním běhu LHC v roce 2017 odhadnut na 11% při dávce 20 kGy.

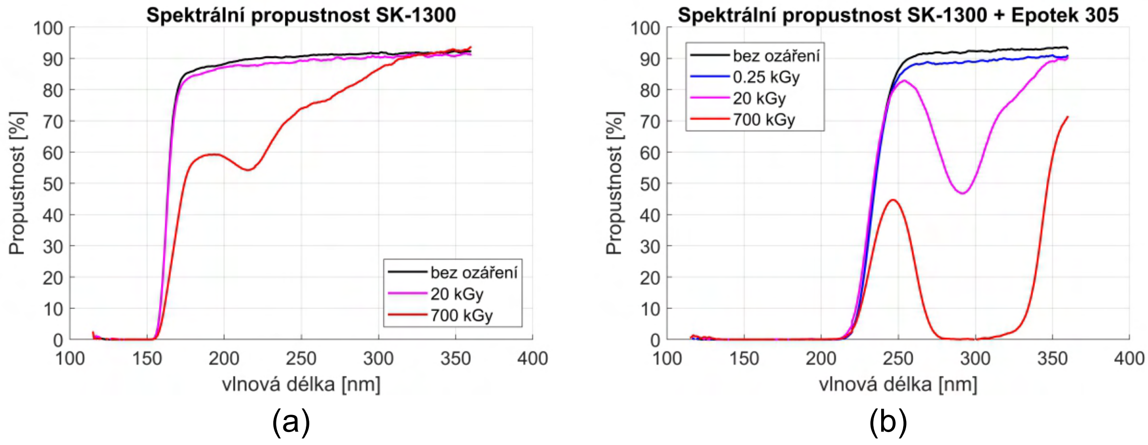

(a) (b)

Obrázek 2.9: Výsledky měření radiační odolnosti optické části detektoru ToF: (a) pokles propustnosti SK-1300 o tloušťce 2 mm, (b) pokles propustnosti SK-1300 s lepidlem Epotek 305 (celková tloušťka skla 4 mm). Dávka odpovídá celkové luminozitě 100 fb^{-1}. Převzato z [20].

2.4 Závěrečné poznámky ke konstrukci detektoru ToF

Více informací o konstrukci detektoru lze nalézt v [29, 30], vybrané výsledky z měření na testovacích svazcích v CERNu a DESY v [15, 31, 20]. Samostatnou prací při vývoji detektoru ToF představovaly fotonásobiče. Středem pozornosti bylo jejich časové rozlišení v závislosti na zisku a závislost jejich signálové odezvy na frekvenci přicházejících pulzů [32, 22]. Během nasazení AFP mezi roky 2017 až 2023 byla funkčnost detektoru ToF ověřována i přímo na svazku LHC. V roce 2017 trpěl detektor sníženou účinností do 10% [33] z důvodu překročení nejvyššího povoleného akumulovaného náboje na fotonásobičích, které činilo až 20 C. To vedlo k poklesu kvantové účinnosti jejich fotokatod a k degradaci mikrokanálkových destiček.

V souladu s tématem této práce jsou následujících kapitoly věnovány otázkám modelování nejdůležitějších částí detektoru ToF, tj. jeho optické části a odezvy fotonásobiče. Tyto simulace sloužily jednak k vývoji geometrie detektoru, tak k odhadu jeho celkové odezvy na výstupu fotonásobiče směrem k zesilovací elektronice. Následující část je blíže věnována základní problematice průchodu elektricky nabitých vysokoenergetických částic materiálem včetně emise Čerenkovova záření.

Kapitola 3

Princip detektoru ToF - emise Čerenkovova záření

Jak již bylo zmíněno v předchozí kapitole, je detektor ToF založen na jevu emise Čerenkovova záření při průchodu protonů materiálem křemenného skla. Tento jev je dobře popsán známou Frankovou-Tamnovou rovnicí. Z ní mimo jiné plyne charakteristický spektrální profil emitovaného záření který je výrazný v ultrafialové oblasti a počet vyzářených fotonů klesá s druhou mocninou vlnové délky. Navíc je světlo na dané vlnovou délce vyzařováno pod specifickým úhlem vzhledem k trajektorii částice, který závisí na indexu lomu prostředí. Na urychlovači LHC se v současné době (kampaň Run-3) využívá přednostně protonových svazků o celkové energii 6,8 TeV. Během vývoje se detektor ToF testoval na svazcích částic π^+ o energii 120 GeV urychlovače SPS (Super Proton Synchrontron) v laboratořích CERN a elektronech o energiích 5 GeV v DESY u Hamburku. Odpovídající hodnoty relativistických veličin $\beta = v/c$ (kde v je rychlost částic a c rychlost světla v vakuu) a Lorentzova faktoru $\gamma = 1/\sqrt{1-\beta^2}$ částic jednotlivých svazků jsou shrnuty v Tabulce 3.1. Ve všech případech je $\beta \approx 1$, jedná se tedy o vysokoenergetické relativistické částice.

Tabulka 3.1: Hodnoty poměru rychlosti částic k rychlosti světla β a Lorentzův faktor γ pro svazky, které byly použity pro testování detektoru ToF nebo pro konečné použití na LHC.

Urychlovač	**typ částice**	**klidová hmotnost**	**Energie**	γ [-]	$1-\beta$ [-]
LHC (CERN)	proton	938 MeV/c^2	6,8 TeV	7249	$9,52 \cdot 10^{-9}$
SPS (CERN)	π^+	139 MeV/c^2	120 GeV	863	$6,70 \cdot 10^{-7}$
DESY II	e^-	0,511 MeV/c^2	5 GeV	9784	$5,22 \cdot 10^{-9}$

3.1 Průchod energetických částic materiálem

Elektricky nabitá vysokoenergetická částice při průchodu materiálem interaguje s elektrony (volnými nebo vázanými) a s atomovými jádry okolního materiálu. Jestliže je procházející částice mnohem těžší než elektrony (např. protony, mezony π, atd.), jsou projevy interakcí s elektrony a jádry atomů rozdílné. S ohledem na velmi malou velikost jádra, vyplňují elektronové obaly atomů a molekul naprostou většinu prostoru materiálu. Lehké elektrony mohou při interakci s částicí odebrat značné množství energie aniž by významně odchýlily částici s původní trajektorie. Oproti tomu, těžká atomová jádra způsobují rozptyl procházející částice. Vzhledem k malým rozměrů jak jádra tak částice, je rozptyl v téměř naprosté většině případů elastický a omezený na malé rozptylové úhly. Těžké částice o vysoké energii si tedy prakticky zachovávají svou původní trajektorii při průchodu materiálem. Lehké částice jako elektrony nebo pozitrony interagují prakticky pouze s elektrony materiálového prostředí. Při těchto srážkách rychle ztrácejí svou energii a dochází k jejich rozptylu. V důsledku toho jsou mnohem snadněji pohlceny materiálem.

Na Obrázku 3.1 je schématicky znázorněn elastický rozptyl částice P, pohybující se rychlostí $\mathbf{v}$ podél osy z, na rozptylovém centru T materiálu (molekula nebo atom). Protože se jedná o elastický rozptyl, je na straně rozptylového centra zprostředkován jeho elektronovým obalem, který způsobuje energetické ztráty procházející částice a její rozptyl (který je pro těžké částice nepatrný). Úhel rozptylu částice θ závisí na kolmé vzdálenosti b trajektorie částice od T, která se nazývá *impaktní parametr*. Hodnota impaktního parametru je zdola omezena hodnotou $b_{min} = \hbar/(\gamma m_e v)$ [34], kde m_e je hmotnost elektronu, $\gamma = 1/\sqrt{1-\beta^2}$ je Lorentzův dilatační faktor, přičemž $\beta = v/c$ je poměr rychlosti částice

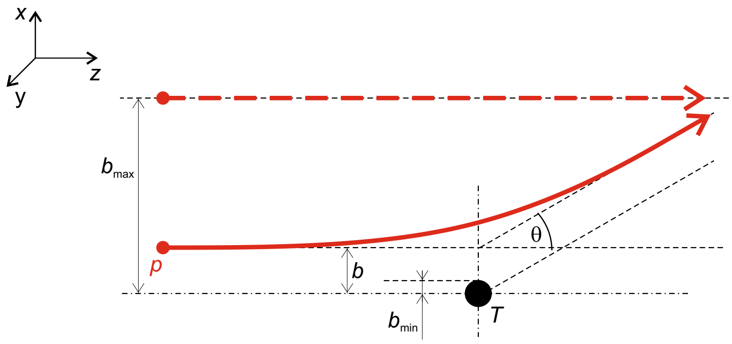

Obrázek 3.1: Schéma kolize částice p s částicí T materiálu.

v souřadnicovém systému T k rychlosti světla. S rostoucí vzdáleností b postupně úhel rozptylu klesá až při $b_{max} = \hbar\gamma v/\epsilon_{exc}$ klesne na nulu. Od této hodnoty výše tedy nedochází k ovlivnění částice p rozptylovým centrem T. Hodnota b_{max} závisí na minimální efektivní excitační energii ϵ_{exc} materiálu, která je v případě SiO_2 (molekula křemenného skla) 120 eV [35].

Pro uvedený dvoučásticový systém $P - T$ jsou hodnoty b_{min} a b_{max} srovnatelné s rozměry atomů a molekul. Ve skutečné materiálovém prostředí však dochází k ovlivňování procházející částice P molekulami v okolí uvažované rozptylové částice T. Elektromagnetické pole vytvářené procházející částicí způsobuje v materiálovém prostředí jejich polarizaci, a vzniklé dipóly zpětně ovlivňují pole generované částicí. Odpovídající hodnota b_{max} je tedy mnohem vyšší než jsou atomární rozměry, zvláště pro vyšší hodnoty γ procházející částice.

Elektromagnetické pole kolem nabité částice procházející materiálem lze pospat příslušnými Maxwellovými rovnicemi, zde uvedené v mikroskopické formě a v jednotkách CGS:

$$\begin{aligned}
\nabla \cdot \mathbf{E} &= \frac{4\pi}{\varepsilon}\rho \ , \\
\nabla \cdot \mathbf{B} &= 0 \ , \\
\nabla \times \mathbf{E} &= -\frac{1}{c}\frac{\partial \mathbf{B}}{\partial t} \ , \\
\nabla \times \mathbf{H} &= \frac{1}{c}\left(4\pi\mathbf{J} + \frac{\partial \mathbf{D}}{\partial t}\right) \ ,
\end{aligned} \tag{3.1}$$

kde **E** je intenzita elektrického pole, **H** intenzita magnetického pole, **D** elektrická indukce, **B** magnetická indukce, ρ hustota volného náboje (vlastní procházející částici), a **J** hustota volného elektrického proudu. Přitom platí materiálové vztahy: $\mathbf{D} = \varepsilon\mathbf{E}$ a $\mathbf{B} = \mu\mathbf{H}$, kde ε je relativní elektrická permitivita a μ relativní magnetická susceptibilita prostředí (relativní v jednotkách CGS). V dalším textu je relativní permitivita prostředí označena pojmem *dielektrická funkce* $\varepsilon(\omega)$, který odráží závislost odezvy materiálového prostředí skrze na dopadající elektromagnetické záření na jeho úhlové frekvenci ω.

Je-li náboj částice q a rychlost $\mathbf{v}$, pak lze psát:

$$\begin{aligned} \rho(\mathbf{r},t) &= q\delta(\mathbf{r} - \mathbf{v}t) \ , \\ \mathbf{J}(\mathbf{r},t) &= \mathbf{v}\rho(\mathbf{r},t) \ . \end{aligned} \tag{3.2}$$

Ekvivalentně lze Maxwellovy rovnice vyjádřit pomocí skalárního a vektorového potenciálu, $\varphi(\mathbf{r},t)$ a $\mathbf{A}(\mathbf{r},t)$, které jsou definovány vztahy:

$$\begin{aligned} \mathbf{B} &= \nabla \times \mathbf{A} \ , \\ \mathbf{E} &= -\nabla\varphi - \frac{\partial \mathbf{A}}{\partial t} \ . \end{aligned} \tag{3.3}$$

Dosazením rovnic (3.3) do (3.1) a použitím Lorenzovy kalibrační podmínky

$$\nabla \cdot \mathbf{A} + \frac{1}{c}\frac{\partial \varphi}{\partial t} = 0 \ , \tag{3.4}$$

nabývají Maxwellovy rovnice tvaru nehomogenních vlnových funkcí:

$$\begin{aligned} \nabla^2\varphi - \frac{1}{c^2}\frac{\partial^2\varphi}{\partial t^2} &= -\frac{4\pi}{\varepsilon}\rho \ , \\ \nabla^2\mathbf{A} - \frac{1}{c^2}\frac{\partial^2\mathbf{A}}{\partial t^2} &= -\frac{4\pi}{c}\mathbf{J} \ . \end{aligned} \tag{3.5}$$

Řešení těchto rovnic pro vyjádření elektromagnetického pole vytvářené pohybující se částicí se snázeji řeší převedením Fourierovou transformací [34] do příslušných Fourierových obrazů $\varphi(\mathbf{k},\omega)$ a $\mathbf{A}(\mathbf{k},\omega)$ (kde $\mathbf{k}$ je vlnový vektor, a ω úhlová frekvence):

$$\begin{aligned} \left[k^2 - \frac{\omega^2}{c^2}\varepsilon(\omega)\right]\varphi(\mathbf{k},\omega) &= \frac{4\pi}{\varepsilon(\omega)}\rho(\mathbf{k},\omega) \ , \\ \left[k^2 - \frac{\omega^2}{c^2}\varepsilon(\omega)\right]\mathbf{A}(\mathbf{k},\omega) &= \frac{4\pi}{c}\mathbf{J}(\mathbf{k},\omega) \ , \end{aligned} \tag{3.6}$$

kde $\rho(\mathbf{k},\omega) = q/(2\pi)\delta(\omega - \mathbf{kv})$ a $\mathbf{J}(\mathbf{k},\omega) = \mathbf{v}\rho(\mathbf{k},\omega)$. Fourierovy obrazy obou potenciálů jsou tedy rovny:

$$\begin{aligned} \varphi(\mathbf{k},\omega) &= \frac{2q}{\varepsilon(\omega)}\frac{\delta(\omega - \mathbf{kv})}{k^2 - \frac{\omega^2}{c^2}\varepsilon(\omega)} \ , \\ \mathbf{A}(\mathbf{k},\omega) &= \varepsilon(\omega)\frac{\mathbf{v}}{c}\varphi(\mathbf{k},\omega) \ . \end{aligned} \tag{3.7}$$

Známe-li hodnoty $\varphi(\mathbf{k},\omega)$ a $\mathbf{A}(\mathbf{k},\omega)$, dostaneme využitím vztahů (3.3) Fourierovy obrazy elektrické intenzity a magnetické indukce:

$$\begin{aligned}\mathbf{E}(\mathbf{k},\omega) &= i\left[\frac{\omega\varepsilon(\omega)}{c^2}\mathbf{v}-\mathbf{k}\right]\varphi(\mathbf{k},\omega)\ ,\\ \mathbf{B}(\mathbf{k},\omega) &= i\frac{\varepsilon(\omega)}{c}(\mathbf{k}\times\mathbf{v})\varphi(\mathbf{k},\omega)\ .\end{aligned}\tag{3.8}$$

Pro výpočet energetických ztrát částice P na rozptylovém centru T, které je vůči částici ve vzdálenosti b, je potřeba určit složky elektromagnetického pole částice v kolmé vzdálenosti b od její trajektorie:

$$\begin{aligned}\mathbf{E}(b,\omega) &= \frac{1}{(2\pi)^{3/2}}\int_k d^3k\mathbf{E}(\mathbf{k},\omega)e^{ibk_x}\ ,\\ \mathbf{B}(b,\omega) &= \frac{1}{(2\pi)^{3/2}}\int_k d^3k\mathbf{B}(\mathbf{k},\omega)e^{ibk_x}\ ,\end{aligned}\tag{3.9}$$

Dosazením rovnic (3.7) a (3.8) do rovnice (3.9), jsou složky elektromagnetického pole rovny [34]:

$$\begin{aligned}E_z(b,\omega) &= \frac{iq\omega}{c^2}\left(\frac{2}{\pi}\right)^{1/2}\left[1-\frac{1}{\beta^2\varepsilon(\omega)}\right]K_0(\lambda b)\ ,\\ E_x(b,\omega) &= \frac{q}{v}\left(\frac{2}{\pi}\right)^{1/2}\frac{\lambda}{\varepsilon(\omega)}K_1(\lambda b)\ ,\\ B_y(b,\omega) &= \varepsilon(\omega)\beta E_x(b,\omega)\ ,\end{aligned}\tag{3.10}$$

kde K_0 a K_1 jsou modifikované Besselovy funkce nultého a prvního řádu a

$$\lambda^2 = \frac{\omega^2}{v^2}\left[1-\beta^2\varepsilon(\omega)\right]\ ,\tag{3.11}$$

přičemž odmocnina výrazu na pravé straně je vybraná tak, aby faktor λ ležel ve čtvrtém kvadrantu. Ostatní složky elektromagnetického pole jsou v tomto případě rovny nule, tj. $E_y = 0$, $B_x = 0$, a $B_z = 0$.

Působením elektromagnetického pole částice dochází předáním části její kinetické energie na elektrony materiálového prostředí podél její trajektorie. Ve vzdálenosti a od osy trajektorie jsou ztráty rovny [34]:

$$\left(\frac{dE}{dx}\right)_{b>a} = \frac{1}{v}\frac{dE}{dt} = -\frac{ca}{2}\int_{-\infty}^{\infty}B_y(t)E_z(t)dt = -ca\int_0^{\infty}B_y^*(\omega)E_z(\omega)d\omega\ ,\tag{3.12}$$

Z výše uvedených vztahů vyplývá frekvenční závislost složek elektromagnetického pole procházející částice podle tvaru dielektrické funkce okolního materiálu. Tyčinky detektoru ToF jsou vyrobeny z křemenného skla (SiO_2). Na Obrázku 3.2a je graficky uvedena závislost indexu lomu tohoto materiálu podle datového listu výrobce O'Hara (v rozmezí 140-2500 nm) doplněné o výsledky v [36] v rozmezí 90-140 nm, ze kterých je zřejmé, že v okolí vlnové délky 100 nm dochází k rezonanční odezvě materiálu na působící elektromagnetické pole doprovázené jeho zvýšeným útlumem. Extinční koeficient k začíná růst už pod 170 nm, ale až pod 140 nm překročí hodnotu 10^{-5}, přičemž je nárůst velmi strmý. Tuto vlnovou délku lze tedy považovat za hraniční, pod kterou se stává SK-1300 prostředím se zvýšenou absorpcí. Odpovídající frekvenční závislost dielektrické funkce je na Obrázku 3.2b.

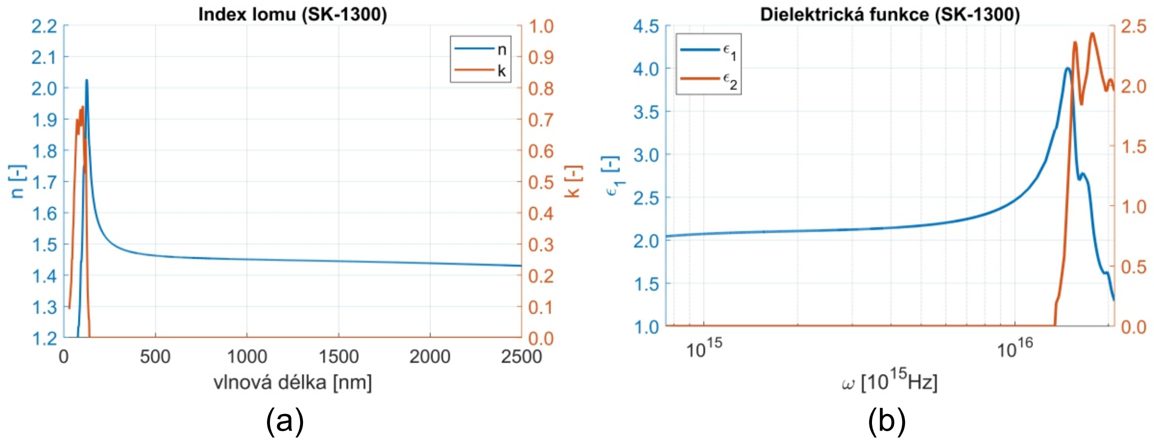

Obrázek 3.2: Optické konstanty křemenného skla SK-1300: (a) experimentální hodnoty indexu lomu dle datového listu výrobce O'Hara (v rozmezí 140-2500 nm) doplněné o výsledky v [36] v rozmezí 90-140 nm, (b) odpovídající frekvenční spektrum dielektrické funkce.

Faktor λ je komplexní veličina závislá tvaru dielektrické funkce. Jeho důležitou vlastností je, že je čistě imaginární, pokud je útlum prostředí minimální. Jeho frekvenční závislost je pro případ skla SK-1300 na Obrázku 3.11a. Červená oblast vyznačuje pracovní oblast fotonásobiče pro potřeby detektoru ToF (viz též předchozí kapitola 2.2.2).

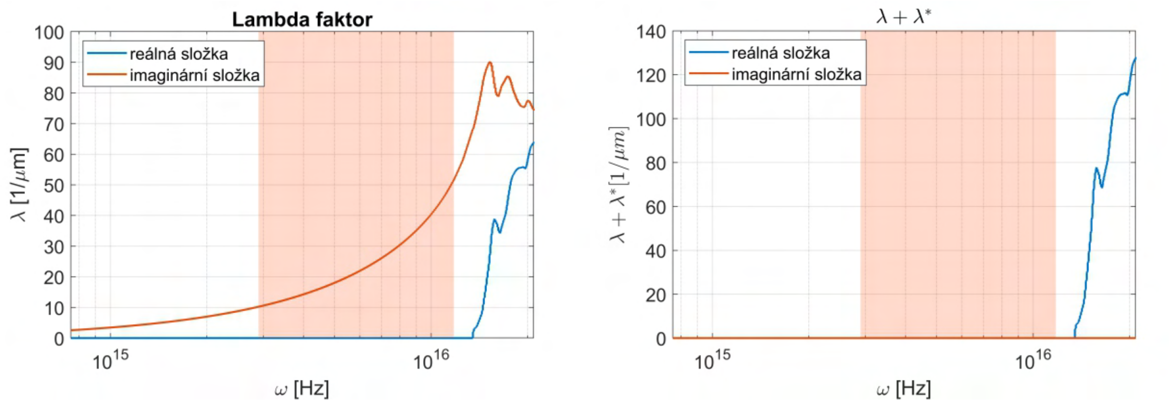

(a) (b)

Obrázek 3.3: (a) Spektrální závislost λ-faktoru pro sklo SK-1300, (b) součet $\lambda + \lambda^*$ vyskytující se v exponentu výpočtu vyzářené energie. Červená oblast vyznačuje pracovní oblast fotonásobiče pro potřeby detektoru ToF.

3.2 Čerenkovovo záření v SK-1300

Emise Čerenkovova záření odpovídá energetickým ztrátám ve velké vzdálenosti od procházející částice. Pro $|\lambda a| \gg 1$ lze Besselovy funkce vyjádřit asymptoticky jako $K_\alpha(x) \to \sqrt{\pi/2}e^{-x}/\sqrt{x}$ a vztahy (3.10) přejdou do tvaru:

$$\begin{aligned} E_z(b,\omega) &= \frac{iq\omega}{c^2}\left[1 - \frac{1}{\beta^2\varepsilon(\omega)}\right]\frac{e^{-\lambda b}}{\sqrt{\lambda b}} \ , \\ E_x(b,\omega) &= \frac{q}{v\varepsilon(\omega)}\sqrt{\frac{\lambda}{b}}e^{-\lambda b} \ , \\ B_y(b,\omega) &= \varepsilon(\omega)\beta E_x(b,\omega) \ , \end{aligned} \tag{3.13}$$

Z podmínky $|\lambda a| \gg 1$ lze při znalosti λ-faktoru odhadnout minimální hodnotu impaktní vzdálenosti b, od které lze toto vyjádření použít. Besselovy funkce K_0 a K_1 lze nahradit uvedeným asymptotickým výrazem pro $\lambda b \approx 2.5$. Pro SK-1300 je $\min(|\lambda|) = 2,6\ \mu\text{m}^{-1}$. Odtud plyne, že b_{min} musí být alespoň rovno 1 μm.

Na Obrázku 3.4 jsou pro zajímavost vykresleny frekvenční obrazy složek elektromagnetického pole pro $b = 1\ \mu m$ ve skle tvořené procházejícím protonem s $\gamma = 7247$ (tj. o energii 6,8 TeV). Všechny složky vykazují silné oscilace reálných a imaginárních částí v závislosti na frekvenci. S rostoucí frekvencí roste hodnota imaginární složky λ s ní i míra

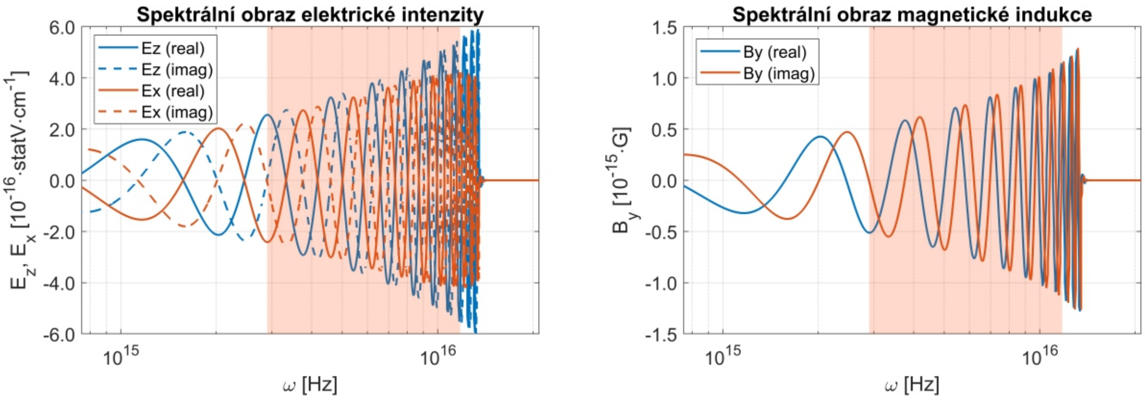

(a) (b)

Obrázek 3.4: Frekvenční obrazy složek elektromagnetického pole vytvářeného protonem o $\gamma = 7247$ (6,8 TeV) v křemenném skle SK-1300 (ve vzdálenosti $b_{min} = 10^{-4}$ cm). Červená oblast vyznačuje pracovní oblast fotonásobiče pro potřeby detektoru ToF.

oscilací (ke stejnému jevu dochází při rostoucím b). Od frekvence $1,35{\cdot}10^{16}$ Hz odpovídající vlnové délce 140 nm, kde narůstá absorpce SK-1300, významně vzroste reálná složka λ-faktoru, Obrázek 3.3a. To způsobí vymizení složek elektromagnetického pole ve větších vzdálenostech pro vyšší frekvence.

Energii vyzářenou ve vzdálenosti $a = b_{min}$ od částice lze odvodit dosazením vztahů (3.13) do rovnice (3.12). V diferenciálním tvaru je rovna:

$$\frac{dE}{dxd\omega} = \frac{q^2\omega}{c^2}\left(-i\sqrt{\frac{\lambda^*}{\lambda}}\right)\left[1 - \frac{1}{\beta^2\varepsilon(\omega)}\right]e^{-(\lambda+\lambda^*)a}\ . \tag{3.14}$$

Graficky je spektrální závislost vyzářené energie uvedena na Obrázku 3.5a. V oblasti, kde má faktor λ svou reálnou část blízké nule, je spektrum nezávislé na a, neboť součet $\lambda + \lambda^*$ v exponentu rovnice (3.14) je roven nule, viz též Obrázek 3.3b. Nad hraniční frekvencí se projeví rostoucí reálná složka tohoto součtu, která má za následek rychlý pokles vyzářené energie směrem k nule, jak již naznačují frekvenční spektra elektromagnetického pole (Obrázek 3.4). Odtud je tedy zřejmé, že ve skle SK-1300 se Čerenkovovo záření emituje od vlnové délky 140 nm. Obecněji lze konstatovat, že extinční koeficient k musí být menší než 10^{-5}, aby bylo možné pozorovat Čerenkovo záření v makroskopickém měřítku.

Vyjádříme-li vyzářenou energii na konkrétní frekvenci v počtu fotonů N, tj. $E = N\hbar\omega$, můžeme z využitím vztahu $dE{=}\hbar\omega dN$ a rovnice pro energii fotonu $dEn = \hbar d\omega$ vyjádřit

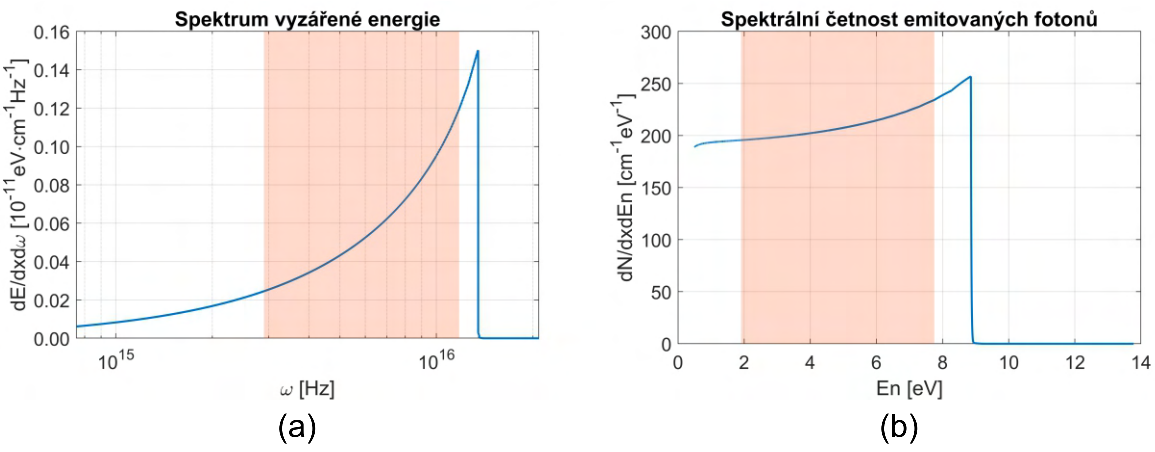

Obrázek 3.5: (a) Spektrum vyzářené energie protonem o $\gamma = 7247$ (6,8 TeV) v křemenném skle SK-1300, (b) četnost emitovaných fotonů Čerenkovova záření. Červená oblast vyznačuje pracovní oblast fotonásobiče pro potřeby detektoru ToF.

emisní spektrum v počtu fotonů:

$$\frac{dN}{dxdE_n} = \frac{q^2}{\hbar^2 c^2} \left(-i\sqrt{\frac{\lambda^*}{\lambda}} \right) \left[1 - \frac{1}{\beta^2 \varepsilon(\omega)} \right] e^{-(\lambda+\lambda^*)a} \, . \tag{3.15}$$

Graficky je spektrum četnosti emitovaných fotonů znázorněno na Obrázku 3.5b. Odtud lze integrací přes pracovní oblast detektoru ToF spočítat celkový počet fotonů, které vzniknou průchodem tyčinkou detektoru ToF. Efektivní vzdálenost průchodu jednou tyčinkou je přibližně 8,07 mm. Tomu odpovídá celkový počet přibližně 1430 vyzářených fotonů.

Z požadavku na hodnoty λ-faktoru se silně potlačenou reálnou složkou plyne, že ke vzniku Čerenkovova jevu musí platit $\lambda^2 < 0$. Podle rovnice 3.11 je tato podmínka splněna, pokud je imaginární (absorpční) složka $\varepsilon(\omega)$ nulová (v praxi velmi blízká nule) a $\beta^2\varepsilon(\omega) > 1$, tj.

$$v > \frac{c}{\sqrt{\varepsilon(\omega)}} = \frac{c}{n} \, . \tag{3.16}$$

Toto je známá podmínka vzniku Čerenkovova záření, totiž, že rychlost částice v prostředí musí být větší než rychlost světla v tomto prostředí. Vhledem k disperzi materiálového prostředí, je tato podmínka závislá na frekvenci. Protože v oblasti emise Čerenkovova záření platí $\lambda \approx -i|\lambda|$, je v rovnicích (3.14) a (3.15) výraz $-i\sqrt{\lambda^*/\lambda} \approx -i \cdot i = +1$ a výraz $\lambda + \lambda^* \approx 0$, jak již bylo naznačeno výše (viz též Obrázek 3.3b). Tím se obě rovnice zjednoduší:

$$\begin{aligned} \frac{dE}{dxd\omega} &= \frac{q^2\omega}{c^2}\left[1-\frac{1}{\beta^2\varepsilon(\omega)}\right] \\ \frac{dN}{dxdE_n} &= \frac{q^2}{\hbar^2c^2}\left[1-\frac{1}{\beta^2\varepsilon(\omega)}\right] \ , \end{aligned} \tag{3.17}$$

což jsou dvě možná vyjádření téže *Frankovy-Tammovy rovnice.*

Směr šíření Čerenkovova záření je dán směrem Poyntingova vektoru $\mathbf{E}\times\mathbf{B}$. Úhel směru šíření vůči trajektorii částice je dán vztahem $\mathrm{tg}\theta_c = -E_1/E_2$. Použitím rovnic (3.13) lze získat vztah:

$$\cos\theta_c = \frac{1}{\beta\sqrt{\varepsilon(\omega)}} = \frac{1}{\beta n} \ . \tag{3.18}$$

S rostoucí vlnovou délkou index lomu skla SK-1300 klesá, viz Obrázek 3.2a, tím klesá i úhel emitovaného záření θ_c, jak je to zřejmé z Obrázku 3.6a. V oblasti od 160–1000 nm se θ_c mění výrazně v rozmezí $46° - 56°$, což se negativně projevuje na způsobu vedení světelného pulzu tyčinkami detektoru ToF. Detailnější rozbor vlivu disperze je v následující kapitole. Pro konstrukci detektoru zvolen úhel 48°, který přibližně odpovídá vlnové délce 300 nm. Tato vlnová délka byla zvolena jako kompromis s ohledem na kvantovou účinnost fotonásobiče, Obrázek 2.7b. Díky symetrii jsou fotony v rovině kolmé na trajektorii částice vyzařovány rovnoměrně (rovnoměrné rozdělení úhlů φ projekce Poyntigova vektoru v rovině $x - y$). Výsledkem je, že pro danou vlnovou délku tvoří Čerenkovovo záření kužel s vrcholovým úhlem $2\theta_c$.

Pro zajímavost je na Obrázku 3.6b uvedeno srovnání minimální celkové energie částice ve svazcích urychlovačů LHC, SPS, a DESY II pro vyvolání Čerenkovova jevu (viz též Tabulka 3.1). Například pro elektrony je její hodnota 0,690 MeV, tj. při klidové hmotnosti elektronu 0,511 MeV/c^2 je jeho minimální kinetická energie 0,179 MeV pro vyvolání Čerenkovova jevu v křemenném skle.

Na závěr této kapitoly je v následující Tabulce 3.2 uvedena celková bilance pro detektor ToF při průchodu částic z výše uvedených urychlovačů (viz též Tabulka 3.1). Bez ohledu na typ svazku (protože u všech platí, že $\beta \approx 1$) je celková vyzářená energie v jedné tyčince přibližně 7 keV. Protože částice procházející detektorem projde vždy jednou ze čtyř řad detektoru se čtyřmi tyčinkami, ztratí vyzářením celkem přibližně 28 keV. V oblasti vlnových délek 160–650 eV se vytvoří přibližně 1000 fotonů.

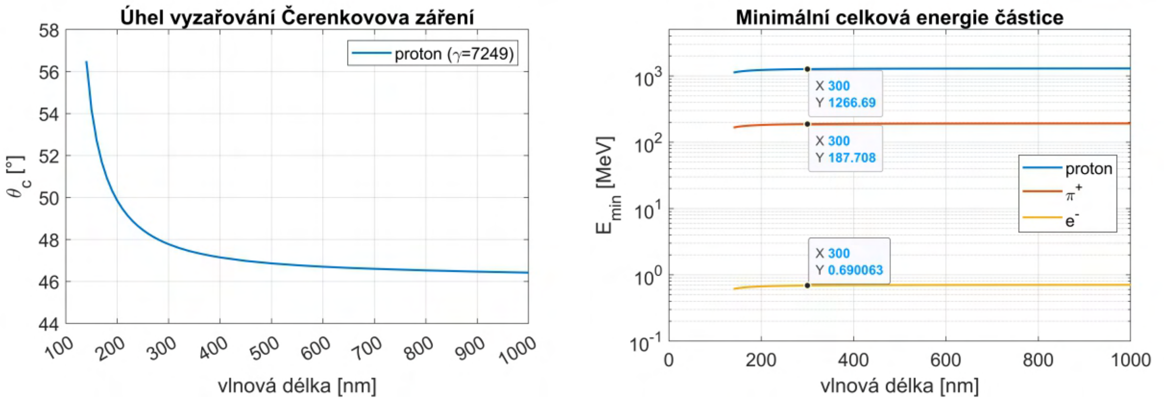

(a) (b)

Obrázek 3.6: (a) Úhel vyzařování Čerenkovova záření v křemenném skle SK-1300 pro částici s $\beta \approx 1$ (zde proton o energii 6,8 TeV), (b) minimální celková energie částic svazku urychlovačů týkajících se detektoru ToF pro AFP. Pro orientaci jsou navíc zobrazeny hodnoty v [MeV] na vlnové délce 300 nm.

Tabulka 3.2: Celková bilance vyzářených ztrát v detektoru ToF při průchodu jedné částice svazku z urychlovačů LHC, SPS a DESY II.

Parametr	**Hodnota**
Celková vyzářená energie (tyčinka/ToF)	$\approx$ 7 keV/28 keV
Celkový počet vyzářených fotonů (tyčinka/ToF)	$\approx$ 1430/5720
Relativní ztráta energie částice průchodem přes ToF	
proton (6,8 TeV)	$4 \cdot 10^{-7}$ %
π^+ (120 GeV)	$2 \cdot 10^{-5}$ %
elektron (5 GeV)	$6 \cdot 10^{-4}$ %
v rozmezí vlnových délek 160–650 nm:	
Celková vyzářená energie (tyčinka/ToF)	$\approx$ 5 keV/20 keV
Celkový počet vyzářených fotonů (tyčinka/ToF)	$\approx$ 1000/4000

Kapitola 4

Modelování v nástroji Geant4

Jádrem všech simulací, které jsou představeny v následujících dvou kapitolách, je software který autor této práce vyvinul v modelovacím nástroji Geant4 [37]. Předmětem této části je pouze krátce představit tento nástroj. Na oficiálních internetových stránkách je k dispozici několik dokumentů, které blíže popisují způsob jeho použití stejně jako fyzikální pozadí řešení problematiky interakce částic s hmotou. Zkrácený popis nástroje lze také nalézt v [38].

Geant4 je simulační nástroj typu Monte Carlo. Jedná se o softwarový produkt vyvíjený mnoha spolupracujícími institucemi v čele s CERN, ESA (European Space Agency), SLAC (Stanford Linear Accelerator Center) a HIP (Helsinki Institute of Physics). V současné době je hojně používán vědeckými pracovišti zabývajícími se problematikou fyziky vysokých energií (CERN, SLAC, Fermilab apod.). Umožňuje simulovat rozsáhlé experimenty, které tato pracoviště realizují (např. projekt ATLAS, CMS, DELPHI) a pomáhat tak při jejich úpravách a odstraňování některých problémů. Geant4, v současné době ve verzi 11.2.1 (v roce 2024), je v podstatě knihovna tříd v jazyce C++, jejichž použitím se vytváří simulační program ve formě spustitelného souboru. Každá z těchto tříd implementuje určitou specifickou část kódu simulace a jejich vhodným "poskládáním" a úpravami se v jazyce C++ vytváří kód určený pro danou simulaci. Otevřený kód zároveň umožňuje ve specifických případech editovat již existující implementaci (viz např. [39]).

Každá třída definovaná v Geant4 popisuje specifický problém spojený se simulací. Podle toho je lze zařadit do jedné z následujících skupin (z pohledu autora této práce):

- **Řízení běhu simulace**: kategorie tříd vztahující se k řízení běhu simulace a vytváření událostí,
- **Řízení trasování**: skupina tříd, které řídí krokování (trasování) běhu simulace. Sledují šíření všech částic existujících v daném kroku simulace a uplatňují na nich relevantní fyzikální procesy.
- **Částice a materiály**: třídy této skupiny umožňují specifikovat částice a materiály použité pro konstrukci modelu detektoru. Samostatnou částí jsou třídy pro definici magnetického pole v částech detektoru.
- **Fyzikální procesy**: tato skupina sdružuje třídy popisující všechny fyzikální procesy, které se účastní interakcí mezi částicemi.
- **Geometrie a rozhraní pro CAD**: třídy spravující geometrii detektorů a vzájemnou polohu jejich dílčích prvků. Geant4 obsahuje návrhář geometrických objektů založený na standardu ISO STEP, a je tak slučitelný se systémy CAD.
- **Záznam dat**: třídy v této kategorii pomáhají se sběrem dat a s uložením do vhodného formátu podle potřeb uživatele, nejčastěji se jedná o formát ROOT [40].
- **Vizualizace a uživatelské rozhraní**: tato kategorie zahrnuje třídy spravující vizualizaci detektoru a trajektorií částic a zadávání příkazů pro řízení simulace. Dále usnadňují komunikaci s ostatními softwarovými technologiemi, např. s databázovými systémy OODBMS, MySQL apod.

Projekt simulace detektoru ToF se nachází na úložišti *https://gitlab.cern.ch/nozka/-AfpToF.git.* Začal jako samostatný projekt, ale časem se velká část kódu přenesla do softwarového prostředí Athena, oficiálního softwarového nástroje projektu detektoru ATLAS na LHC. V současnosti projekt simulace obsahuje 40 souborů s kódem jazyka C++ včetně sedmi souborů s kódem pro zpracování výstupu nástrojem ROOT. Celkově je projekt tvořen přibližně 9500 řádky kódu.

Simulační program v sobě obsahuje experimentální hodnoty indexu lomu materiálu skla SK-1300. Ostatní specifikace materiálu pro potřeby modelování interakce částic svazků

LHC, SPS a DESY-II jsou součástí jádra nástroje Geant4 [1]. Co se týče modelu chování fotonásobiče, simulace obsahuje experimentálně určenou kvantovou účinnost fotokatody použitých fotonásobičů dle [41].

Simulační program umožňuje modelovat rozličné konstrukční varianty tyčinek optické části [18] se snadným nastavením jejich geometrie. Jedním z výstupů programu jsou podklady pro technické výkresy jednotlivých tyčinek a soubory pro vizualizaci ve standardu VRML. Stěžejním výstupem jsou datové soubory formátu *.root*, který se běžně používá v částicové fyzice. Datové soubory poskytují rozličné záznamy týkajících se tvořeným pulzů Čerenkovova záření, zásahů fotonů fotokatodou fotonásobiče a další podpůrná metadata. V následující kapitole jsou veškeré výstupy vytvořeny makry nad těmito výstupy.

---

[1] Pro tyto účely je nutné zadat složení materiálu a jeho hustotu.

Kapitola 5

Šíření světelného pulzu optickou části detektoru ToF

Jak plyne z Obrázku 2.6 na straně 11, je optická část detektoru ToF postavena do cesty odchýleným protonům tak, že každá z těchto částic prochází vždy právě jednou ze čtyř řad tyčinek, které se označují T1, T2, T3, a T4 (zkratka z anglického slova *Train*). Nejblíže se ose svazku LHC (svazek nevychýlených protonů) přibližuje řada T1. V dané řadě částice postupně prochází čtyřmi tyčinkami A, B, C, a D, tj. v případě řady T1 jsou to tyčinky 1A – 1D apod. pro ostatní řady. Každá z tyčinek má tvar písmene *L*. Jeden konec tyčinek je seříznut o referenční Čerenkovův úhel 48°. Odpovídající rameno tyčinky se označuje jako *radiátor*. Seříznutá hrana radiátoru se označuje jako *hrana tyčinky*. Naproti tomu druhá část tyčinky dosedá na fotonásobič a nese označení *světlovod*. Každá z tyčinek má své jedinečné rozměry tak, že seříznuté hrany tyčinek leží v jedné specifické rovině, která nese označení *rovina hrany detektoru*.

V místě zalomení tyčinek jsou tyčinky seříznuté v úhlu 45° a na seříznuté ploše je nanesena odrazná vrstva hliníku zaručující odraz světla do světlovodu. V tomto standardním uspořádání mají tyčinky v obou ramenech příčný průřez 5 × 6 mm^2 (šířka 5 mm z pohledu přicházející částice), takže délka trajektorie částice v jedné tyčince je 6 mm$/sin(48°) = 8,07$ mm. Rozměry tyčinek se v průběhu let do určité míry měnily, v Příloze A jsou uvedeny výrobní výkresy tyčinek určené pro poslední nasazení na LHC v kampani Run-3 (2022 – 2025). Největší tyčinkou je 1A jejíž délka ramen je 65,5 mm (radiátor) a 73,3 mm. Naopak nejkratší tyčinkou je 4D s rozměry 29,3 mm a 62,0 mm. Každé tyčince optické části detektoru ToF odpovídá podle návrhu jeden pixel fotonásobiče o rozměru $5,8 \times 5,8$ mm^2, který primárně detekuje světelný pulz vycházející z dané tyčinky. V další části textu se pixely odpovídající dané tyčince označují příponou 'P-' ke značce tyčinky, např. P-1A apod.

Ve specifické geometrii tyčinek podstupuje emitované světlo sérii odrazů na jejich stěnách a poté dopadá na fotokatodu fotonásobiče. Ačkoliv lze analyticky vysledovat trajektorii jednotlivých fotonů [42], je pro komplexnější popis vhodnější modelování vhodným softwarovým nástrojem typu Monte Carlo, jakým je nástroj Geant4. V následujících částech této kapitoly jsou použity výsledky simulací v tomto nástroji. Většina z nich byla publikována v rámci autorských publikací věnovaných vývoji detektoru ToF. Simulace byly určené ke srovnání s experimenty na urychlovači SPS a DESY-II, ve kterých byl použit refereční trigrovací detektor s akceptancí 3×3 mm^2, viz též Obrázek 2.8 na straně 12. Proto byl během modelování používán simulovaný svazek s odpovídajícím čtvercovým příčným průřezem.

5.1 Šíření světelného pulzu tyčinkou ToF

Odchýlené protony vstupují do tyčinky v určité vzdálenosti od její hrany, Obrázek 5.1a. V závislosti na vlnové délce se pod různými úhly šíří z trajektorie částice fotony Čerenkovova záření, kterých připadá přibližně 1000 na každou tyčinku. Část z nich se na druhý konec tyčinky dostane přímo přes odraz v místě zalomení, část nich se do fotonásobiče dostane několikanásobným totální odrazem o stěny tyčinek, Obrázek 5.1b. Tyčinky řad T1 a T2 jsou navíc vybaveny dodatečným zkosením o 18°, Obrázek 5.1c, který část světelného svazku směruje přímo k fotonásobiči. Uvedený úhel zkosení byl stanoven na základě modelování. Podrobnější informace lze nalézt v [18]. Vedlejším důsledkem dodatečného úkosu je snížení šířky radiátoru tyčinky. Pro tyčinky určené pro Run-3 je toto snížení na 3 mm v řadách T1 a T2. Toto zúžení je částečně vykompenzované širší řadou T4 (5,5 mm). Jednotlivé konfigurace tyčinek pro různá nasazení se rozlišují právě šířkou jednotlivých řad. Například pro testovací měření byly původně vyrobeny tyčinky v konfiguraci (postupně od T1 k T4) 2-5-5-5 mm. Pro kampaň LHC Run-2 (2015 – 2018) to byla konfigurace 2-4-5-5,5 mm (lepené tyčinky). V následujícím jsou diskutovány výsledky modelování nad konfigurací nelepených tyčinek 3-3-5-5,5 mm určenou pro poslední instalaci na urychlovači LHC (kampaň Run-3).

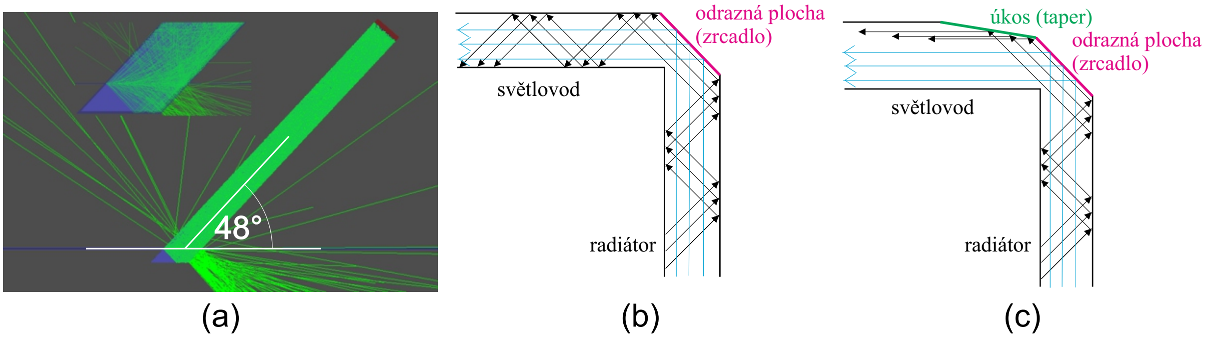

Obrázek 5.1: (a) Vizualizace emise Čerenkovova záření v simulačním nástroji Geant4, (b) detail postupu optického signálu přes standardní zalomení tyčinky přímo (modré šipky) nebo totálním odrazem (černé šipky), (c) totéž s přídavným úkosem.

Jak je patrné z Obrázku 5.1a, část vzniklých fotonů postupuje k hraně tyčinky, kde se odrazí a postupuje směrem k druhému konci. Avšak část z nich opustí tyčinku dříve, než dosáhne hrany a vstoupí do následující tyčinky, kde se odrazí od její hrany a směřuje druhou tyčinkou, Obrázek 5.2a. V závislosti na vzdálenosti trajektorie částice od hrany tyčinky, může část fotonů proniknout až do vzdálenějších tyčinek a stát se součástí signálu z těchto tyčinek nebo zcela opustí optickou část detektoru ToF. Míra zastoupení ”parazitních”fotonů v tyčince je patrná na příkladu tyčinky 1B na Obrázku 5.2b [31], která přijímá část fotonů emitovaných v tyčince 1A. Zde je třeba poznamenat, že výsledky v tomto grafu jsou založeny na použití svazku částic o čtvercovém příčném průřezu diskutovaném výše. Vzdálenost svazku v simulaci byl nastaven tak, že vzdáleností od svazku na ose x se míní vzdálenost bližší hrany svazku. Střed svazku je o 1,5 mm dál od hrany. Důvodem bylo sladění s experimenty a zachování statistiky nabíraných dat.

Z grafu vyplývají dvě skutečnosti. Za prvé, s rostoucí vzdáleností částice od hrany tyčinky klesá počet fotonů, které dorazí na konec světlovodu (k fotonásobiči) v téže tyčince, přičemž od 4 mm se tento pokles zastaví. Za druhé, největší podíl parazitních fotonů z

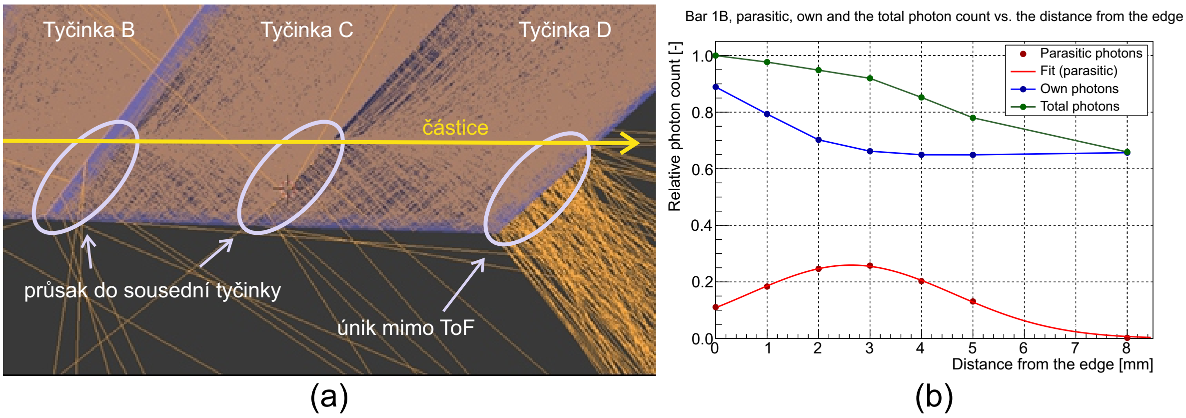

Obrázek 5.2: Optický průsak mezi tyčinkami v rámci téže řady v blízkosti hrany tyčinky: (a) vizualizace v nástroji Geant4, (b) relativní příspěvek parazitních fotonů z tyčinky 1A v tyčince 1B (převzato z [31]).

předchozí tyčinky nastává ve vzdálenosti 3 mm od hrany detektoru (střed svaku 4,5 mm od hrany). Poté s rostoucí vzdáleností jejich podíl klesá, protože přecházejí až do dalších tyčinek v řadě. Z obrázku je také patrné, že největší počet fotonů se dostane k fotonásobiči, pokud se trajektorie částice nachází v blízkosti hrany tyčinky (zelená křivka v grafu).

K optickému průsaku částečně dochází i na druhé straně tyčinek. V oddělovacím sklíčku o tloušťce 2,9 mm mezi tyčinkami a fotonásobičem část fotonů přejde do prostoru, který spadá po pixel fotonásobiče přiléhající jedné ze sousedních tyčinek. Tento optický přeslech způsobuje registraci světelných pulzů i do pixelů sousedních řad (kudy částice neprochází).

Důsledkem obou optických průsaků je chování tyčinek z hlediska vedení světla silně provázané a to především v rámci dané řady, jak je ukázáno na příkladu 1. řady v souhrnné Tabulce 5.1 pro vzdálenost částice 5 mm od hrany tyčinek. Z tabulky je patrné, že z 1000 emitovaných fotonů pouze 18–19 % fotonů vytvořených tyčinkou dopadne na odpovídající pixel fotonásobiče. Přibližně 10 % fotonů přijmou následující dvě tyčinky. Do ostatních řad proniknou 2–3 % fotonů. Zničeno nebo pohlceno je přibližně 70–80 %vytvořených fotonů. Do detektoru se dostane přibližně 30 % emitovaných fotonů z tyčinek A, B a C, a 20 % fotonů vytvořených v tyčince D. S přibližující se vzdáleností částice k hraně tyčinek stoupá množství fotonů dopadajících na pixel odpovídající tyčince kde byly vyzářeny, konkrétně na hraně tyčinky je to 29 % a pouze 5 % přechází a zužitkuje se v sousedních tyčinkách.

Přibližně 60 % fotonů je ztraceno. Z celkového počtu 1000 fotonů na tyčinku se jich tedy k fotonásobiči dostane 200–300 za každou tyčinku v zasažené řadě a to závislosti na vzdálenosti trajektorie částice od hrany detektoru ToF. V řadách tyčinek T3 a T4 bez přídavného zkosení je počet přijatých tyčinek přibližně poloviční, na fotonásobič dostane přibližně 100–150 fotonů na tyčinku.

Tabulka 5.1: Poměrné zastoupení fotonů vytvořených v tyčinkách řady T1 na pixelech fotonásobiče včetně zničených (pohlcených materiálem nebo opuštivších detektor). Hodnoty jsou vztaženy k celkovému počtu ≈ 1000 vytvořených fotonů a pro vzdálenost částice 5 mm od hrany detektoru ToF.

Tyčinka	**P-1A**	**P-1B**	**P-1C**	**P-1D**	**Ostatní**	**Zničeno/Pohlceno**
1A	19%	7%	3%	1%	3%	66%
1B	1%	18%	7%	3%	3%	68%
1C	0%	1%	19%	7%	2%	71%
1D	0%	0%	1%	19%	2%	78%

Vlivem různě dlouhých trajektorií fotonů při jejich cestě tyčinkou k fotonásobiči, které budou blíže diskutovány v další části, a díky disperzi, se výsledný světelný pulz na druhém konci tyčinky v čase natáhne do 600 ps. Pro srovnání, procházející částicí trvá necelých 108 ps než projde celou řadou tyčinek, tj. 27 ps na jednu tyčinku. První a nejvýznamnější část tvoří fotony, které přichází v přímém směru. To se týká fotonů, jejichž Čerenkovský úhel leží v blízkosti referenčního úhlu, tj. 48°±2°. Při pohledu na Obrázek 3.6a na straně 26 je zřejmé, že se jedná fotony s vlnovými délkami nad 200 nm.

Z časového hlediska má geometrie tyčinek důležitou vlastnost kompenzace časového rozposunutí vytvořených fotonů vlivem rozdílných časů emise během působení částice, viz Obrázek 5.3. Podle obrázku je mezi prvními emitovanými fotony v tyčince A a posledními emitovanými fotony v tyčince D časový rozdíl L/c. Aby první fotony byly od druhého konce tyčinky stejně vzdáleny jako fotony poslední a dosáhly fotonásobiče ve stejný čas, musí během této doby urazit dráhu s. Čas potřebný k dosažení této vzdálenosti je:

$$\tau = \frac{ns}{c} = \frac{nL\cos\alpha}{c} \ , \tag{5.1}$$

kde $\alpha = \theta_c(300\ nm) = 48^\circ$ je referenční Čerenkovův úhel. Protože podle (3.18) platí $\cos\alpha = 1/n$, plyne odtud:

$$\tau = \frac{L}{c}\ , \tag{5.2}$$

což je rovno době průchodu částice tyčinkami. Časové rozdíly ve vyzařování fotonů jsou tedy efektivně kompenzovány geometrií tyčinek. Všechny tyčinky v řadě tedy přenesou vytvořený světelný pulz ve stejném čase do fotonásobiče.

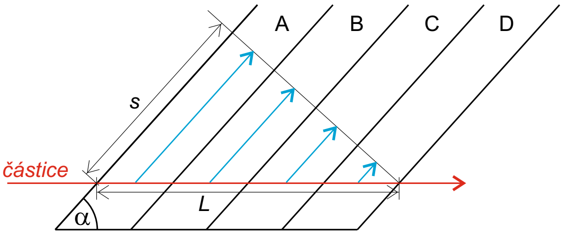

Obrázek 5.3: Princip kompenzace času emitovaného světelného pulzu v řadě tyčinek při průchodu primární částice.

5.2 Tvar a spektrum optického pulzu

Vlivem disperze a relativně složitého tvaru tyčinek se optický signál nešíří tyčinkou triviálně a dochází k jeho natažení v čase. Podél trajektorie prolétávající částice je Čerenkovovo záření emitováno ve tvaru kužele s vrcholovým úhlem $\theta = 2\theta_c(\lambda)$ podle vztahu (3.18) a s rovnoměrným rozdělením úhlu φ v rovině kolmé na trajektorii částice, viz definice úhlů na Obrázku 5.4 a zelenkavá křivka na Obrázku 5.5.

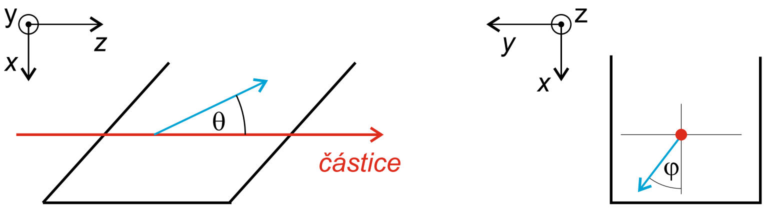

Obrázek 5.4: Definice směru emise fotonů podél trajektorie částice pomocí úhlů θ a φ.

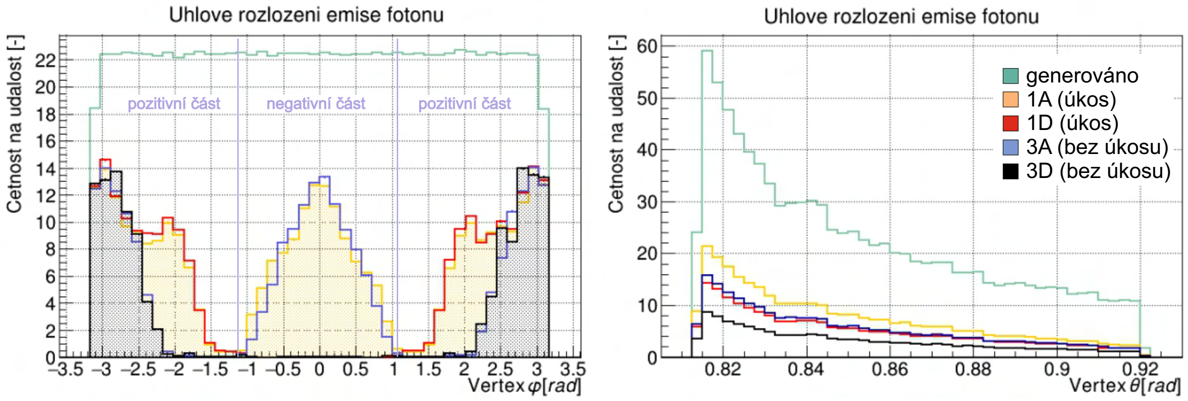

(a) (b)

Obrázek 5.5: Rozdělení úhlů (a) φ a (b) θ fotonů v místě jejich vzniku (ve vrcholu/vertexu) v tyčinkách 1A, 1D, 3A a 3D, které se dostaly na fotokatodu fotonásobiče. Vzdálenost svazku protonů o energii 6,8 TeV byla 5 mm od okrajů tyčinek.

Vlivem geometrie tyčinek se na fotokatodu fotonásobiče dostanou pouze fotony vyzářené pod určitým úhlem φ a s různou pravděpodobností, jak je vidět na Obrázku 5.5a. Histogramy byly vytvořeny pro fotony vyzářené tyčinkami 3A a 3D bez úkosu a 1A a 1D s úkosem, a za použití svazku protonů (6,8 TeV) ve vzdálenosti 5 mm od kraje tyčinek [1]. Jsou odtud zřejmé dvě oblasti rozložení φ. První, pozitivní část, odpovídá směrům přímého šíření fotonů tyčinkou směrem k fotonásobiči. Druhá, negativní část, odpovídá směrům šíření opačným směrem (odtud označení pozitivní a negativní část). Fotony negativního směru se šíří směrem k hraně tyčinky, kde se odrazí a směřují k fotonásobiči. Díky 5 mm vzdálenosti od hrany se fotony tyčinek A nedostanou k jejich hranám a odrazí se až v tyčinkách B, jak bylo již diskutováno v předchozí části. Negativní část tyčinek A je tedy tvořena fotony, které byly registrovány v pixelech přiléhajících k tyčinkám B (převážně), C a D. Naopak, fotony vyzářené tyčinkami D a jdoucí ke hraně tyčinek, opouštějí ToF a proto těmto tyčinkám chybí negativní část v úhlovém rozložení φ. Pro svazek procházející blízko hrany tyčinek se negativní část distribuce objevuje i u tyčinek D. Dále je z obrázku zřejmé, že dodatečné zkosení u tyčinek 1A a 1D způsobuje navýšení fotonů emitovaných pod úhly

---

[1] Je nutno vzít v potaz, že se jedná o vzdálenost nejbližší strany čtvercového profilu svazku jak je vysvětleno na začátku kapitoly.

$\varphi \approx \pm(1,2-2,5)$ rad (v pozitivní části rozdělení). Oproti tomu, rozdělení úhlů θ fotonů, které se dostaly na fotokatodu, viz Obrázek 5.5b, sleduje rozložení vlivem disperze indexu lomu, jak je tomu na Obrázku 3.6a na straně 26.

Na následujícím Obrázku 5.6 jsou dva příklady rozložení úhlů φ v závislosti na době příchodu fotonů na fotokatodu fotonásobiče pro pixely P-3B a P-1B. Z obrázku je vidět, že Čerenkovský pulz je široký přibližně 600 ps s tím, že většina z nich přichází během 400 ps. Z Obrázku 5.6b je patrné navýšení počtu fotonů na tyčince 1B vlivem zkosení, které přichází s větším zpožděním v čase mezi 100–600 ps po příchodu prvních (přímých) fotonů.

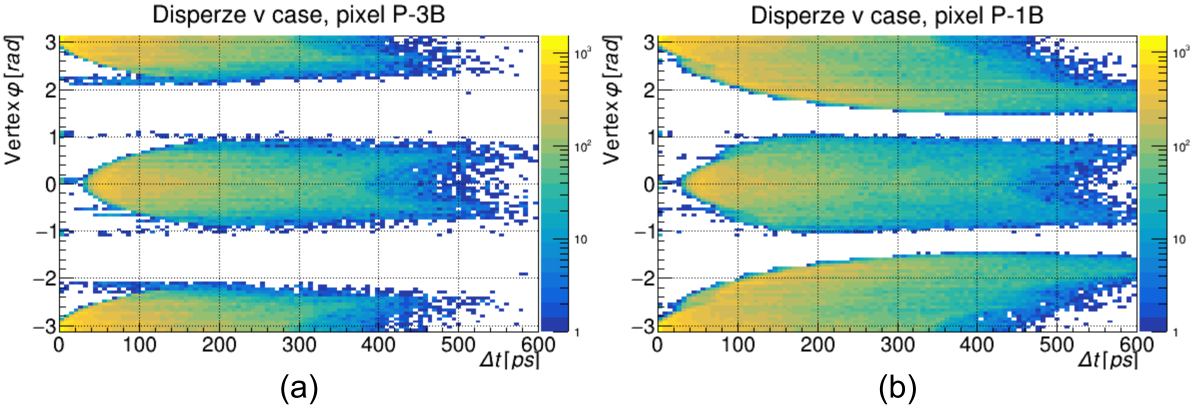

Obrázek 5.6: Rozdělení úhlů φ v závislosti na době příchodu fotonů na fotokatodu fotonásobiče pro (a) pixel P-3B (řada tyčinek bez úkosu), (b) pixel P-1B (s úkosem). Vzdálenost svazku protonů o energii 6,8 TeV byla 5 mm od okrajů tyčinek. Čas Δt je doba průchodu tyčinkou a je počítaný od příchodu prvního fotonu na fotokatodu.

Vliv disperze skla SK-1300 je patrný především z časového rozložení příchodů fotonů do fotonásobiče v závislosti na jejich vlnové délce, jak je vidět na Obrázku 5.7a na příkladu tyčinky 3A. Fotokatoda fotonásobiče konvertuje dopadnuvší fotony na fotoelektrony v závislosti na své kvantové účinnosti. Je-li průměrná kvantová účinnost přibližně 15 % a kolekční účinnost 0,6, vytvoří se v zasažených částech fotokatody přibližně 10–30 fotoelektronů na jeden pixel. Přesnější odhad podává výstup ze simulace na Obrázku 5.7b, kde je znázorněn časový rozvoj vytvořených fotoelektronů pro pixely tyčinek A a D z řad T1 a T3. Ve vysvětlivkách k obrázku jsou také uvedeny odhady počtu vytvořených fotoelektronů. Tyčinky s přídavným zkosením svým zvýšeným optickým prostupem zvyšují četnost vytvořených fotoelektronů faktorem 1,7–1,8, což se příznivě projevuje na zlepšení časového rozlišení detektoru. Protože však zkosení způsobuje snížení šířky radiátoru tyčinky, není možné zkosení provést ve všech čtyřech řadách detektoru aniž by došlo ke zmenšení jeho akceptačního okna.

Je nutné poznamenat, že výsledky uvedené v této kapitole jsou založeny na vyzařování Čerenkovova záření samotnou primární částicí. Sekundární částice, vzniklé působením odlišných fyzikálních procesů na primární částici v materiálu tyčinek, vyzařují dodatečné Čerenkovovo záření, které přispívá do celkové bilance počtu fotonů. Tomuto tématu se věnuje následující kapitola.

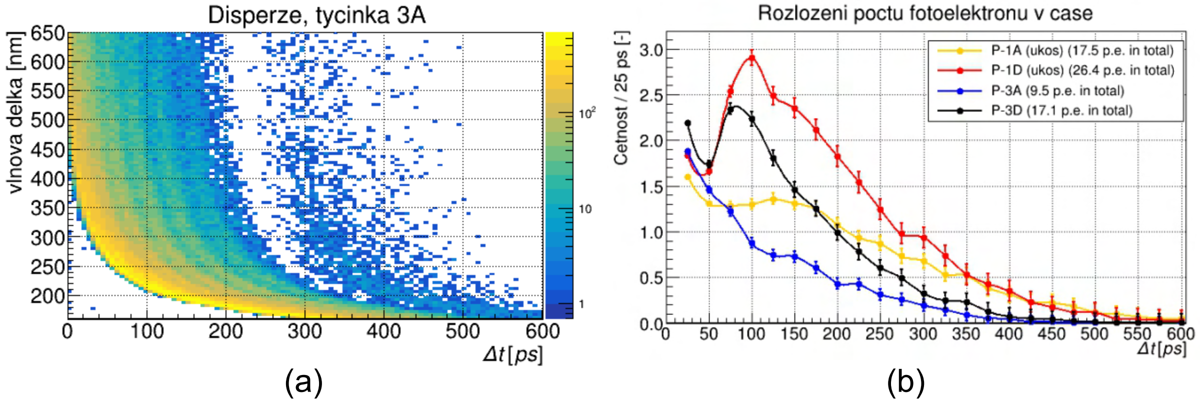

Obrázek 5.7: (a) Vliv disperze SK-1300 na době příletu fotonů na fotokatodu fotonásobiče (v příkladu tyčinky 3A a pixelu P-3A), (b) časový rozvoj počtu fotoelektronů registrovaných fotonásobičem s kvantovou účinností dle [41] pro vybrané pixely. Vzdálenost svazku protonů o energii 6,8 TeV byla 5 mm od okrajů tyčinek. Čas Δt je doba průchodu tyčinkou a je počítaný od příchodu prvního fotonu na fotokatodu.

Kapitola 6

Vliv sekundárních částic na odezvě detektoru ToF

V předchozí části bylo předpokládáno, že procházející nabitá částice ztrácí energii pouze procesem vyzařování Čerenkovova záření. Protože všechny tři typy částic LHC, SPS a DESY-II mají stejný elektrický náboj a $\beta \approx 1$ u všech, je jejich odezva v tomto směru stejná. Během průchodu materiálem částice podstupují hned několik fyzikálních interakcí, které způsobují ztrátu jejich kinetické energie. Může docházet k ionizaci materiálu (tj. uvolnění elektronů z valenčního pásu molekul), k vyvolání brzdného záření (bremsstrahlung) ve formě gama záření, které může zpětně podstoupit fotoelektrický jev nebo Comptonův rozptyl s uvolněním dalších elektronů apod. Při těchto procesech vznikají spršky sekundárních částic, které, pokud jsou nabité a mají dostatečnou kinetickou energii, mohou samy vyzařovat Čerenkovovo záření.

Vlivem sekundárních částice se skupina ToF začala intenzivněji zabývat od roku 2018, kdy se kvůli dlouhodobé odstávce urychlovače SPS v CERNu přesunula měření do laboratoří DESY u Hamburku, kde je v provozu synchrotron DESY-II produkující svazek elektronů o energiích 1-8 GeV [43]. Některé výsledky těchto studií byly publikovány v [20] a v této kapitole jsou uvedeny v rozšířenější podobě.

Na Obrázku 6.1 je zobrazen příklad průchodu elektronu o energii 5 GeV tyčinkami detektoru ToF s viditelnými trajektoriemi vzniklých sekundárních částic. Míra kontaminace Čerenkovovým zářením způsobené sekundárními částicemi závisí na výši energetických

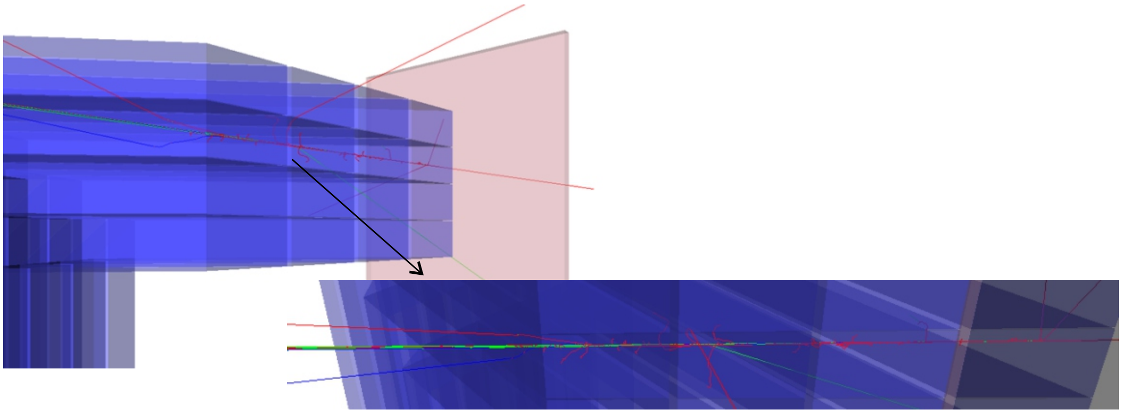

Obrázek 6.1: Vizualizace průchodu elektronu o energii 5 GeV tyčinkami detektoru ToF s viditelnými trajektoriemi vzniklých sekundárních částic.

ztrát primární částice svazku v materiálu a ta je závislá na typu a energii procházející primární částice. Dá se očekávat, že lehké elektrony svazku DESY-II budou v materiálu tyčinek produkovat bohatší spršky sekundárních částic, které významně ovlivní celkovou bilanci počtu fotonů, které dopadnou na fotokatodu fotonásobiče po projití tyčinkami.

Rozdělení energetických ztrát pro všechny tři typy svazků je zobrazeno na Obrázku 6.2a. Odtud je zřejmé, že elektrony svazku DESY-II vykazují výrazně vyšší ztráty své energie oproti LHC a SPS, a se zvýšenou pravděpodobností (přibližně 10/2000=0.5 %) jsou zachyceny v tyčinkách. Ztráty částic svazků LHC a SPS jsou nanejvýš do 500 MeV, přičemž většinou se jedná o hodnoty 50 MeV a nižší, Obrázek 6.2b. Jak vyplývá z Tabulky 3.2 na straně 26, ztráty v důsledku vyzařování Čerenkovova záření tvoří pouze zlomek celkových ztrát v materiálu tyčinek.

Vlivem energetických ztrát klesá celková hybnost primární částice a dochází k jejímu odchýlení od původního směru. Ta je v případě svazku LHC v jednotkách mikroradiánů, jak naznačuje Obrázek 6.3a. Vezmeme-li typickou hodnotu vychýlení 1 μrad, bude to na vzdálenosti 12 m mezi blízkými a vzdálenějšími stanicemi AFP, Obrázek 2.3, znamenat posun o 12 μm, což je o řád vyšší hodnota než je rozlišení detektoru SiT, které je 2,8 μm. To je jeden z důvodů, proč nebyly detektory ToF instalovány v blízkých stanicích.

V případě testovacího svazku SPS je důležité znát úhlovou disperzi odchozích primárních

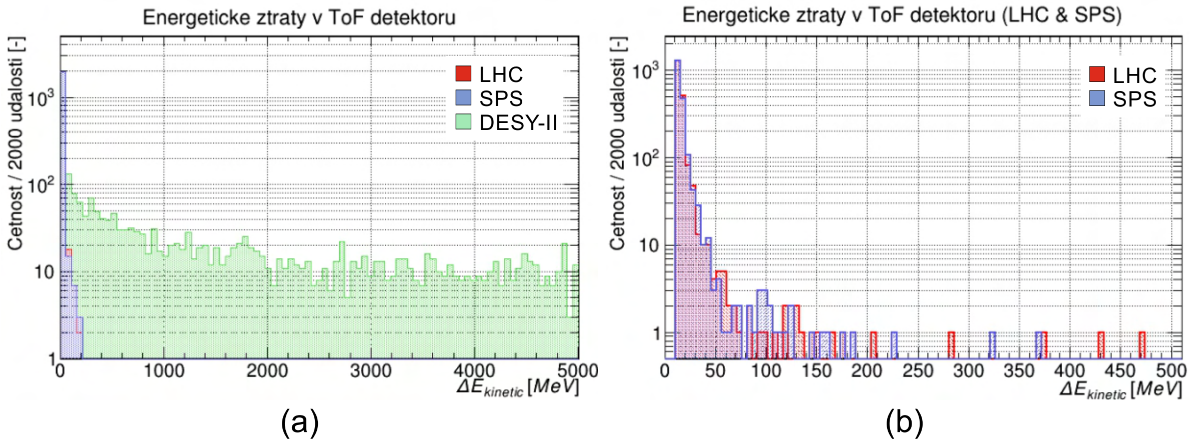

Obrázek 6.2: (a) Energetické ztráty částic svazků LHC (proton, 6,8 TeV), SPS (π^+, 120 GeV) a DESY-II (e^-, 5 GeV) v jedné řadě tyčinek detektoru ToF, (b) detail ztrát pro LHC a SPS.

částic z důvodu následné detekce referenčními trigrovacími detektory SiPM, které jsou vzdáleny od detektoru až o 30 cm po svazku. Ty jsou mimo jiné používány k ověřování účinnosti detekce detektoru ToF. Na svazku SPS je rozptyl až o dva řády vyšší než pro LHC, do 250 μrad, typicky 60 μrad, Obrázek 6.3b. Přesto je to dostatečně málo na to, aby se tím ovlivnila měření účinnosti detektoru ToF, pro které byla hraniční hodnota stanovena na 200 μrad v rovině referenčních detektorů.[1]

Úhlová disperze odchozích primárních elektronů svazku DESY-II je oproti svazku SPS ještě o další řád vyšší až do 10 mrad a typicky 2 mrad, Obrázek 6.3c. Tento fakt komplikoval instalaci detektoru na testovacích měřeních v DESY, neboť bylo nutné minimalizovat vzdálenost referenčních detektorů od detektoru ToF. V typické vzdálenosti 30 cm je rozptyl v průměru 0,6 mm a často vyšší (do 3 mm), což bylo nepřijatelné. V minimální možné vzdálenosti 70 mm je odchylka 0,14 mm, ale často až 0,7 mm.

V následujícím je uveden detailnější pohled na vliv sekundárních částic pro jednotlivé urychlovače zvlášť.

---

[1] Hodnotě 200 μrad odpovídá odchylka 60 μm na 30 cm, což byla typická vzdálenost detektorů SiPM od ToF. Přesnost instalace těchto detektorů nebyla lepší než 0,1 mm.

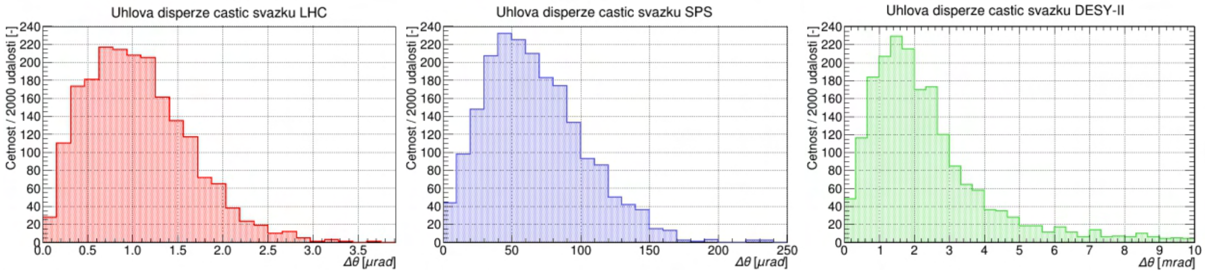

(a) (b) (c)

Obrázek 6.3: Úhlová disperze primárních částic vlivem interakcí v materiálovém prostředí detektoru ToF vyjádřeno úhlem odchýlení od nominální trajektorie. Histogramy jsou vytořeny postupně pro (a) primární částice protonů o energii 6,8 TeV svazku LHC, (b)) primární částice π^+ o energii 120 GeV svazku SPS, a (c) primární částice elektronů o energii 5 GeV svazku DESY-II.

6.1 Sekundární částice vzniklé průchodem protonu 6,8 TeV

Proton svazku LHC o celkové energii 6,8 TeV vykazuje energetické ztráty do 500 MeV, viz Obrázek 6.2b. Bližší rozbor simulace ukazuje, že jsou tyto ztráty způsobeny ionizací elektronů vázaných v materiálu skla SK-1300. Ionizací získají elektrony kinetickou energii a postupují materiálem. Tyto elektrony tvoří první generaci sekundárních částic. Obrázek 6.4a ukazuje statistické rozdělení počáteční kinetické energie těchto uvolněných elektronů. Výtěžnost sekundárních elektronů první generace je v průměru dN_e/dx=24 mm^{-1}. Tyto volné elektrony samy interagují s materiálem. Ionizací způsobují uvolnění dalších elektronů z materiálu nebo procesem brzdného záření (bremsstrahlung) emitují fotony gama záření (obojí tvoří částice druhé generace). Ty buď na základě fotoelektrického jevu nebo Comptonova rozptylu uvolňují další elektrony, které mohou podstoupit zmíněné procesy a vytvořit sekundární částice vyšších generací. Výsledkem je sprška energetických částic, která se šíří tyčinkami detektoru ToF. Rozložení energií sekundárních částic od druhé generace a výše je na Obrázku 6.4b a jejich výtěžnost vzhledem k trajektorii primární částice je souhrnně uvedena v Tabulce 6.1.

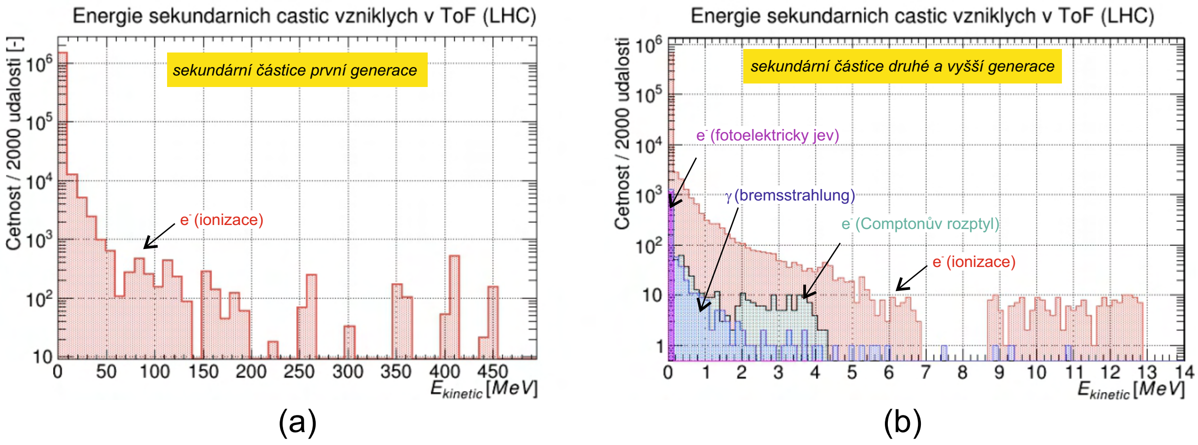

Obrázek 6.4: (a) Rozdělení kinetické energie elektronů uvolněných interakcí primární částice protonu o energii 6,8 TeV s materiálem křemenného skla jedné řady tyčinek (první generace sekundárních částic), (b) rozdělení kinetické energie sekundárních částic druhé a vyšší generace, které následně vznikly interakcí sekundárních elektronů první generace se stejným prostředím.

Podle výstupů z předchozí kapitoly, viz též Obrázek 3.6b na straně 26, elektrony o celkové energii 0,690 MeV a vyšší, tj. o kinetické energii 0,179 MeV a vyšší, vyzařují Čerenkovo záření. To tvoří dodatečný příspěvek do celkové bilance vytvořených fotonů, které doputují do fotonásobiče. V Tabulce 6.1 je uvedena výtěžnost těchto elektronů s procentuálním zastoupením vzhledem k celkovému počtu dané generaci. Odtud je zřejmé, že dodatečné Čerenkovo záření je tvořeno převážně elektrony první generace. Výtěžnost dodatečných fotonů je přibližně 130 na jednu tyčinku, to je 11 % z celkově vytvořených fotonů. Na fotokatodu se dostane přibližně 20 fotonů na tyčinku (7 % z celkového počtu). To odpovídá přibližně třem dodatečně vytvořeným fotoelektronům.

Na Obrázku 6.5a je detailnější pohled na úhlovém rozložení směru vyzářených fotonů vzhledem ke směru šíření primární částice. Rozložení fotonů vyzářených primární částicí (červeně) sleduje profil podle Obrázků 3.6a (strana 26) a 5.5b (strana 36). V případě fotonů vyzářených sekundárními částicemi je distribuce mnohem širší (světle modře), což naznačuje, že sekundární částice se šíří v rozličných směrech. Geometrií tyčinek jsou některé směry dále potlačeny a na fotokatodu se světlo z některých směrů nedostane, konkrétně v

Tabulka 6.1: Druhy sekundárních částic vzniklých průchodem protonu o celkové energii 6,8 TeV materiálem SK-1300 a jejich výtěžnost vzhledem k trajektorii primární částice. Zvlášť je uvedena výtěžnost těch částic (elektronů), které mají kinetickou energii dostatečnou k vyvolání Čerenkovova záření.

Druh částice	**Proces vzniku**	**Působící částice**	**Výtěžnost dN/dx**
První generace:			
e^-	ionizace	proton	24 mm^{-1}
e^- $(E_k > 0,179$ MeV$)$			3,4 mm^{-1} (14 %)
Druhá a vyšší generace:			
e^-	ionizace	e^-	11 mm^{-1}
γ	bremsstrahlung	e^-	0,02 mm^{-1}
e^-	fotoel. jev	γ	0,02 mm^{-1}
e^-	Comptonův rozptyl	γ	0,008 mm^{-1}
e^- $(E_k > 0,179$ MeV$)$			0,17 mm^{-1} (1,5 %)

oblasti nad 2,6 rad (150°) jak ukazuje sytě modře zbarvená distribuce.

Na Obrázku 6.5b je podrobněji znázorněno srovnání příspěvku primární částicí a sekundárních částic v rámci rozložení vytvořených fotoelektronů v čase. Srovnání je provedeno pro pixely P-2A a P-2D druhé řady tyčinek s úkosem. S postupující a rozvíjející se spрškou se dá očekávat větší relativní příspěvek sekundárních částic v zadní tyčince 2D oproti tyčince 2A. Ten je přibližně 1,3 (2D/2A), což je nižší nárůst oproti případu s primární částici s navýšením 1,5.

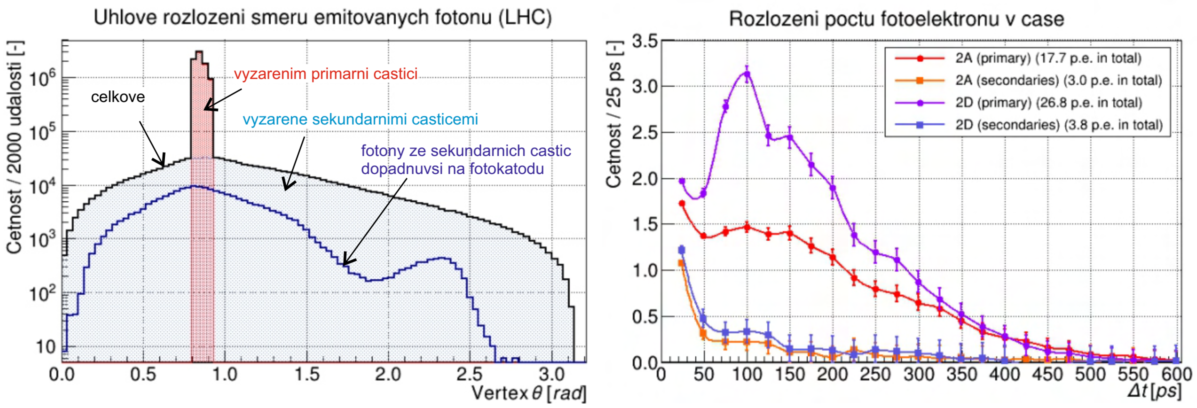

(a) (b)

Obrázek 6.5: (a) Úhlové rozložení směrů šíření fotonů vyzařovaných protony svazku LHC o energii 6,8 TeV v jedné řadě tyčinek ToF s příspěvkem sekundárních částic, (b) rozložení počtu fotoelektronů na pixelech P-2A a P-2D s rozlišením příspěvku primární částice a sekundárních částic. Pro výpočet byl použit model fotonásobiče s kvantovou účinností dle [41] a kolektivní účinností 0,6.

6.2 Sekundární částice vzniklé průchodem pionů o energii 120 GeV

Studium vlivu sekundárních částic v důsledku průchodu svazku pionů urychlovače SPS mělo své opodstatnění při testovacích měřeních. V těchto měření se mimo jiné porovnávala účinnost detekce detektorem ToF vzhledem k referenčním detektorům SiPM [17]. Případná větší disperze svazku vlivem detektoru by se projevila na umělém snížení účinnosti detekce.

Vzhledem k tomu, že spektrum energetických ztrát na SPS je podobné jako v případě LHC, viz Obrázek 6.2b, dá se očekávat podobné zastoupení fyzikálních procesů, které se uplatňují při tvorbě spršek sekundárních částic, stejně jako struktura struktura těchto spršek. Jak naznačuje Obrázek 6.6a je rozdělení energií sekundárních částic první generace (elektronů) podobné jako v případě LHC, zastoupení vyšších energií je však nižší. Tyto elektrony podstupují stejné fyzikální procesy, viz Obrázek 6.6b. Za povšimnutí stojí potlačená tvorba sekundárních elektronů Comptonovým rozptylem nad 1 MeV.

Výtěžnosti sekundárních částic vzhledem k trajektorii primární částice je v Tabulce 6.2

a jsou srovnatelné s hodnotami pro svazek LHC. Tomu odpovídá i podobná výtěžnost Čerenkovských fotonů: 125 fotonů vytvořených v každé tyčince a 23 fotonů dopadajících na fotokatodu fotonásobiče. Distribuce směrů emitovaných fotonů sekundárních částic, Obrázek 6.7a, v podstatě kopíruje výsledky pro svazek LHC. Stejně tak je tomu v případě odhadovaného rozdělení počtu fotoelektronů v čase podle Obrázku 6.7b. Z tohoto důvodu se dá očekávat, že odezva detektoru ToF na svazku SPS je stejná jako na svazku LHC, a tudíž, že experimentální ověřovací měření na SPS jsou dostatečně relevantní pro vývoj detektoru ToF.

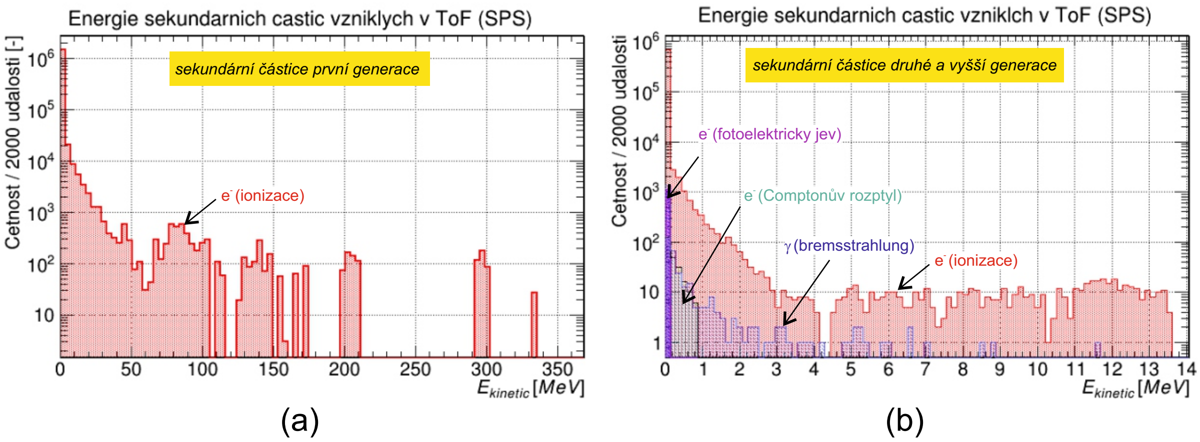

Obrázek 6.6: (a) Rozdělení kinetické energie elektronů uvolněných interakcí primární částice π^+ o energii 120 GeV s materiálem křemenného skla jedné řady tyčinek (první generace sekundárních částic), (b) rozdělení kinetické energie sekundárních částic druhé a vyšší generace, které následně vznikly interakcí sekundárních elektronů první generace se stejným prostředím.

Tabulka 6.2: Druhy sekundárních částic vzniklých průchodem π^+ o celkové energii 120 GeV materiálem SK-1300 a jejich výtěžnost vzhledem k trajektorii primární částice. Zvlášť je uvedena výtěžnost těch částic (elektronů), které mají kinetickou energii dostatečnou k vyvolání Čerenkovova záření.

Druh částice	**Proces vzniku**	**Působící částice**	**Výtěžnost dN/dx**
První generace:			
e^-	ionizace	π^+	24 mm^{-1}
e^- ($E_k > 0,179$ MeV)			3,1 mm^{-1} (13 %)
Druhá a vyšší generace:			
e^-	ionizace	e^-	11 mm^{-1}
γ	bremsstrahlung	e^-	0,02 mm^{-1}
e^-	fotoel. jev	γ	0,02 mm^{-1}
e^-	Comptonův rozptyl	γ	0,004 mm^{-1}
e^- ($E_k > 0,179$ MeV)			0,14 mm^{-1} (1,2 %)

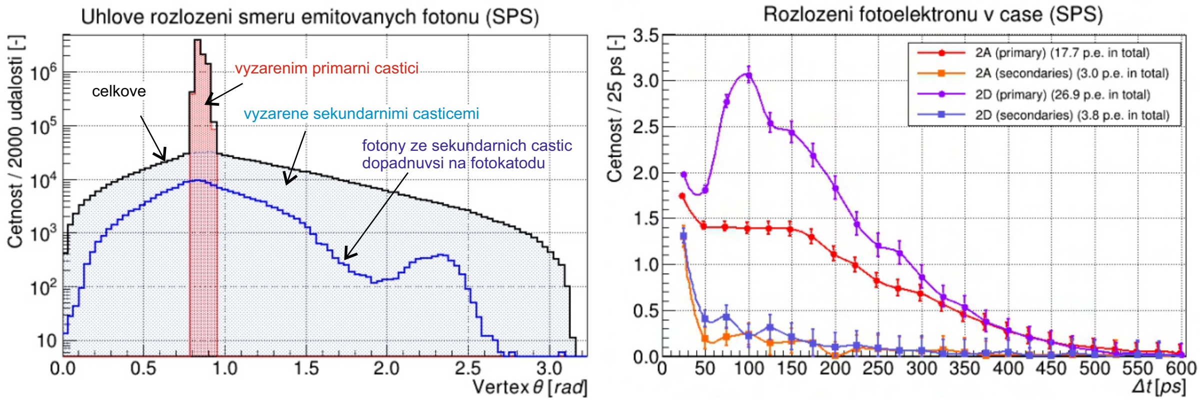

(a) (b)

Obrázek 6.7: (a) Úhlové rozložení směrů šíření fotonů vyzařovaných částicemi π^+ svazku SPS o energii 120 GeV v jedné řadě tyčinek ToF s příspěvkem sekundárních částic, (b) rozložení počtu fotoelektronů na pixelech P-2A a P-2D s rozlišením příspěvku primární částice a sekundárních částic. Pro výpočet byl použit model fotonásobiče s kvantovou účinností dle [41] a kolektivní účinností 0,6.

6.3 Sekundární částice vzniklé průchodem elektronu 5 GeV

V případě elektronů o energiích v jednotkách GeV je výsledný vliv sekundárních částic odlišný oproti oběma předchozím případům. Elektrony intenzivně interagují se svými protějšky vázanými v materiálu a výsledkem jsou značné energetické ztráty, jak ukazuje Obrázek 6.2a. Ty se přetaví ve tvorbu spršek bohatých na druhotné částice a v konečném důsledku i na fotony Čerenkovova záření, které registruje fotonásobič.

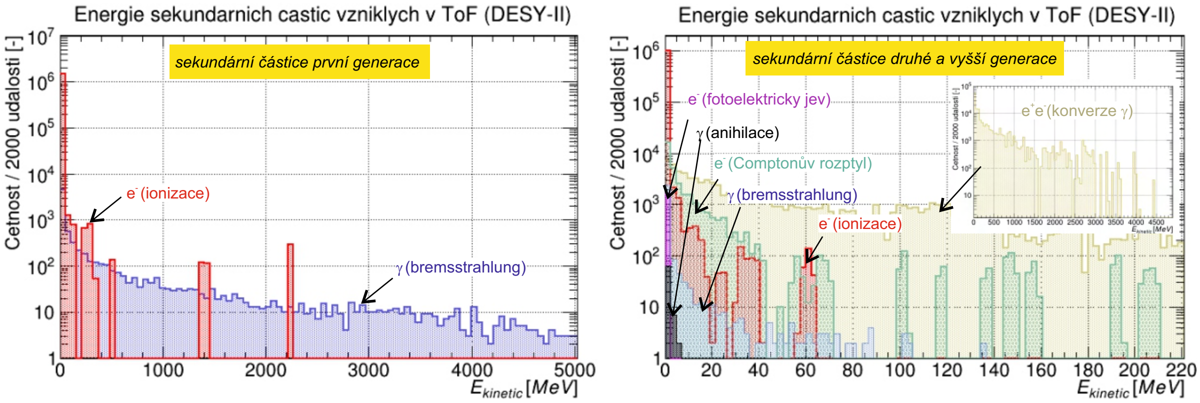

(a) (b)

Obrázek 6.8: (a) Rozdělení kinetické energie elektronů a fotonů gama uvolněných interakcí primární částice elektronu o energii 5 GeV s materiálem křemenného skla jedné řady tyčinek (první generace sekundárních částic), (b) rozdělení kinetické energie sekundárních částic druhé a vyšší generace, které následně vznikly interakcí sekundárních částic první generace se stejným prostředím.

Během průchodu materiálem SK-1300 podléhá primární částice elektronu dvěma procesům: ionizaci, při které dochází k uvolnění elektronů vázaných v materiálu, a brzdnému záření, při němž se tvoří fotony (záření gama). Jak je ukázáno na Obrázku 6.8a, fotony gama záření se tvoří v širokém spektru energií až do 5 GeV, při které ztratí primární částice veškerou kinetickou energii a je zachycena materiálem. Jejich výtěžnost je přibližně 0,12 mm^{-1} počítáno k trajektorii primární částice. Ionizace probíhá převážně při energiích pod 100 MeV. Výtěžnost ionizovaných elektronů je okolo 23 mm^{-1}, je tedy o dva řády

Tabulka 6.3: Druhy sekundárních částic vzniklých průchodem e^- o celkové energii 5 GeV materiálem SK-1300 a jejich výtěžnost vzhledem k trajektorii primární částice. Zvlášť je uvedena výtěžnost těch částic (e^- a e^+), které mají kinetickou energii dostatečnou k vyvolání Čerenkovova záření.

Druh částice	**Proces vzniku**	**Působící částice**	**Výtěžnost dN/dx**
První generace:			
e^-	ionizace	e^-	23 mm^{-1}
γ	bremsstrahlung	e^-	0,1 mm^{-1}
e^- ($E_k > 0,179$ MeV)			3,1 mm^{-1} (13 %)
Druhá a vyšší generace:			
e^-	ionizace	e^-	16 mm^{-1}
e^-	gama konverze	γ	1 mm^{-1}
e^+	gama konverze	γ	1 mm^{-1}
e^-	Comptonův rozptyl	γ	0,5 mm^{-1}
γ	bremsstrahlung	e^-	0,04 mm^{-1}
e^-	fotoel. jev	γ	0,03 mm^{-1}
γ	anihilace	e^+	0,001 mm^{-1}
e^- ($E_k > 0,179$ MeV)			2 mm^{-1} (12 %)
e^+ ($E_k > 0,179$ MeV)			1 mm^{-1} (100 %)

vyšší než v případě tvorby fotonů brzdným zářením.

Tyto sekundární částice první generace následně interakcí s týmž materiálem v tyčinkách vytváří další částice druhé generace atd. Na rozdíl od předchozích případů se ve sprškách nachází gama fotony o vysokých energiích až do 5 GeV. Tyto fotony podléhají v přítomnosti atomových jader materiálu procesu gama-konverze nebo-li procesu produkce páru elektron-pozitron. Rozložení energie sekundárních částic druhé a vyšší generace je na Obrázku 6.8b podle procesů při kterých vznikly. Jejich výtěžnost vzhledem k trajektorii primární částice je uvedena v Tabulce 6.3.

Celkově se ve sprškách vytvoří přibližně 1100 fotonů, tj. v průměru 275 fotonů na tyčinku (22 % z celkového počtu). Z nich do fotonásobiče dorazí 235 (16 %). Z rozložení směrů vyzařování fotonů primárními částicemi, červený histogram Obrázek 6.9a, je zřejmé, že nemálo vychylujících se primárních elektronů způsobují rozšíření rozložení podélného směru vyzařování Čerenkovových fotonů. Rozložení počtu vytvořených fotoelektronů v čase je na Obrázku 6.9b. Odtud je zřejmé, že na pixelech tyčinek A tvoří fotoelektrony, mající původ v sekundárních sprškách, 15 % celkové bilance. Na pixelech posledních tyčinek D tvoří tyto fotoelektrony téměř třetinu (32 %) celkové bilance. Zároveň jejich počet vykazuje vysoké fluktuace.

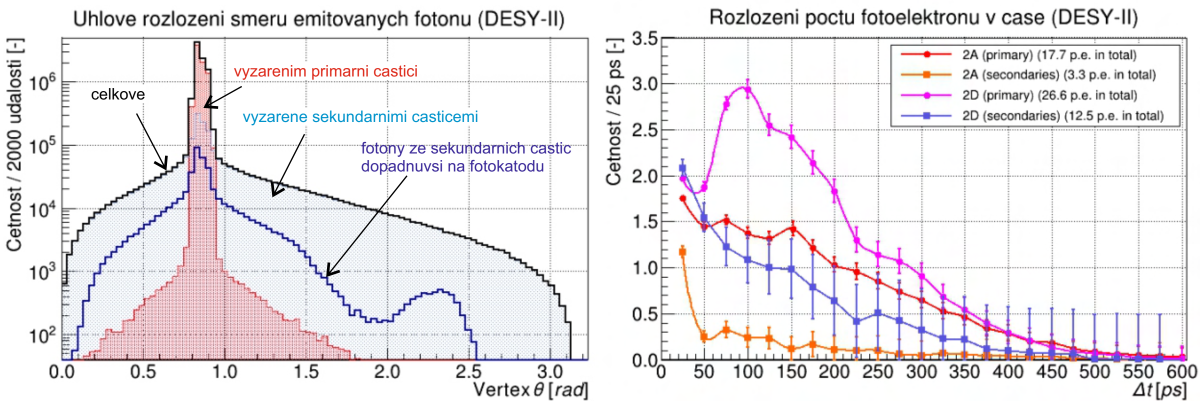

(a) (b)

Obrázek 6.9: (a) Úhlové rozložení směrů šíření fotonů vyzařovaných elektrony svazku DESY-II o energii 5 GeV v jedné řadě tyčinek ToF s příspěvkem sekundárních částic, (b) rozložení počtu fotoelektronů na pixelech P-2A a P-2D s rozlišením příspěvku primární částice a sekundárních částic. Pro výpočet byl použit model fotonásobiče s kvantovou účinností dle [41] a kolektivní účinností 0,6.

Kapitola 7

Simulace odezvy fotonásobiče

Konečným požadovaným výstupem simulace detektoru ToF v nástroji Geant4 byl kvalifikovaný odhad počtu fotoelektronů, které se vytvoří na základě interakce procházejících částic, jejichž čas průchodu je cílem stanovit, v materiálu tyčinek optické části detektoru. Komplexní přístup umožňuje zjistit různé aspekty šíření Čerenkovova záření v celé optické části včetně vlivu oddělovacího sklíčka mezi tyčinkami a fotonásobičem.

Při řešení úprav fotonásobičů také došlo na modelování jejich odezvy na příchozí fotoelektrony v čase. Tato tématika byla poprvé blíže zpracována v [22] a rozpracována v [17]. Jádrem těchto studií je model fotonásobiče v podobě jeho dostatečně komplexního náhradního elektrického schématu. Elektrické schéma bylo původně vytvořeno pro potřeby vývoje nové zadní elektroniky samotného fotonásobiče miniPLANACON XPM85112 v rámci úprav pro kampaň Run-3. Z důvodu vysoké luminozity svazku LHC v této kampani bylo nutné upravit fotonásobiče tak, aby byly schopné běžet na frekvenci 20 MHz na jednu řadu tyčinek bez významného poklesu zesílení mikrokanálkových destiček (dále označených zkratkou MCP z angl. Micro Channel Plate) fotonásobiče [22]. Jednalo se o optimalizaci stávajících řešení, které mělo za úkol potlačit přeslech mezi kanály a překmity ve výstupních signálech.

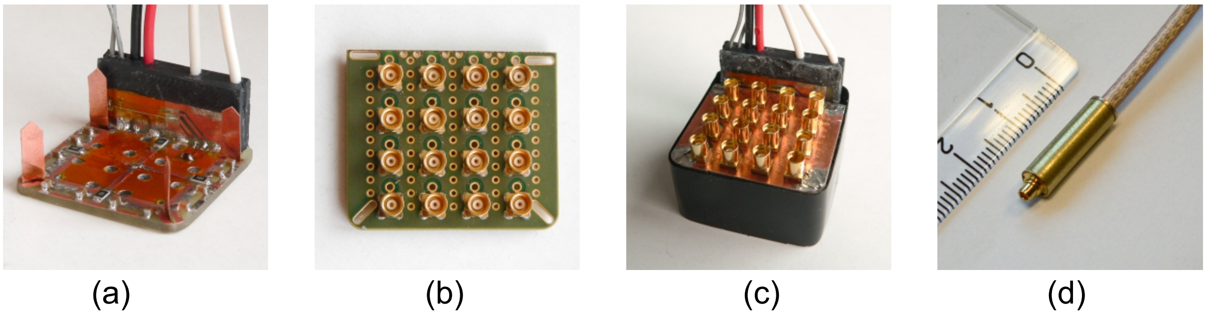

Obrázek 7.1: Ukázky z konstrukce prototypu upraveného fotonásobiče miniPLANACON XPM85112: (a) plošný spoj napájení s černým vstupním blokem vysokého napětí a čtyřmi niklovými zemnícími páskami, (b) anodový plošný spoj se samičími konektory MMCX, (c) pohled na sestavený prototyp, (d) koaxiální jednokanálový předzesilovač PA-a se samčím konektorem MMCX.

7.1 Fotonásobiče pro kampaň Run-3

Ve spolupráci se společností Photonis, Inc. pracoviště SLO provedlo návrh úprav fotonásobiče [17]. Na základě vytvoření náhradního modelu fotonásobiče a následných simulací na našem pracovišti byl navržen nový plošný spoj (PCB, z angl. Printed Circuit Board) napájení a navrženo nové řešení připojení tohoto PCB k obnaženému tělu fotonásobiče pomocí širokých pásků z niklové fólie o tloušťce 50 μm, Obrázek 7.1a. Toto řešení vede k výraznému snížení indukčnosti propojení PCB a elektrod MCP a díky tomu i ke snížení úrovně přeslechů mezi jednotlivými kanály. Součástí změn bylo také nové rozhraní analogových výstupů pixelů fotonásobiče ve formě samičích konektorů MMCX, Obrázek 7.1b,c. Toto řešení umožnilo přímé napojení prvního stupně zesilovačů PA-a, viz též schéma na Obrázku 2.8 na straně 12, které byly navrženy ve formě koaxiálního kabelu se zesilovačem na jednom konci přiléhajícímu k fotonásobiči, Obrázek 7.1d [1].

Na základě těchto úprav společnost Photonis, Inc. vyrobila celkem čtyři fotonásobiče pro kampaň Run- 3: S/N 9002196 (dále označen jako #2196, odpor MCP 44 MΩ), S/N

---

[1] Signálové vedení od anody fotonásobiče k prvnímu stupni zesilovače, včetně samotného konektoru, je velmi náchylné na indukování rušení vnějším elektromagnetickým polem, což se negativně projevuje na časovém rozlišení detektoru. Zařazení předzesilovače přímo za fotonásobič přes kvalitně stíněný konektor bylo nezbytným cílem úprav.

9002199 (#2199, 35 MΩ), S/N 9002200 (#2200, 27 MΩ) a S/N 9002201 (#2201, 55 MΩ) [2]. První dva fotonásobiče (#2196 a #2199) byly vyrobeny se standardní anodovou mezerou 2,9 mm a zbylé dva se sníženou mezerou 0,6 mm. Oproti předchozím byly mikrokanálkové destičky nových fotonásobičů opatřeny tenkou vrstvou ochranného povlaku pomocí technologie ALD ke zvýšení životnosti [44]. S ohledem na nižší hodnotu odporu MCP byly pro instalaci na LHC použity fotonásobiče #2199 a #2200. Fotonásobič #2196 je primárně určen jako náhradní fotodetektor a #2201 je uvažován pro další radiační testy. Bližší informace k fotonásobičům stejně jako k výsledkům jejich ověřování jsou v [22, 30].

7.2 Model fotonásobiče

7.2.1 Náhradní elektrické schéma

Na Obrázku 7.2 je znázorněno náhradní elektrické schéma upravených fotonásobičů mini-Planacon XPM85112 společně s prvním zesilovacím stupněm (PA-a) [17]. Schéma obsahuje impedance reálných elektrických prvků (černě) a parazitních prvků (šedě). Vzhledem k tomu, že fotonásobič je technicky vzato proudový zdroj, slouží PA-a jako měnič proudu na napětí. K tomu je určen zátěžový (anodový) odpor $R_a = 50\,\Omega$ na straně PA-a. Vnitřní vstupní impedance Z_i má také hodnotu 50 Ω a je v paralelním zapojení s R_a. Celková zátěž je tedy přibližně $Z_L = 25\ \Omega$ (pokud zanedbáme vliv vstupní kapacity zesilovače $C_i = 0,7$ pF)[3].

Hodnoty parazitních impedancí byly odhadnuty přímým výpočtem na základě geometrických a materiálových specifikací. Uvedené náhradní elektrické schéma bylo zapracováno do modelovacího nástroje LtSPICE [45]. Pomocí tohoto nástroje byl sledován vliv jednotlivých parazitních impedancí na amplitudu výstupního signálu pro jednotkový referenční vstup na výstupu z MCP. Parazitní impedance, které významně ovlivňují tvar a výšku výstupního signálu, jsou uvedeny v Tabulce 7.1 spolu s jejich jmenovitými hodnotami,

---

[2] V původním zadání bylo vyrobit fotonásobiče s odporem MCP do 20 MΩ s ohledem na rychlejší dočerpání odchozího náboje z mikrokanálků. Společnosti Photonis se však z technologických důvodů nepodařilo splnit tento požadavek a navíc byl rozptyl odporů MCP dosti značný.

[3] Vstupní impedance PA-a mírně závisí na frekvenci. Uvedená střední hodnota je určena s nejistotou ±5 % v okolí jmenovité hodnoty.

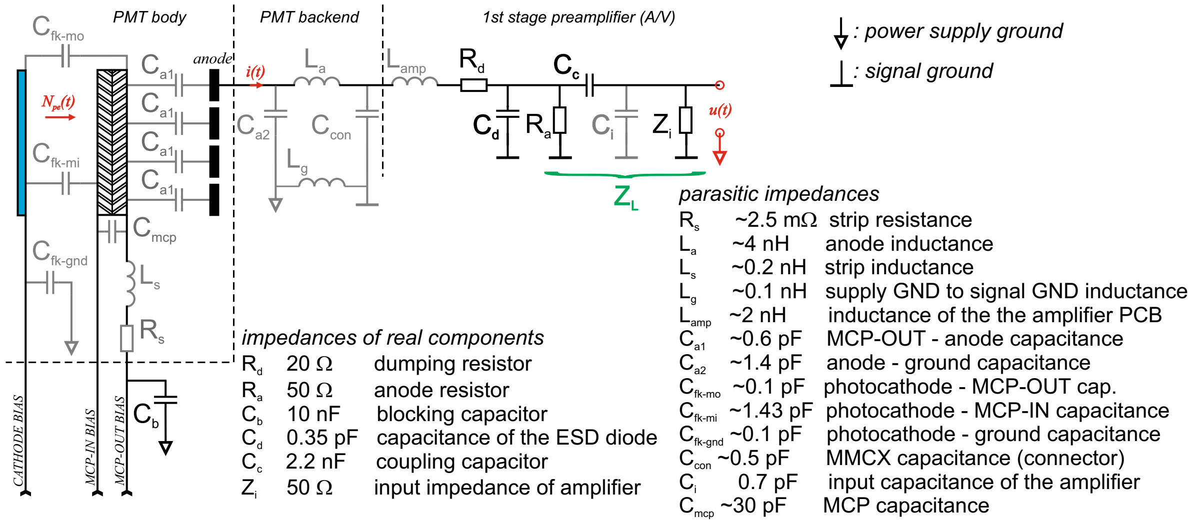

impedances of real components

R_d	20 Ω	dumping resistor
R_a	50 Ω	anode resistor
C_b	10 nF	blocking capacitor
C_d	0.35 pF	capacitance of the ESD diode
C_c	2.2 nF	coupling capacitor
Z_i	50 Ω	input impedance of amplifier

parasitic impedances

R_s	~2.5 mΩ	strip resistance
L_a	~4 nH	anode inductance
L_s	~0.2 nH	strip inductance
L_g	~0.1 nH	supply GND to signal GND inductance
L_{amp}	~2 nH	inductance of the the amplifier PCB
C_{a1}	~0.6 pF	MCP-OUT - anode capacitance
C_{a2}	~1.4 pF	anode - ground capacitance
$C_{fk\text{-}mo}$	~0.1 pF	photocathode - MCP-OUT cap.
$C_{fk\text{-}mi}$	~1.43 pF	photocathode - MCP-IN capacitance
$C_{fk\text{-}gnd}$	~0.1 pF	photocathode - ground capacitance
C_{con}	~0.5 pF	MMCX capacitance (connector)
C_i	0.7 pF	input capacitance of the amplifier
C_{mcp}	~30 pF	MCP capacitance

Obrázek 7.2: Náhradní elektrické schéma fotonásobiče miniPlanacon XPM85112 (jeden kanál) včetně prvního předzesilovacího stupně PA-a. Šedou barvou jsou označeny parazitní impedance, černou barvou reálné elektrické prvky. Z_L je celková zátěžová impedance pro jeden anodový výstup fotonásobiče. Převzato z [17].

rozsahem realisticky možných hodnot, a vlivu na výstupní signál z PA-a. Zbylé parazitní impedance v modelu mají nepatrný vliv na tvar výstupního signálu, protože nejsou přímo součástí signálové cesty.

Uvedený obvod se chová jako dolnofrekvenční propust, jak je ukázáno na Obrázku 7.3a. Mezní frekvence je závislá na velikosti anodové mezery. V případě fotonásobičů #2196 a #2199 se standardní mezerou má hodnotu 2,5 GHz. U fotonásobičů #2200 a #2201 se sníženou anodovou mezerou je hodnota mezní frekvence 2,2 GHz.

7.2.2 Odezva fotonásobiče

Pomocí nástroje LTspice byla studována odezva fotonásobičů na příchozí fotoelektrony v čase [17]. V modelu byly přitom použity nominální hodnoty impedancí podle Obrázku 7.2 a Tabulky 7.1. Sledovaným údajem bylo napětí na zátěži Z_L. Mikrokanálkové destičky byly modelovány jako proudové zdroje tvořící proudové impulzy v závislosti na počtu fotoelektronů v čase získaných ze simulací v Geant4. Pro následující ukázky byly použity pixely P-3A (s očekávaným nejslabším výstupem) a P-2D (nejsilnější výstup) fotonásobiče

Tabulka 7.1: Parazitní impedance, jejich odhadované jmenovité hodnoty a rozsahy možných hodnot (ostatní parazitní impedance na Obrázku 7.2 jsou považovány za známé s danou jmenovitou hodnotou). Korelace (kladná) či antikorelace (záporná) impedance s hodnotou amplitudy signálu na výstupu z anody značí, že s rostoucí hodnotou impedance roste či klesá amplituda signálu (v její absolutní hodnotě).

Impedance	**Jmenovitá hodnota**	**Dolní mez**	**Horní mez**	**Vliv na amplitudu signálu**
C_{a1}	0.1 pF (2.9 mm)[1]	–	–	antikorelace, pokles o 8% při
	0,5 pF (0,6 mm)[1]	–	–	změně od 0,1 do 0,5 pF
C_i	0,7 pF	0,3pF	2,1 pF	antikorelace, 7%[2]
C_{con}	0,9 pF	0,2 pF	1 pF	antikorelace, 3%[2]
L_a	2,5 nH	1,5 nH	9,5 nH	korelace, 3%[2]
L_s	0,2 nH	0,05 nH	1,25 nH	korelace, 6%[2]
L_{amp}	2 nH	0,5 nH	3 nH	korelace, 0,3%[2]
L_g	0,1 nH	0,05 nH	1,3 nH	korelace, 1%[2]

[1] Hodnota C_{a1} závisí na velikosti anodové mezery (2,9 mm pro #2196 a #2199, 0,6 mm pro#2200 a #2201),

[2] Relativní změna amplitudy při změně impedance z dolní meze na horní mez.

#2200, viz Obrázek 7.3b. Pro výstup MCP byl navržen výstup v podobě trojúhelníkového proudového pulzu o délce $\tau = 175$ ps podle Obrázku 7.4a. Zvolená délka pulzu přibližně odpovídá době množení elektronů v MCP [46]. Je-li N_{pe}^{slice} počet fotoelektronů (které byly vytvořeny v 25 ps dlouhém časovém úseku), je amplituda proudového pulzu z MCP rovna

$$I_0 = 2\frac{q_e N_{pe}^{slice} G_{mcp}}{\tau} \tag{7.1}$$

kde q_e je náboj elektronu a $G_{mcp} = G/\eta$ je zesílení MCP, G celkové zesílení fotonásobiče a $\eta \approx 0,6$ je kolektivní účinnost fotonásobiče [4]. Jak postupně přichází fotoelektrony v čase, vytvoří se na výstupu z MCP pilovitý signál, jak je tomu na Obrázku 7.4b pro fotonásobič #2200 se zesílením $G = 2100$, tj. $G_{mcp} = 3500$.

Diskrétní změny výstupního signálu leží v oblasti nad 10 GHz a jsou tedy zadní elektronikou fotonásobiče potlačeny. Výsledný signál na výstupu z fotonásobiče, konkrétně na Z_L, je na Obrázku 7.5 společně s odpovídajícím frekvenčním obrazem.

Plocha A_u^L tvořená křivkou napětí $u(t)$ pulzu na anodové zátěží Z_L (přesněji integrál

---

[4] Detailnější diskuze k zesílení MCP je v [17], kde je použito označení G_{SPE}.

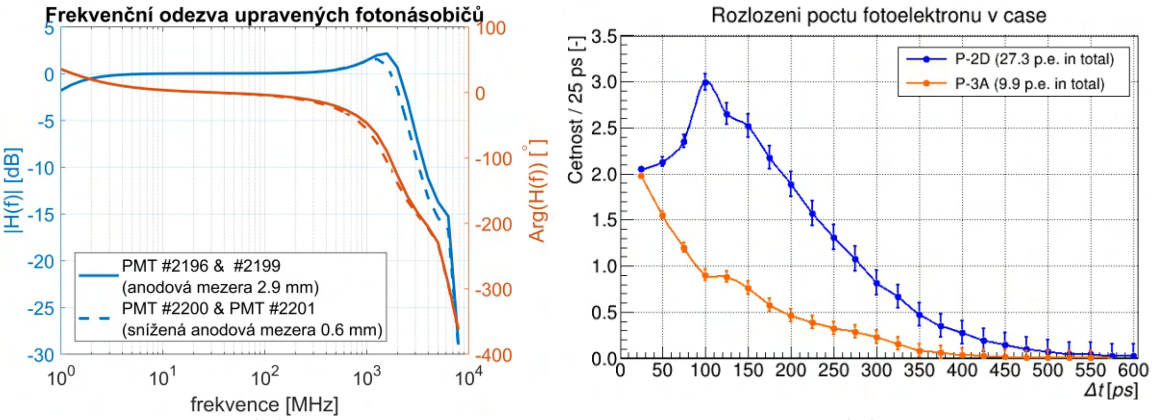

(a) (b)

Obrázek 7.3: (a) Frekvenční odezva fotonásobičů miniPlanacon XPM85112, (b) časový průběh vytvořených fotoelektronů na pixelech P-3A a P-2D kde se očekává nejnižší resp. nejvyšší výtěžnost fotoelektronů použitých pro modelování odezvy fotonásobiče (pro svazek LHC 6,8 TeV, 5 mm od kraje tyčinek).

pulzu), je podle definice úměrná celkovému náboji Q odčerpanému z MCP při vytvoření pulzu:

$$Q = \int_0^\infty i(t)dt = \frac{1}{Z_L}\int_0^\infty u(t)dt = \frac{1}{Z_L}A_u^L\,, \tag{7.2}$$

kde $i(t)$ je proud přes anodovou zátěž. Je-li $N_{pe} = \sum N_{pe}^{slice}$ celkový počet fotoelektronů na vstupu MCP, je celkový náboj vytvořený v MCP roven $Q = q_e N_{pe} G_{mcp}$. Dosazením do (7.2) vyplývá následující přímá úměra mezi plochou výstupního signálu a celkovým počtem fotoelektronů na vstupu:

$$A_u^L = q_e G_{mcp} Z_L N_{pe} \equiv p N_{pe}\,. \tag{7.3}$$

Za předpokladu, že Z_L se nemění, je konstanta úměrnosti p závislá pouze na použitém zesílení fotonásobiče. Amplituda a_u^L výstupního signálu silně koreluje s plochou signálu [17], tj. lze psát $A_u^L = k_s a_u^L$. Konstanta k_s má rozměr času a jedná se o šířku ekvivalentního (virtuálního) obdelníkového pulzu s výškou rovnající se amplitudě výstupního pulzu a se stejným obsahem přeneseného elektrického náboje. Dosazením do (7.3) lze dostat následující vztah mezi amplitudou výstupního signálu a počtem fotoelektronů na vstupu:

$$a_u^L = \frac{q_e Z_L G_{mcp}}{k_s} N_{pe} \equiv k N_{pe}\,, \tag{7.4}$$

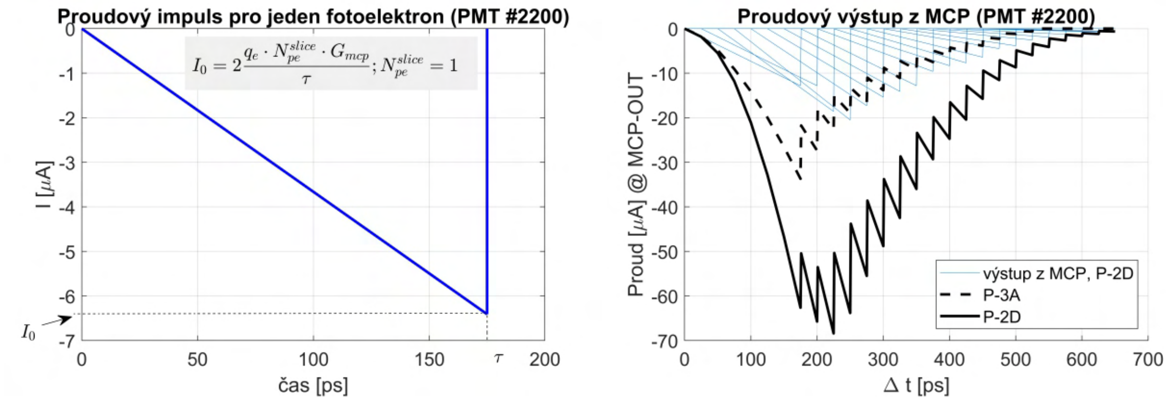

Obrázek 7.4: (a) Proudový impuls vycházející z MCP pro jeden příchozí fotoelektron, (b) celkový proudový signál z MCP pro fotonásobič #2200 se zesílením 2100 pro vstupy na P-3A a P-2D podle Obrázku 7.3b.

kde konstanta k je v jednotkách [V/p.e.] a lze ji považovat za výtěžnost výstupní amplitudy na jeden vstupní fotoelektron.

Podle definice $p = k_s k$, kde k_s závisí na tvaru pulzu. Tím jak je postupně veden vyčítací elektronikou, se signálový pulz natahuje v čase. Amplituda pulzu klesá při zachování své plochy (nepočítáme-li samotné zesílení v předzesilovačích). Následkem toho k_s roste při konstantním p. Proto je potřeba při odhadu počtu fotoelektronů z naměřených pulzů počítat s plochou signálu a nikoliv s jeho amplitudou. Hodnoty konstant k, k_s a p byly pro jednotlivé fotonásobiče vyčísleny na základě simulací v [17]. Například pro fotonásobič #2200 $k = -45$ μV/p.e., $k_s = 252$ ps a $p = -12$ fWb/p.e. S ohledem na nejistoty hodnot parazitních impedancí a odhadovaného počtu fotoelektronů v čase je nejistota v jejich určení ze simulací 10 %.

Na základě předchozího rozboru lze opačně odhadnout počet fotoelektronů ze znalosti průběhu výstupního signálu. Je-li střední plocha měřeného signálu $\langle A_u \rangle$, pak střední hodnota počtu fotoelektronů vytvořených ve fotonásobiči je rovna [17]:

$$\langle N_{pe} \rangle = \frac{1}{q_e Z_L G_{mcp}} \langle A_u^L \rangle = \frac{1}{gp} \langle A_u \rangle \,, \tag{7.5}$$

kde $g = 1000$ je celkové zesílení vyčítací elektroniky (konkrétně PA-a a PA-b).

Na Obrázku 7.6 je příklad takového rozboru převzatého z [17]. Tento rozbor byl prove-

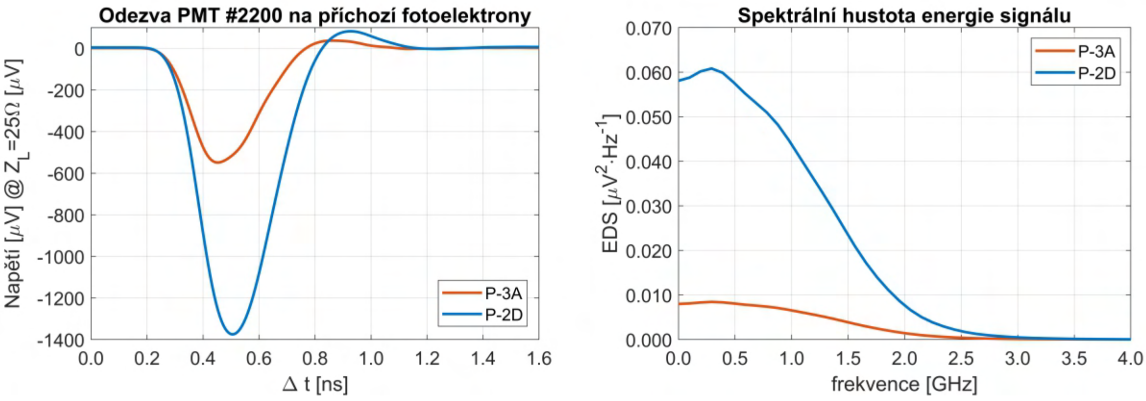

(a) (b)

Obrázek 7.5: Příklad simulace odezvy fotonásobiče #2200 při zesílení 2100 na pixelech P-3A a P-2D: (a) elektrické napětí na anodové zátěži Z_L předzesilovače PA-a, (b) odpovídající spektrální hustota energie signálu.

den na základě srovnávacích měření na lepených a nelepených tyčinkách řady T2 (v testovací konfiguraci bez dodatečného úkosu). Obrázek 7.6a ukazuje příklad silné korelace mezi amplitudou signálu a jeho plochou na pixelu tyčinky 2C s $k_s = 0,507$ ns. Obrázek 7.6b pak ukauje srovnání simulace a dat na základě srovnání odhadovaného počtu fotoelektronů dané simulací a experimentálně získanými daty za použití rovnice (7.5). Na první pohled simulace lehce podhodnocuje počet fotoelektronů ve srovnání s daty, a to v průměru o 2,6 fotoelektronů. Nicméně s ohledem na nejistoty v modelu a parametrů nastavení výpočtu odhadu N_{pe} v rovnici (7.5) je shoda dostatečná.

Věrohodnost předpovědi výstupu fotonásobiče detektoru ToF pomocí náhradního elektrického schématu podle Obrázku 7.2 je do značné míry závislá na jeho komplexitě a na správném odhadu hodnot všech jeho prvků, především parazitních impedancí. Model byl během vývoje detektoru ToF několikrát zpřesňován na základě experimentálních dat z urychlovače SPS, jako například zmíněná měření z roku 2021, a dat z laboratorních měření na laseru. V druhém případě byla velmi přínosná měření na jedno-fotoelektronových úrovních [32, 22] za použití pikosekundového laseru na vlnové délce 405 nm. Srovnání simulace s daty na urychlovači je zatíženo dodatečnou nejistotou a to z důvodu neznámé kvantové účinnosti fotonásobiče na vlnových délkách pod 200 nm, kde je vyšší výtěžnost

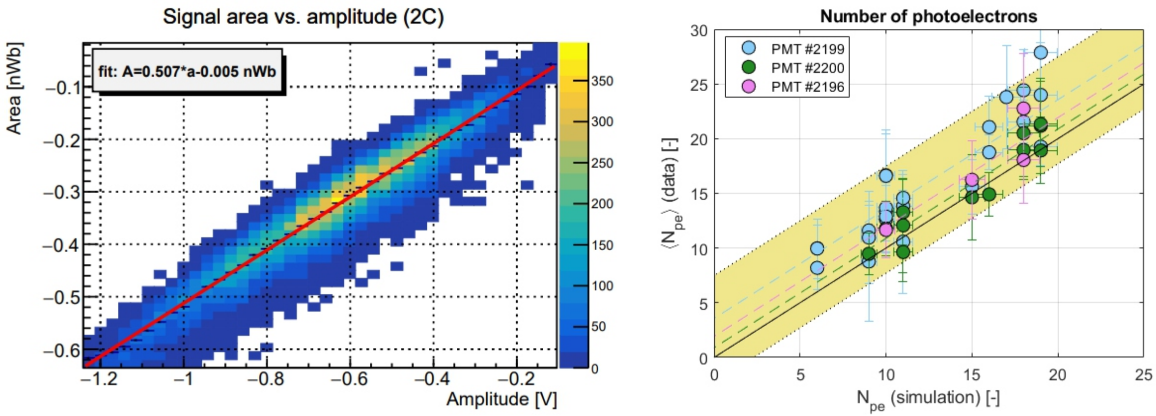

(a) (b)

Obrázek 7.6: Výsledky z testovacích měření na svazku SPS v roce 2021 (převzato z [17]): (a) ukázka silné provázanosti amplitudy a plochy výstupního signálu z detektoru ToF na příkladu pixelu P-2C, (b) srovnání počtu fotoelektronů ze simulace a experimentálních dat. Výsledek byl získán na základě měření na fotonásobičích #2196, #2199 a #2200 s lepenými a nelepenými tyčinkami řady T2 (bez úkosu).

fotonů Čerenkovova záření. Přesto studie odezvy fotonásobiče byly podstatné pro celkové pochopení chování detektoru ToF.

Kapitola 8

Závěr

Projekt AFP započal během roku 2004 prvními studiemi a upřesněním fyzikálního programu. V roce 2010 se rozběhly práce na vývoji hardwaru a pracoviště SLO se do projektu zapojilo o rok později. Naše první úkoly kopírovaly ty, kterým jsme se věnovali na předchůdci AFP a tím byl projekt ALFA. Zprvu se jednalo se výlučně o tvorbu simulačních nástrojů, ale těžiště práce brzy přešlo do modelování odezvy detektoru ToF v nástroji Geant4. Hlavní zodpovědnost za tuto činnost měl autor této práce. Model se během let upřesňoval a rozvíjel na základě potřeb, které vzešly z výsledků experimentálních měření a z pozměňovacích požadavků na konstrukci detektoru.

Simulace nebyly jediným zapojením našeho pracoviště do projektu. Dalším významným příspěvkem pracoviště SLO byl návrh a konstrukce unikátní optické části detektoru ToF. To bylo umožněno díky zkušenostem a vybavení zdejší optické dílny. Postupem času jsme se také začali věnovat vývoji části vyčítací elektroniky od konstrukci zadní elektroniky fotonásobičů po oba stupně zesilovačů. Naše činnost nakonec pokrývala simulace, konstrukci detektoru a jeho instalaci na urychlovači LHC. V rámci těchto činností pracovníci a studenti pracoviště získali cenné zkušenosti v oblasti hardwaru a softwaru. Téma AFP pokrylo celkem čtyři bakalářské, tři diplomové a dvě dizertační práce. Výsledky naší práce byly zveřejněny v 13 publikacích, na 16-ti příspěvcích na konferencích a 10-ti seminářích. Získané znalosti jsou postupně zužitkovány i v ostatních projektech, na kterých se podílí pracoviště SLO.

Detektorům ToF se nevyhnuly problémy při nasazení během kapaně Run-2 urychlovače

LHC v letech 2015 – 2018. Ostrý provoz urychlovače odhalil mnoho nedostatků, které se neprojevily během testovacích měřeních nebo nebyly předtím dostatečně zhodnoceny. Především se jednalo o problémy s fotonásobiči, v té době v podobě standardního řešení nabízeného výrobcem. Vysoká radiace a nevhodná konstrukce vedla k velkému poklesu jejich odezvy. To vedlo k významnému poklesu účinnosti, přestože si detektor zachoval skvělé rozlišení 25 ps na jednu stanici, čemuž odpovídalo prostorové rozlišení 6 mm v interakčním bodě detektoru ATLAS [33] [1].

Po těchto zkušenostech byla konstrukce detektoru ToF přepracována. Lepené tyčinky byly po dokončení vývoje nového technologického postupu nahrazeny nelepenými. Hlavní pozornost se obrátila na úpravy fotonásobiče a jeho přenesení mimo evakuovaný prostor detektoru AFP. Všechny tyto změny byly doprovázeny novými simulačními studiemi a výpočty. V současné době běží detektory ToF spolu s ostatními částmi AFP v rámci kampaně Run-3. Účinnost detektoru se podstatně zlepšila až na 60 % i přes zvýšenou intenzitu (luminozitu) svazku LHC.

V následující kampani Run-4 se bude nadále zvyšovat luminozita svazku LHC. Protože stávající koncepce nebude vhodná pro tyto intenzity, bude potřeba pracovat na nových řešeních. Naše skupina se plánujeme zapojit do přípravných simulačních studií a pokud bude zvoleno řešení na bázi optiky, bude naší snahou se zapojit i do vývoje konstrukce detektoru.

---

[1] Vnitřní časové rozlišení samotného detektoru bez vlivu vyčítací elektroniky je 20–25 ps v režimu zesílení fotonásobičů v řádu 10^3 [17]. Při optimálním zesílení v řádu 10^4 bylo dosaženo časového rozlišení 14 ps [29].

Seznam použité literatury

[1] T.S. Virdee. „The LHC project: The accelerator and the experiments“. In: *Nuclear Instruments and Methods in Physics Research Section A: Accelerators, Spectrometers, Detectors and Associated Equipment* 623.1 (2010). 1st International Conference on Technology and Instrumentation in Particle Physics, strany 1–10. ISSN: 0168-9002. DOI: `https://doi.org/10.1016/j.nima.2010.02.142` (citováno na straně 2).

[2] S. Abdel Khalek et al. „The ALFA Roman Pot detectors of ATLAS“. In: *Journal of Instrumentation* 11.11 (lis. 2016), P11013. DOI: `10.1088/1748-0221/11/11/P11013` (citováno na straně 2).

[3] ATLAS Collaboration. „Measurement of exclusive pion pair production in proton-proton collisions at $\sqrt{s}$=7 TeV with the ATLAS detector“. In: *Eur. Phys. J. C* 83 (pros. 2023), strana 627. DOI: `10.1140/epjc/s10052-023-11700-x` (citováno na straně 2).

[4] ATLAS Collaboration. „Measurement of the total cross section from elastic scattering in pp collisions at $\sqrt{s}$=7 TeV with the ATLAS detector“. In: *Nuclear Physics B* 889 (2014), strany 486–548. ISSN: 0550-3213. DOI: `10.1016/j.nuclphysb.2014.10.019` (citováno na straně 2).

[5] ATLAS Collaboration. „Measurement of the total cross section from elastic scattering in pp collisions at $\sqrt{s}$=8 TeV with the ATLAS detector“. In: *Physics Letters B* 761 (2016), strany 158–178. ISSN: 0370-2693. DOI: `10.1016/j.physletb.2016.08.020` (citováno na straně 2).

[6] L. Adamczyk, E. Banas, A. Brandt, M. Bruschi, S. Grinstein, J. Lange, M. Rijssenbeek, P. Sicho, R. Staszewski, T. Sykora, M. Trzebinski, J. Chwastowski a K. Korcyl.

Technical Design Report for the ATLAS Forward Proton Detector. Technical Report CERN-LHCC-2015-009. ATLAS-TDR-024. 2015 (citováno na stranách 4, 7, 14).

[7] M. Heath. „The New ATLAS Fast Calorimeter Simulation". In: *EPS-HEP 2017, European Physical Society conference on High Energy Physics.* 2017 (citováno na straně 4).

[8] Vincenzo Barone a Enrico Predazzi. *High Energy Particle Diffraction.* Springer-Verlag Berlin Heidelberg, led. 2002. ISBN: 978-3-642-07567-4. DOI: `10.1007/978-3-662-04724-8` (citováno na straně 6).

[9] G. Chew a S. Frautschi. „Detection of vacuum ultraviolet light by means of SiPM for high energy physics experiments". In: *Phys. Rev. Lett.* 7 (1961), strana 394 (citováno na straně 6).

[10] V. Kus. „Diffraction and rapidity gap measurements with ATLAS". In: *International Conference on the Structure and the Interactions of the Photon including the 20th International Workshop on Photon-Photon Collisions and the International Workshop on High Energy Photon Linear Colliders, Paris, France.* 2013 (citováno na straně 7).

[11] K. Cerny, T. Sykora, M. Tasevsky a R. Zlebcik. „Performance studies of Time-of-Flight detectors at LHC". In: *Journal of Instrumentation* 16 (2021), P01030 (citováno na straně 7).

[12] V. Lysenko. „Efficiency and accuracy of time-of-flight detector measurements in the ATLAS experiment and di-photon vertex reconstruction for the search for an axion-like particle in data from LHC Run-3". Disertační práce. Karlova Univerzita v Praze, 2023 (citováno na straně 7).

[13] Lyndon Evans a Philip Bryant. „LHC Machine". In: *Journal of Instrumentation* 3.08 (srp. 2008), S08001. DOI: `10.1088/1748-0221/3/08/S08001`. URL: `https://dx.doi.org/10.1088/1748-0221/3/08/S08001` (citováno na straně 8).

[14] V. Georgiev, O. Vavroch, J. Zich a L. Nozka. „Diagnostic Device for Photomultiplier Tubes at ARP ToF Detector". In: *2020 International Conference on Applied Electronics (AE).* 2020, strany 1–4. DOI: `10.23919/AE49394.2020.9232820` (citováno na straně 8).

[15] J. Lange, L. Adamczyk, G. Avoni, E. Banas, A. Brandt, M. Bruschi, P. Buglewicz, E. Cavallaro, D. Caforio, G. Chiodini, L. Chytka, K. Cieśla, P. M. Davis, M. Dyndal, S. Grinstein, K. Janas, K. Jirakova, M. Kocian, K. Korcyl, I. L. Paz, D. Northacker, L. Nozka, M. Rijssenbeek, L. Seabra, R. Staszewski, P. Świerska a T. Sykora. „Beam tests of an integrated prototype of the ATLAS forward proton detector“. In: *Journal of Instrumentation* 11 (2016), P09005 (citováno na stranách 9, 10, 15).

[16] J. Lange, E. Cavallaro, S. Grinstein a I. Lopez Paz. „3D silicon pixel detectors for the ATLAS Forward Physics experiment“. In: *Journal of Instrumentation* 10 (2015), strana C03031 (citováno na straně 9).

[17] L. Nozka, G. Avoni, E. Banas, A. Brandt, K. Cerny, P. M. Davis, S. Duarte Pinto, V. Georgiev, M. Hrabovsky, T. Komarek, K. Korcyl, I. Lopez-Paz, M. Milovanovic, G. Mladenovic, D. A. Orlov, M. Rijssenbeek, P. Schovanek, T. Sykora, M. Trzebinski, V. Urbasek a J. Zich. „Upgraded Cherenkov time-of-flight detector for the AFP project“. In: *Opt. Express* 31.3 (led. 2023), strany 3998–4014. DOI: `10.1364/OE.480624` (citováno na stranách 9, 11, 45, 51–57, 59, 61).

[18] L. Nozka, A. Brandt, M. Rijssenbeek, T. Sykora, T. Hoffman, J. Griffiths, J. Steffens, P. Hamal, L. Chytka a M. Hrabovsky. „Design of Cherenkov bars for the optical part of the time-of-flight detector in Geant4“. In: *Optics Express* 22 (2014), strany 28984–28996 (citováno na stranách 10, 12, 29, 31).

[19] *Epoxy Technology, Inc., Epotek 305 datasheet.* (Citováno na straně 11).

[20] L. Nozka, A. Brandt, K. Cerny, M. Hrabovsky, T. Komarek, F. Krizek, D. Mandat, M. Milovanovic, M. Rijssenbeek, P. Schovanek, T. Sykora, V. Urbášek a J. Zatloukal. „Performance studies of new optics for the time-of-flight detector of the AFP project“. In: *Optics Express* 28 (2020), strany 19783–19796 (citováno na stranách 11, 15, 39).

[21] *Photonis USA Pensylvania, Inc., miniPlanacon XPM85112 datasheet.* (Citováno na stranách 11, 13).

[22] T. Komarek, V. Urbasek, A. Brandt, K. Cerny, J. DeFazio, V. Georgiev, M. Hrabovsky, Z. Kubik, L. Nozka, D. Orlov, S. Duarte Pinto, M. Rijssebeek, T. Sykora a J. Zich. „Characterization of the miniPlanacon XPM85112-S-R2D2 MCP-PMT with a custom modified backend electronics“. In: *Nuclear Instruments and Methods in Physics Research Section A: Accelerators, Spectrometers, Detectors and Associated Equipment* 1041 (2022), strana 167330 (citováno na stranách 12, 15, 51, 53, 58).

[23] L. Chytka, M. Hrabovsky, T. Komarek, V. Michalek, L. Nozka, T. Sykora a V. Urbasek. „Time resolution of the SiPM-NUV3S“. In: *Nuclear Instruments and Methods in Physics Research Section A: Accelerators, Spectrometers, Detectors and Associated Equipment* 935 (2019), strany 51–55 (citováno na straně 13).

[24] S.I. Parker, C.J. Kenney a J. Segal. „3D — A proposed new architecture for solid-state radiation detectors“. In: *Nuclear Instruments and Methods in Physics Research Section A: Accelerators, Spectrometers, Detectors and Associated Equipment* 395.3 (1997). Proceedings of the Third International Workshop on Semiconductor Pixel Detectors for Particles and X-rays, strany 328–343. ISSN: 0168-9002. DOI: `10.1016/S0168-9002(97)00694-3` (citováno na straně 14).

[25] C. Da Via, M. Boscardin, G. Dalla Betta, G. Darbo, C. Fleta, C. Gemme, P. Grenier, S. Grinstein, T.E. Hansen, J. Hasi, C. Kenney, A. Kok, S. Parker, G. Pellegrini, E. Vianello a N. Zorzi. „3D silicon sensors: Design, large area production and quality assurance for the ATLAS IBL pixel detector upgrade“. In: *Nuclear Instruments and Methods in Physics Research Section A: Accelerators, Spectrometers, Detectors and Associated Equipment* 694 (2012), strany 321–330. ISSN: 0168-9002. DOI: `10.1016/j.nima.2012.07.058` (citováno na straně 14).

[26] A. Lehmann, M. Böhm, A. Britting, W. Eyrich, M. Pfaffinger, F. Uhlig, A. Belias, R. Dzhygadlo, A. Gerhardt, K. Götzen, G. Kalicy, M. Krebs, D. Lehmann, F. Nerling, M. Patsyuk, K. Peters, G. Schepers, L. Schmitt, C. Schwarz, J. Schwiening, M. Traxler, M. Zühlsdorf, M. Düren, E. Etzelmüller, K. Föhl, A. Hayrapetyan, B. Kröck, O. Merle, J. Rieke, M. Schmidt, T. Wasem, E. Cowie, T. Keri, P. Achenbach, M. Cardinali, M. Hoek, W. Lauth, S. Schlimme, C. Sfienti a M. Thiel. „Recent developments with microchannel-plate PMTs“. In: *Nuclear Instruments and Methods in*

Physics Research Section A: Accelerators, Spectrometers, Detectors and Associated Equipment 876 (2017). The 9th international workshop on Ring Imaging Cherenkov Detectors (RICH2016), strany 42–47. ISSN: 0168-9002. DOI: `10.1016/j.nima.2016.12.063` (citováno na straně 14).

[27] A. Lehmann, M. Böhm, W. Eyrich, D. Miehling, M. Pfaffinger, S. Stelter, F. Uhlig, A. Ali, A. Belias, R. Dzhygadlo, A. Gerhardt, K. Götzen, G. Kalicy, M. Krebs, D. Lehmann, F. Nerling, M. Patsyuk, K. Peters, G. Schepers, L. Schmitt, C. Schwarz, J. Schwiening, M. Traxler, M. Düren, E. Etzelmüller, K. Föhl, A. Hayrapetyan, K. Kreutzfeld, O. Merle, J. Rieke, M. Schmidt, T. Wasem, P. Achenbach, M. Cardinali, M. Hoek, W. Lauth, S. Schlimme, C. Sfienti a M. Thiel. „Lifetime of MCP-PMTs and other performance features“. In: *Journal of Instrumentation* 13.02 (ún. 2018), strana C02010. DOI: `10.1088/1748-0221/13/02/C02010` (citováno na straně 14).

[28] F. Křížek, J. Ferencei, T. Matlocha, J. Pospíšil, P. Príbeli, V. Raskina, A. Isakov, J. Štursa, T. Vaňát a K. Vysoká. „Irradiation setup at the U-120M cyclotron facility“. In: *Nuclear Instruments and Methods in Physics Research Section A: Accelerators, Spectrometers, Detectors and Associated Equipment* 894 (2018), strany 87–95. ISSN: 0168-9002. DOI: `10.1016/j.nima.2018.03.066` (citováno na straně 14).

[29] L. Nozka, L. Adamczyk, G. Avoni, A. Brandt, P. Buglewicz, E. Cavallaro, G. Chiodini, L. Chytka, K. Ciesla, P. M. Davis, M. Dyndal, S. Grinstein, P. Hamal, M. Hrabovsky, K. Janas, K. Jirakova, M. Kocian, T. Komarek, K. Korcyl, J. Lange, D. Mandat, V. Michalek, I. Lopez Paz, D. Northacker, M. Rijssenbeek, L. Seabra, P. Schovanek, R. Staszewski, P. Swierska a T. Sykora. „Construction of the optical part of a time-of-flight detector prototype for the AFP detector“. In: *Optics Express* 24 (2016), strany 27951–27960 (citováno na stranách 15, 61).

[30] T. Komárek. „Vývoj detektoru času průletu vysokoenergetických částic“. Disertační práce. Univerzita Palackého v Olomouci, 2023 (citováno na stranách 15, 53).

[31] L. Chytka, G. Avoni, A. Brandt, E. Cavallaro, P. M. Davis, F. Foerster, M. Hrabovsky, Y. Huang, K. Jirakova, M. Kocian, T. Komarek, K. Korcyl, J. Lange, V. Michalek, L. Nozka, I. Lopez Paz, M. Rijssenbeek, P. Schovanek, T. Sykora a V.

Urbasek. „Timing resolution studies of the optical part of the AFP time-of-flight detector“. In: *Optics Express* 26 (2018), strany 8028–8039 (citováno na stranách 15, 32, 33).

[32] T. Komarek, A. Brandt, V. Chirayath, L. Chytka, M. Hrabovsky, L. Nozka, M. Rijssenbeek, T. Sykora a V. Urbasek. „Timing resolution and rate capability of Photonis miniPlanacon XPM85212/A1-S MCP-PMT“. In: *Nuclear Instruments and Methods in Physics Research Section A: Accelerators, Spectrometers, Detectors and Associated Equipment* 985 (2021), strana 164705 (citováno na stranách 15, 58).

[33] ATLAS Collaboration. „Performance of the ATLAS forward proton Time-of-Flight detector in Run 2“. In: *Journal of Instrumentation* 19 (2024), P05054. DOI: `10.1088/1748-0221/19/05/P05054` (citováno na stranách 15, 61).

[34] John David Jackson. *Classical Electrodynamics*. John Wiley & Sons, Inc., New York, 1999. ISBN: 0-471-30932-X (citováno na stranách 17, 19, 20).

[35] L.E. Porter. „Mean excitation energies of Al2O3 and SiO2 extracted from alpha particle stopping power measurements“. In: *Nuclear Instruments and Methods in Physics Research Section B: Beam Interactions with Materials and Atoms* 95.3 (1995), strany 285–288. ISSN: 0168-583X. DOI: `10.1016/0168-583X(94)00438-2` (citováno na straně 18).

[36] L.V. Rodriguez-de Marcos, J.I. Larruquert, J.A. Mendez a J.A. Aznarez. „Self-consistent optical constants of SiO2 and Ta2O5 films“. In: *Opt. Mater. Express* 6.11 (lis. 2016), strany 3622–3637. DOI: `10.1364/OME.6.003622` (citováno na straně 21).

[37] Geant4 Collaboration. „Recent developments in Geant4“. In: *Nucl. Instrum. Meth. A* 835 (2016), strany 185–225 (citováno na straně 27).

[38] L. Nožka. *Modelování fyzikálních procesů pomocí trasovacího nástroje Geant4*. Univerzita Palackého v Olomouci, 2012. ISBN: 978-80-244-3078-2 (citováno na straně 27).

[39] L. Nozka, M. Pech, H. Hiklova, D. Mandat, M. Hrabovsky, P. Schovanek a M. Palatka. „BRDF profile of Tyvek and its implementation in the Geant4 simulation toolkit“. In: *Opt. Express* 19.5 (ún. 2011), strany 4199–4209. DOI: `10.1364/OE.19.004199` (citováno na straně 27).

[40] R. Brun a F. Rademakers. „ROOT — An object oriented data analysis framework“. In: *Nuclear Instruments and Methods in Physics Research Section A: Accelerators, Spectrometers, Detectors and Associated Equipment* 389.1 (1997). New Computing Techniques in Physics Research V, strany 81–86. ISSN: 0168-9002. DOI: `10.1016/S0168-9002(97)00048-X` (citováno na straně 28).

[41] P. M. Duarte. „QUARTIC: An ultra-fast time-Of-flight counter“. Disertační práce. The University of Texas, Arlington, 2007 (citováno na stranách 29, 38, 45, 47, 50).

[42] K. Jirákova. „Rychlá simulace šíření čerenkovských fotonů optickou částí detektoru AFP“. diplomová práce. Univerzita Palackého v Olomouci, 2017 (citováno na straně 31).

[43] R. Diener, J. Dreyling-Eschweiler, H. Ehrlichmann, I.M. Gregor, U. Kötz, U. Krämer, N. Meyners, N. Potylitsina-Kube, A. Schütz, P. Schütze a M. Stanitzki. „The DESY II test beam facility“. In: *Nuclear Instruments and Methods in Physics Research Section A: Accelerators, Spectrometers, Detectors and Associated Equipment* 922 (2019), strany 265–286. ISSN: 0168-9002. DOI: `10.1016/j.nima.2018.11.133` (citováno na straně 39).

[44] Yu. Melikyan, T. Sýkora, T. Komárek, L. Nožka, D. Serebryakov a V. Urbášek. „Load capacity and recovery behaviour of ALD-coated MCP-PMTs“. In: *Nuclear Instruments and Methods in Physics Research Section A: Accelerators, Spectrometers, Detectors and Associated Equipment* 949 (2020), strana 162854. ISSN: 0168-9002. DOI: `10.1016/j.nima.2019.162854` (citováno na straně 53).

[45] G. Brocard. *The LTspice IV Simulator: Manual, Methods and Applications.* Swiridoff Verlag, Wurth. 2013 (citováno na straně 53).

[46] F. Tang. *Modeling for MCP-PMT Output Signal.* presentation in frame of LAPPD project. 2008 (citováno na straně 55).

Příloha A

Rozměry tyčinek detektoru ToF

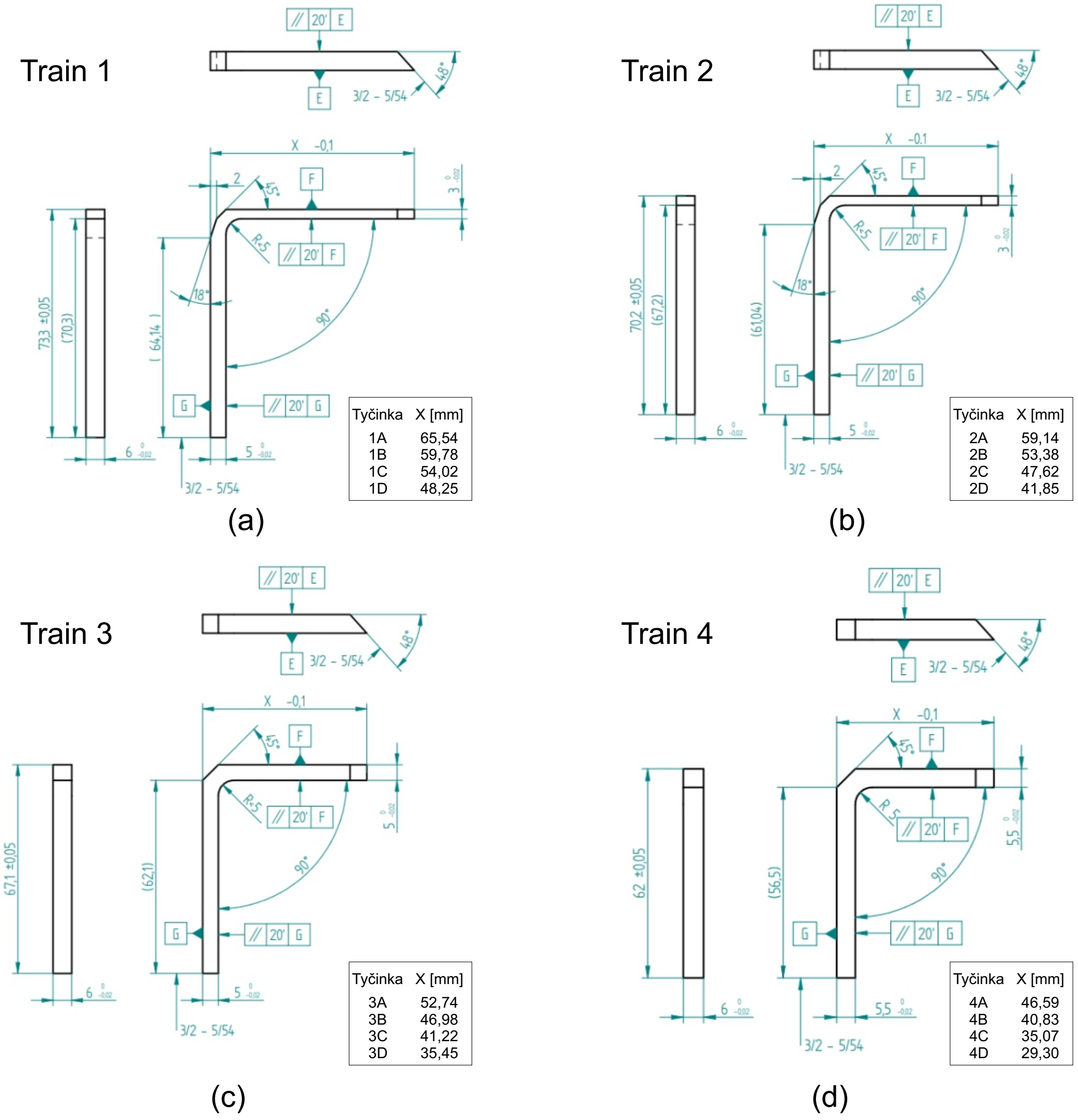

Tyčinka	X [mm]
1A	65,54
1B	59,78
1C	54,02
1D	48,25

Tyčinka	X [mm]
2A	59,14
2B	53,38
2C	47,62
2D	41,85

Tyčinka	X [mm]
3A	52,74
3B	46,98
3C	41,22
3D	35,45

Tyčinka	X [mm]
4A	46,59
4B	40,83
4C	35,07
4D	29,30

Obrázek A.1: Výrobní výkresy bezlepidlových tyčinek pro kampaň Run-3 LHC (2022–2025): (a) 1. řada tyčinek (Train 1), (b) 2. řada tyčinek (Train 2), (c) 3. řada tyčinek (Train 3), (d) 4. řada tyčinek (Train 4).

Příloha B

Seznam autorských a spoluautorských článků související s vývojem detektoru ToF

1. L. Nozka, A. Brandt, M. Rijssenbeek, T. Sykora, T. Hoffman, J. Griffiths, J. Steffens, P. Hamal, L. Chytka a M. Hrabovsky. „Design of Cherenkov bars for the optical part of the time-of-flight detector in Geant4“. In: *Optics Express* 22 (2014), strany 28984–28996
2. L. Nozka, L. Adamczyk, G. Avoni, A. Brandt, P. Buglewicz, E. Cavallaro, G. Chiodini, L. Chytka, K. Ciesla, P. M. Davis, M. Dyndal, S. Grinstein, P. Hamal, M. Hrabovsky, K. Janas, K. Jirakova, M. Kocian, T. Komarek, K. Korcyl, J. Lange, D. Mandat, V. Michalek, I. Lopez Paz, D. Northacker, M. Rijssenbeek, L. Seabra, P. Schovanek, R. Staszewski, P. Swierska a T. Sykora. „Construction of the optical part of a time-of-flight detector prototype for the AFP detector“. In: *Optics Express* 24 (2016), strany 27951–27960
3. J. Lange, L. Adamczyk, G. Avoni, E. Banas, A. Brandt, M. Bruschi, P. Buglewicz, E. Cavallaro, D. Caforio, G. Chiodini, L. Chytka, K. Cieśla, P. M. Davis, M. Dyndal, S. Grinstein, K. Janas, K. Jirakova, M. Kocian, K. Korcyl, I. L. Paz, D. Northacker, L. Nozka, M. Rijssenbeek, L. Seabra, R. Staszewski, P. Świerska a T. Sykora. „Beam

tests of an integrated prototype of the ATLAS forward proton detector“. In: *Journal of Instrumentation* 11 (2016), P09005

4. L. Chytka, G. Avoni, A. Brandt, E. Cavallaro, P. M. Davis, F. Foerster, M. Hrabovsky, Y. Huang, K. Jirakova, M. Kocian, T. Komarek, K. Korcyl, J. Lange, V. Michalek, L. Nozka, I. Lopez Paz, M. Rijssenbeek, P. Schovanek, T. Sykora a V. Urbasek. „Timing resolution studies of the optical part of the AFP time-of-flight detector“. In: *Optics Express* 26 (2018), strany 8028–8039

5. L. Chytka, M. Hrabovsky, T. Komarek, V. Michalek, L. Nozka, T. Sykora a V. Urbasek. „Time resolution of the SiPM-NUV3S“. In: *Nuclear Instruments and Methods in Physics Research Section A: Accelerators, Spectrometers, Detectors and Associated Equipment* 935 (2019), strany 51–55

6. L. Nozka, A. Brandt, K. Cerny, M. Hrabovsky, T. Komarek, F. Krizek, D. Mandat, M. Milovanovic, M. Rijssenbeek, P. Schovanek, T. Sykora, V. Urbášek a J. Zatloukal. „Performance studies of new optics for the time-of-flight detector of the AFP project“. In: *Optics Express* 28 (2020), strany 19783–19796

7. T. Komarek, A. Brandt, V. Chirayath, L. Chytka, M. Hrabovsky, L. Nozka, M. Rijssenbeek, T. Sykora a V. Urbasek. „Timing resolution and rate capability of Photonis miniPlanacon XPM85212/A1-S MCP-PMT“. In: *Nuclear Instruments and Methods in Physics Research Section A: Accelerators, Spectrometers, Detectors and Associated Equipment* 985 (2021), strana 164705

8. T. Komarek, V. Urbasek, A. Brandt, K. Cerny, J. DeFazio, V. Georgiev, M. Hrabovsky, Z. Kubik, L. Nozka, D. Orlov, S. Duarte Pinto, M. Rijssebeek, T. Sykora a J. Zich. „Characterization of the miniPlanacon XPM85112-S-R2D2 MCP-PMT with a custom modified backend electronics“. In: *Nuclear Instruments and Methods in Physics Research Section A: Accelerators, Spectrometers, Detectors and Associated Equipment* 1041 (2022), strana 167330

9. L. Nozka, G. Avoni, E. Banas, A. Brandt, K. Cerny, P. M. Davis, S. Duarte Pinto, V. Georgiev, M. Hrabovsky, T. Komarek, K. Korcyl, I. Lopez-Paz, M. Milovanovic, G.

Mladenovic, D. A. Orlov, M. Rijssenbeek, P. Schovanek, T. Sykora, M. Trzebinski, V. Urbasek a J. Zich. „Upgraded Cherenkov time-of-flight detector for the AFP project". In: *Opt. Express* 31.3 (led. 2023), strany 3998–4014. DOI: `10.1364/OE.480624`

10. J. Lange, M. Carulla, E. Cavallaro, L. Chytka, P.M. Davis, D. Flores, F. Foerster, S. Grinstein, S. Hidalgo, T. Komarek, G. Kramberger, I. Mandic, A. Merlos, L. Nozka, G. Pellegrini, D. Quirion a T. Sykora. „Gain and time resolution of 45 μm thin Low Gain Avalanche Detectors before and after irradiation up to a fluence of $10^1$5 neq/cm^2". In: *Journal of Instrumentation* 12.05 (květ. 2017), P05003. DOI: `10.1088/1748-0221/12/05/P05003`

11. Yu. Melikyan, T. Sýkora, T. Komárek, L. Nožka, D. Serebryakov a V. Urbášek. „Load capacity and recovery behaviour of ALD-coated MCP-PMTs". In: *Nuclear Instruments and Methods in Physics Research Section A: Accelerators, Spectrometers, Detectors and Associated Equipment* 949 (2020), strana 162854. ISSN: 0168-9002. DOI: `10.1016/j.nima.2019.162854`

12. V. Georgiev, O. Vavroch, J. Zich a L. Nozka. „Diagnostic Device for Photomultiplier Tubes at ARP ToF Detector". In: *2020 International Conference on Applied Electronics (AE)*. 2020, strany 1–4. DOI: `10.23919/AE49394.2020.9232820`

13. ATLAS Collaboration. „Performance of the ATLAS forward proton Time-of-Flight detector in Run 2". In: *Journal of Instrumentation* 19 (2024), P05054. DOI: `10.1088/1748-0221/19/05/P05054`

Příloha C

Autorské a spoluautorské články k problematice AFP/ToF

Design of Cherenkov bars for the optical part of the time-of-flight detector in Geant4

L. Nozka,[1,*] A. Brandt,[2] M. Rijssenbeek,[3] T. Sykora,[1,4] T. Hoffman,[2] J. Griffiths,[2] J. Steffens,[3] P. Hamal,[1] L. Chytka,[1] and M. Hrabovsky[1]

[1] *Regional Centre of Advanced Technologies and Materials, Joint Laboratory of Optics, Faculty of Science, Palacky University, 17. listopadu 50a, 771 46 Olomouc, Czech Republic*
[2] *University of Texas, Arlington, USA*
[3] *Stony Brook University, New York, USA*
[4] *Institute of Particle and Nuclear Physics, Faculty of Mathematics and Physics, Charles University in Prague, Czech Republic*
[*] *libor.nozka@upol.cz*

Abstract: We present the results of studies devoted to the development and optimization of the optical part of a high precision time-of-flight (TOF) detector for the Large Hadron Collider (LHC). This work was motivated by a proposal to use such a detector in conjunction with a silicon detector to tag and measure protons from interactions of the type $p + p \rightarrow p + X + p$, where the two outgoing protons are scattered in the very forward directions. The fast timing detector uses fused silica (quartz) bars that emit Cherenkov radiation as a relativistic particle passes through and the emitted Cherenkov photons are detected by, for instance, a micro-channel plate multi-anode Photomultiplier Tube (MCP-PMT). Several possible designs are implemented in Geant4 and studied for timing optimization as a function of the arrival time, and the number of Cherenkov photons reaching the photo-sensor.

©2014 Optical Society of America

OCIS codes: (120.4570) Optical design of instruments; (350.4990) Particles.

References and links

1. M. W. U. van Dijk, N. H. Brook, L. Castillo García, E. N. Cowie, D. Cussans, C. D. Ambrosio, J. Fopma, R. Forty, C. Frei, R. Gao, T. Gys, N. Harnew, T. Keri, and D. Piedigrossi, "TORCH—a Cherenkov based time-of-flight detector," Nucl. Instrum. Methods Phys. Res. A (to be published).
2. A. De Roeck, V. A. Khoze, A. D. Martin, R. Orava, and M. G. Ryskin, "Ways to detect a light Higgs boson at the LHC," Eur. Phys. J. C **25**(3), 391–403 (2002).
3. A. B. Kaidalov, V. A. Khoze, A. D. Martin, and M. G. Ryskin, "Extending the study of the higgs sector at the LHC by proton tagging," Eur. Phys. J. C **33**(2), 261–271 (2004).
4. M. G. Albrow and A. Rostovtsev, "Searching for the Higgs boson at hadron colliders using the missing mass method," arXiv:hep-ph/0009336 (2000).
5. M. G. Albrow, M. Atac, P. Booth, P. Crosby, I. Dunietz, D. A. Finley, B. Heinemann, M. Lancaster, R. Lauhakangas, D. Litvintsev, T. Liu, S. Marti-Garcia, D. McGivern, C. D. Moore, R. Orava, A. Rostovtsev, R. Snihur, S. Tapprogge, W. Wester, A. Wyatt, and K. Osterberg, "A Search for the Higgs Boson using very forward tracking detectors with CDF, Letter of Intent to Fermilab PAC," hep-ex/0511057 (2001).
6. M. G. Albrow, R. B. Appleby, M. Arneodo, G. Atoian, I. L. Azhgirey, R. Barlow, I. S. Bayshev, W. Beaumont, L. Bonnet, A. Brandt, P. Bussey, C. Buttar, J. M. Butterworth, M. Carter, B. E. Cox, D. Dattola, C. D. Via, J. Favereau, D. d'Enterria, P. D. Remigis, A. D. Roeck, E. A. D. Wolf, P. Duarte, J. R. Ellis, B. Florins, J. R. Forshaw, J. Freestone, K. Goulianos, J. Gronberg, M. Grothe, J. F. Gunion, J. Hasi, S. Heinemeyer, J. J. Hollar, S. Houston, V. Issakov, R. M. Jones, M. Kelly, C. Kenney, V. A. Khoze, S. Kolya, N. Konstantinidis, H. Kowalski, H. E. Larsen, V. Lemaitre, S.-L. Liu, A. Lyapine, F. K. Loebinger, R. Marshall, A. D. Martin, J. Monk, I. Nasteva, P. Nemegeer, M. M. Obertino, R. Orava, V. O'Shea, S. Ovyn, A. Pal, S. Parker, J. Pater, A.-L. Perrot, T. Pierzchala, A. D. Pilkington, J. Pinfold, K. Piotrzkowski, W. Plano, A. Poblaguev, V. Popov, K. M. Potter, F. Roncarolo, A. Rostovtsev, X. Rouby, M. Ruspa, M. G. Ryskin, A. Santoro, N. Schul, G. Sellers, A. Solano, S. Spivey, W. J. Stirling, D. Swoboda, M. Tasevsky, R. Thompson, T. Tsang, P. V. Mechelen, A. V. Pereira, S. J. Watts, M. R. M. Warren, G. Weiglein, T. Wengler, S. N. White, B. Winter, Y. Yao, D. Zaborov, A. Zampieri, M. Zeller, and A. Zhokin, FP420 Collaboration, "The FP420 R&D project: Higgs and New Physics with forward protons at the LHC," Journal of Instrumentation **4**(10), 10001 (2009).
7. K. Inami, N. Kishimoto, Y. Enari, M. Nagamine, and T. Ohshima, "A 5 ps TOF-counter with an MCP–PMT," Nucl. Inst. and Methods in Phys. Res. Sec. A **560**(2), 303–308 (2006).

#220016 - $15.00 USD Received 5 Aug 2014; revised 28 Sep 2014; accepted 20 Oct 2014; published 12 Nov 2014

8. M. G. Albrow, H. Kim, S. Los, M. Mazzillo, E. Ramberg, A. Ronzhin, V. Samoylenko, H. Wenzel, and A. Zatserklyaniy, “Quartz Cherenkov counters for fast timing: QUARTIC,” Journal of Instrumentation **7**(10), 10027 (2012).
9. ATLAS Collaboration, “Letter of Intent for the Phase-I Upgrade of the ATLAS Experiment,” CERN-LHCC-2011–012 (2012).
10. A. Brandt, “Fast timing system for LHC time-of-flight detector,” presented at the Workshop on picosecond photon sensors for physics and medical applications, Clermont-Ferrand, France, 12–14 March, 2014.
11. L. Mapelli for ALFA Collaboration, “Development of a detector (ALFA) to measure the absolute LHC luminosity at ATLAS,” Astroparticle, Particle, Space Physics, Radiation Interaction, Detectors and Medical Physics Applications **4**, 984–988 (2008).
12. G. Antchev, P. Aspell, I. Atanassov, V. Avati, J. Baechler, M. G. Bagliesi, V. Berardi, M. Berretti, E. Bossini, U. Bottigli, M. Bozzo, E. Brücken, A. Buzzo, F. S. Cafagna, M. G. Catanesi, R. Cecchi, C. Covault, M. Csanád, T. Csörgő, M. Deile, M. Doubek, K. Eggert, V. Eremin, F. Ferro, A. Fiergolski, F. Garcia, S. Giani, V. Greco, L. Grzanka, J. Heino, T. Hilden, A. Karev, J. Kašpar, J. Kopal, V. Kundrát, S. Lami, G. Latino, R. Lauhakangas, T. Leszko, E. Lippmaa, J. Lippmaa, M. Lokajíček, L. Losurdo, M. L. O. Vetere, F. L. U. C. A. S. Rodríguez, M. Macrí, T. Mäki, A. Mercadante, N. Minafra, S. Minutoli, F. Nemes, H. Niewiadomski, E. Oliveri, F. Oljemark, R. Orava, M. Oriunno, K. Österberg, P. Palazzi, E. Pedreschi, J. Procházka, M. Quinto, E. Radermacher, E. Radicioni, F. Ravotti, E. Robutti, L. Ropelewski, G. Ruggiero, H. Saarikko, A. Scribano, J. Smajek, W. Snoeys, F. Spinella, J. Sziklai, C. Taylor, A. Thys, N. Turini, V. Vacek, M. Vítek, J. Welti, J. Whitmore, and P. Wyszkowski, G. Antchev for the TOTEM Collaboration, “Performance of the TOTEM detectors at the LHC,” Int. J. Mod. Phys. A **28**(31), 1330046 (2013).
13. S. Agostinelli, J. Allison, K. Amako, J. Apostolakis, H. Araujo, P. Arce, M. Asai, D. Axen, S. Banerjee, G. Barrand, F. Behner, L. Bellagamba, J. Boudreau, L. Broglia, A. Brunengo, H. Burkhardt, S. Chauvie, J. Chuma, R. Chytracek, G. Cooperman, G. Cosmo, P. Degtyarenko, A. Dell’Acqua, G. Depaola, D. Dietrich, R. Enami, A. Feliciello, C. Ferguson, H. Fesefeldt, G. Folger, F. Foppiano, A. Forti, S. Garelli, S. Giani, R. Giannitrapani, D. Gibin, J. J. Gómez Cadenas, I. González, G. Gracia Abril, G. Greeniaus, W. Greiner, V. Grichine, A. Grossheim, S. Guatelli, P. Gumplinger, R. Hamatsu, K. Hashimoto, H. Hasui, A. Heikkinen, A. Howard, V. Ivanchenko, A. Johnson, F. W. Jones, J. Kallenbach, N. Kanaya, M. Kawabata, Y. Kawabata, M. Kawaguti, S. Kelner, P. Kent, A. Kimura, T. Kodama, R. Kokoulin, M. Kossov, H. Kurashige, E. Lamanna, T. Lampén, V. Lara, V. Lefebure, F. Lei, M. Liendl, W. Lockman, F. Longo, S. Magni, M. Maire, E. Medernach, K. Minamimoto, P. Mora de Freitas, Y. Morita, K. Murakami, M. Nagamatu, R. Nartallo, P. Nieminen, T. Nishimura, K. Ohtsubo, M. Okamura, S. O’Neale, Y. Oohata, K. Paech, J. Perl, A. Pfeiffer, M. G. Pia, F. Ranjard, A. Rybin, S. Sadilov, E. Di Salvo, G. Santin, T. Sasaki, N. Savvas, Y. Sawada, S. Scherer, S. Sei, V. Sirotenko, D. Smith, N. Starkov, H. Stoecker, J. Sulkimo, M. Takahata, S. Tanaka, E. Tcherniaev, E. Safai Tehrani, M. Tropeano, P. Truscott, H. Uno, L. Urban, P. Urban, M. Verderi, A. Walkden, W. Wander, H. Weber, J. P. Wellisch, T. Wenaus, D. C. Williams, D. Wright, T. Yamada, H. Yoshida, and D. Zschiesche, “Geant4—a simulation toolkit,” Nucl. Instrum. Methods Phys. Res. A **506**(3), 250–303 (2003).
14. P. M. Duarte, “QUARTIC: An ultra-fast time-Of-flight counter,” M.Sci. Thesis, The University of Texas, Arlington, 2007.

1. Introduction

Precision timing is useful for many applications, ranging from Positron Electron Tomography (PET) scans to particle physics (for example TORCH at LHCb [1]). For PET scans, information about the time of the arriving photon pair helps improve the position resolution by determining the locus of the electron-positron pair annihilation, while for high energy physics, it has typically been used in conjunction with a momentum measurement to determine the mass of the particle, which in turn defines the particle’s identity.

Timing detectors can be used as a part of the proton tagging detectors to decrease the background to central exclusive production (CEP) events $p + p \to p + X + p$ where X stands for the centrally produced system, which could consist of a pair of jets, a pair of intermediate vector bosons (W + W-), or even a Higgs boson H [2, 3]. For the rare processes above, high luminosity is required, which implies that multiple interactions take place in every proton bunch crossing (pile-up). By using timing detectors on both sides of the interaction point, the background is rejected from protons that do not originate from the same vertex as the central system X. The time difference measurement to reduce pile-up was first proposed as an upgrade of the CDF experiment at Fermilab [4, 5], but was not implemented. This idea was then adopted by the joint ATLAS-CMS FP420 R&D collaboration for the LHC [6].

At high luminosity, the LHC environment places stringent demands on the timing detectors: unprecedented resolution (~10 ps, equivalent to 2.1 mm interaction vertex resolution), high rate capability (5 to 10 MHz), radiation hardness (integrated charge of 10

C/cm2/yr), and multi-proton detection capabilities (~1 background proton/detector is expected per bunch crossing at standard luminosity).

The first detector to achieve 10 ps resolution was developed by Nagoya, and consisted of a short quartz bar connected to a microchannel plate photomultiplier (MCP-PMT); the charged particle travels the length of the bar with the entire Cherenkov cone captured by the PMT [7]. Building on this concept, Albrow proposed the QUARTIC detector, a matrix of straight quartz bars oriented at the Cherenkov angle (~48 degrees for fused silica). This design has the advantage that the PMT is out of the direct beam and it effectively compensates for time differences between photons emitted at different points along the proton's path [8].

The QUARTIC design has been studied extensively by FP420 [6, 8] and AFP (ATLAS Forward Proton programme) [9], and with some modifications to the MCP-PMT to improve its lifetime [10] the system meets all requirements for operation at the LHC. Because of concerns about the PMT lifetime, CMS investigated a promising alternative, using Silicon photomultipliers (SiPMTs) to read out the fused silica bars. Since the resolution of the SiPMTs are inferior to the MCP-PMT, Albrow proposed a new "L" shape (L-bar) which combines the virtues of having the Cherenkov radiator bar parallel to the beam to maximize the light, with a perpendicular light guide bar to allow the photodetector to be positioned away from the beam [8].

Recently the planned interface to the accelerator was changed from a movable section of beam pipe (Hamburg pipe) to a more traditional Roman pot approach [11, 12], which does not have space for QUARTIC, but could house an L(Q)Bar detector. The primary aim of this paper is to study the LQBar performance, as well as several new designs devised to both fit in a 140 mm diameter Roman Pot and to satisfy the resolution goals. This goal is accomplished by simulating and analyzing the propagation of the Cherenkov photons through the different detector geometries to the photo-sensor, studying the resulting hit distributions, and comparing the results to benchmark straight bar detector.

2. Designs for a Roman-pot-based Quartz Cherenkov detector

2.1. Dimension constraints in Roman pot

Despite the excellent resolution of QUARTIC, measured by ATLAS to be better than 15 ps [10], it is not a viable option for a Roman pot (hosting movable device) due to space constraints (the PMT is in-line with the sensors at the Cherenkov angle). In the LBar design, the radiator bar is parallel to the beam and collects more light than QUARTIC because the condition for total reflection is fulfilled along the whole pathway. However, the LBar design lacks time compensation and the amount of material it presents to particles is relatively large.

In this work, we propose a shape which combines the best features of the QUARTIC and LBar designs while satisfying the dimensional constraints imposed by a Roman pot, Fig. 1(a). The basic component of the new detector is the LQBar, which is a modified LBar with the radiator oriented at the Cherenkov angle as in the QUARTIC design, see Fig. 1(b). This design suggests one train of bars with the radiator arm of the cross-section 2x6 mm (due to higher exposure to the beam), the second one with the radiator cross-section 3x6 mm, and the remaining trains with the radiator cross-section 5x6 mm.

In contrast to the LBar where the condition for total reflection is fulfilled along the whole pathway to the photodetector, the LQBar requires a mirrored 45 degree elbow (0.79 rad) to get the light up the light guide bar to the PMT. The critical angle of fused silica varies between 40.2 degrees to 43.2 degrees (0.70 rad – 0.75 rad) within the wavelength range 200-600 nm, thus the condition of the total reflection is still fulfilled on side walls of the LQBar (except the elbow). To minimize the effects of color dispersion, one could replace parts of the quartz or fused silica with an air light guide, for example an (internally polished) aluminum tube. Below we present simulation results evaluating different options.

#220016 - $15.00 USD Received 5 Aug 2014; revised 28 Sep 2014; accepted 20 Oct 2014; published 12 Nov 2014

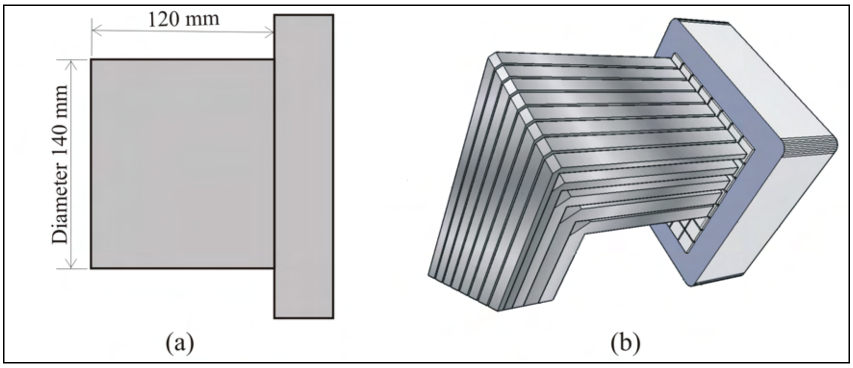

Fig. 1. (a) Typical Roman pot dimensions, (b) proposed design of new TOF with matrix of LQBars with various cross-section profiles of radiator arm.

2.2. Radiator and Light Guide design

Studies to optimize the design were performed using Geant4 [13]. The Geant4 simulation focuses on optimizing the details of the LQBar implementation, since neither the LBar nor the straight bar (QBar) fit in the available space. A straight bar of the same total length as the LQBar is simulated, however, since it is the performance standard, and it can be used to connect the simulation to real data [10].

Figure 2 shows the basic size and shape of the LQBar, which is geometrically divided into a radiator arm (vertical arm) traversed by the proton and a light-guide arm (horizontal one) channeling the light to the photo-sensor (the red element at the end of the light guide).

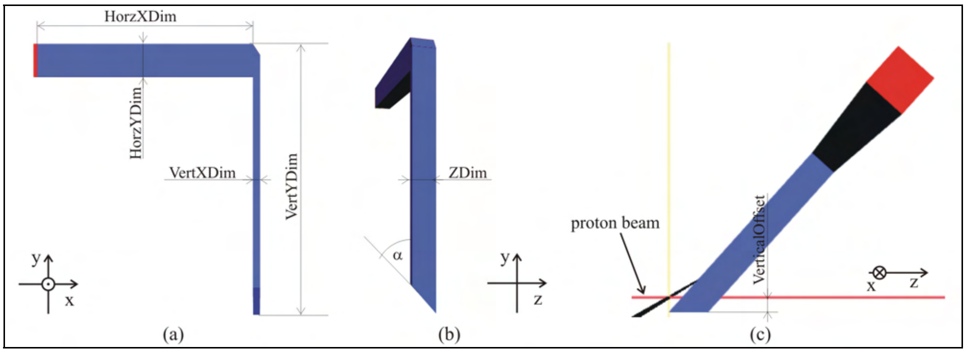

Fig. 2. Dimensions of a basic LQBar.

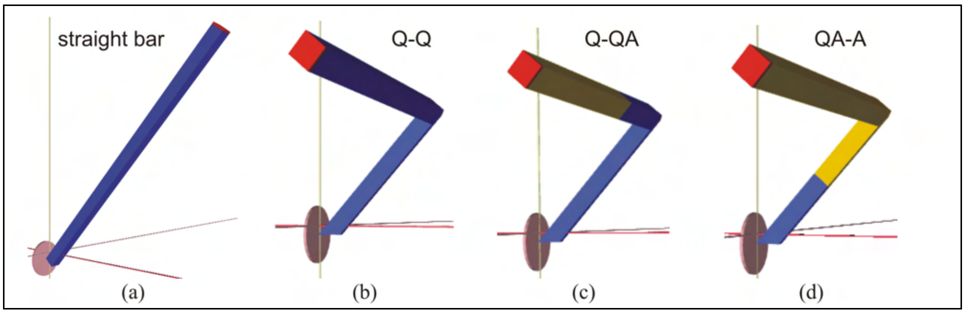

Fig. 3. Types of studied LQBar designs including the straight bar.

#220016 - $15.00 USD Received 5 Aug 2014; revised 28 Sep 2014; accepted 20 Oct 2014; published 12 Nov 2014

The average Cherenkov angle θ_c for fused silica is 48 degrees (0.84 rad) for relativistic protons with β (= v/c) close to one. The angle is a function of wavelength. The value 48 degrees was calculated for the UV region (200-400 nm). The bottom face of the radiator bar is generally made absorbing since this light is directed away from the photo-sensor. However, by making a cut parallel to the beam at $\alpha = \theta_c$ (Fig. 2(c)), these downward emitted photons are redirected back up through the bar and recovered for particles passing close to the bottom end of the radiator bar. Another feature of the LQbar is the "elbow" between the two bars, which is cut at 45 degrees and aluminized to maximize the light transmission. The following detector geometries were studied, see also Fig. 3 (blue colour stands for a fused silica part, yellow colour stands for an air light guide):

1. A straight QBar of fused silica, see Fig. 3(a), where the pink circle is the position of the proton track; note that the radiator bar has a square-cut bottom side because this geometry was studied experimentally [10, 14] and serves as a benchmark, *parameters in analysis:* 150 mm long, arm square profile 6 × 6 mm^2,
2. A regular all fused silica LQBar with a metalized elbow, Fig. 3(b); denoted as Q-Q, *parameters in analysis:* aluminized elbow (90% reflectivity), radiator arm: length 60 mm and cross section 2 × 6 mm^2, and light-guide arm: length 90 mm, cross profile 6 × 6 mm^2,
3. An LQBar with the radiator arm of fused silica, and the light-guide arm divided into part fused silica and part air-filled light guide, see Fig. 3(c), denoted as Q-QA, *parameters in analysis:* 90% reflectivity of air light–guide walls, radiator arm: length 60 mm, cross profile 2x6 mm, and light-guide arm: length 90 mm of which 30 mm made of fused silica, cross profile 6x6 mm,
4. An LQBar with the radiator of fused silica and the light guide filled with air denoted as QA-A, Fig. 3(d), *parameters in analysis:* 90% reflectivity of air light-guide walls, radiator arm: length 60 mm of which 30 mm made of fused silica, cross profile 2x6 mm, and light-guide arm: air guide, length 90 mm, cross profile 6x6 mm.

The Q-A configuration is omitted because it gives very poor results as much of the light gets trapped in the radiator bar. For completeness we also implemented the LBar option.

2.3. Material properties

The properties of the materials implemented in the simulation are those of suprasil (fused silica) with an index of refraction and absorption length as plotted in Fig. 4(a). The air-filled light guide is implemented as a vacuum. The photosensor is represented by its entrance window with index of refraction 1.474. The choice of the material is not important, however, due to a usual scheme of a sensor handling in the Geant4 by means of the concept of so-called sensitive volumes. When a photon hits the sensor, its state information is stored and then it is killed and not propagated anymore. A spectral sensitivity of the sensor is implemented through its photodetection efficiency discussed below.

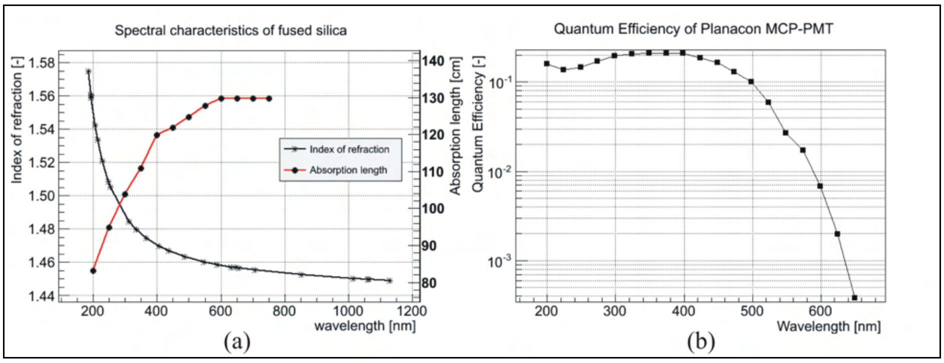

Fig. 4. (a) Material properties of fused silica, (b) quantum efficiency of Planacon MCP-PMT.

2.4. Photoelectron generation

The photoelectron statistics for an event is the number of generated photons that are converted to photoelectrons and measured by the photosensor. The number of photoelectrons is given by

$$N = 2\pi\alpha L\int_{\lambda_1}^{\lambda_2}\frac{\varepsilon(\lambda)}{\lambda^2}\left(1-\frac{1}{n^2(\lambda)}\right)d\lambda. \qquad (1)$$

The number of generated photons is linearly dependent on L, the path length of proton in the radiator, and scales with the inverse square of the index of refraction (n) and the wavelength of the radiated photons λ. The photosensor type determines the acceptance of the wavelength range (λ_1 and λ_2). In Eq. (1), α denotes the fine structure constant, and ε the photodetection efficiency. The accepted wavelength range for the Planacon MCP-PMT is 185 nm to 650 nm [14]. The path length of the proton through the radiator is L = ZDim/sin(θ_c), where ZDim is the thickness of the QBar; in our case ZDim = 6 mm, and L = 8.1 mm.

When the optical photon reaches the sensor (which is actually the sensitive volume in Geant4), two efficiencies are applied that govern the conversion to photoelectrons: the photodetection efficiency (PDE) and the collection efficiency. If the photoelectron survives, a 'hit' is registered (as photoelectron) for analysis. We adopted photocathode quantum efficiency data of the Planacon MCP-PMT published in [14], see Fig. 4(b), and the collection efficiency is set to 0.6. In the case of a full fused silica bar (Q-Q) of 150 mm in the length, losses caused by absorption in the medium (a fused silica radiator and/or a waveguide) and by multiple reflections on the medium boundaries are approximately 30% of the signal, giving a maximum number of accepted photoelectrons N~50 from Eq. (1). Losses in the Q-QA and the QA-A are significantly higher due to the presence of the extra optical boundary between fused silica and air. This in particular affects photons propagated via multiple total reflections on sides of the bar (noted as side wings in this paper, see below).

3. Simulation studies and results

The LQBar geometry studies are divided into two parts. First, we compare the various types of LQBars to the QBar (straight bar) for which there is test beam data [10]. The light guide is always given as a square 6 × 6 mm^2 cross section to match the pixel size of the Planacon MCP-PMT, and ends flush against the PMT entrance window (in simulation there is a slight overlap between the light guide volume and the window to ensure a good connection; in practice a good contact must be mechanically ensured, unless an index-matching radiation-tolerant high- transmission gel is obtained).

In the second part of the study, we introduce various geometrical modifications of the basic designs in order to further improve the hit statistics at the sensor.

In all studies, protons with 7 TeV were used to generate Cherenkov light while passing bars without smearing of their direction and position. The simulation was set up so that the beam direction was along the z-axis in the simulation scene.

3.1 Comparison among types of LQBars

First, we compared the QBar and the three types of LQBars: Q-Q, Q-QA and QA-A as listed in section 2.2 a visualized in Fig. 3. All four designs have the same total geometrical path length of 150 mm and the light guides all have a cross section of 6 × 6 mm^2.

Simulated time profiles are plotted in Fig. 5(a) for a 1 ns wide time window and a 3.0 mm vertical offset of the beam (see Fig. 2(c)). More than 90% of all hits fall inside this time window, except for the straight QBar, which has a significant tail at longer arrival times. Because of the different optical path lengths, the first hits generally occur sooner in the case of LQBars with air light guides (Q-QA and QA-A). For instance, the first hit on the sensor occurs at 541 ps measured from the time the proton enters the trigger volume, compared to 730 ps in a straight bar (see t_0 in legend). The optical path length for the Q-Q LQBar is the same as for the straight QBar, thus their first hit arrival times are the same. In the case of the Q-Q LQBar, the total signal is split between a first and a second (late) peak. The late peak is linked to the presence of the so-called side wings of the photon trajectories, see Fig. 7 and text below.

Cutting the radiator bar at the bottom parallel to the beam significantly increases the total hit count, and results in a strong dependence of the total hit count on the vertical beam offset. This behavior is illustrated in Fig. 5(b) and occurs for vertical offsets in the range from 0 mm to 4 mm (this depends on the cross section of the radiator). For larger offsets, most of the downward Cherenkov photons leave the bar.

For a very small offset, for instance 0.1 mm, the light yield is significantly higher than for a large offset. In the case of the Q-QA design the yield factor is almost 2, and for the Q-Q design the factor is 1.3, which brings it to the level of the straight bar. One can design the detector to take advantage of this behavior when the beam position has a small spread in height.

Note that this effect is negligible for the QA-A LQBar as it corresponds to the strong angular selection of photon directions in that design. In general, the hit count is independent of the vertical offset if the radiator bar is square cut, as is the case of the reference straight QBar. Both effects are further discussed below in the context of the photon acceptance as a function of the origin. Unless noted otherwise a parallel cut of 3mm will be used as the default.

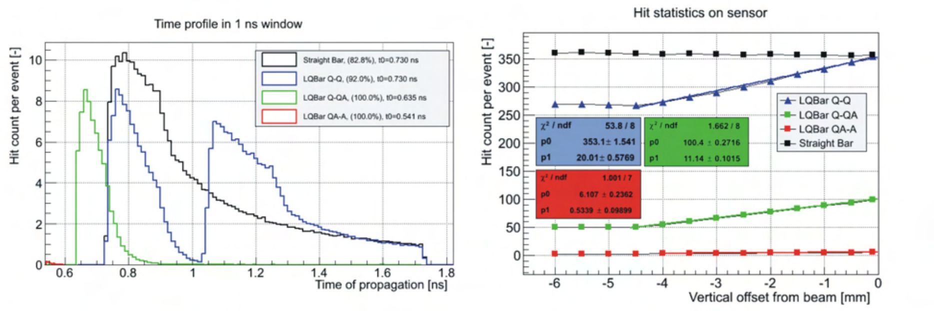

(a) (b)

Fig. 5. (a) Time profile of hits in 1 ns window, (b) dependency on vertical offset from beam.

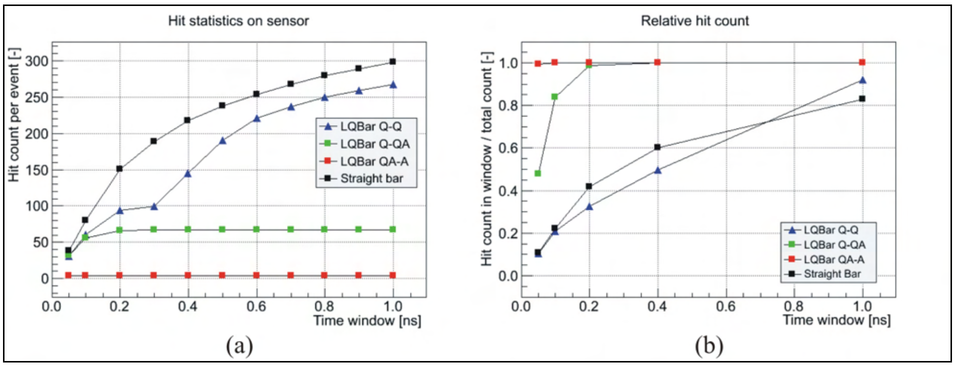

Fig. 6. (a) Absolute, and (b) relative hit amount of Cherenkov photons per one passing proton.

Figure 6(a) summarizes hit statistics per event for all these time windows. Only the Q-Q LQBar design approaches the reference bar in hit count. As for total hit count, the Q-QA and QA-A designs suffer from reflections at the extra optical boundary between the fused silica and air light guide because of intrinsic reflection (4%), and additional total internal reflection of photons incident on the interface at large angle. As for the Q-Q design, there is a jump of the hit count between 0.3 and 0.4 ns due to arrival of the second peak, see Fig. 5(a).

In Fig. 6(b), the percentage of hits in an arrival time window of the total is plotted as function of the time window size for several LQBar designs. In the case of the hybrid Q-QA design, almost all photons reach the sensor in the first 200 ps (97%), while for the QA-A case, all photons arrive even within the first 50 ps. This is explained by the fact that photons move faster and with less velocity dispersion within a hybrid design because of the shorter optical path. However, the total hit count is low compared to all fused silica designs because of reflections on the extra Q-A boundary. Therefore Q-Q and Straight Bar designs perform better for time windows greater than 400 ps. The total hit count is 360 per passing proton in the reference QBar design. Referring to Fig. 5, the hit count for the Q-Q LQBar design is similar for a vertical beam offsets close to zero.

The distribution of azimuth emission angle φ (the angle in the plane perpendicular to the beam direction) of the generated Cherenkov photons is plotted in Fig. 7(a). Except for the reference straight bar QBar design, the φ distributions feature empty intervals caused by the geometry which strongly influences the acceptance of the photons. As seen in Fig. 7(b), the φ distribution has wings in the φ vs. arrival time distribution.

Referring to Fig. 7(a), gaps occur in the distributions for the hybrid Q-QA and QA-A designs for the intervals from -0.73 rad to $+ 0.73$ rad, from $+ 2.4$ rad to $+ \pi$ rad, and from $-\pi$ rad to -2.4 rad (so-called 'side regions'). These intervals correspond to those outside of area of total internal reflections in the interface between the fused silica and air light guide. The φ distribution wing lying at around 1.57 rad (90 degrees) corresponds to those photons traveling straight to the sensor (thus called the direct wing in the direct region). The decrease from the central peak at 1.57 rad is due to an increase in optical path length including one or more reflections. Note the additional φ wing at negative φ between -2.4 rad and -0.73 rad which corresponds to similar photons but after reflection off the cut at the bottom end of the radiator bar. The detailed photon content of this negative φ wing depends on the vertical offset of the beam. In our case, a 6 mm wide bar, the photon content diminishes for offsets higher than 4 mm, see Fig. 5(a). Because the reference straight QBar has a square-cut bottom the negative φ photons are all lost.

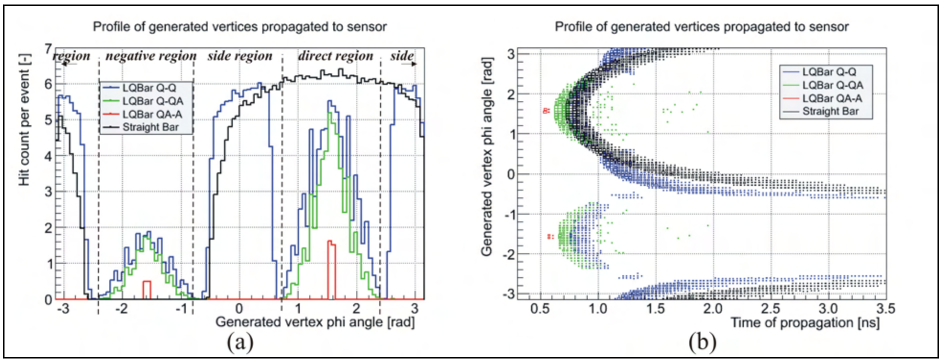

Fig. 7. (a) Vertex φ distribution of generated vertices, (b) its profile as function of arrival time.

Peaks in the photon arrival time distribution are seen in the QA-A design; this is caused by a strong φ dependence of the photon survival ('hits') and it corresponds to the total internal reflection of all photons emitted away from the vertical direction ($\varphi = \pm 1.57$ rad) on the Q/A boundary. This applies to the Q-QA case as well, but there is not such a strict φ selection. A scan varying the length of the fused silica part indicates that the radiator length has a minor effect on the total hit count (~5%). Additionally, for square-cut LQbar versions, the φ distribution is almost identical to the parallel-cut counterparts except for the missing negative φ wing.

Referring to Fig. 7(b), one can note that photons in the wings are increasingly delayed going away from the vertical. Notably for the Q-Q LQBar design, the fronts of the wings in the side regions are delayed by 270 ps with respect to the front of the direct wing (which is identical in shape to the direct wing of the straight Qbar). This corresponds to the second peak in the time profile (Fig. 5). The time delay of the negative φ wing with respect to the direct wing depends on the beam offset. For vertical offsets in the range from 0 mm to 4 mm, the time delay increases 7 ps/mm. For higher offsets it grows roughly 200 ps/mm but bigger portion of the negative wing go outside the bar until it diminishes at the offset of 5.5 mm.

It is obvious that only the Q-Q LQBar comes close to the straight bar in terms of photon efficiency. The other bars suffer from the additional optical boundary between the fused silica and air light guide. On the other hand, the Q-Q LQbar signal is divided into a main, early photon bunch represented by direct wing (along with weaker negative φ wing) and two delayed side wings resulting in a spread in photon arrival time. However, much of this time spread can be countered by additional design modifications discussed in the next section.

3.2. Geometry extensions of Q-Q LQBar

In order to catch as many photons as possible in the shortest possible time window in the Q-Q LQBar design, small modifications of the light guide were studied, see Fig. 8. These consist in a shift of the light guide (dimension *exty* – extended vertical shift) in the vertical direction and tapering near the 90 degree elbow at a given taper angle. Unsurprisingly, the tapered part together with 45° elbow act as a rough approximation to a semi-parabolic collimating mirror, see Fig. 8(b).

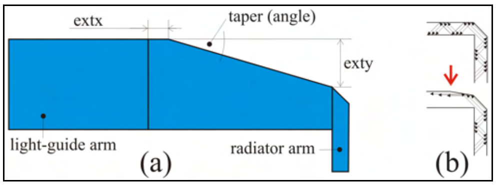

Fig. 8. Geometry extension of light-guide arm.

A variety of shifts and taper angles was studied. The taper angle was varied over the interval from 0 degrees to 35 degrees in 5 degree steps (2 degree steps in the vicinity of the optimal taper of 25 degrees), taking a fixed vertical shift value of 2 mm. The vertical shift was varied over the range from 0 mm to 4 mm in 0.5 mm steps with a fixed 22 degree taper angle.

The hit count distributions as function of shift and taper angle are summarized in Fig. 9 for 200 ps, 400 ps, and full photon arrival time windows. The maximum hit count is obtained for shifts between 2.0 and 2.5 mm for all these time windows. The hit count maximum is reached for taper angles between 20 and 25 degrees for the 200 ps and the full time windows. However for the 400 ps window, the optimal taper angle is shifted to 15 degrees. The maximum hit count in the full time window is 408 per proton for the modified Q-Q LQBar design with optimized parameters (those maximizing hit count), i.e. a factor 1.10 higher compared to the reference straight QBar design (hit count 370). This value is obtained for a vertical beam offset of −3 mm from beam axis.

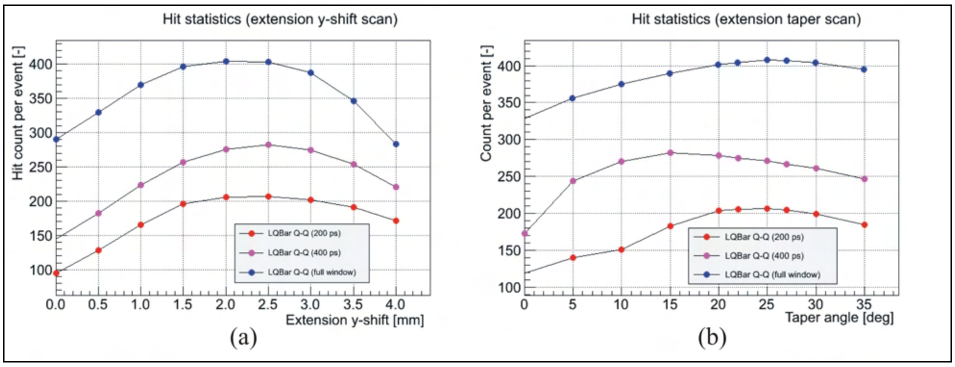

(a) (b)

Fig. 9. Hit count as a function of (a) light guide vertical shift, (b) taper angle.

The modified/optimized Q-Q LQBar design, with a vertical shift 2.5 mm and the taper angle of 25 degrees, is compared with the original Q-Q LQBar design and with the reference straight QBar. The resulting distributions are plotted in Fig. 10. It is obvious that the modifications result in a shift of the side wings by about 200 ps towards shorter arrival times, see Fig. 10(b). The same applies to the negative φ region. This wing shift gives a higher hit count of 408 compared to 290 for the non-modified Q-Q bar design, an increase by a factor 1.4. This results in a beneficial time compression of the arrival time distribution.

The number of accepted photoelectrons (PE) by the photosensor is plotted in Fig. 11(a) for various arrival time windows up to 500 ps. The PE statistics of the optimized Q-Q LQbar design are generally higher than those of the straight QBar design. Distributions of photoelectrons accepted in the sensor in first 400 ps are plotted in Fig. 11(b). This particular size of time window was chosen because it is thought to best approximate the real signal acquisition conditions of the AFP DAQ system. The modified Q-Q LQBar design is better at photoelectron detection than the reference straight QBar (25 vs. 20 photoelectrons) and almost two times better than unmodified Q-Q LQBar.

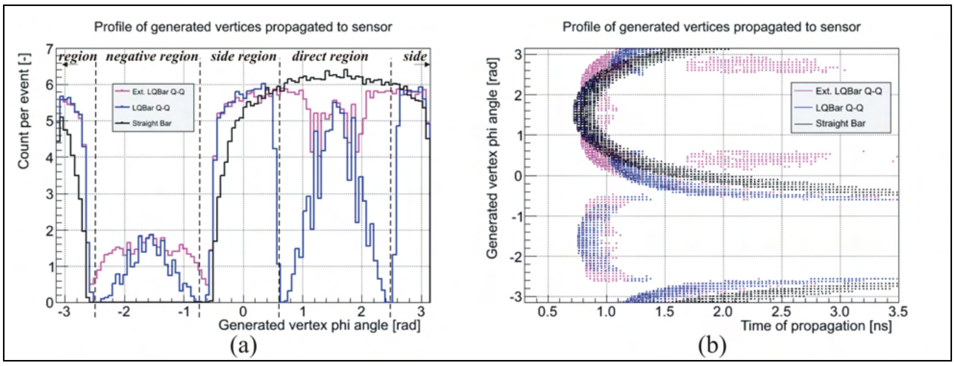

Fig. 10. Comparison of the optimized Q-Q LQBar design compared to the non-modified LQBar: (a) distribution of generated photon φ angle, (b) photon arrival time distribution.

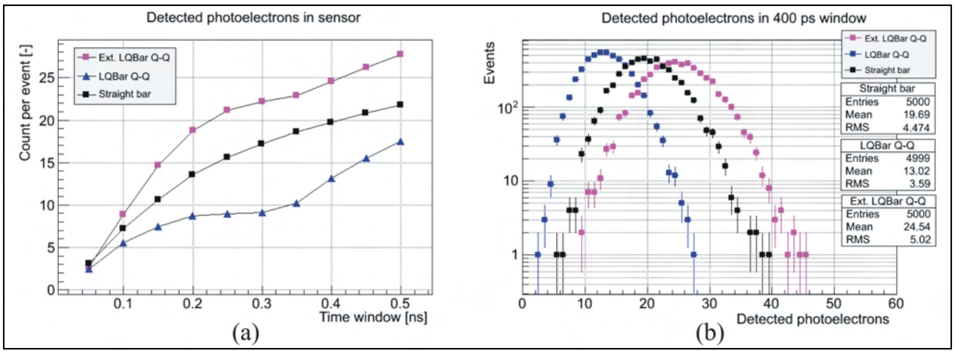

Fig. 11. (a) Statistics of photoelectrons accepted in sensor, (b) dependency on time window.

4. Hit characteristics on sensor surface

The studies discussed above are intended guide design of a modified LQBar geometry optimizing the photon hit statistics and arrival time distribution. In this section, the focus is on the hit count distribution at the surface of the sensor with the optimized Q-Q LQBar design. Note that the following results are based on hits passing the PDE and collection efficiency criteria (see section 2.4 above). These criteria affect the accepted photon wavelength distribution and are therefore somewhat coupled with the time-of-arrival distribution and the resulting PE pulse profile. Due to the dispersion, see Fig. 4(a), photons with higher wavelengths reach the sensor sooner but their contribution is reduced due to lower quantum efficiency of the sensor in the region, Fig. 4(b). This in turn affects a sharpness of the pulse.

Figures 12 and 13 show histograms of the number of photoelectrons as a function of photon wavelength, generated photon φ angle, and the time of arrival at the sensor surface. The distribution of the optical signal at the sensor surface is plotted in Fig. 12(a). It is noted that the signal is not uniform in the z-direction along the sensor surface (which corresponds to the beam direction rotated by the Cherenkov angle in the plane containing the beam and the vertical axis). Figure 12(b) shows the wavelength distribution of photons hitting the sensor as a function of arrival time. One notes that photons of 200 nm – 400 nm wavelengths dominate the first 270 ps of the pulse. Thus an appropriate optical band-pass filter within this range could filter out a portion of an eventual light background. Figure 13 shows the distribution of generated photon φ angle as function of time and photon wavelength. Note the high statistics (red and orange colors) in the direct and negative wings in the first 270 ps of the pulse, see Fig. 13(a). The wavelengths of photons in this part of the pulse are mostly in the 200 nm – 400 nm range, see Fig. 13(b).

Timestamps of accepted hits are used for a crude preliminary estimate of the timing resolution of a device consisting of the optimized extended Q-Q LQBar, the PMT and a constant fraction discriminator (CFD). This analysis does not include all aspects of the signal processing which is outside of the scope of this paper. Instead, we use a simplified model of the PMT timing performance by means of its impulse response. The impulse response is a function of a rise time, a fall time, a transit time, a transit time spread, and a gain of the PMT. We use following values: the rise time of 300 ps, the fall time of 1500 ps (the Planacon 85011-501 datasheet), a transit time spread of 35 ps (based on [14]), and a gain of 10^5. The transit time itself has no effect on the timing performance in this model and it is set to 0 ns. The constant fraction value of the CFD is set 20% of the signal amplitude. First, the timing model is validated on results of the reference straight bar with a measured $\sigma = 19$ ps [10]. The model is then applied to the optimized Q-Q LQBar. We obtain $\sigma \sim 15$ ps for a single bar. Adding N bars in a train of the QUARTIC detector, the timing resolution improves to σ/sqrt(N). This gives the timing resolution of 8 ps for the QUARTIC of $N = 4$ bars per train and a beam without position smearing.

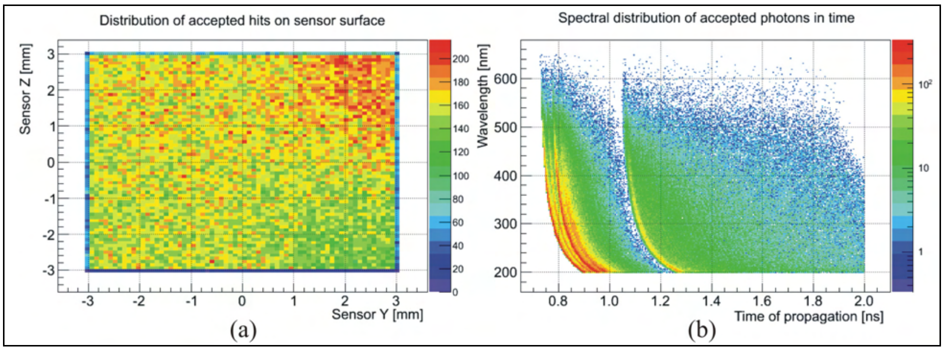

Fig. 12. (a) Statistics of photoelectrons accepted in sensor, (b) time distribution of spectra.

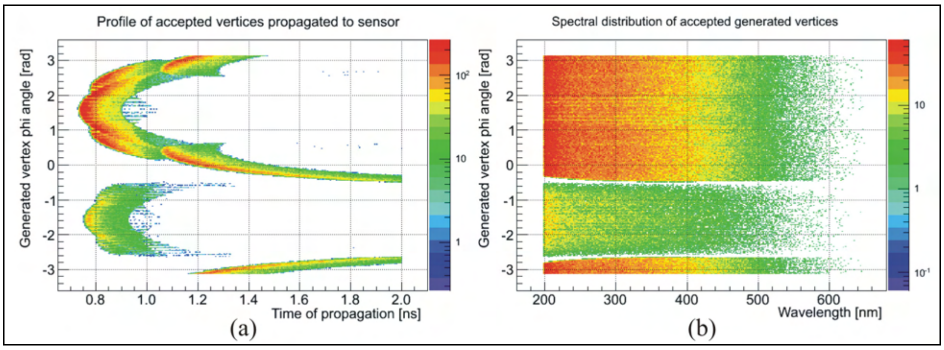

Fig. 13. Distribution of generated vertex φ angle (a) in time, (b) over wavelength range.

5. Conclusion

We have studied several possible designs of an LQBar Cherenkov radiator for a new Time-Of-Flight (TOF) detector suitable for measurements in the vicinity of proton beams at high luminosity. The Roman Pot near-beam interface is well established for such measurements, but presents severe space constraints on the design of suitable TOF detectors. We performed simulation studies of several different LQBar designs, and a variety of possible modifications, compared to a straight QBar design which has well known characteristics from test beam measurements [10].

A hybrid combination of fused silica radiator and an air light guide (QA-A or Q-QA LQBar designs) was studied and was found to be promising because of the narrow hit profile in time. Almost all photons reach the sensor in the first 200 ps (97%) in the case of the Q-QA hybrid variant, compared to 43% for the reference straight QBar, see Fig. 6(b). However, the QA-A hybrid gives a significantly lower hit count and therefore it is not a satisfactory design. The Q-QA hit count is comparable to the regular Q-Q designs for short arrival time windows (less than 300 ps). Thus for timing purposes, the Q-QA is also a promising design in a sense that its light pulse is more compressed than the one for the Q-Q type, see also Fig. 6(a).

Geometric modifications (taper, light guide shift) are proposed to further improve the LQBar design. These modifications are seen to strongly improve the arrival time distribution of the Q-Q LQBar design with an optimal vertical light guide shift of about 2.5 mm and a taper angle around 25 degrees. The Q-QA type, however, shows only a small improvement with design modifications, therefore it is also discarded in favor of the Q-Q design.

The modified and optimized version of the Q-Q LQBar design is thus a promising solution for the AFP TOF detector because of its narrow hit profile and improved hit count in short arrival times. In fact this design gives a higher signal than the reference straight bar by a factor of 1.25 assuming the vertical offset of 3 mm, and the factor is still higher if the beam passes closer to the bottom cut. One can design the detector to take advantage of this behavior when the beam position has a small spread in height. Noting that wavelengths in the range from 200 mm to 400 nm dominate the first 300 ps of the light pulse, adding a band-pass filter could further improve the detector performance.

The final steps to measure the resolution of the detector/MCP-PMT system would be to model how the phototube converts the photon time distribution to an electrical pulse, and then simulate the constant fraction discriminator and TDC operation, a task that is well outside the scope of this paper. Given the straight bar normalization point of 19 ps, however, a reasonable estimate of the resolution/bar can be obtained by scaling this by the square root of the ratio of the amount of photons (LQBar/straight bar) in the relevant time window, implying that an LQBar-based detector could exceed the performance of QUARTIC by 10-40%.

In summary, we can conclude that it is possible to construct the Q-Q based detector with a resolution better than the standard QUARTIC detector.

Acknowledgments

The authors gratefully acknowledge the support by the “Mezinarodni experiment ATLAS-CERN (MSMT INGO II č. LG13009)”, the U.S. National Science Foundation grants PHY1068677 and PHY1119200 and the U.S. Department of Energy grant DE-SC0007054 (Stony Brook University), IGA_PrF_2014005 of the Palacky University, and Texas ARP, Department of Energy (UTA).

Research Article
Vol. 24, No. 24 | 28 Nov 2016 | OPTICS EXPRESS 27951
Optics EXPRESS

Construction of the optical part of a time-of-flight detector prototype for the AFP detector

L. NOZKA,[1,*] L. ADAMCZYK,[2] G. AVONI,[3] A. BRANDT,[4] P. BUGLEWICZ,[5] E. CAVALLARO,[6] G. CHIODINI,[7] L. CHYTKA,[1] K. CIESLA,[5] P.M. DAVIS,[8] M. DYNDAL,[2] S. GRINSTEIN,[6] P. HAMAL,[1] M. HRABOVSKY,[1] K. JANAS,[2] K. JIRAKOVA,[1] M. KOCIAN,[9] T. KOMAREK,[1] K. KORCYL,[5] J. LANGE,[6] D. MANDAT,[1] V. MICHALEK,[1] I. LOPEZ PAZ,[6] D. NORTHACKER,[10] M. RIJSSENBEEK,[10] L. SEABRA,[11] P. SCHOVANEK,[1] R. STASZEWSKI,[5] P. SWIERSKA,[5] AND T. SYKORA[12]

[1]*Palacky University, RCPTM, Olomouc, Czech Republic*
[2]*AGH University of Science and Technology, Faculty of Physics and Applied Computer Science, al. Mickiewicza 30, PL-30059 Cracow, Poland*
[3]*INFN Bologna and Universita di Bologna, Dipartimento di Fisica, viale C. Berti Pichat, 6/2, IT – 40127 Bologna, Italy*
[4]*The University of Texas at Arlington, Department of Physics, Box 19059, Arlington, TX 76019, USA*
[5]*H. Niewodniczanski Institute of Nuclear Physics PAN, Cracow, Poland*
[6]*Institut de Fısica d'Altes Energies, Universitat Autonoma de Barcelona, Edifici Cn, ES - 08193 Bellaterra (Barcelona), Spain*
[7]*INFN Lecce and Universita del Salento, Dipartimento di Fisica, Via Arnesano IT - 73100 Lecce, Italy*
[8]*Centre for Particle Physics, Department of Physics, University of Alberta, Edmonton, AB T6G 2G7, Canada*
[9]*Stanford Linear Accelerator Center, Stanford, California 94309, USA*
[10]*Stony Brook University, Dept. of Physics and Astronomy, Nicolls Road, Stony Brook, NY 11794-3800, USA*
[11]*Laboratorio de Instrumentacao e Fısica Experimental de Partıculas, LIP, Av. Elias Garcia 14, Lisbon, Portugal*
[12]*Charles University in Prague, Faculty of Mathematics and Physics, Institute of Particle and Nuclear Physics, V Holesovickach 2, CZ - 18000 Praha 8, Czech Republic*
**libor.nozka@upol.cz*

Abstract: We present the construction of the optical part of the ToF (time-of-flight) subdetector prototype for the AFP (ATLAS Forward Proton) detector. The ToF detector in conjunction with a 3D silicon pixel tracker will tag and measure protons originating in central exclusive interactions p + p → p + X + p, where the two outgoing protons are scattered in the very forward directions. The ToF is required to reduce so-called pileup backgrounds that arise from multiple proton interactions in the same bunch crossing at high luminosity. The background can fake the signal of interest, and the extra rejection from the ToF allows the proton tagger to operate at the high luminosity required for measurement of the processes. The prototype detector uses fused silica bars emitting Cherenkov radiation as a relativistic particle passes through it. The emitted Cherenkov photons are detected by a micro-channel plate multi-anode Photomultiplier Tube (MCP-PMT) and processed by fast electronics.

© 2016 Optical Society of America

OCIS codes: (120.4570) Optical design of instruments; (350.4990) Particles.

References and links

1. M. G. Albrow and A. Rostovtsev, "Searching for the Higgs boson at hadron colliders using the missing mass method," https://arxiv.org/abs/hep-ph/0009336 (2000).
2. A. B. Kaidalov, V. A. Khoze, A. D. Martin, and M. G. Ryskin, "Extending the study of the Higgs sector at the LHC by proton tagging," Eur. Phys. J. C **33**(2), 261–271 (2004).
3. J. Bonnet, J. Liao, and K. Piotrzkowski, "Study on GASTOF – A 10 ps resolution timing detector," Nucl. Instrum. Methods Phys. Res. A **762**, 77–84 (2014).

#273464 http://dx.doi.org/10.1364/OE.24.027951
Journal © 2016 Received 24 Aug 2016; revised 19 Oct 2016; accepted 6 Nov 2016; published 22 Nov 2016

4. L. Nozka, A. Brandt, M. Rijssenbeek, T. Sykora, T. Hoffman, J. Griffiths, J. Steffens, P. Hamal, L. Chytka, and M. Hrabovsky, "Design of Cherenkov bars for the optical part of the time-of-flight detector in Geant4," Opt. Express **22**(23), 28984–28996 (2014).
5. M. G. Albrow, H. Kim, S. Los, M. Mazzillo, E. Ramberg, A. Ronzhin, V. Samoylenko, H. Wenzel, and A. Zatserklyaniy, "Quartz Cherenkov counters for fast timing: QUARTIC," J. Instrum. **7**(10), P10027 (2012).
6. ATLAS-TDR-024–2015, 2015.
7. J. Lange, E. Cavallaro, S. Grinstein, and I. L. Paz, "3D silicon pixel detectors for the ATLAS Forward Physics experiment," J. Instrum. **10**(03), C03031 (2015).
8. PHOTONIS USA Pennsylvania, Inc., XPM85112 datasheet.
9. Epoxy Technology, Inc., Epotek 305 datasheet.
10. S. Agostinelli, J. Allison, K. Amako, J. Apostolakis, H. Araujo, P. Arce, M. Asai, D. Axen, S. Banerjee, G. Barrand, F. Behner, L. Bellagamba, J. Boudreau, L. Broglia, A. Brunengo, H. Burkhardt, S. Chauvie, J. Chuma, R. Chytracek, G. Cooperman, G. Cosmo, P. Degtyarenko, A. Dell'Acqua, G. Depaola, D. Dietrich, R. Enami, A. Feliciello, C. Ferguson, H. Fesefeldt, G. Folger, F. Foppiano, A. Forti, S. Garelli, S. Giani, R. Giannitrapani, D. Gibin, J. J. Gómez Cadenas, I. González, G. Gracia Abril, G. Greeniaus, W. Greiner, V. Grichine, A. Grossheim, S. Guatelli, P. Gumplinger, R. Hamatsu, K. Hashimoto, H. Hasui, A. Heikkinen, A. Howard, V. Ivanchenko, A. Johnson, F. W. Jones, J. Kallenbach, N. Kanaya, M. Kawabata, Y. Kawabata, M. Kawaguti, S. Kelner, P. Kent, A. Kimura, T. Kodama, R. Kokoulin, M. Kossov, H. Kurashige, E. Lamanna, T. Lampén, V. Lara, V. Lefebure, F. Lei, M. Liendl, W. Lockman, F. Longo, S. Magni, M. Maire, E. Medernach, K. Minamimoto, P. Mora de Freitas, Y. Morita, K. Murakami, M. Nagamatu, R. Nartallo, P. Nieminen, T. Nishimura, K. Ohtsubo, M. Okamura, S. O'Neale, Y. Oohata, K. Paech, J. Perl, A. Pfeiffer, M. G. Pia, F. Ranjard, A. Rybin, S. Sadilov, E. Di Salvo, G. Santin, T. Sasaki, N. Savvas, Y. Sawada, S. Scherer, S. Sei, V. Sirotenko, D. Smith, N. Starkov, H. Stoecker, J. Sulkimo, M. Takahata, S. Tanaka, E. Tcherniaev, E. Safai Tehrani, M. Tropeano, P. Truscott, H. Uno, L. Urban, P. Urban, M. Verderi, A. Walkden, W. Wander, H. Weber, J. P. Wellisch, T. Wenaus, D. C. Williams, D. Wright, T. Yamada, H. Yoshida, and D. Zschiesche, "Geant4—a simulation toolkit," Nucl. Instrum. Methods Phys. Res. A **506**(3), 250–303 (2003).
11. McPherson,Inc., VUVAS 2000 datasheet.
12. P. M. Duarte, "QUARTIC: An ultra-fast time-Of-flight counter," M.Sci. Thesis, The University of Texas, Arlington, 2007.
13. J. Lange, L. Adamczyk, G. Avoni, E. Banas, A. Brandt, M. Bruschi, P. Buglewicz, E. Cavallaro, D. Caforio, G. Chiodini, L. Chytka, K. Ciesla, P. M. Davis, M. Dyndal, S. Grinstein, K. Janas, K. Jirakova, M. Kocian, K. Korcyl, I. L. Paz, D. Northacker, L. Nozka, M. Rijssenbeek, L. Seabra, R. Staszewski, P. Swierska, and T. Sykora, "Beam Tests of an Integrated Prototype of the ATLAS Forward Proton Detector," J. Instrum. **11**(09), P09005 (2016).

1. Introduction

Precision timing is useful for many applications, ranging from Positron Electron Tomography (PET) scans to particle physics. For PET scans, information about the time difference of the arriving photons helps improve the position resolution by determining the location of the electron-positron pair annihilation, while for high energy physics, it has typically been used in conjunction with a momentum measurement to determine the mass of the particle, which in turn defines the particle's identity. Timing detectors can be used as well as a part of the proton tagging detectors to decrease the background to central exclusive production (CEP) events $p + p \rightarrow p + X + p$ where X stands for the centrally produced system, which could consist of a pair of jets or particles, a pair of intermediate vector bosons (W^+W^-), or even a Higgs boson H [1, 2].

At high luminosity, the environment of the Large Hadron Collider (LHC) places stringent demands on the timing detectors: high resolution (~10 – 20 ps, equivalent to 2.1 – 4.2 mm interaction vertex resolution), high rate capability (5 to 10 MHz), radiation hardness (integrated charge of 10 C/cm2/yr), and multi-proton detection capabilities. ToF detectors based on Cherenkov emission in fused silica radiators are treated as an optimal choice. On the other hand, detectors based on emission in a gas, for instance the GASTOF detector with C_4F_{10} gas [3], have better intrinsic time resolution but a low signal level. Back to fused silica, relativistic protons emit a Cherenkov light pulse in the UV region (in the 200 to 400 nm range predominantly) in a Cherenkov cone of 48 degrees. The radiator also acts as a light guide to direct the light to a sensor with a high quantum efficiency in the UV region. Typically a fast micro-channel plate multi-anode Photomultiplier Tube (MCP-PMT) or a silicon photomultiplier (SiPM) is used. A multi-channel MCP-PMT is an option where pixelization is required. Which is also the case of the detector in this study.

The ToF design described here is based on benchmark studies published in [4]. These studies introduced several key concepts adopted in the final design and construction of the ToF prototype. The main design feature is an L-shape geometry, Fig. 1(a), first introduced by M. Albrow and his group [5]. Here we denote a bar arm crossing the beam as the radiator whilst an arm leading towards the sensor as the light guide. Albrow's design is based on the light propagation by virtue of total reflections on the bar sides. On the other hand, our design largely relies on a direct fast light propagation to the sensor (approximately 60% of all photon tracks in a bar accepted by the sensor). This means a bar has to be rotated so that its radiator is tilted by the Cherenkov angle of 48 degrees with respect to the beam axis, see Fig. 1(a). In addition, direct pathways need to be reflected on the bar elbow which means a 45 degrees cut coated with an appropriate reflection layer. The part of the light propagated using total reflections is delayed with respect to the fast direct propagation. The aforementioned studies proposed a so-called taper to speed-up total-reflection pathways. On the other hand, adding a taper results in a correspondingly thinner radiator of a lower acceptance, see Fig. 1(a). Moreover, a radiator cut is another design improvement allowing higher signal due to the additional back reflection light with details described in [4].

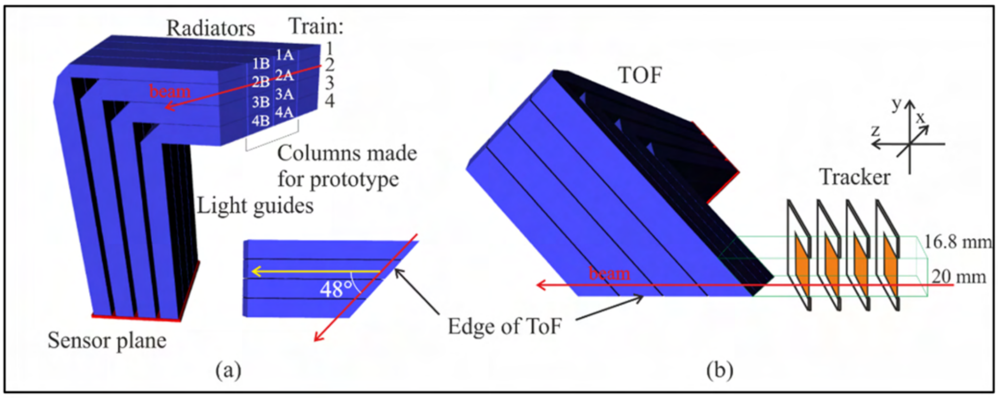

Fig. 1. (a) Geometry of the ToF, (b) the ToF with the tracker modules (not in scale).

2. Design of the ToF detector prototype

The AFP detector [6] is composed of four stations, two stations on each side of the ATLAS Interaction Point at distances of 206 m (inner stations) and 214 m (outer stations). Inner stations consist of silicon detectors (trackers) [7] placed in dedicated Roman pots while outer stations consist of trackers accompanied by time-of-flight detectors (in identical Roman pots as well), see Fig. 1(b). In the figure, the coordinate system is chosen so that the beam axis is parallel to the z axis, the x axis is horizontal and the y axis is vertical. The aim of the tracker is to precisely measure the trajectory of scattered protons while the aim of the ToF detector is to reject the so-called pileup background which can fake the signal of interest.

The ToF part has to fulfill the following performance requirements: time resolution below 20 ps, radiation hardness up to 700 kGy ($3\text{x}10^{15}$ n_{eq} cm^{-2}, at a distance of 5 mm from the beam axis) [6], high rate capability (5 to 10 MHz), and multi-proton detection capabilities (~1 background proton/detector is expected per bunch crossing at standard luminosity).

The AFP detector acceptance is 16.8 × 20.0 mm^2 given by the tracker dimensions [7] as illustrated in Fig. 1(b). From the ToF point of view the area is divided into four segments alongside the x axis. Each segment is composed of a set of four bars denoted as a train, see Fig. 1(a). This arrangement results in a matrix of 4 × 4 bars. This division is closely related to Photonis XPM85112 MCP-PMT (miniPlanacon) with 4 × 4 channel pixelization [8]. This detector was chosen for its enhanced timing performance (transit-time spread, TTS, below 35 ps at 405 nm) and its dimensions.

Dimension constraints to the ToF are due to the limited space inside the Roman pot and due to the pixel size 6.25×6.25 mm^2 of the PMT. The first factor predetermines the overall L-shape of bars (and the optical part of ToF as a whole) while the pixel size determines the cross-section dimensions of the bars. Bars of each train have light guide arms of the same dimensions. On the other hand, each radiator is unique in its dimensions. Their length is set so that their cut sides lie in one plane called the edge of the ToF (bottom-cut plane), see Fig. 1.

For the first prototype, we did not construct the whole matrix of 4 × 4 bars. Instead, we decided to produce a matrix 2 × 4 of bars so that the middle columns were produced, see also Fig. 1(a). Such a configuration was sufficient for integration tests (tracker and ToF integration) and initial performance studies. Bars were labelled as indicated in Figs. 1(a) and 2(b): 1A and 1B in the train 1 etc. with the A bars in the front as seen from the beam direction.

3. Construction of the bars

The bars of the AFP ToF detector are L-shaped and made of suprasil. There is a possibility to produce L-shaped bars as one piece [5]. In our design there are at least two cuts (45 or 48 degrees) plus optionally the taper cut (18 degrees). It was difficult to construct such bars as one suprasil piece assumed dimension tolerances and polishing precision (see below). Instead we decided to produce the light guide and the radiator separately and glue them together, see Fig. 2(a).

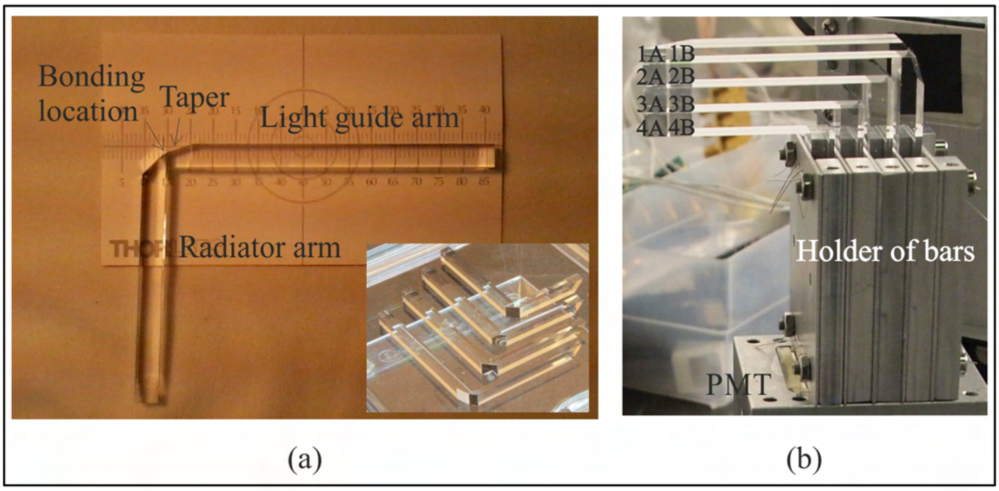

Fig. 2. (a) Example of a fused silica bar with the taper and a set of bars, (b) the set of 2x4 bars forming the ToF prototype.

The dimensions of the bars for the ToF prototype are summarized in the Table 1. The dimension tolerances are: ± 0.05 mm for all dimensions of the light guide and cross-section dimensions of the radiator, ± 0.1 mm for the length of the radiator, and ± 2’ (± 0.017 degrees) for cuts. The higher tolerance for the length of the radiator is due to the two cuts resulting in two sharp edges preventing stringent toleration. Polishing precision was stated to three interference fringes at 550 nm. It was decided to coat the elbow cut with a reflection layer made of aluminum with a thickness of at least 200 nm and protected by a SiO_2 layer of the thickness 120 nm (protection against oxidation and mechanical abrasion). The deposition was carried out by means of a standard PVD (Physical Vacuum Deposition) technique.

Table 1. Dimensions of the bars for the ToF prototype in millimeters.

Train	A bars		B bars	
	Radiator	Light guide	Radiator	Light guide
1	3 × 6 × 57.8	5 × 6 × 70.3	3 × 6 × 52.2	5 × 6 × 70.3
2	5 × 6 × 53.5	5 × 6 × 65.2	5 × 6 × 47.9	5 × 6 × 65.2
3	5 × 6 × 47.3	5 × 6 × 60.1	5 × 6 × 41.7	5 × 6 × 60.1
4	5 × 6 × 41.0	5 × 6 × 55.0	5 × 6 × 35.4	5 × 6 × 55.0

All pieces (the radiators and the light bars) were produced from a bulk of suprasil material. We used approximately 150 g of a suprasil bulk to produce all pieces as listed in Table 1 (the total weight 53 g) and spares for miscellaneous testing. Cutting, milling, and polishing were carried out by means of a common optical technology. By design, the light guides were produced in the form of pure cuboids. Since the light guides have the same length in a given train, they were made at once. As each radiator has a unique length their uncut intermediates were produced piece by piece. There are two cuts at each end side of the radiator (45 and 48 degrees rotated by 90 degrees with respect to each other). For a given cut type, radiators were cut together (per four pieces).

Finally, radiators and light guides were glued together. Nowadays UV cementation is the most popular technique for bonding optical surfaces allowing fast, precise, and handy manipulation. However, this technique is only applicable for optical solutions in visible and infrared region because UV cements significantly absorb UV light. Finally we decided to use the Epotek 305 epoxy glue [9] assuring high transparency down to 250 nm and sufficient transparency down to 235 nm. The thickness of the glue layer did not exceed 20 µm which is the standard tolerance in the optics designing.

4. Constraints given by the materials

Construction of the bar includes the mirror production and optical coupling of the radiator and the light guide by means of an optical cement. These extra factors generally introduce other signal losses due to the transmittance of glue and mirror reflection. Here we report the results of the analysis of signal attenuation due to both factors. In addition, signal attenuation of suprasil itself is reported.

4.1 Mirror performance

Reflectivity of an optical surface is, in general, a function of the polarization state of the incident light. Cherenkov light is linearly polarized with polarization vector perpendicular to the Cherenkov cone. The calculated reflectance profile of the bar mirror is drawn in Fig. 3(a) for the incidence angle of 45 degrees (valid for the prominent direct photon pathways). The distributions of s and p polarization components on the mirror were calculated by means of a Geant4 simulation [10]. Results are plotted in Fig. 3(b) in terms of their ratio s/p (normalized, logarithmic plot). The higher statistics is below $s/p<1$ (53% of the total amount) which means that the p component prevails (the peak is at 0.34). Back to Fig. 3(a), the reflectivity of the mirror elbow is between the red and the black curve (below 90%). This means a loss of 10 – 12% in the wavelength region from 200 nm to 400 nm which is of the most interest (see Introduction above and [4]). One can obtain a higher reflectivity by means of a dielectric mirror made of a system of a thin layer dielectric stack. For example, a system of 50 layers (better 70 layers) of SiO_2/HfO_2 will increase reflectivity by up to 96% in the wavelength region from 200 nm to 400 nm meaning a loss of 4% by reflection. However, we decided to use a simpler solution with aluminum coating for the ToF prototype assuming less light by 6% with respect to the dielectric solution.

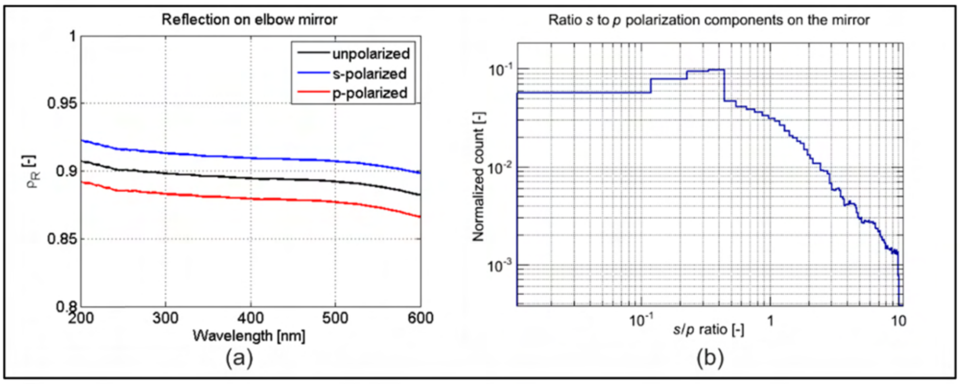

Fig. 3. (a) Reflectivity of the coated elbow cut, (b) ratio between the polarization components.

4.2 Transmittance of glue and suprasil

Figure 4(a) shows the results of transmittance measurements of suprasil and Epotek 305 glue. The measurements were performed with a DUV/UV spectrometer VUVAS 2000 ([11]). For the measurement of the suprasil itself, we used samples in the form of round suprasil pieces (20 mm diameter, 4 mm thick). Concerning transmittance measurements of the glue, we used samples in the form of two round suprasil pieces (20 mm diameter, 2 mm thick) bonded together with the glue. The red curve in the plot stands for the transmittance of the suprasil itself (including Fresnel reflection losses). Suprasil material of the thickness 4 mm cuts wavelengths below 166 nm (drop to half of the maximum). The blue curve corresponds to the transmittance of the whole system suprasil plus glue. Our results find a transparency edge at 233 nm. The transmission cut incorporates additional signal loss in the region below 233 nm.

Based on our simulations, the wavelengths accepted by the MCP-PMT are plotted in Fig. 4(b) with a significant loss region below 233 nm. A comparison was made for a bar without taper. Similar results stand for bars with taper. The calculated loss is about 18% – 19% (with or without a taper). This loss is valid for the wavelength region from 200 nm to 600 nm where the quantum efficiency of the photomultiplier is known [4, 12]. Thus the glue plays a significant role in attenuation of the signal.

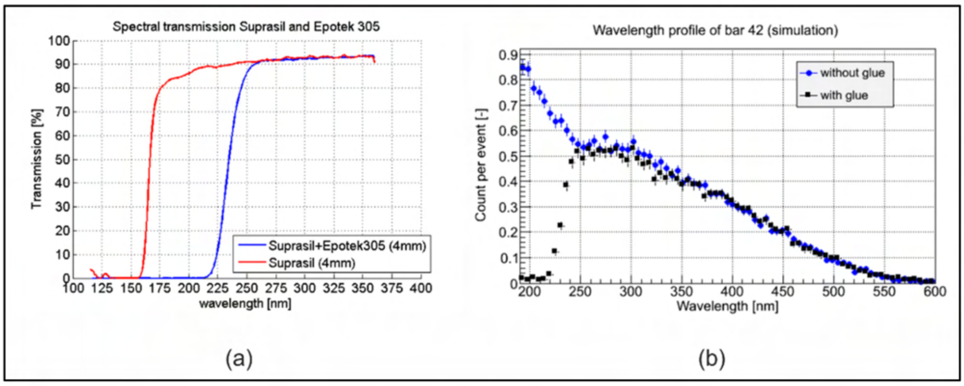

Fig. 4. (a) Measured transmittances of suprasil and Epotek 305, (b) spectral attenuation of Epotek 305 based on the accepted wavelength profile in the sensor (simulation, bar 1A).

5. Signal response of the bars

The ToF prototype was tested during two test campaigns at the CERN-SPS test-beam facility (120 GeV π + particles) in November 2014 and September 2015 in the frame of the AFP integration test beam measurements [13]. The scheme of the measurement setup is shown in Fig. 5. The beam passed through the bars and the trigger. The trigger consisted of a 30 mm long fused silica bar of 3 × 3 mm^2 cross-section clamped to a silicon photomultiplier (SiPM). Its detection is also based on Cherenkov radiation. For the ToF module, each bar in the 2 × 4 matrix was brought into contact (without the use of optical grease) with the Planacon MCP-PMT XPM815112. It operated at the high voltage of 1870 V and the gain $5{\cdot}10^5$ for an optimal separation of the useful signal from the pedestal (rejection threshold at −100 mV, see below). The signal output the MCP-PMT was amplified by means of two-stage preamplifiers. Its first stage consisted of a current-to-voltage (A-V) converter with a 1 kΩ resistor and a voltage amplifier with the gain of 10. The second stage was a voltage amplifier with the same gain of 10. For raw signal studies, the amplified signal was then analyzed with a LeCroy SDA760ZI oscilloscope (6 GHz, 20 GS/s, 4 channels). For timing studies, the raw signal was preprocessed with a constant fraction discriminator (CFD). The CFD threshold level was set to −100 mV for the pedestal rejection. In both cases, the signal was triggered with the SiPM detector signal processed with another CFD module (here the threshold was set to –200 mV). The trigger detector was moved vertically in order to select a specific train for measurements.

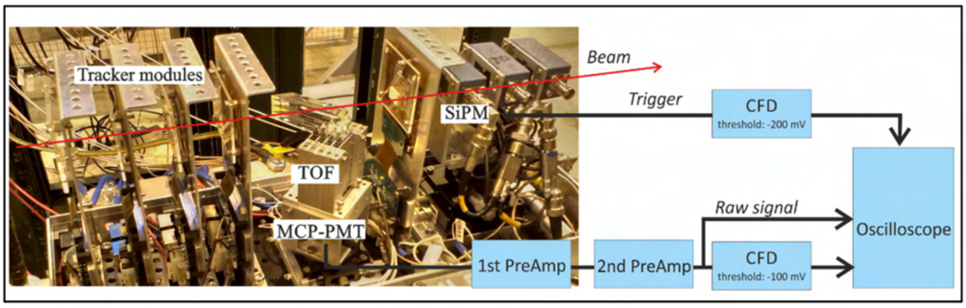

Fig. 5. Setup of the test beam measurements.

The following results are based on measurements with bars optically isolated from each other to prevent a possible undesired optical cross-talk between bars. Moreover they occupied separated pixels to prevent electronic cross-talk. The data was collected near the edge of the bars (area 3 × 3 mm^2 given by the SiPM trigger detector). The distributions of signal amplitudes of all bars are plotted in Fig. 6(a) in the form of boxplots. Each distribution is described by a blue box defining the interval from 25% (Q1) to 75% (Q2) quantiles of the distribution with a red level mark inside indicating the mean value M (50% quantile). The dash line with ending defines the interval from the minimum value to the maximum value of the distribution excluding outliers (red points). The lower outliers are the values lower than Q1-1.5*(Q2-Q1). The mean amplitude differs from bar to bar which is a result of their different geometry and different response among pixels of the PMT. Our laboratory tests with a femtosecond laser at 420 nm showed the mean amplitude variation of 7% among the pixels.

Despite their highest length, the bars in the first train (1A and 1B) generated the highest output (level of −350 mV in amplitude) by virtue of their taper modification. Other bars produced lower signal output with amplitudes around –250 mV on average (drop by 30%). These results confirm that the taper modification in the bar elbow increases the signal output of the bar as predicted by simulation studies [4].

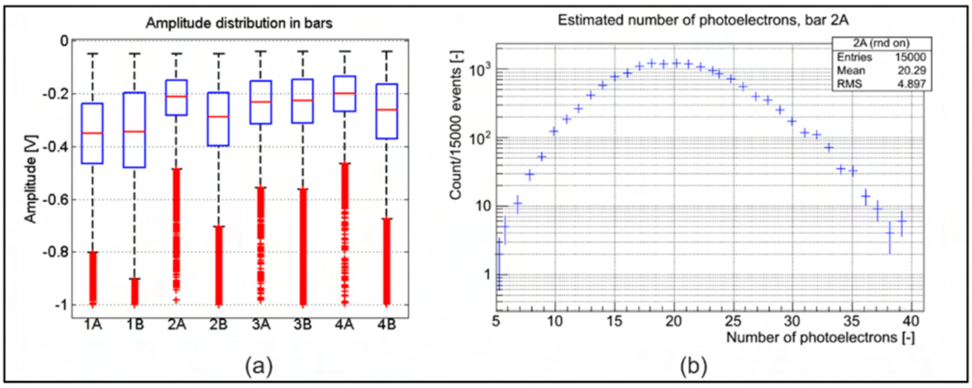

(a) (b)

Fig. 6. (a) Distribution of the amplitude, (b) estimated distribution of generated photoelectrons given by simulation.

The signal outputs from all bars embody relatively high fluctuation (Q2-Q1)/M in the range of 30% – 40% given by the response of the PMT channels and by fluctuations of signal pathways in the bars. Fluctuations of the signal are the consequence of random processes existing in each stage of the signal chain starting with the Cherenkov emission and ending with the signal registration. The estimated fluctuation of the signal originating from the photomultiplier is about 7%, the same for all pixels (given by laser tests at 420 nm). Thus fluctuations of the signal in the optical part dominate. To understand the origin of such fluctuations we estimated the number of generated photoelectrons in our simulations (see [4] for details) and assumed the photodetection efficiency (PDE) of the PMT specified in [12].

In Fig. 6(b) the estimated number of photoelectrons (pe) produced per event is plotted for the model of bar 2A. It was calculated for randomly generated particle positions in a square of 3 × 3 mm^2 to mimic the SiPM trigger detector defining the area of acceptance. In terms of quantiles Q1 and Q2 defined above, Q1 = 17 pe and Q2 = 23 pe with the mean M = 20 pe (Fig. 6(b)) giving a fluctuation estimate of (Q2-Q1)/M = 30% which corresponds to the observed fluctuation level in the signal.

The 30% level fluctuations embody the variance of the number of generated Cherenkov photons, fluctuations in the bar (transport in the bar, reflections, escaping, attenuation of the glue), and fluctuations due to the PMT. The first term (Cherenkov effect) is in the 5% range based on simulations (the distribution of generated photons is characterized by Q1 = 690, Q2 = 725, and M = 708 in our bars). Fluctuations coming from the photomultiplier are at a level of 7% for a constant optical signal level. Fluctuation of signal due to transport in the bar thus dominates. This study did not take into account cross-talk contributions from the adjacent pixels (the bars were tested separately). We measured a higher level of fluctuations by 2 – 4% per bar when both bars per train were used. However, this result needs a verification.

6. Resolution of the trains

The aim of the ToF detector is the measurement of arrival time with a resolution below 20 ps. For the given configuration, we studied the timing performance with two bars per train only. For such studies we preprocessed the output signal by means of the CFD module, see Fig. 5. The timestamp of the leading edge was treated as the arrival time of a signal pulse. The arrival time of a signal pulse from the PMT was calculated with respect to the arrival time of the SiPM detector serving as a trigger (the first SiPM in the chain, see Fig. 5). The SiPM detectors were measured between each other to evaluate their time resolutions. The time resolution of the SiPM trigger was measured as 12 ps.

As an example, results of time measurements of the train 2 are plotted in Fig. 7. Note that the resolutions are calculated from the Gaussian fits. Here, the sigma values embody a contribution from the trigger SiPM detector. The mean values are artificial and have no meaning. The arrival time of the train was calculated as the arithmetic average of the arrival times of each bar in the train. The distributions deviate from the Gaussian distribution at the tails. The origin of the tails is still not fully understood and it will be investigated in next test beam measurements.

The results of timing measurements are summarized in Table 2 for all trains. The contribution of the SiPM trigger was subtracted. We estimated the measurement error ± 2 ps based on results from 5 independent measurements. The measured resolutions vary with the position of the beam with respect to the train edge (see also Fig. 1 for the edge specification) due to the fact that the signal amplitude decreases with the distance from the edge (this effect was studied in [4]). At first sight, the B bars embody better timing resolutions compared to the A bars. This originates from the fact that the signal of the B bars is enriched by photons coming from the A bars. The infiltration takes place near the edges of the bars. According to simulations, the hit count of the B bars grows by 5% at the edge and by 40% at 5 mm from the edge. However, this optical cross-talk does not contribute to the signal correlation between bars because photons are generated independently and each photon contributes to a one channel (a PMT pixel) only. Assuming the case of four bars per train, all bars receive a contribution of photons generated in the foregoing bar except the first one. Thus the first bar suffers from a smaller hit count which could eventually result in a worse resolution based on the PMT response (timing resolution vs. number of photoelectrons, to be specific).

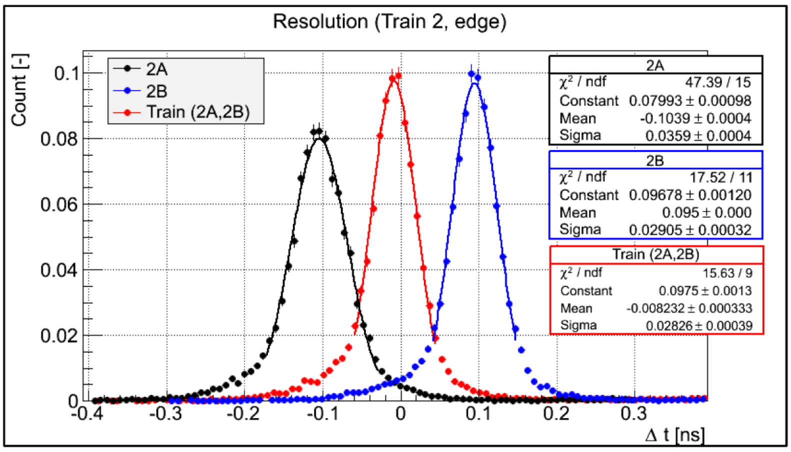

Fig. 7. Time resolution of the train 2 at the edge.

In Table 2, the resolution difference between the A bars and the B bars is emphasized at 5 mm from the edge (9 – 12 ps) compared to the edge position (5 – 8 ps). Only the 1A bar profited from its taper having a higher signal level, see Fig. 6(a), which partly compensated for the lack of signal. The resolution of the train arrival time is theoretically lower than the one of single bars by the factor $1/\sqrt{N}$, where N is the number of bars in the train, providing the output signals from the bars are mutually independent (uncorrelated) and the time resolutions of bars are similar. The latter condition is not apparently met in our case. We expect it to be more closely to the $1/\sqrt{N}$ rule for the full train scenario and a new PMT with better timing performance.

Correlations between bars generally worsen the time resolution of the whole train. A charge sharing between the PMT pixels causes a correlation between signal outputs at some level. Based on our raw signal analysis, we estimated the amplitude correlations to be approximately 10% between the A bars and the B bars caused by the charge sharing.

Table 2. Resolutions of the bars and the trains in picoseconds (estimated error ± 2 ps).

Train	Position	Bar A	Bar B	Whole train
1	edge	31	26	23
	5 mm from edge	40	31	28
2	edge	34	26	25
	5 mm from edge	42	31	33
3	edge	31	26	25
	5 mm from edge	41	31	34
4	edge	33	26	27
	5 mm from edge	42	29	33

Although we used only two bars per train, i.e. half of the design number of bars, the resolution values at the edge of the ToF detector are already close to the final specification of 10 – 20 ps. For next studies we plan to have a setup with four bars in trains and a PMT with suppressed charge sharing and a better timing performance.

7. Conclusion

We have presented the design, construction, and initial performance measurements of the ToF prototype for the AFP project. The selected geometry of the bars was determined and based on our previous simulation studies. The produced bars were tested at the CERN-SPS test-beam facility (120 GeV π + particles) in November 2014 and September 2015. Besides this, additional studies and measurements were performed to estimate the limits of the design, in particular the study of the elbow mirror reflection, and the transmission of suprasil and the glue in the deep UV region. Radiation hardness of these components are outside the scope of the paper and will be published separately.

The reflection on the mirror layer on the bar elbow introduces a loss of 10 – 12% and depends on the polarization state of the light as the Cherenkov light is strongly polarized. Our simulation studies showed that the *p* component of the incoming photons prevails over the *s* component (peak of *s*/*p* ratio at 0.34) in the frame of the bar design. Suprasil material has the transmission edge at 166 nm (for the thickness of 4 mm). For the wavelengths above this limit, the transmission reaches 91%. Concerning the glue, the main issue is a shift of the transmission edge up to 233 nm. This results in a signal loss of at least 20%.

Measurements in test beams at the SPS at CERN have proven the usefulness of the taper solution as described in [4] which increased the signal level by 30%. On the other hand, adding a taper results in a thinner radiator and therefore lower acceptance. Thus, in order to fully cover the required acceptance window, one needs either to omit the taper or to increase the number of trains. The latter option amounts to a higher pixelization.

The resolutions of the trains of bars were measured to be in the range from 20 to 33 ps and worsen with the increasing distance of the beam from the edge. In the presented setup, we focused on the overall timing performance of the ToF prototype with just two bars per train. A full train setup will be used in next test beam measurements, which will allow us to study more aspects of the ToF performance issues.

Funding

MSMT of Czech Republic (INGO II no. LG15052, RCPTM-NPU no. LO1305), Palacky University (IGA_PrF_2016_002), Horizon 2020 (654168).

Acknowledgment

The authors gratefully acknowledge the support from projects of MSMT of Czech Republic and from the European Union’s Horizon 2020 Research and Innovation programme.

Research Article
Vol. 26, No. 7 | 2 Apr 2018 | OPTICS EXPRESS 8028
Optics EXPRESS

Timing resolution studies of the optical part of the AFP Time-of-flight detector

L. CHYTKA,[1,*] G. AVONI,[2] A. BRANDT,[3] E. CAVALLARO,[4] P. M. DAVIS,[5] F. FÖRSTER,[4] M. HRABOVSKY,[1] Y. HUANG,[6] K. JIRAKOVA,[1] M. KOCIAN,[7] T. KOMAREK,[1] K. KORCYL,[8] J. LANGE,[4] V. MICHALEK,[1] L. NOZKA,[1] I. LOPEZ PAZ,[4] M. RIJSSENBEEK,[9] P. SCHOVANEK,[1] T. SYKORA[10] AND V. URBASEK[1]

[1]*Palacky University, Faculty of Science, RCPTM, Joint Laboratory of Optics of Palacky University and Institute of Physics of the Academy of Sciences of the Czech Republic, 17. listopadu 12, Olomouc, 771 46, Czech Republic*
[2]*INFN Bologna and Universita di Bologna, Dipartimento di Fisica, viale C. Berti Pichat, 6/2, IT 40127 Bologna, Italy*
[3]*The University of Texas at Arlington, Department of Physics, Box 19059, Arlington, TX 76019, USA*
[4]*Institut de Física d'Altes Energies (IFAE), The Barcelona Institute of Science and Technology (BIST), Campus UAB, 08193 Bellaterra (Barcelona), Spain*
[5]*Centre for Particle Physics, Department of Physics, University of Alberta, Edmonton, AB T6G 2G7, Canada*
[6]*University of Science and Technology of China, Hefei 230026, China*
[7]*Stanford Linear Accelerator Center, Stanford, California 94309, USA*
[8]*The Henryk Niewodniczanski Institute of Nuclear Physics Polish Academy of Sciences, ul Radzikowskiego 152, 31-342 Krakow, Poland*
[9]*Stony Brook University, Dept. of Physics and Astronomy, Nicolls Road, Stony Brook, NY 11794-3800, USA*
[10]*Charles University in Prague, Faculty of Mathematics and Physics, Institute of Particle and Nuclear Physics, V Holesovickach 2, CZ 18000 Praha 8, Czech Republic*
**ladislav.chytka@upol.cz*

Abstract: We present results of the timing performance studies of the optical part and front-end electronics of the time-of-flight subdetector prototype for the ATLAS Forward Proton (AFP) detector obtained during the test campaigns at the CERN-SPS test-beam facility (120 GeV π^+ particles) in July 2016 and October 2016. The time-of-flight (ToF) detector in conjunction with a 3D silicon pixel tracker will tag and measure protons originating in central exclusive interactions $p + p \rightarrow p + X + p$, where the two outgoing protons are scattered in the very forward directions. The ToF is required to reduce so-called pileup backgrounds that arise from multiple proton interactions in the same bunch crossing at high luminosity. The background can fake the signal of interest, and the extra rejection from the ToF allows the proton tagger to operate at the high luminosity required for the measurement of the processes. The prototype detector uses fused silica bars emitting Cherenkov radiation as a relativistic particle passes through them. The emitted Cherenkov photons are detected by a multi-anode micro-channel plate photomultiplier tube (MCP-PMT) and processed by fast electronics.

© 2018 Optical Society of America under the terms of the OSA Open Access Publishing Agreement

OCIS codes: (120.4570) Optical design of instruments; (350.4990) Particles.

References and links

1. A. De Roeck, V. A. Khoze, A. D. Martin, R. Orava, and M. G. Ryskin, "Ways to detect a light Higgs boson at the LHC," Eur. Phys. J. C **25**(3), 391–403 (2002).
2. A. B. Kaidalov, V. A. Khoze, A. D. Martin, and M. G. Ryskin, "Extending the study of the higgs sector at the LHC by proton tagging," Eur. Phys. J. C **33**(2), 261–271 (2004).
3. M. G. Albrow, H. Kim, S. Los, M. Mazzillo, E. Ramberg, A. Ronzhin, V. Samoylenko, H. Wenzel, and A. Zatserklyaniy, "Quartz Cherenkov counters for fast timing: QUARTIC," J. Instrum. **7**(10), P10027 (2012).

#320281
https://doi.org/10.1364/OE.26.008028
Journal © 2018
Received 24 Jan 2018; revised 28 Feb 2018; accepted 2 Mar 2018; published 20 Mar 2018

4. L. Nozka, A. Brandt, M. Rijssenbeek, T. Sykora, T. Hoffman, J. Griffiths, J. Steffens, P. Hamal, L. Chytka, and M. Hrabovsky, "Design of Cherenkov bars for the optical part of the time-of-flight detector in Geant4," Opt. Express **22**(23), 28984–28996 (2014).
5. Epoxy Technology, Inc., Epotek 305 datasheet.
6. L. Nozka, L. Adamczyk, G. Avoni, A. Brandt, P. Buglewicz, E. Cavallaro, G. Chiodini, L. Chytka, K. Ciesla, P. M. Davis, M. Dyndal, S. Grinstein, P. Hamal, M. Hrabovsky, K. Janas, K. Jirakova, M. Kocian, T. Komarek, K. Korcyl, J. Lange, D. Mandat, V. Michalek, I. L. Paz, D. Northacker, M. Rijssenbeek, L. Seabra, P. Schovanek, R. Staszewski, P. Swierska, and T. Sykora, "Construction of the optical part of a time-of-flight detector prototype for the AFP detector," Opt. Express **24**(24), 27951–27960 (2016).
7. J. Lange, E. Cavallaro, S. Grinstein, and I. L. Paz, "3D silicon pixel detectors for the ATLAS Forward Physics experiment," J. Instrum. **10**(03), C03031 (2015).
8. Photonis USA Pensylvania, Inc., miniPlanacon XPM85112 datasheet.
9. T. Komárek, *Simulation of optical part of high-energy particle time-of-flight detector and comparison with data*, Master's thesis, Olomouc (2016) [https://theses.cz/id/zts9l9/].
10. J. Lange, L. Adamczyk, G. Avoni, E. Banas, A. Brandt, M. Bruschi, P. Buglewicz, E. Cavallaro, D. Caforio, G. Chiodini, L. Chytka, K. Cieśla, P. M. Davis, M. Dyndal, S. Grinstein, K. Janas, K. Jirakova, M. Kocian, K. Korcyl, I. L. Paz, D. Northacker, L. Nozka, M. Rijssenbeek, L. Seabra, R. Staszewski, P. Świerska, and T. Sykora, "Beam tests of an integrated prototype of the ATLAS forward proton detector," J. Instrum. **11**(09), P09005 (2016).
11. S. Agostinelli, J. Allison, K. Amako, J. Apostolakis, H. Araujo, P. Arce, M. Asai, D. Axen, S. Banerjee, G. Barrand, F. Behner, L. Bellagamba, J. Boudreau, L. Broglia, A. Brunengo, H. Burkhardt, S. Chauvie, J. Chuma, R. Chytracek, G. Cooperman, G. Cosmo, P. Degtyarenko, A. Dell'Acqua, G. Depaola, D. Dietrich, R. Enami, A. Feliciello, C. Ferguson, H. Fesefeldt, G. Folger, F. Foppiano, A. Forti, S. Garelli, S. Giani, R. Giannitrapani, D. Gibin, J. J. Gómez Cadenas, I. González, G. Gracia Abril, G. Greeniaus, W. Greiner, V. Grichine, A. Grossheim, S. Guatelli, P. Gumplinger, R. Hamatsu, K. Hashimoto, H. Hasui, A. Heikkinen, A. Howard, V. Ivanchenko, A. Johnson, F. W. Jones, J. Kallenbach, N. Kanaya, M. Kawabata, Y. Kawabata, M. Kawaguti, S. Kelner, P. Kent, A. Kimura, T. Kodama, R. Kokoulin, M. Kossov, H. Kurashige, E. Lamanna, T. Lampén, V. Lara, V. Lefebure, F. Lei, M. Liendl, W. Lockman, F. Longo, S. Magni, M. Maire, E. Medernach, K. Minamimoto, P. Mora de Freitas, Y. Morita, K. Murakami, M. Nagamatu, R. Nartallo, P. Nieminen, T. Nishimura, K. Ohtsubo, M. Okamura, S. O'Neale, Y. Oohata, K. Paech, J. Perl, A. Pfeiffer, M. G. Pia, F. Ranjard, A. Rybin, S. Sadilov, E. Di Salvo, G. Santin, T. Sasaki, N. Savvas, Y. Sawada, S. Scherer, S. Sei, V. Sirotenko, D. Smith, N. Starkov, H. Stoecker, J. Sulkimo, M. Takahata, S. Tanaka, E. Tcherniaev, E. Safai Tehrani, M. Tropeano, P. Truscott, H. Uno, L. Urban, P. Urban, M. Verderi, A. Walkden, W. Wander, H. Weber, J. P. Wellisch, T. Wenaus, D. C. Williams, D. Wright, T. Yamada, H. Yoshida, and D. Zschiesche, "Geant4—a simulation toolkit," Nucl. Instrum. Meth. A **506**(3), 250–303 (2003).
12. M. Mota and J. Christiansen, "A high-resolution time interpolator based on a delay locked loop and an RC delay line, IEEE J. Solid-St. Circulation **34**(10), 1360–1366 (1999).

1. Introduction

Precision timing is necessary for many applications, ranging from Positron Electron Tomography (PET) scans to particle physics. For high energy physics, it is typically combined with a momentum measurement to determine the mass of the particle, which in turn defines the particle's identity. Timing detectors can be used as well as a part of the proton tagging detectors to decrease the background to central exclusive production (CEP) events $p + p \to p + X + p$, where X stands for the centrally produced system, which could consist of a pair of jets or particles, a pair of intermediate vector bosons (W^+W^-), or even a Higgs boson H [1,2]. At a high luminosity, the environment of the Large Hadron Collider (LHC) places stringent demands on the timing detectors: high resolution (~10–20 ps, equivalent to the 2.1–4.2 mm interaction vertex resolution), radiation hardness, long lifetime (the integrated charge of at least 10 C/cm^2/yr), and multi-proton detection capabilities. To access low masses of the centrally produced system X, it is crucial to measure as close to the proton beam as possible, therefore an edgeless design is required. ToF detectors based on Cherenkov emission in fused silica radiators [3] are treated as an interesting choice.

The AFP detector is designed to tag protons outgoing from ATLAS interaction point (IP) in the very forward direction. For this purpose, it consists of two near stations (at 206 m from IP), one per side, fitted with a 3D silicon pixel tracker; and two far stations (at 217 m from IP, one per side) with the silicon tracker together with a ToF detector. The two ToF detectors provide a time difference between the times of flight of the two protons in the CEP events. As the speed of the protons differs from the speed of light by a negligible amount, it is possible to determine where the protons originated from (the longitudinal primary vertex position) based on the time difference, which provides high background rejection when combined with other means of the vertex reconstruction.

The ToF design for the AFP project is based on benchmark studies [4]. The ToF geometry is outlined in Fig. 1. It consists of a 4 × 4 matrix of L-shaped bars made of fused silica. Each bar serves both as a Cherenkov radiator and a light guide towards a fast MCP-PMT device. The rows of four bars alongside the beam axis are called trains and labeled with a number, Fig. 1(a). The columns are labeled with letters A, B, C, and D along the direction of the incoming particle. In this way, the bars in the Train 1 are labeled 1A, 1B, 1C, and 1D and so on for the other trains. We produced two extra sets of bars (constituting full trains) with different geometries for the positions of the Train 1 and the Train 2. We labeled them the Train 5 and 6 to distinguish the original trains from the new ones (still having at most four trains in a ToF installation).

The selected shape originates from the space limitation given by the available space inside the housing that AFP uses (the Roman pot). The benchmark study [4] introduced several key concepts adopted in the final design and construction of our ToF prototype and also shown simulation results for the developed geometry. Particularly a taper cut was proposed to speed-up total-reflection pathways. Also, the radiators are tilted at an angle of 48° with respect to the beam, which corresponds to the Cherenkov angle for the fused silica. Because of this, the direct photons from all bars within a train arrive at the same time. The bars are produced from 2 pieces and glued by the Epotek 305 UV transparent glue [5]. All the surfaces of the bars are polished and only the area of the 45° cut on the outside of the right angle joint of the radiator and light guide parts is aluminized, since it is the only part where the total reflection condition is not met for a substantial fraction of photons. Construction details are discussed in the previous study [6] together with the first timing results.

The edge plane of the ToF detector is an important characteristic which is formed by individual edges of all bars, Fig. 1(a). It is the place where the detector has the best resolution as discussed throughout the paper. The AFP detector acceptance area is 16.3 × 20.0 mm^2 given by the tracker dimensions [7] and the tracker tilt as illustrated in Fig. 1(b).

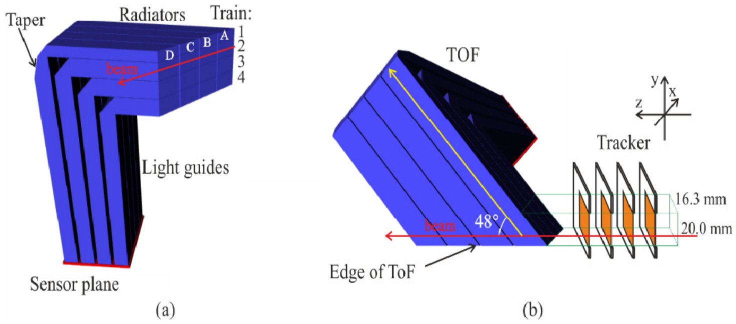

(a) (b)

Fig. 1. (a) Geometry of ToF, (b) ToF with tracker modules (not in scale).

2. Experimental setup

The ToF prototype was tested during several test campaigns at the CERN-SPS test-beam facility (120 GeV $\pi +$ particles) in the last three years. Here we present results from the campaign in July 2016 and October 2016 which were dedicated to timing studies.

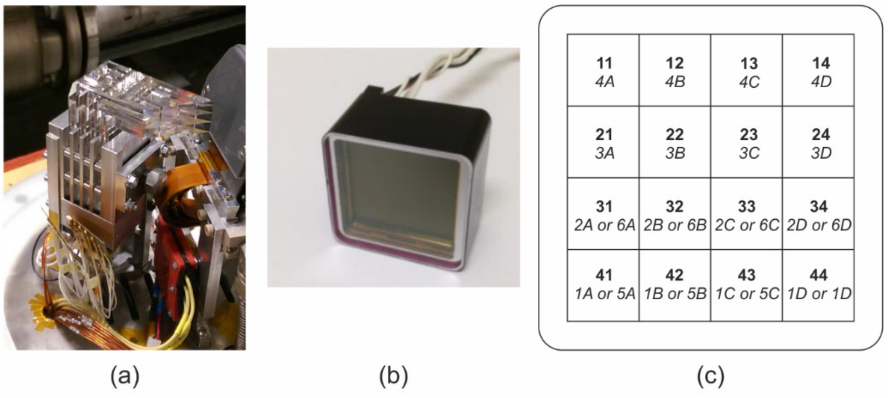

Fig. 2. (a) Detail view of the ToF subdetector, (b) the Planacon XPM85112 MCP-PMT, (c) the layout of the occupancy of the PMT pixels with bars.

The ToF subdetector is depicted in Fig. 2. The matrix of 4 × 4 bars is fixed to the PMT by a duralumin holder, Fig. 2(a). The bars are held by the duralumin plates within machined grooves. The plates are partially separating the light guide part of the bars of different trains. The grooves are designed to provide firm placement of the bars while keeping the minimal touching surface between the bar and the holder. The PMT is a new Planacon XPM85112 MCP-PMT [8] with 16 pixels (channels) in the 4 × 4 matrix, Fig. 2(b). Each bar is designed for a dedicated pixel. The layout of pixels occupancy is sketched in Fig. 2(c). The trains 1 and 2 were alternatively replaced by the trains 5 and 6, respectively, during the studies. Table 1 summarizes dimensions of the bars. See Fig. 1(a) for the meaning of the light guide and the radiator and [6] for the geometry and the construction details.

Table 1. Dimensions of the ToF bars.

Train	Light guide length [mm]	Length of the radiator [mm]				Radiator height [mm]	Taper* [mm]
		Bar A	Bar B	Bar C	Bar D		
1	70.3	63.4	57.8	52.2	46.5	3	2
2	65.2	59.2	53.5	47.9	42.3	5	0
3	60.1	52.9	47.3	41.7	36.0	5	0
4	55.0	46.6	41.0	35.4	29.8	5	0
5	70.3	62.4	56.8	51.2	45.5	2	3
6	66.2	58.2	52.5	46.9	41.3	4	1

The cross-section dimension of all light guides is 5 × 6 mm^2, the thickness of all radiators is 6 mm [6].

**The taper value is the difference between the nominal and tapered light guide width at the narrowest place. For more details on the taper optimization, see the design study [4].*

The photograph of the measurement setup is shown in Fig. 3. The beam passed through two tracker modules, the ToF subdetector under study, an auxiliary ToF module, other two tracker modules, and two SiPM detectors used as a trigger. The auxiliary PMT detector was added for complementary studies and it is not discussed in the paper.

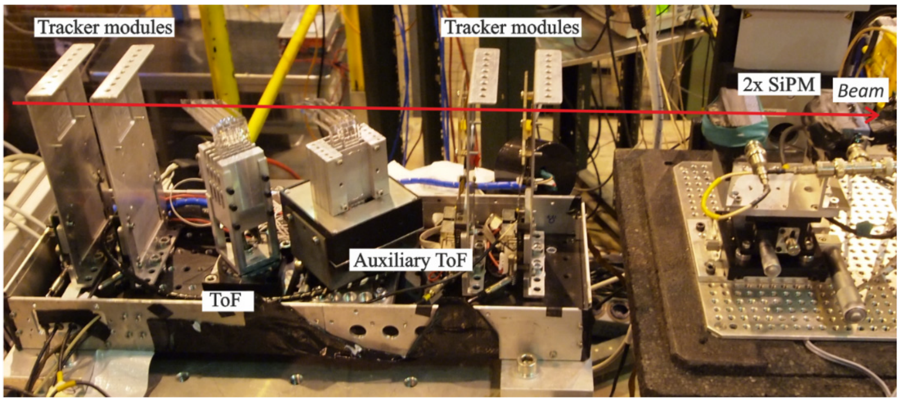

Fig. 3. Experimental setup.

Each SiPM trigger detector consisted of a 30 mm long fused silica bar of 3 × 3 mm^2 cross-section coupled to a silicon photomultiplier (SiPM) manufactured by ST Microelectronics (NRD09_1 with 3.5 × 3.5 mm^2 and 58 µm cell size). The SiPM detectors are also based on Cherenkov radiation. The trigger detectors were placed on a two-axis movable stage (remotely controlled) to select dedicated areas of the ToF detector for timing studies. We mostly used the first SiPM detector (closer to the ToF part) as a trigger. The latter one was used for the measurement of their mutual resolution and in turn the resolution of the first one. We added another SiPM detector (not in the figure) to measure the timing resolution of the first and the second SiPM detectors at the beginning of the timing performance studies. The third SiPM detector comprised of SensL SiPM sensor (MicroFC-SMA-30050 with 3 × 3 mm^2 and 50 µm cell size) coupled to 10 mm long fused silica bar of 3 × 3 mm^2 cross-section. In the following, we use the term trigger for the first SiPM detector.

The Planacon XPM85112 MCP-PMT operated at the high voltage of 2100 V, corresponding to the gain $5 \cdot 10^4$ for an optimal separation of the useful signal from the pedestal (see distribution of signal amplitudes in Fig. 4(b) – the noise pedestal is represented by narrow peaks reaching down to –100 mV, while the useful signal amplitudes fall below –150 mV). The signal output of the MCP-PMT was amplified by two-stage preamplifiers. The first stage consisted of a current-to-voltage (A-V) converter with a 1 kΩ resistor and a voltage amplifier with the amplification of 10 (the gain of 20 dB). The second stage was a voltage amplifier (V-V) with the same amplification of 10. For raw signal studies, the amplified signal was then directly analyzed with the Agilent Infiniium DSA91204A oscilloscope (12 GHz, 40 GS/s, 4 channels) together with the LeCroy WavePro 7200A (2 GHz, 10 GS/s, 4 channels) in a slave mode. For timing studies, the raw signal was preprocessed with a constant fraction discriminator (CFD) with the constant fraction tuned for the MCP-PMT signal shape (42%). Apart from the constant fraction, there is also a fixed threshold in the CFD, above which, the signal is rejected. The threshold level was set to –150 mV for the pedestal rejection. In both cases, the signal was triggered with the SiPM detector signal amplified by a 32 dB amplifier and processed with another CFD module (here the threshold was set to –400 mV). The trigger detector was moved vertically to select a specific train for measurements.

3. Measurements and results

During all measurements, we positioned the trigger to have its coincidence with a dedicated ToF area in the beam. We used the tracker module to align and mark the positions of the trigger to have the coincidence with any of the trains (the vertical position of the trigger) both at the edge of the ToF and at the distance of 5 mm from the edge (the horizontal position). There was a special scan of the timing resolution in the range of distances from the edge. The measurements on the (ToF) edge were done having the edge of the SiPM trigger (with the 3 × 3 mm^2 cross-section) aligned to the ToF edge. Thus, the measurements on the edge were in fact aggregate measurements in the range of distances from 0 mm to 3 mm from the edge and similarly the measurements at 5 mm from the edge were aggregate measurements in the range of distances from 5 mm to 8 mm from the edge.

In the following, we refer to the measurements at each train having in mind the chain of bars in the given train and corresponding pixels of the PMT. In several places the results are presented for a single bar, where all bars, but the one under study, were removed from the ToF detector. This provides a useful insight about a crosstalk and an uncorrelated time resolution.

Raw signal measurements

Measurements of the raw signal were important for setting up the operating high voltage of the PMT and the threshold of the CFD modules. As we mentioned in the previous section, we found the optimal operating high voltage of 2100 V. The thresholds of the CFD modules were set to −150 mV. Moreover, a crosstalk between the PMT pixels was studied in the raw signal domain.

A typical signal output from the bar 6B is plotted in Fig. 4(a) in the overlapped mode to see how the signal fluctuates within run. Figure 4(b) shows several histograms of the signal amplitudes of the bars in the Train 6 to compare the signal level at the edge of the trains and at the distance of 5 mm from the edge. There is a significant decrease of the signal amplitude of the bar 6A (and the A bars in general) by 29% at the distance of 5 mm from the edge compared to the situation at the edge due to a missing contribution of the Cherenkov cone otherwise reflected from the edge side. This missing part of the cone is accepted by subsequent bars. We measured the decrease by 19% for the bar 6B, 6% for the bar 6C, and 2% for the bar 6D. The analogous decrease in case of the Train 2 was 46% (!) for the bar 2A, 24% for the bar 2B, 14% for the bar 2C, and no change in case of the bar 2D. The situation is analogous for the other trains. This effect was partly studied in the design study [4] and it is discussed in the Discussion section below.

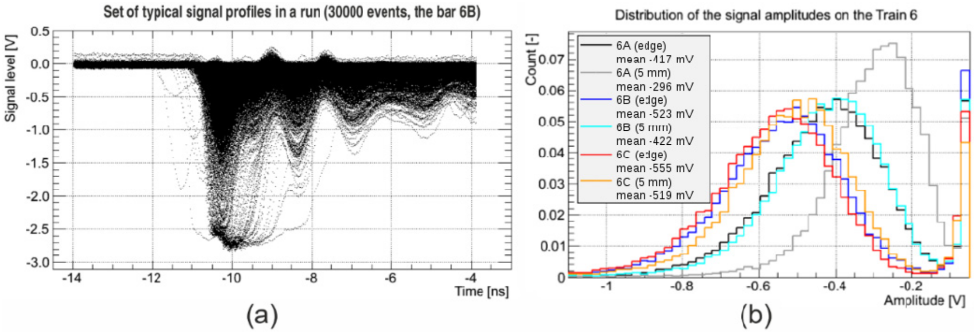

Fig. 4. (a) Overlapped set of typical output signal profiles in the Train 6, (b) examples of the amplitude distributions.

Concerning the effect of the taper, we found the signal coming from the bars with the taper to be higher by at least 33% with respect to the bars without the taper (on average, the mean values –450 mV or –400 mV compared to –300 mV). This was also observed in the previous measurement campaigns [6,9]. As a result, the efficiency of the detection is higher for the bars with the taper. The detector efficiency was not the subject of the presented measurements as the measurements in combination with the tracker provide more information [10]. The preliminary result, based on the presented raw measurements, is that the efficiency with respect to the trigger of single bars in the Trains 2, 3, and 4 (without the taper) is at least 72% for given HV and threshold settings and it is higher by 5-10% in the Train 5 (with the taper). Furthermore, the efficiency is higher when all bars are installed, where the efficiency of all but A bars is above 85%.

We were also interested in the leakage of the signal from a single bar into adjacent pixels of the PMT. Selected results of the crosstalk studies for the bars 6A and 6B are plotted in the Fig. 5(a). Here, each cell represents a pixel of the PMT and the layout corresponds to the one in Fig. 2(c). The pixel occupied by a bar is red. The crosstalk was treated as a relative level of signal coincidences between the pixel occupied by a bar and a given adjacent pixel - in other words, how often an adjacent pixel and the pixel occupied by the bar produced a signal above the specific amplitude level in the same event. This quantity is labeled *ci* in the plots in Fig. 5 and three values are displayed for three thresholds of the amplitudes: −100 mV (the pedestal limit), −150 mV (the CFD thresholds), and −200 mV. The *m* quantity is the mean amplitude of the signal detected in a pixel. Note that we found the pixel 21 to be noisy (the mean pedestal amplitude *m* was higher by the factor of 1.4).

The threshold −100 mV is approximately the limit of the pedestal region, see Fig. 4(b), thus the *ci*(−100 mV) indicates the total signal coincidences regardless the amplitude threshold except the pedestal. The level of coincidences is less than 5% at this threshold across all measured pixels (except the noisy pixel 21). The amplitude level −150 mV is the CFD threshold value. Thus, the coincidence above this level refers to the signals used in the timing processing. The level of coincidences is less than 2% at this threshold across all measured pixels. We added the amplitude threshold –200 mV for the test of eventual change of the CFD threshold setup. We got 0.5% of coincidences in this case.

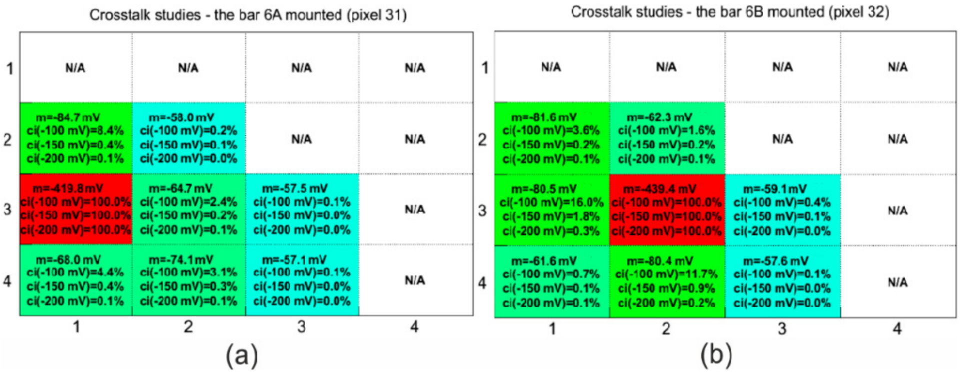

Crosstalk studies - the bar 6A mounted (pixel 31)

	1	2	3	4
1	N/A	N/A	N/A	N/A
2	m=-84.7 mV ci(-100 mV)=8.4% ci(-150 mV)=0.4% ci(-200 mV)=0.1%	m=-58.0 mV ci(-100 mV)=0.2% ci(-150 mV)=0.1% ci(-200 mV)=0.0%	N/A	N/A
3	m=-419.8 mV ci(-100 mV)=100.0% ci(-150 mV)=100.0% ci(-200 mV)=100.0%	m=-64.7 mV ci(-100 mV)=2.4% ci(-150 mV)=0.2% ci(-200 mV)=0.1%	m=-57.5 mV ci(-100 mV)=0.1% ci(-150 mV)=0.0% ci(-200 mV)=0.0%	N/A
4	m=-68.0 mV ci(-100 mV)=4.4% ci(-150 mV)=0.4% ci(-200 mV)=0.1%	m=-74.1 mV ci(-100 mV)=3.1% ci(-150 mV)=0.3% ci(-200 mV)=0.1%	m=-57.1 mV ci(-100 mV)=0.1% ci(-150 mV)=0.0% ci(-200 mV)=0.0%	N/A

(a)

Crosstalk studies - the bar 6B mounted (pixel 32)

	1	2	3	4
1	N/A	N/A	N/A	N/A
2	m=-81.6 mV ci(-100 mV)=3.6% ci(-150 mV)=0.2% ci(-200 mV)=0.1%	m=-62.3 mV ci(-100 mV)=1.6% ci(-150 mV)=0.2% ci(-200 mV)=0.1%	N/A	N/A
3	m=-80.5 mV ci(-100 mV)=16.0% ci(-150 mV)=1.8% ci(-200 mV)=0.3%	m=-439.4 mV ci(-100 mV)=100.0% ci(-150 mV)=100.0% ci(-200 mV)=100.0%	m=-59.1 mV ci(-100 mV)=0.4% ci(-150 mV)=0.1% ci(-200 mV)=0.0%	N/A
4	m=-61.6 mV ci(-100 mV)=0.7% ci(-150 mV)=0.1% ci(-200 mV)=0.1%	m=-80.4 mV ci(-100 mV)=11.7% ci(-150 mV)=0.9% ci(-200 mV)=0.2%	m=-57.6 mV ci(-100 mV)=0.1% ci(-150 mV)=0.0% ci(-200 mV)=0.0%	N/A

(b)

Fig. 5. Leakage of the signal to adjacent pixels from (a) the bar 6A, (b) the bar 6B. The axes give the MCP-PMT pixel number, as shown in Fig. 2(c).

Of course, the crosstalk to an empty pixel is enhanced if two adjacent bars are occupied by bars producing a signal. Figure 6(a) plots coincidence results on selected pixels in the scenario with the bars 6A (the pixel 31) and 6C (the pixel 33) involved. In this case we studied the signal coincidence of the empty pixel 32 when the both bars triggered a signal in the same event. The level of coincidences grew up to 7% at the threshold of −150 mV. Figure 6(b) compares histograms of the signal amplitudes in the pixel 32 in three cases: (1) with no bar anywhere (the pedestal), (2) with one bar on the pixel 31, and (3) with the situation using the two bars on the pixels 31 and 33. The last case indicates the crosstalk level between pixels in the train. As we can see, the mean amplitude of the signal grew up by –43 mV from the value of –56 mV (the pedestal) to –99 mV. As the mean amplitude of the signal from the bar 6B is –523 mV, see Fig. 4(b), the crosstalk contribution from the adjacent bars (pixels) is approximately 8%. This is already a relevant factor influencing the timing performance of trains because the correlation between bars in a train has a negative impact on the train’s timing resolution.

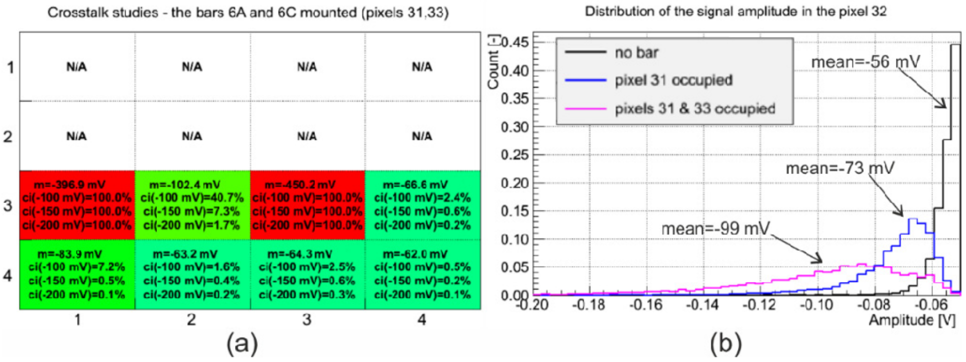

	1	2	3	4
1	N/A	N/A	N/A	N/A
2	N/A	N/A	N/A	N/A
3	m=-396.9 mV ci(-100 mV)=100.0% ci(-150 mV)=100.0% ci(-200 mV)=100.0%	m=-102.4 mV ci(-100 mV)=40.7% ci(-150 mV)=7.3% ci(-200 mV)=1.7%	m=-450.2 mV ci(-100 mV)=100.0% ci(-150 mV)=100.0% ci(-200 mV)=100.0%	m=-66.6 mV ci(-100 mV)=2.4% ci(-150 mV)=0.6% ci(-200 mV)=0.2%
4	m=-83.9 mV ci(-100 mV)=7.2% ci(-150 mV)=0.5% ci(-200 mV)=0.1%	m=-63.2 mV ci(-100 mV)=1.6% ci(-150 mV)=0.4% ci(-200 mV)=0.2%	m=-64.3 mV ci(-100 mV)=2.5% ci(-150 mV)=0.6% ci(-200 mV)=0.3%	m=-62.0 mV ci(-100 mV)=0.5% ci(-150 mV)=0.2% ci(-200 mV)=0.1%

Fig. 6. (a) Leakage of the signal to adjacent pixels from the pair of bars 6A and 6C (the axes give the MCP-PMT pixel number, as shown in Fig. 2(c)), (b) histogram of the signal amplitudes in the empty pixel 32 in different bars configuration.

Timing measurements

The measurements of the timing resolution of the bars and the whole trains were performed with respect to the first SiPM detector acting as the trigger. Its cross-section dimension of 3 × 3 mm^2 defined the spatial resolution in the characterization of the ToF timing performance. We preprocessed the output signal by the CFD module. The timestamp of the leading edge was treated as the arrival time of a signal pulse. The arrival time of a signal pulse from a PMT pixel was determined relative to the arrival time of the trigger (the time difference). In the following, we express the timing resolution by the sigma parameter σ_{fit} of the Gaussian fit of the timestamps distributions, see the example in Fig. 7(a), and by the full width at half maximum (FWHM) of the measured data sample.

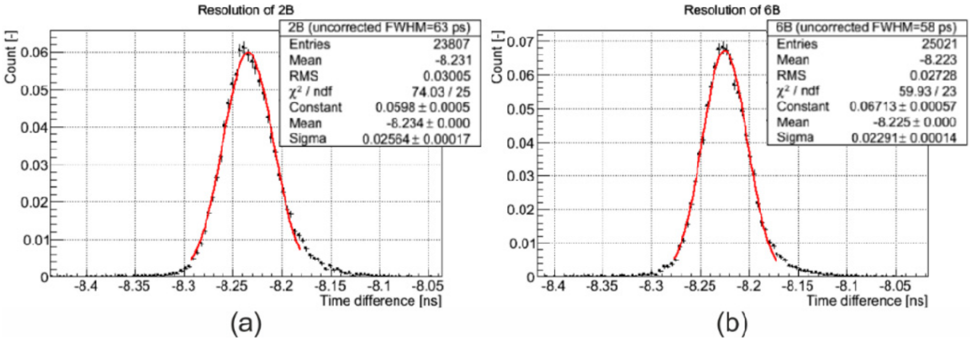

Fig. 7. Timing resolution of single bars 2B and 6(b) at the edge.

First, the timing resolution of the trigger was investigated. To do so, we added the third SiPM detector to the setup right after the second SiPM detector. We measured the mutual timing resolution of all SiPM detectors using each detector one after another as a trigger. The resolution of the first SiPM detector was resolved to $\sigma_{\text{fit}} = 10$ ps (FWHM 25 ps). The stability of its timing performance was then repeatedly verified with respect to the second SiPM detector. The third SiPM was then dismounted from the setup.

We mainly focused on the timing resolution of all trains at the edge and 5 mm from the edge and of selected single bars at the edge. Note the train resolution is the time resolution obtained from the distribution of the average times $t_{train} = \frac{1}{4}\sum_{i=1}^{4} t_i$, where t_i is the time with respect to the trigger measured by i-th bar in the train in a given event. Figure 7 plots examples of the timing resolution of the bars 2B a 6B at the edge. Note that the sigma parameter in the statistics box is the sigma of the distribution fit which is not corrected to the contribution of the trigger. Table 2 summarizes the timing resolution of dedicated bars at their edge. The bars 2A and 2B without the taper have a slightly worse resolution by 2 ps compared to the rest of the bars in with the taper. Measurement uncertainty was estimated from 5 independent measurements of the same bar to be ± 2 ps in terms of standard deviation σ (± 5 ps in FWHM), which corresponds to ± 1 ps uncertainty of the train time resolution σ (± 2 ps in FWHM).

Table 2. Timing resolution of selected single bars at their edges (uncertainty ± 2 ps in σ_{fit}, ± 5 ps in FWHM).

Bar	σ_{fit} [ps]	FWHM [ps]	Bar	σ_{fit} [ps]	FWHM [ps]
1B	22	54	5B	22	53
2A	24	58	6A	20	50
2B	24	58	6B	21	52
5A	23	60			

Measurements of the timing resolution of the whole trains were the main scope of the presented test campaigns. We measured the resolutions at the ToF edge and at the distance of 5 mm from the edge. The example of the timing resolution of the Train 6 is shown in Fig. 8. Results of the timing studies for all trains are summarized in Table 3.

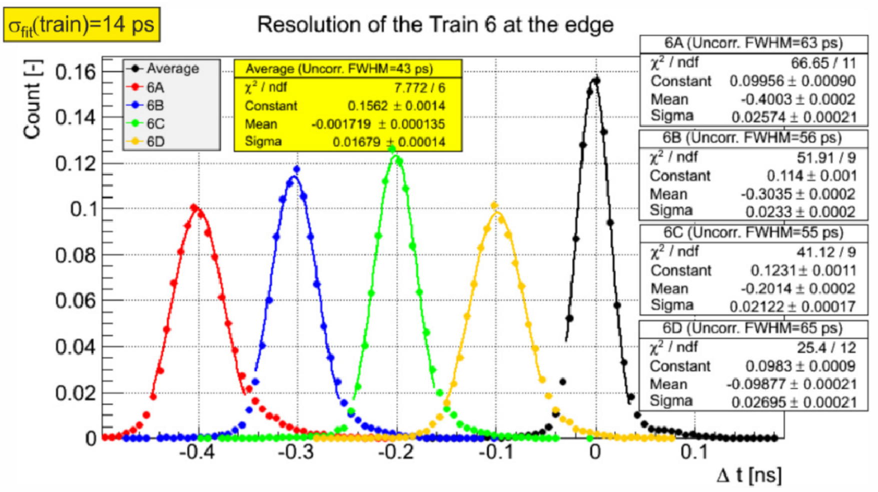

Fig. 8. Timing resolution of the Train 6 at the edge.

Table 3. Timing resolution of trains (uncertainty ± 1 ps in σ_{fit}, ± 2 ps in FWHM).

Train	edge of the ToF		5 mm from the edge	
	σ_{fit} [ps]	FWHM [ps]	σ_{fit} [ps]	FWHM [ps]
1	14	34	15	38
2	15	34	17	41
3	15	34	17	42
4	15	35	17	43
5	14	36	17	36
6	14	35	15	37

The Train 2 was also the subject of the scan over the range of distances from 0 to 20 mm from the edge. As in all the previous cases, the distance value is the lower bound of the 3 mm interval given by the 3 × 3 mm^2 trigger. Therefore, the 0 mm corresponds to aggregate measurements in the range of distances from 0 mm to 3 mm from the edge and similarly e.g.

20 mm from the edge were aggregate measurements in the range of distances from 20 mm to 23 mm from the edge.

The timing resolution of the Train 2 as a function of the distance from the edge is plotted in Fig. 9(a). The timing resolution is approximately linearly dependent on the distance from the edge (however, there is a deviation from the linear fit in case of the FWHM). σ and FWHM values are in a good agreement as shown in Fig. 9(b) (for a Gaussian distribution FWHM $\cong 2.35\sigma$), which justifies the use of the σ for the timing resolution, even though the time distribution, as shown in Fig. 8, slightly differs from a Gaussian distribution.

4. Discussion

The raw signal studies confirmed a variable strength of the signal across the bars in a train. We expected a lower signal level at the A bars compared to the rest of the bars in the train due to the leakage of the optical signal near the train edge. According to the simulations, the part of the Cherenkov cone leading to the edge of the bar is totally reflected towards the sensor. We call this part of the Cherenkov cone a negative wing, as in the previous studies [4]. However, photons of the negative wing also leak to the successive bars near the back end of the bar as visualized in Fig. 10(a) using the Geant4 toolkit [9,11].

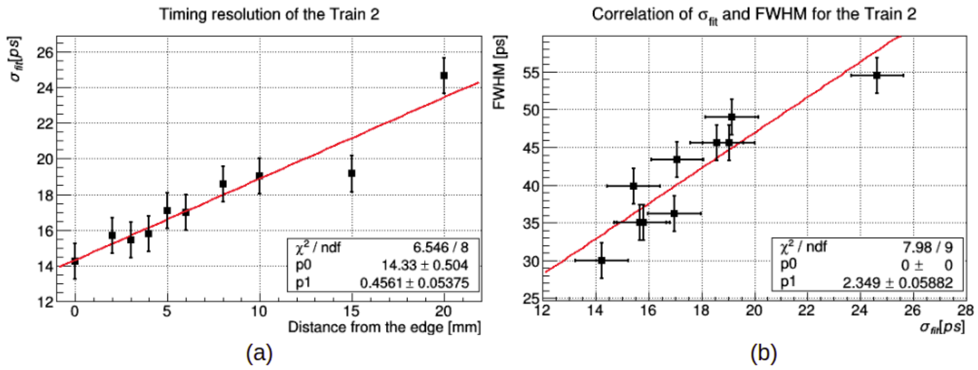

Fig. 9. (a) Timing resolution of the Train 2 as a function of the distance from the edge; (b) correlation of σ and FWHM measures of the timing resolution.

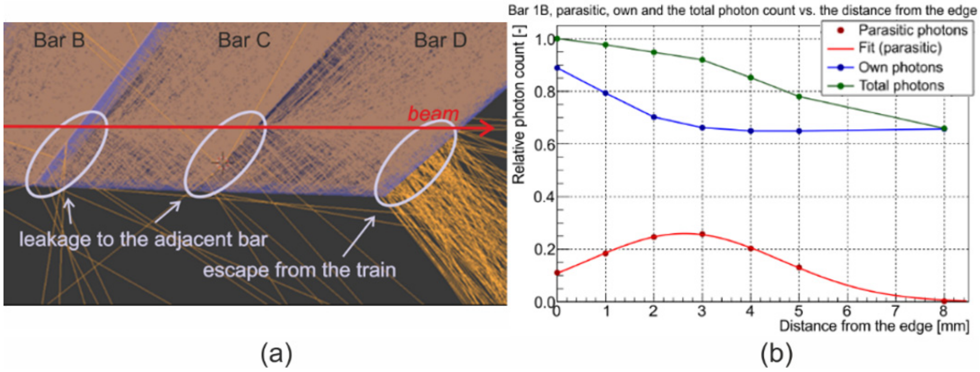

Fig. 10. Optical leakage between bars near the train edge, (a) visualization in Geant4, (b) contribution of the own and the parasitic fractions to the total hit count in the sensor.

This effect strongly depends on the distance of the beam particle from the edge as seen in Fig. 10(b) for the case of the pair of the bars 1A and 1B (the models). In the plot, the green curve plots the total amount of photons generated by a proton traversing the bars at the given distance from the edge, reaching the detector pixel for the bar 1B normalized to the case at the edge. It is the sum of the contribution of the photons generated in the bar 1B itself (the blue curve) and of the contribution of the parasitic photons generated in the bar 1A (the red curve). As there is no bar in front of the A bars, those bars suffer from the missing parasitic fraction resulting in a lower signal level and in turn a worse timing resolution and efficiency.

We can see that the total number of detected photons (the green curve) decreases with the distance from the edge. This results in the worsening of the bar resolution with the increased distance of the beam from the bar edge. At the distances above 10 mm the effect diminishes because all photons from the negative wing leave the ToF and they do not contribute to the signal output from the train. This has a negative impact on the timing resolution of the bars and of the trains themselves as seen in Fig. 9. Moreover, a lower signal level also means a lower detection efficiency of a single bar.

The measurements of the bars with the taper are in agreement with the expectation from the simulation results presented in the design study [4]. However, the uncertainty of the simulation is large due to the lack of a more precise PMT response model. The simulation predicted an increase of the number of detected photons by 20-50% depending on the collection time of the PMT, while the presented measurements show at least 33% increase.

The obtained timing resolution comprises of time smearing in bars and MCP-PMT, and a jitter of the CFD module ($\sigma = 5$ ps). In addition, there is a systematic shortening of an optical path of the fastest photons as the distance of a hit from the edge increases. The shorter optical path is partially compensated by a longer time of flight of a beam particle before reaching the bar. Since we are triggering on the 3×3 mm^2 SiPM detector, the obtained time distributions are smeared mixture distributions for the range of hit positions. We calculated the combined contribution σ to be less than 3 ps.

There is still an additional contribution of a TDC used to read out the ToF system, which is not included in the presented results. The currently used HPTDC [12] based unit adds 14 ps [10] in quadrature to a single bar time resolution (specific channel combinations might lead to a larger contribution), but there is a planned upgrade to a picoTDC based unit (which is under development), where the jitter should be below 3 ps.

Concerning the timing resolution of the whole trains, the electronic crosstalk would play a significant role (since the optical signal from all bars in a train arrives at the MCP-PMT at the same time, optical crosstalk is not causing deterioration). As seen in Fig. 6, its level was approximately 7% based on the contribution from both adjacent pixels (in frame of the train alone). Although it increases the signal amplitude of the channel (the bar plus the pixel), it has no positive effect on the timing resolution of the channel comparing results of the timing studies of single bars to the ones of the whole trains, see the sigma values of the bar 6B in Fig. 7(a) and Fig. 8. Conversely, this crosstalk deteriorates the resolution of the whole train.

Theoretically, the timing resolution of the train is better than the one of single bars by the factor of $1/\sqrt{N}$, where N is the number of bars in the train, providing the output signals from the bars are mutually independent (uncorrelated) and the time resolutions of bars are similar. For instance, it is visible in Fig. 8, that the bars of the Train 6 have the timing resolution approximately 22 ps on average (after the subtraction of the trigger contribution). This theoretically leads to the timing resolution of 11 ps of the whole train. Due to the crosstalk, the measured resolution is 14 ps instead. We obtained similar results in our previous measurements with a different PMT [6] where we estimated the level of crosstalk to be 10%.

5. Conclusion

Despite the negative contributions of the crosstalk, we measured the time resolution of the ToF optical part and front-end electronics to be below 20 ps. The ToF was installed to the LHC tunnel together with the AFP detector in March 2017 and it is being tuned now to achieve a requested operational performance.

There are still several issues to be solved. The production of the bars is based on the bonding of the bar arms together with a suitable glue [6]. The glue itself attenuates the signal approximately by 20% in the deep UV region. In the near future, the development of a single-piece bar production is of the highest priority.

Funding

Horizon 2020 (654168); MSMT of Czech Republic (LM 2015058, RCPTM-NPU LO1305, CZ.02.1.01/0.0/0.0/16_019/0000754); Palacky University (IGA_PrF_2017_005); MINECO of Spain (FPA2013-48308-C2-1-P, FPA2015-69260-C3-2-R, FPA2015-69260-C3-3-R, SEV-2012-0234, Juan de la Cierva programme); Catalan Government (AGAUR SGR 2014 1177).

Acknowledgments

The authors thank the CERN SPS and NA teams for their support during test beam campaigns. The equipment and detectors were provided by the following institutes and people: the LQ bars and LeCroy WavePro 7200A by Palacky University, the MCP-PMT by Photonis, the SiPM reference detectors by M. Albrow and H. Sadrozinski, the pre-amplifiers and the mechanical setup by Stony Brook University and Palacky University, the CFDs and HPTDC by University of Alberta, the Agilent Infiniium DS91204A by CERN, the pixel modules by IFAE Barcelona and INFN Genova, the RCE system by SLAC and the pixel holders and cables by ATLAS ITk pixel test-beam group.

147.231.27.222 {ts '2018-03-23 08:17:13'}

Nuclear Inst. and Methods in Physics Research, A 985 (2021) 164705

Contents lists available at ScienceDirect

Nuclear Inst. and Methods in Physics Research, A

journal homepage: www.elsevier.com/locate/nima

Timing resolution and rate capability of Photonis miniPlanacon XPM85212/A1-S MCP-PMT

T. Komárek [a,*], V. Urbášek [a], A. Brandt [b], V.A. Chirayath [b], L. Chytka [a], M. Hrabovský [a], L. Nožka [a], M. Rijssenbeek [c], T. Sýkora [d]

[a] *Joint Laboratory of Optics, RCPTM, Palacký University, 17. listopadu 50A, 77207 Olomouc, Czech Republic*
[b] *The University of Texas at Arlington, 701 S. Nedderman Drive, Arlington, TX 76019, USA*
[c] *Stony Brook University, Department of Physics and Astronomy, Nicolls Road, Stony Brook, NY 11794-3800, USA*
[d] *Charles University, Faculty of Mathematics and Physics, Institute of Particle and Nuclear Physics, V Holešovičkách 2, 18000 Praha 8, Czech Republic*

ARTICLE INFO

Keywords:
Micro-channel plate photo-multiplier tubes
Time-of-flight
Fast timing
Cherenkov radiation

ABSTRACT

We report here on a set of experiments that focus on measuring the timing performance of the Photonis miniPlanacon XPM85212/A1-S microchannel plate photomultiplier tubes along with the detector response at high event rates. The detector has a single photoelectron timing resolution of 30 ps at low rates (10 kHz). We show that both the gain and the timing start to deteriorate around 1 MHz with 20 photoelectrons per channel at 10^4 target gain, giving the current per unit of area limits of 1.38 μA/cm^2 and 2.38 μA/cm^2 for the two tested devices. Photo-multiplier tubes with lower micro-channel plate resistivity exhibit a better rate capability due to the faster replenishment of the charge inside the microchannels. As we demonstrate, another method to improve the rate capability is to operate the photon detector tubes at a lower gain by reducing the supply voltage and compensating for the loss of amplitude by an additional amplification stage at the expense of the achieved timing resolution. The tube active area over which the beam is spread also plays a role since the same amount of light yields a better rate capability when spread over a larger area. The tubes exposed to high event rates showed an uncharacteristically slow recovery back to its initial gain with 80 % of the initial gain recovered only after several tens of minutes.

1. Introduction

Photomultiplier Tubes (PMTs) are widely employed in particle physics experiments to detect photon fluxes as low as single photon events. Micro channel plate (MCP) PMTs are preferred in environments with strong magnetic fields where the conventional PMTs show severe degradation in performance [1,2], or where timing resolution of the order of few tens of pico seconds is required [3,4]. They also have a very compact size and allow for easy pixelisation through the use of multiple anode pads.

MCP-PMTs have been proposed as the photon detectors in the Quartz Cherenkov ToF (Time-of-Flight) detector system [5], which is a forward proton detector that has been added to the ATLAS detector at the Large Hadron Collider. This system uses the Cherenkov radiation produced within quartz bars as a trigger [6,7] and aims to achieve a timing resolution of $10-20$ ps [8]. Unlike typical ToF systems that have the start and stop signals to measure particle velocity, we propose to use the time difference of the outgoing protons from diffractive events to measure the vertex position and compare it to the vertex measured with the central detector, enabling the rejection of the background due to the pile-up events [5]. In order to measure the time difference between the two outgoing protons with the required timing resolution, the time of arrival of the proton is determined by averaging the four timing signals corresponding to the proton traversing through the four quartz bars. A proton hit on one quartz bar will result in Cherenkov photons (200-450 nm) with the proton event rates exceeding 10 MHz. The Cherenkov photons are expected to result in 15–20 Pe (photoelectrons) in the MCP-PMT per quartz bar and thus, the proposed detector needs to provide optimum performance at event rates exceeding 10 MHz with 15–20 photoelectrons.

We report here on the performance of two candidate MCP-PMTs (miniPLANACON XPM85212) by Photonis. These are one inch square devices with 16 channels in a 4 × 4 matrix (5.8 mm channel size with a 6.4 mm pitch) [9]. The MCPs within these PMTs have 6.5 μm pores that are specially coated using ALD (Atomic Layer Deposition) techniques that have been demonstrated to extend the lifetime of devices similar to that required for our application ($\sim 10\,\mathrm{C/cm^2}$) [10].

---

[*] Corresponding author.
E-mail address: tomas.komarek@cern.ch (T. Komárek).

https://doi.org/10.1016/j.nima.2020.164705
Received 11 December 2019; Received in revised form 6 September 2020; Accepted 23 September 2020
Available online 25 September 2020
0168-9002/© 2020 Elsevier B.V. All rights reserved.

Fig. 1. MCP front face image obtained with a confocal scanning microscope. The pores are 6.5 μm in diameter in a hexagonal layout. The macroscopic hexagonal tile structure edges and occasional minor defects are also visible. From the confocal microscope image, we determined the pore coverage to be 60 %.

Table 1
PMT parameters.

Manufacturer's specification using the recommended HV divider				
PMT serial	R_{MCP}	HV for 10^5 gain	HV for 10^6 gain	
9002096	36 MΩ	2005 V	2310 V	
9002097	29 MΩ	1920 V	2165 V	
Estimates for both PMTs				
Pore size				6.5 µm
Pore coverage				60 %
Photocathode — MCP in gap				~4 mm
MCP thickness				1.2 mm
MCP out — anodes gap				0.5 mm
Amplifier load resistor			R_a	50 Ω
MCP out blocking resistor			R_b	~0.1 Ω
Anode inductance			L_a	~10 nH
MCP out blocking capacitor			C_b	4 × 10 nF
Photocathode — MCP in capacitance			$C_{\mathrm{fk-mi}}$	~1.43 pF
Photocathode — MCP out capacitance			$C_{\mathrm{fk-mo}}$	~0.1 pF
Photocathode — ground capacitance			$C_{\mathrm{fk-gnd}}$	~0.1 pF
MCP capacitance			C_{MCP}	~38.1 pF
MCP out — anode capacitance			C_{a1}	~0.6 pF
Anode — ground capacitance			C_{a2}	~0.64 pF
Amplifier input capacitance			C_i	~2.5 pF

2. General considerations

The MCP-PMTs tested here were specified to have TTS (Transit Time Spread, a single photoelectron timing resolution) < 50 ps, but TTS < 35 ps can typically be achieved under operating conditions. The photocathode quantum efficiency peaks in the range of 300-400 nm at above 20 % [9]. The MCP pore coverage was measured using a confocal microscope scan of the MCP input side, as seen in Fig. 1. The recommended high voltage divider for these PMTs has 510k–5.1M–510k resistor stages. We used this divider design in our tests.

2.1. Pulse shape

Many aspects of the PMT behaviour can be calculated or simulated based on the PMT specifications and some estimated internal parameters as listed in Table 1. We have electrically modelled the MCP-PMT behaviour using the specified internal dimensions and the materials (that gives an estimate of the capacitive couplings and inductances) used inside the MCP-PMT along with the back-end readout electronics. The model equivalent circuit with a current source representing the operation of the MCP-PMT is shown in Fig. 2. The L_a, C_i and R_a form a low-pass filter with a cut-off frequency of 1 GHz that will influence the output pulse shape and rise-time, but not the rate capability.

Table 2
PMT rate capability estimates at gain 10^4 and $N_{pe} = 20$ based on Eq. (1).

PMT serial	MCP HV[a]	Rate limit estimate
9002096	1384 V	7.5 MHz
9002097	1356 V	9.1 MHz

[a] The applied MCP voltages for these are calculated based on the resistive divider with 510k–5.1M–510k resistor stages and the actual R of the MCPs.

2.2. Rate capability

The numerous beam tests of the prototype ToF detector [8] were performed with low rates in the range of $5-20$ kHz (based on the beam profile and the intensity) over all the PMT channels combined. As we could not easily obtain a beam of suitable particles at megahertz rates for our tests, the rate capability test was done using laser pulses as the light source instead.

We used theoretical calculation to estimate the rate capability of the PMTs. To produce such an estimate we consider the MCP recharge current and charge per hit transferred to anodes based on gain. Based on the results of simulations [6] and the PMT quantum efficiency, we estimate each particle passing through the detector generates on average $N_{\mathrm{pe}} = 20$ photoelectrons in the PMT per bar, times 4 bars hit. However, assuming complete locality of the rate capability, we must load the whole PMT in this scenario, multiplying the N_{pe} by 16 (the total number of channels). The target PMT gain (using three signal amplification stages) is $g = 10^4$. The high voltage U_{P} needed to apply over the MCP through HV divider to achieve that gain as well as the MCP resistance values R_{MCP} vary from piece to piece (see values in Table 1, the HV for other gains than specified by manufacturer are later determined from fitted gain curves in Fig. 3a).

Considering the elementary charge e and a given rate f, the current drawn from the MCP by electron multiplication is

$$I_{\mathrm{m}} = 16efgN_{\mathrm{pe}}.$$

The strip current replenishing the charge is

$$I_{\mathrm{sc}} = U_{\mathrm{P}}/R_{\mathrm{MCP}}.$$

We now calculate the rate at which these two currents are equal, so the charge drawn per hit $16egN_{\mathrm{pe}}$ is equal to the charge replenished through the MCP strip current $U_{\mathrm{P}}/R_{\mathrm{MCP}}$ between hits. When the rate approaches $\sim 10\,\%$ of this value, the gain is expected to decline due to the lack of available electrons in the MCP [11]. The maximum rate estimate without this decline is therefore

$$f = 0.1\frac{U_{\mathrm{P}}}{16egR_{\mathrm{MCP}}N_{\mathrm{pe}}}, \tag{1}$$

where g is a function of U_{P} for a given PMT piece.

HV in Table 1 is the total voltage over the high voltage divider, which supplies 5/6 of the total voltage to the MCP[1] [9]. A summary of the calculated rate capabilities using both methods can be found in Table 2. While the results of both estimates differ by a factor of three, they are at the same order of magnitude, forming our baseline expectation of the PMT rate capability. The gain curves for both PMTs and the variation of the rate capability based on the second estimate method can be seen in Fig. 3.

The MCP resistance R_{MCP} is of a major importance here as it directly influences the strip current and the MCP recharge speed. However, it cannot be decreased to very low values as that would mean much more heat being generated in the MCP where ways of removing heat are extremely limited [12].

---

[1] In reality this is closer to ~ 4.3/5.3 due to the MCP being parallel to the centre stage of the divider. This is taken into account in the calculations with the actual R of the MCPs.

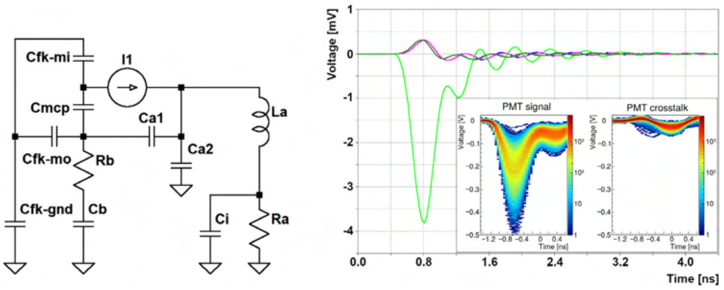

Fig. 2. A semi-realistic model of a single channel of the PMT using the equivalent circuit is shown on the left (see Table 1 for parameter explanations and values). The microchannel behaviour is emulated using a linearly-rising current source. Crosstalk can be simulated by connecting a 4 × 4 matrix of these single channel models. On the right, a resulting signal and crosstalk in neighbouring channels are shown with an overlay of a real signal heatmap for comparison. The simulated signal has a slightly sharper edge (150 ps rise time), which matches the PMT rise time when measured without amplifiers (see Fig. 7).

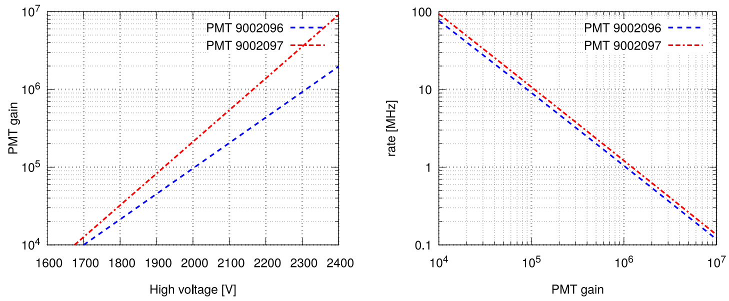

a)   b)

Fig. 3. PMT gain curves based on datasheets (the voltage is applied using the recommended divider) and calculated rate capability estimates using the strip current limit method (given by Eq. (1)) for $N_{\mathrm{pe}} = 20$.

The PMT gain is also very important. One proposed method to improve the rate capability is to add another signal amplification stage. The reduction of the PMT gain is achieved by a reduction of high voltage which in turn influences the strip current as well, but the slight decrease of strip current is negligible compared to the gain change that spans orders of magnitude. Therefore the rate capability should increase by about the same factor as the PMT gain decreases — as shown in Fig. 3b.

Moving gain from PMT to amplifiers means much more effort must be focused on removing any sources of noise while shielding the setup against interference. The timing performance can otherwise be compromised.

Another factor that can influence the rate capability of the MCP-PMT is the non-uniformity of the light intensity over the MCP-PMT window. Some level of local effects are expected to occur, and so if the PMT is loaded by pulses of the same intensity only over a part of the window, projecting to a part of MCP, a lower rate capability is expected in that area. This effect will also play some role in the real detector, as the bars closer to the LHC beam can be hit more often in some scenarios. The magnitude of the local effect is however hard to predict [13].

3. Measurement setup and protocol

3.1. Setup description

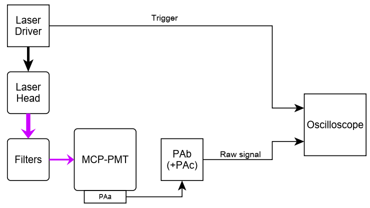

Fig. 4. Measurement setup scheme.

The measurement setup scheme is shown in Fig. 4. The Hamamatsu M10303-29 laser system (405.6 nm, 64.9 ps square pulses) was used as a light source. The beam spot size in each channel was 6 mm^2 unless specified otherwise. The PMT output signals were amplified using custom broadband amplifiers (PAa + PAb), each with a gain of 20 db [5]. In many measurements, a third amplification stage (PAc) equivalent to the second stage was used for additional gain. The signal was then observed with an oscilloscope triggered by the laser driver. The oscilloscope we used was the LeCroy WavePro 760Zi with 6 GHz bandwidth and a 40/20 GS/s sampling rate depending on the number of channels in use.

Measurements other than TTS were performed using optical fibres (either one or more) to guide the light into the desired PMT channels.[2] Four channels are typically hit simultaneously in the AFP ToF detector,

---

[2] The optical fibres used could spread the laser pulse in time, so for TTS measurements the beam was directed to the PMT window with a mirror instead. The fibres were necessary to hit multiple channels in a predictable way.

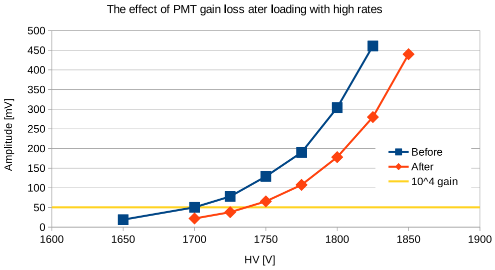

Fig. 5. High rate load effect on gain for the 9002096 PMT at 20 Pe per pulse. Note how the supply voltage needed for the 10^4 gain shifts to higher values.

therefore many measurements were done with four channels in a single column being illuminated. The PMT anode region and the first stage amplifiers (PAa) were carefully shielded against interference by using a fine copper mesh. The second and third stage amplifiers PAb and PAc had their own enclosures which provided sufficient shielding.

3.2. Measurement protocol

For timing measurement purposes, a software CFD (Constant Fraction Discriminator) was implemented to determine the 42 %[3] signal level trigger point of the PMT signal in order to correct for time walk. The software CFD was also proven to perform within 1 ps of a properly tuned hardware CFD circuit. For TTS measurements, a low light level corresponding to 0.05 photoelectrons per pulse was used to minimize the number of events with two or more photoelectrons.

After measuring the gain behaviour of a single channel at low laser repetition rates (10 kHz) recorded as pulse amplitude dependence on the supply voltage, the PMT channel was loaded with a high rate 10 MHz light beam for one minute at 10^5 gain, corresponding to 50 μA/cm^2. An effect of a decreased PMT gain was observed when subsequently remeasured at low rates. This is illustrated in Fig. 5. Repeated high rate runs did not decrease the gain further. A short-term partial recovery in the order of minutes was observed, this effect is discussed in more detail in Section 4.

Any influence of the short-term partial recovery after high rate loading was mitigated by waiting before performing the next rate scan. Scans were always done from lower to higher rates.

When performing the rate scans with 3 amplifier stages, the high voltage was varied and a rate scan was performed for each value. The PAb gain was also varied with attenuators to compensate for PMT gain changes at different voltages. Four channels were illuminated in these particular measurements using fibres with 20 photoelectrons per pulse in each channel.

With two amplifier stages, a test where one or four channels were illuminated was performed. In this case, the measurement was done with 7 photoelectrons per channel for each pulse.

A test of the illuminated area variation in a single channel was done by retracting the fibre by a set of distances from the PMT front face. The overall amount of light was not changed for the different positions. Only the area over which it was spread was larger than the 6 mm^2 used in other measurements, up to 50 mm^2. Stronger pulses of ∼ 200 Pe were used for this test.

The rate capability threshold was always evaluated as the point where the gain drops to 80 % of the gain at very low rates (10 kHz) using linear interpolation between the data points.

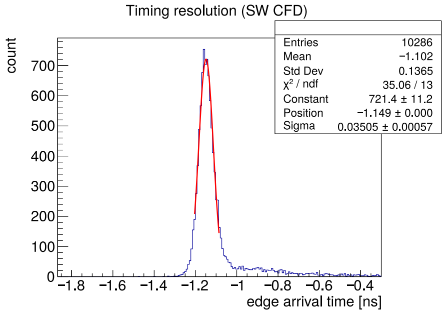

Fig. 6. TTS (transit time spread) of single photoelectrons in the 9002097 PMT at 10^6 gain.

4. Results

The TTS of the 9002097 PMT was measured to be 29.7 ± 0.5 ps after subtracting the 65 ps contribution of the laser pulse width.[4] A 10^6 PMT gain had to be used to achieve single Pe sensitivity. The distribution can be seen in Fig. 6. The small tail on the right is caused by photoelectrons that backscattered off the MCP input surface before being collected and amplified by an MCP pore [14].

The rise time between 20 % – 80 % amplitude of both PMTs with 20 photoelectrons per pulse and 10^5 gain as measured with our setup was comparable at around 240 ps. However, when measured without the amplifiers, the rise time was 150 ps, showing that the amplifier bandwidth is a limiting factor. The rise time distributions can be seen in Fig. 7.

As can be seen in Fig. 8, the signal amplitude and therefore the PMT gain starts to drop as the rates get to the megahertz range. The lowering of the gain at which the PMT is operated (allowed by the third amplifier stage) pushes the onset of this effect to higher rates while compromising the timing resolution to a certain extent. The rate limit at 10^4 gain is 2.6 MHz (1.38 μA/cm^2) for PMT 2096 and 4.2 MHz (2.38 μA/cm^2) for PMT 2097.

Fig. 9 (left) shows that the rate capability is dependent on the number of channels illuminated. The rate capability drops to 40 % when four channels are illuminated as compared to a single channel, keeping the same amount of light per channel.

The rate capability also varies with the area illuminated (without changing the total amount of light of ∼ 200 Pe during the measurement) as shown in Fig. 9 (right). The results reveal a linear dependence, proving the saturation effect is mostly local. The current per area limit stays close to 2.2 μA/cm^2 regardless of the area illuminated for PMT 2097, which is close to the previously established value.

After the PMT was loaded with high rates, the recovery to the original gain took an unusually long time – several minutes for recovery to 80 % of the original gain (with full recovery being reached only the next day) – as compared to a few milliseconds with a typical non-ALD MCP-PMT. This has been observed for ALD-treated MCP-PMTs from other manufacturers as well [15]. Fig. 10 shows the initial recovery for various lengths of the load time with 10 MHz pulse rates, corresponding to 50 μA/cm^2. A different behaviour was observed with 1 s load time and resulted in an initially faster recovery, but the long-term recovery behaviour remained the same.

---

[3] The 42 % pulse height fraction was previously determined to yield the best timing resolution.

[4] This timing resolution subtraction was supported by a Monte Carlo toy model of a Gaussian (true TTS) and a square (laser) distribution convolution.

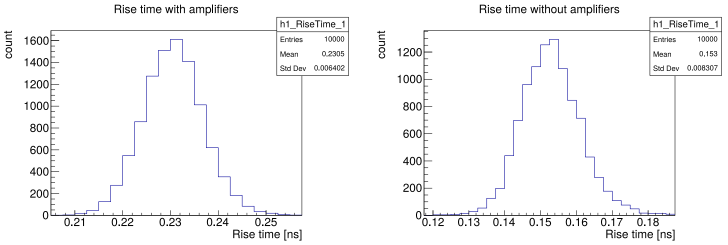

Fig. 7. The typical $20\,\% - 80\,\%$ rise time of the PMT 2097 at 10^5 gain with 20 Pe pulses. On the left as measured with amplifiers (two stages); on the right without.

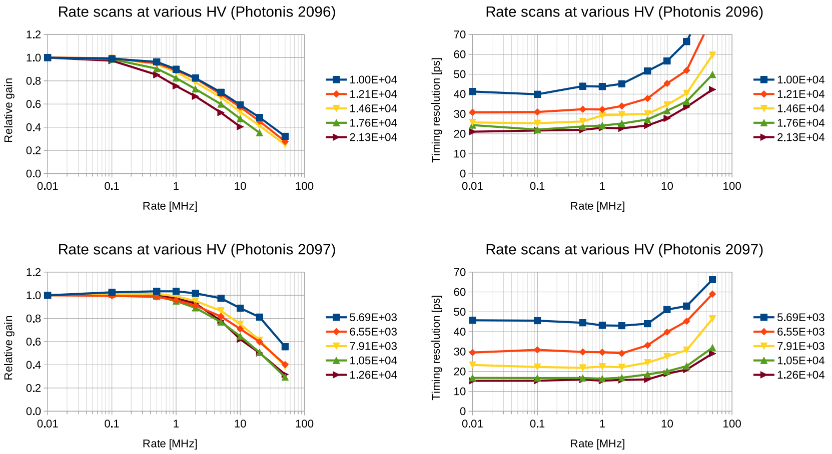

Fig. 8. Rate scan results for both PMTs with four channels illuminated with 20 Pe pulses each. To aid readability, the legend labels are included in the same order (with increasing gain) as the data series are stacked.

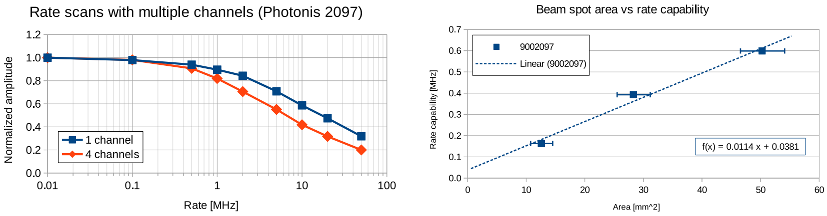

Fig. 9. Rate scan results for PMT 9002097 with one and four channels illuminated with fixed beam spot area per channel of 6 mm^2 at 10^5 gain with 7 Pe per pulse (left); dependence of the rate capability on the illuminated area within a single channel for PMT 2097 at $5.7 \cdot 10^4$ gain and 200 Pe per pulse (right).

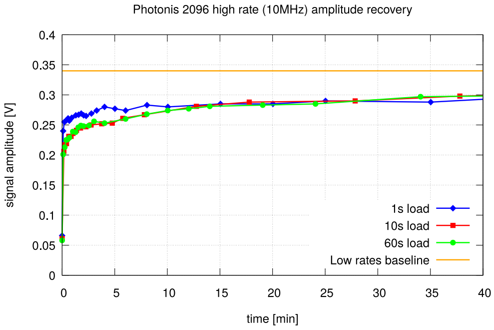

Fig. 10. Recovery behaviour after loading the PMT with 10 MHz pulse rates of $N_{pe} = 20$ at 10^5 gain for various lengths of time.

5. Discussion

The electrical model of Photonis miniPlanacons introduced in Section 2 is matching observations in terms of signal, cross-talk and rise time that was measured to be 150 ps. This value increases to ∼ 240 ps when amplifiers are used.

The PMT single photoelectron time resolution is 29.7 ± 0.5 ps and matches the manufacturer's specification.

The rate capability is, as can be seen, limited and results in gain losses in the megahertz range (Fig. 8). The rate capability for a 10^4 gain shows a gain reduction of 80 % at 2.6 MHz for PMT 9002096 and 4.2 MHz for 9002097. By taking into account the beam spot size and gain, these then correspond to 1.38 μA/cm^2 and 2.38 μA/cm^2.

To compare these results to the theoretical rate limit predictions in Section 2, we have to first correct those to the smaller beam spot of 6 mm^2 as compared to the 41 mm^2 channel area (1/16 of the total active

PMT area) for which they were calculated. This correction gives us a theoretical rate limit of 1.10 MHz for PMT 2096 and 1.34 MHz for PMT 2097. These match the measured limits very well, as they represent the expected rate where the gain starts dropping, while the measured rate limits represent the slightly higher rates where the gain already drops to 80 %. Also the fact that only 1/4 of the MCP was loaded with light during the measurement could play some role. PMT 9002097 performs better than PMT 9002096 due to its lower MCP resistance and therefore a higher current that is replenishing the charge, which is also as predicted.

Reducing the HV and therefore the gain has a positive influence on the rate capability. However, as the SNR (signal-to-noise ratio) degrades, it starts to negatively influence the timing resolution at the same time. The plots in Fig. 8 can serve as a way to choose an appropriate operating voltage where the trade-off between rates and timing performances is acceptable, which would be 1750 V ($1.46 \cdot 10^4$ gain) for 9002096 and 1650 V ($7.91 \cdot 10^3$ gain) for 9002097.

The rate capability of the PMT includes significant local effects. When the beam is focused on a small area, the rate capability is significantly worse than when spread over most of the PMT channel (Fig. 9), keeping the limit at around the above mentioned values of 1.38 μA/cm^2 and 2.38 μA/cm^2. Therefore, achieving a good signal uniformity in real applications for all the channels allows for a better rate capability, while most likely increasing crosstalk near the channel boundaries.

The rate capability (again established as the rate at which gain is reduced to 80 %) drops to 40 % of the original rate when four channels are illuminated instead of one (Fig. 9). This also shows that the effect is not simply completely local (as no change would be observed), nor is it completely global (as it would drop to 25 %). This effect suggests that nearby microchannels could be helping to replenish the charge where it is depleted. This can no longer happen when those areas are depleted as well.

As compared to the milliseconds needed with conventional (non ALD-processed) MCP-PMTs, the recovery of the PMT gain after loading with high pulse rates (10 MHz) takes an extremely long time — about 10 min for partial recovery to 80 % and a full day for complete recovery.

6. Conclusion

Two Photonis miniPLANACON XPM85212/A1-S MCP-PMTs were measured using 405.6 nm laser pulses. The measurements were focused on the pulse rate capability of said MCP-PMTs and on factors that can help improve it. In particular, lower MCP resistance and operation at lower gain were proven to play a vital role in efforts to improve the rate capability.

However, both approaches have limitations. Too low MCP resistance would cause overheating of the MCP unless it is possible to cool it sufficiently. PMT operation at a lower gain (compensated by a third amplifier stage) then results in a lower SNR, causing a degraded trigger efficiency and also a worse timing performance. Low-noise amplifiers (especially the first stage) and good electromagnetic shielding from any external interference are therefore critical.

The illuminated area has a strong effect on the rate capability and when spreading the same amount of light over a larger area, it helps to achieve a proportionally better rate capability as well.

Given the limitations discussed above, these standard ALD PMTs do not meet the requirements of the AFP ToF system. At 10 MHz the time resolution would be significantly degraded. In addition the long recovery times are ill-suited to operational needs. On the other hand, non-ALD devices without these rate issues will not survive long enough to be useful. We are therefore exploring alternative solutions.[5]

CRediT authorship contribution statement

T. Komárek: Methodology, Software, Validation, Formal analysis, Investigation, Data curation, Writing - original draft, Writing - review & editing, Visualization. **V. Urbášek:** Methodology, Investigation. **A. Brandt:** Conceptualization, Methodology, Investigation, Resources, Data curation, Writing - review & editing. **V.A. Chirayath:** Investigation, Data curation. **L. Chytka:** Methodology, Formal analysis. **M. Hrabovský:** Supervision, Project administration, Funding acquisition. **L. Nožka:** Software, Validation, Formal analysis, Writing - review & editing, Supervision. **M. Rijssenbeek:** Conceptualization, Resources, Supervision, Project administration, Funding acquisition. **T. Sýkora:** Conceptualization, Validation, Writing - review & editing, Supervision, Project administration.

Declaration of competing interest

The authors declare that they have no known competing financial interests or personal relationships that could have appeared to influence the work reported in this paper.

Funding

The authors gratefully acknowledge the support from the Operational Programme Research Development and Education – European Regional Development Fund, project no. CZ.02.1.01/0.0/0.0/16_019/0000754 of the Ministry of Education, Youth and Sports of the Czech Republic (MSMT); from MSMT no. CZ.02.1.01/0.0/0.0/17_049/0008422; from MSMT of the Czech Republic LM LM2018104; from MSMT of the Czech Republic LM 2015058; from Palacky University IGA_PrF_2020_007; and from the U.S. Department of Energy DE-SC0011686.

References

[1] P. Antonioli, A. Kluge, W. Riegler, ALICE Collaboration, Upgrade of the ALICE Readout & Trigger System, Tech. Rep CERN-LHCC-2013-019. ALICE-TDR-015, 2013, URL https://cds.cern.ch/record/1603472, Presently we require a LHCC-TDR reference number. At a later stage we will fill the required information.

[2] S. Hirose, Performance of the MCP-PMT for the Belle II TOP counter in a magnetic field, Nucl. Instrum. Methods Phys. Res. A 766 (2014) 163–166, http://dx.doi.org/10.1016/j.nima.2014.05.012, URL http://www.sciencedirect.com/science/article/pii/S0168900214005117, RICH2013 Proceedings of the Eighth International Workshop on Ring Imaging Cherenkov Detectors Shonan, Kanagawa, Japan, December 2–6, 2013.

[3] M.G. Albrow, H. Kim, S. Los, M. Mazzillo, E. Ramberg, A. Ronzhin, V. Samoylenko, H. Wenzel, A. Zatserklyaniy, Quartz Cherenkov counters for fast timing: QUARTIC, J. Instrum. 7 (10) (2012) P10027, http://dx.doi.org/10.1088/1748-0221/7/10/p10027, URL https://doi.org/10.1088/1748-0221/7/10/p10027.

[4] K. Inami, N. Kishimoto, Y. Enari, M. Nagamine, T. Ohshima, A 5 ps TOF-counter with an MCP–PMT, Nucl. Instrum. Methods Phys. Res. A 560 (2) (2006) 303–308, http://dx.doi.org/10.1016/j.nima.2006.01.027, URL http://www.sciencedirect.com/science/article/pii/S0168900206000611.

[5] L. Adamczyk, E. Banaś, A. Brandt, M. Bruschi, S. Grinstein, J. Lange, M. Rijssenbeek, P. Sicho, R. Staszewski, T. Sykora, M. Trzebiński, J. Chwastowski, K. Korcyl, Technical Design Report for the ATLAS Forward Proton Detector, Tech. Rep. CERN-LHCC-2015-009. ATLAS-TDR-024, 2015, URL https://cds.cern.ch/record/2017378.

[6] L. Nozka, A. Brandt, M. Rijssenbeek, T. Sykora, T. Hoffman, J. Griffiths, J. Steffens, P. Hamal, L. Chytka, M. Hrabovsky, Design of Cherenkov bars for the optical part of the time-of-flight detector in Geant4, Opt. Express 22 (23) (2014) 28984–28996, http://dx.doi.org/10.1364/OE.22.028984, URL http://www.opticsexpress.org/abstract.cfm?URI=oe-22-23-28984.

[7] L. Nozka, L. Adamczyk, G. Avoni, A. Brandt, P. Buglewicz, E. Cavallaro, G. Chiodini, L. Chytka, K. Ciesla, P. Davis, M. Dyndal, S. Grinstein, P. Hamal, M. Hrabovsky, K. Janas, K. Jirakova, M. Kocian, T. Komarek, K. Korcyl, J. Lange, D. Mandat, V. Michalek, I.L. Paz, D. Northacker, M. Rijssenbeek, L. Seabra, P. Schovanek, R. Staszewski, P. Swierska, T. Sykora, Construction of the optical part of a time-of-flight detector prototype for the AFP detector, Opt. Express 24 (24) (2016) 27951–27960, http://dx.doi.org/10.1364/OE.24.027951, URL http://www.opticsexpress.org/abstract.cfm?URI=oe-24-24-27951.

---

[5] XP85112/A1-URD, the candidate we will be exploring, features MCP treated with a modified ALD process sequence and is expected not to suffer from the extremely slow recovery. We also aim at a lower MCP R. This type has however not been previously produced in the miniPlanacon form factor.

[8] L. Chytka, G. Avoni, A. Brandt, E. Cavallaro, P.M. Davis, F. Förster, M. Hrabovsky, Y. Huang, K. Jirakova, M. Kocian, T. Komarek, K. Korcyl, J. Lange, V. Michalek, L. Nozka, I.L. Paz, M. Rijssenbeek, P. Schovanek, T. Sykora, V. Urbasek, Timing resolution studies of the optical part of the AFP Time-of-flight detector, Opt. Express 26 (7) (2018) 8028–8039, http://dx.doi.org/10.1364/OE.26.008028, URL http://www.opticsexpress.org/abstract.cfm?URI=oe-26-7-8028.

[9] PHOTONIS USA Pennsylvania, Inc., miniPLANACON XPM85212 datasheet.

[10] A. Lehmann, M. Böhm, W. Eyrich, D. Miehling, M. Pfaffinger, S. Stelter, F. Uhlig, A. Ali, A. Belias, R. Dzhygadlo, A. Gerhardt, K. Götzen, G. Kalicy, M. Krebs, D. Lehmann, F. Nerling, M. Patsyuk, K. Peters, G. Schepers, L. Schmitt, C. Schwarz, J. Schwiening, M. Traxler, M. Düren, E. Etzelmüller, K. Föhl, A. Hayrapetyan, K. Kreutzfeld, O. Merle, J. Rieke, M. Schmidt, T. Wasem, P. Achenbach, M. Cardinali, M. Hoek, W. Lauth, S. Schlimme, C. Sfienti, M. Thiel, Lifetime of MCP-PMTs and other performance features, J. Instrum. 13 (02) (2018) C02010, http://dx.doi.org/10.1088/1748-0221/13/02/c02010, URL https://doi.org/10.1088/1748-0221/13/02/c02010.

[11] J.L. Wiza, Microchannel plate detectors, Nucl. Instrum. Methods 162 (1) (1979) 587–601, http://dx.doi.org/10.1016/0029-554X(79)90734-1, URL http://www.sciencedirect.com/science/article/pii/0029554X79907341.

[12] W. Feller, Conductively cooled microchannel plates, Nucl. Instrum. Methods Phys. Res. A 310 (1) (1991) 249–250, http://dx.doi.org/10.1016/0168-9002(91)91037-V, URL http://www.sciencedirect.com/science/article/pii/016890029191037V.

[13] A. Tremsin, J. Pearson, G. Fraser, W. Feller, P. White, Microchannel plate operation at high count rates: new results, Nucl. Instrum. Methods Phys. Res. A 379 (1) (1996) 139–151, http://dx.doi.org/10.1016/0168-9002(96)00482-2, URL http://www.sciencedirect.com/science/article/pii/0168900296004822.

[14] A.G. Brandt, Development of a 10 Picosecond Time-Of-Flight Counter, Tech. Rep, The University of Texas at Arlington, 2010, URL https://digital.library.unt.edu/ark:/67531/metadc929506.

[15] Y. Melikyan, T. Sýkora, T. Komárek, L. Nožka, D. Serebryakov, V. Urbášek, Load capacity and recovery behaviour of ALD-coated MCP-PMTs, Nucl. Instrum. Methods Phys. Res. A 949 (2020) 162854, http://dx.doi.org/10.1016/j.nima.2019.162854, URL http://www.sciencedirect.com/science/article/pii/S0168900219312811.

Research Article Vol. 28, No. 13 / 22 June 2020 / Optics Express 19783

Optics EXPRESS

Performance studies of new optics for the time-of-flight detector of the AFP project

Libor Nozka,[1,*] Andrew Brandt,[2] Karel Cerny,[1] Miroslav Hrabovsky,[1] Tomas Komarek,[1] Filip Krizek,[3] Dusan Mandat,[4] Marko Milovanovic,[5] Michael Rijssenbeek,[6] Petr Schovanek,[4] Tomas Sykora,[7] Vladimir Urbasek,[4] and Jaromir Zatloukal[4]

[1] *Regional Centre of Advanced Technologies and Materials, Joint Laboratory of Optics of Palacky University and Institute of Physics AS CR, Faculty of Science, Palacky University, 17. listopadu 12, 771 46 Olomouc, Czech Republic*
[2] *The University of Texas at Arlington, Department of Physics, Box 19059, Arlington, TX 76019, USA*
[3] *Nuclear Physics Institute of the Czech Academy of Sciences, Husinec - Rez 130, 250 68 Rez, Czech Republic*
[4] *Institute of Physics of the Academy of Sciences of the Czech Republic, Na Slovance 2, Prague, Czech Republic*
[5] *DESY, Platanenallee 6 D-15738 Zeuthen, Germany*
[6] *Stony Brook University, Dept. of Physics and Astronomy, Nicolls Road, Stony Brook, NY 11794-3800, USA*
[7] *Charles University, Faculty of Mathematics and Physics, Institute of Particle and Nuclear Physics, V Holesovickach 2, CZ - 18000 Praha 8, Czech Republic*
[*] *libor.nozka@upol.cz*

Abstract: We present the results of performance studies of the upgraded optical part of the time-of-flight subdetector prototype for the AFP (ATLAS Forward Proton) detector obtained during the test campaign in a synchrotron test-beam facility with 5 GeV electrons at the DESY laboratory (Hamburg, Germany) in June 2019. The detection of the particle arrival time is based on generation of Cherenkov light in an L-shaped fused silica bar. In the previous version of the ToF, all bars were made of two pieces (radiator and light guide) glued together with a dedicated glue (Epotek 305). This solution suffers from additional radiation damage of glue. We adopted a new technique of bar production without the need of glue. The new bars have a higher optical throughput by a factor of 1.6, reduced fragility, and better geometrical precision.

© 2020 Optical Society of America under the terms of the OSA Open Access Publishing Agreement

1. Introduction

The design and the physics motivation for the need of time-of-flight (ToF) subdetector of the AFP project itself was already described thoroughly in our previous papers: the physics concept in [1,2], simulation benchmark studies [3], details of the optics in [4], and timing studies in [4,5]. The detection of the particle arrival time is based on generation of Cherenkov light in an L-shaped fused silica bar. For clarity, the geometry of the ToF detector is depicted in Fig. 1 together with its detailed view. The ToF assemblage consists of a 4×4 matrix of L-shaped bars made of fused silica (SK-1300 by O'Hara). Each bar serves both as a Cherenkov radiator and a light guide towards a fast multichannel-plate photomultiplier (MCP-PMT) device (the sensor plane in Fig. 1). The rows of four bars along the beam direction are called trains and are labeled with a number. The bars in each train are labeled with letters A, B, C, and D along the direction of the incoming particles. In this way, the bars in the Train 1 are labeled 1A, 1B, 1C, and 1D and so on for the other trains.

The L-shape design largely relies on a direct fast light propagation to the sensor (approximately 60% of all photon tracks in a bar accepted by the sensor). This means a bar has to be rotated

#394582 https://doi.org/10.1364/OE.394582
Journal © 2020 Received 8 Apr 2020; revised 12 Jun 2020; accepted 14 Jun 2020; published 19 Jun 2020

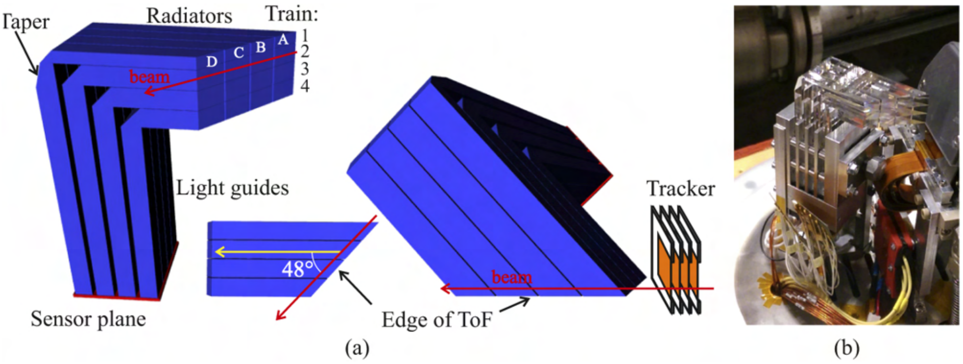

Fig. 1. (a) Geometry of the ToF subdetector, (b) a detailed view of installed ToF bars (reprint from [5]).

so that its radiator is tilted by the Cherenkov angle of 48 degrees with respect to the beam axis, Fig. 1(a). In addition, direct pathways need to be reflected on the bar elbow which means a 45 degrees cut coated with an appropriate reflection layer. The part of the light propagated using total reflections is delayed with respect to the fast direct propagation. The aforementioned studies [3] proposed a so-called taper to speed-up total-reflection pathways. On the other hand, adding a taper results in a correspondingly thinner radiator of a lower acceptance, see Fig. 1(a), Train 1. Moreover, a radiator cut is another design improvement allowing higher signal due to the additional back reflection of light with details described in [3]. Geometry of each bar is designed so that the cut planes of all bar radiators form an edge plane of the ToF detector, Fig. 1(a). Dimensions of the bars used in presented studies are summarized in Table 1 at the end of this section. Dimensions of all bars can be found in [4]. The passage length of beam particles through a radiator is 8.1 mm given by its thickness (6 mm) and tilt (48 degrees) with respect to the beam axis. The acceptance area of the AFP detector is 16.8×20.0 mm^2, given by dimensions of a tracker module in front [6] and its tilt as illustrated in Fig. 1(a).

Table 1. Dimensions of bars in Train 2. The bar elbow with the 45 degrees cut is part of the radiator.

	Radiator			Light guide		
Bar	Height [mm]	Thickness [mm]	Length [mm]	Width [mm]	Thickness [mm]	Length [mm]
2A	5	6	59.2	5	6	65.2
2B	5	6	53.5	5	6	65.2
2C	5	6	47.9	5	6	65.2
2D	5	6	42.3	5	6	65.2

The ToF detector was installed as a part of the AFP detectors in the forward region of the ATLAS detector on the Large Hardon Collider (LHC) in March of 2017. It was inserted into a movable Roman Pot together with the tracker [7] at about 220 m on both sides downstream the two beamlines. The working position was 1.5 mm from the beam centre. It ran till the end of 2017 in the LHC environment. The optics (and to a lesser extent the electronics) of the detector was exposed to high radiation at the level of 700 kGy at a distance of 5 mm from the beam centre. The bars themselves occupied a space in the region from 1.5 mm to 74.8 mm from the beam axis. There is a large gradient in the radiation level about 15 kGy/mm [7], as well as a specific shape of the illumination of the detector. This resulted in the development of activated hot spots in the bars as measured after their removal from the LHC tunnel.

We had tested the radiation hardness of the used fused silica glass SK-1300 and the glue Epotek 305 by means of a proton beam (30 MeV) generated in the cyclotron facility in Nuclear Physics Institute of the Czech Academy of Sciences in Rez near Prague (Czech Republic) [8]. We used circular samples (with outer diameter of 20 mm, and 2 mm thickness), some of them glued together with the Epotek 305 for the glue tests. The radiation effects were measured as a decrease of transmittance of the samples due to degradation of fused silica and of glue. The spectral region was in the interval from 115 nm to 350 nm set by the vacuum spectrometer used (the region of our interest was from 200 to 400 nm [3]). Figure 2(a) summarizes results relevant for this work. We applied radiation doses according to predicted levels in the LHC [3] (the *neq* stands for a neutron equivalent dose of the energy of 1 MeV): 700 kGy ($neq = 3 \cdot 10^{15} cm^{-2}$) for pure glass samples, 20 kGy ($neq = 9 \cdot 10^{13} cm^{-2}$) for the samples with the glue (the glue junction was at least 50 mm far from the beam center in the installation in the LHC).

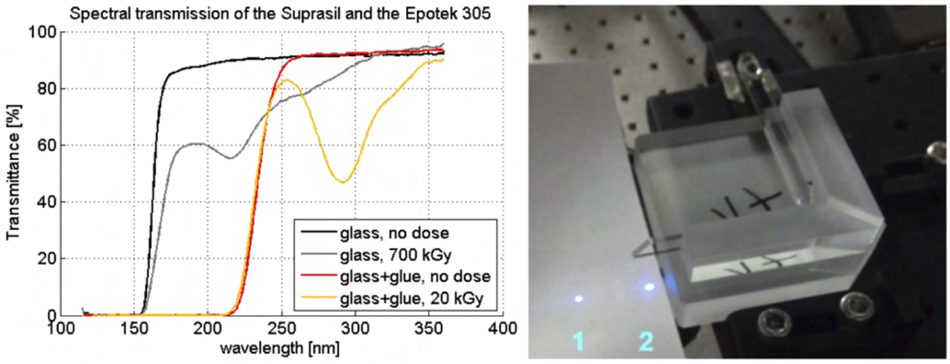

(a) (b)

Fig. 2. (a) Transmission spectra of the SK-1300 and Epotek 305 before and after radiation (including Fresnell losses), (b) splitting of a laser beam observed during transmittance measurements of irradiated bars.

The glass material of the bars was found to be sufficiently radiation hard. The transmittance of the glass stays above 50% within the wavelength range of 200–400 nm up to 700 kGy of irradiation dose. A significant decrease of transmittance due to irradiation occurs for wavelengths below 200 nm where the quantum efficiency of the photomultipliers is unknown but is expected not to be negligible. The glue itself deteriorates due to radiation in the order of tens of kGy and exhibits a transmittance drop around a wavelength of 292 nm, see Fig. 2(a). Thus, even while the bar material is sufficiently radiation hard, the glue reduces the radiation hardness of the full bars. This resulted in a steady decrease of their optical throughput during the operation in the LHC.

We measured the total decrease of transmittance of one of the irradiated bars (with the label 1D) after the operation in the LHC. The transmittance was measured by means of a laser beam of 280 nm wavelength (accidentally close to the transmittance drop of the glue). The measurement aimed to compare the signal power of the light beam passing the irradiated bar with one of non-irradiated bars of the same geometry. The observed decrease of transmittance was 38% ± 2% due to radiation at that wavelength. Moreover, during the measurement we noticed that the laser beam split at the glue layer as seen in Fig. 2(b). In the figure, the ordinary (expected) beam spot is labeled 2 and the parasitic spot is labelled 1. The intensity of the parasitic light beam was 40% of the signal level of the ordinary light beam.

The deterioration of the optical performance of the ToF detector due to permanent radiation damage contributed to the decline of its efficiency during operation. The efficiency is directly proportional to the average signal-to-noise ratio of the detector which in turn depends on the gain of the photomultiplier. The gain is determined by the high voltage applied. However, the gain of photomultipliers for a constant high voltage decreases with higher rates of incoming light pulses [9,10]. This is critical for applications at the LHC which operates at the frequency of 40 MHz.

The development of L-shaped bars without a need of glue junction was highly desirable to improve the ToF timing performance and efficiency (including radiation hardness). The production of solid one-piece L-shaped bars was not trivial. The technique was chosen such that the skeleton of the whole train (four bars) was produced in one step considering a designed spacing of 0.4 mm between the bars in the installation. This allowed for precise alignment of adjacent surfaces of the bars, mainly at the edge of the ToF, see Fig. 1(a). Thus, the misalignment of the radiator arms (which was present in the case of glued L-bars) was removed. Then bars were polished individually. Train no. 2 of four solid (glueless) bars was produced for the June 2019 measurements at DESY in Hamburg. Their dimensions are summarized in Table 1.

In the following sections, we present results of the comparative measurement of the previously designed bars with the glue junction. Simulations were done to estimate the increase of number of photoelectrons compared to glued bars. We also needed to understand possible differences due to electron beam at the DESY test beam facility compared to the SPS (the Super Proton Synchrontron) beam at CERN we had used previously [5] (the SPS facility was closed during 2019). These studies are presented first.

2. Preparatory simulation studies

We focused on two tasks: (1) to perform studies of the effect of secondaries produced in the bars by the primary electron beam with energy of 5 GeV, (2) to assess the yield of photoelectrons given by solid bars compared to that of glued bars. The effect of secondaries is negligible in the case of the SPS beam at CERN (π^+ 120 GeV) as well as of the LHC beam (from this point of view the measurements with the SPS beam suited our needs better). Simulations of primary beam interactions with the whole Train 2 model were performed in the Geant4 framework [11]. The model contained the geometry of bars (Table 1), a model of the photomultiplier with its quantum efficiency [3] and a model of the stainless-steel entry window of the Roman pot which is 300 μm thick [7]. The beam goes into the Roman pot through this window. It is a thinned part of the Roman pot body. In the simulation, the photodetection efficiency (PDE) of the photomultiplier model was extrapolated down to 160 nm as a constant function of the wavelength with the value of 16% taken from the lowest known value at the wavelength of 200 nm.

Geant4 simulated the production of secondary electrons, positrons, and gamma photons induced by the primary electrons of the DESY beam passing the bars of the ToF detector. The gamma particles then partly convert to other electron-positron pairs. The electrons and positrons with kinetic energy above the threshold of 0.160 MeV generate additional Cherenkov photons. A negligible number of secondary positrons is generated in the case of the SPS beam. In total, according to the simulation, the DESY beam generates more secondary particles by a factor of 2.25 in the ToF detector than the SPS beam (only those secondary particles producing Cherenkov photons are counted here).

In the case showers are induced by the primary particles, the amount of secondary particles increases as the shower develops. As a result, the number of photoelectrons steadily increases from bar 2A to bar 2D. The comparison of the number of photoelectrons generated in the solid and glued bars 2A and 2D in full train is shown in Fig. 3 for the case of incident electron beam. Histograms were generated for 1000 events. In the case of bar 2A, the primary particles (the beam particles) generated 33 ± 6 photoelectrons, and secondary particles contributed with 7^{+10}_{-7} photoelectrons (there are large fluctuations). The total number of photoelectrons was 36 ± 9 (the filled histogram). In the case of bar 2D, we found 37 ± 6 photoelectrons by primary particles, and 23^{+30}_{-23} by secondaries, and 47 ± 21 photoelectrons in total. The number of photoelectrons given by secondary particles fluctuates strongly. This is due to relatively long interaction length of relativistic electrons in fused silica for production of secondary gammas, electrons, and positrons (excluding Cherenkov photons) where the secondary electrons and positrons are generated by the conversion of secondary bremsstrahlung gammas.

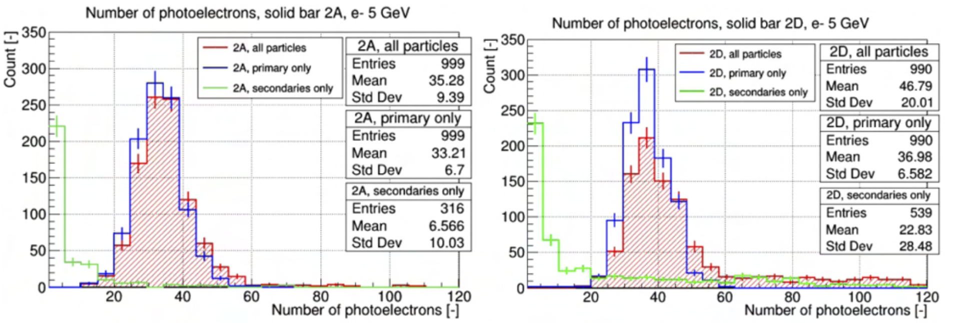

(a) (b)

Fig. 3. Simulated distribution of photoelectrons generated in the pixel of (a) the solid bar 2A, (b) the solid bar 2D for the 5 GeV e^- beam. Histograms were generated for 1000 events and full train installation.

In the case of the SPS beam, the influence of secondary particles is partly suppressed as the interaction length of relativistic pions in fused silica is even longer than for DESY electrons. Furthermore, the production of bremsstrahlung gammas is negligible compared to electron beams, and pions at 120 GeV have zero bremsstrahlung. Quantitatively, in the case of the bar 2A, the primary particles generated 34 ± 6 photoelectrons, secondary particles contribute with 5^{+6}_{-5} photoelectrons. The total number of photoelectrons is 35 ± 8. This is the same as for the bar 2A in the DESY beam. In the case of the bar 2D, we found 38 ± 6 photoelectrons by primary particles, 6^{+9}_{-6} by secondaries, and 40 ± 9 photoelectrons in total. Thus, the contribution by secondaries is almost the same across the whole train.

Concerning the yield of photoelectrons given by solid bars with respect to that of glued bars, we took the simulation with the DESY beam including contribution of secondaries. In this study we accounted for the spectral cut of the glue, see Fig. 2(a) (red curve). The result of this comparison study is shown in Fig. 4. It presents the simulated distributions of the total

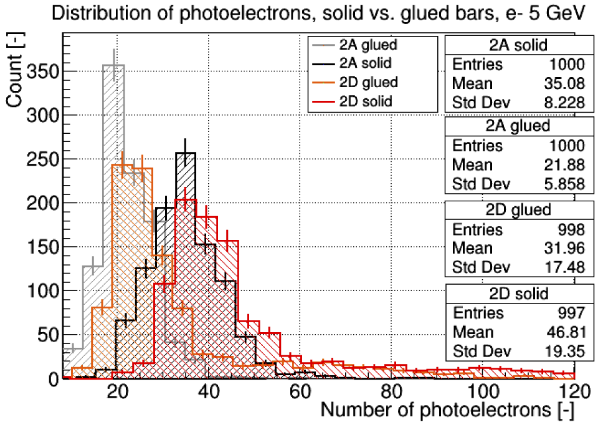

Fig. 4. Distributions of number of photoelectrons of selected solid and glued bars for the 5 GeV e^- beam. Histograms were generated for 1000 events and full train installation.

number of photoelectrons generated in the pixels occupied by the bars 2A and 2D in the full train scenario. Comparing the mean values relevant to all particles, we can derive an improvement in the number of photoelectrons. The bar 2A improved by a factor of 1.6. This stands for all single bars including a single 2D bar (we did comparisons for all single bars, we excluded corresponding histograms for brevity). In the case of bar 2D in the full train installation, the improvement factor dropped to 1.5 (partly due to a relatively smaller increase of contribution by secondaries by a factor of 1.3, and partly due to a higher attenuation of those deep UV photons coming from upstream bars).

Note that the presented ToF model lacks a model of the photomultiplier response. In reality, there is an extra electronic crosstalk between pixels which additionally strengthen the signal in each of them in the case of full train installation [5].

3. Experimental setup

The experimental measurements were done on the T22 beamline of the DESY II synchrotron [12] in the last week of June 2019. The synchrotron facility provided an electron beam which was set to an energy of 5 GeV. The experimental setup was similar to the one used in previous measurements [4,5]. The only change was to use the Roman pot instead of the auxiliary duralumin dark box. The scheme of the measurement setup is shown in Fig. 5 together with a picture.

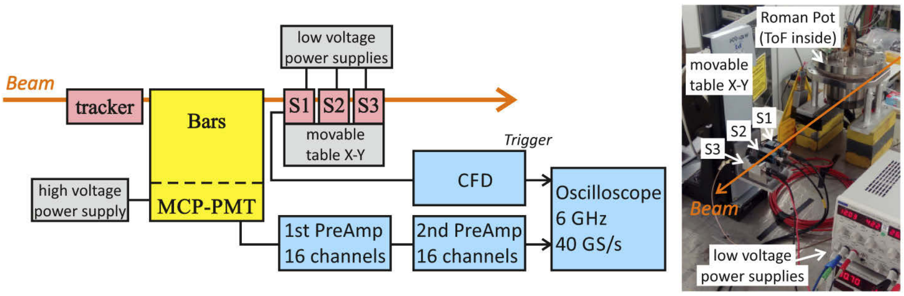

(a) (b)

Fig. 5. (a) Scheme of the experimental setup, (b) picture of the installation in DESY.

We used the MCP photomultiplier Photonis XPM85112/A1-S (SN 9002091) with 4 × 4 pixelization, and a sapphire entrance window, and a reduced anode gap. Its MCP (multichannel plate) resistance was 16 MΩ, a gain of 10^5 at an overall high voltage of 2190 V, and a gain 10^6 at 2525 V. Train 2 with the full complement of 4 bars (solid or glued) was installed on top of the photomultiplier aligned to its pixelization [5]. The output signal from each pixel (channel) was amplified by two stages of voltage preamplifiers (each with a gain of 10) and collected by means of a fast LeCroy WaveMaster 806Zi-B oscilloscope (bandwidth 6 GHz, sampling 40 GS/s). The oscilloscope was triggered by the signal from one of three detectors S1, S2, and S3 downstream of the beam. Each trigger detector consisted of a 15 mm long fused silica bar of 3×3 mm^2 cross-section coupled to a silicon photomultiplier (SiPM) manufactured by ST Microelectronics (S1, S2, type: NRD09_1 with 3.5×3.5 mm^2 and 58 μm cell size) [13] or by SensL (S3) [14] that detected Cherenkov radiation. They were placed on a two-axis movable stage (remotely controlled) to select a specific area of the ToF detector for study. We mostly used the first detector S1 (the closest to the ToF) as a trigger. The others were used for the measurement of their mutual resolution and, in turn, the resolution of the S1. The signal from the S1 detector was preprocessed by a CFD unit (Constant Fraction Discriminator) to minimize its time-walk (with a threshold value of -400 mV).

Optics EXPRESS

4. Measurements and results

During all measurements, we positioned the trigger to have its coincidence with the following ToF areas in the beam: 0 mm from the edge (the edge position, see Fig. 1(a)), 5 mm, and 9 mm from the edge. First, we measured the timing resolution of the trigger (S1) by means of a comparative timing resolution measurement among all SiPM detectors. The timing resolution of the trigger S1 detector was found to be 13 ± 1 ps. Then we measured single bars and the whole train of the glued and the solid bars for different gains of the photomultiplier. The gain was set by varying levels of the applied high voltage.

4.1. *Signal strength*

Figure 6 shows the signal strength (amplitude) of single bars for both the solid (the rich colors) and the glued (the pale colors) versions measured at a distance of 5 mm from the edge of the bars. The bars were measured at high voltages of 2050 V, 2100 V, 2150 V, and 2200 V. The signal strength of the glued bars at 2050 V was poor and is not plotted. Similarly, solid bars produced too saturating signal pulses at 2200 V, so we decided to omit this measurement. Each distribution is described by a box defining the interval from the 25% (Q1) to 75% (Q2) quantiles of the amplitude distribution with a level mark inside indicating the median value (50% quantile). The dashed line with endings defines the interval from the minimum value to the maximum value of the distribution excluding outliers (red points in the tail). The lower outliers are the values lower than Q1-1.5*(Q2-Q1). The results exhibit large fluctuations which is a characteristic for the ToF detector and due to low level of the input Cherenkov signal [4]. Concerning the median values, we required an optimum level of -300 mV for a good separation of the signal from the pedestal for the given amplification. The pedestal was a white noise produced by a PMT anode resistor (50 Ω), dark counts of the PMT, and both preamplifier stages. The pedestal cut itself was -150 mV. Similar results from measurements at the edge and at a distance of 9 mm from the edge are not presented here for the sake of brevity but they are mentioned in text.

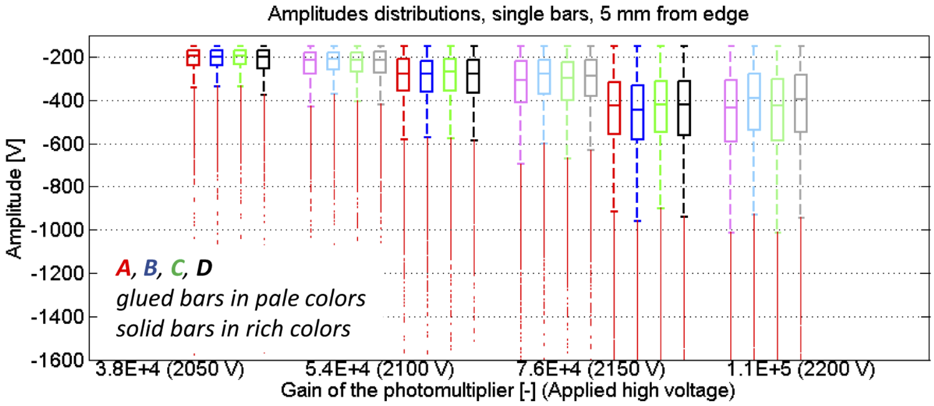

Fig. 6. Signal strength of single bars measured at a distance of 5 mm from the edge of the ToF for various gains of the photomultiplier.

At the distance of 5 mm from the edge, the setup with solid bars reached the optimum level at a gain of $7.6 \cdot 10^4$ (corresponding HV=2150 V) and the one with glued bars at a gain of $1.1 \cdot 10^5$ (2200 V). At the edge, the values of the gain were $5.4 \cdot 10^4$ (2100 V) and $7.6 \cdot 10^4$ (2150 V) for the solid bars and glued bars respectively. As for the 9 mm case, the optimal gain values were almost the same as for the case of 5 mm from the ToF edge. The main conclusion of these results is that single solid bars produced a signal higher by a factor of 1.6–1.8 compared to the glued bars for the same PMT gain. Further interpretation is done in the Discussion section below.

The situation changed with the bars installed in the full train as seen in Fig. 7. Due to light leakage from the upstream bars, the downstream bars profit from the photon enrichment and consequently register higher number of photons by a factor up to 1.4 [4]. Besides, any secondaries produced further increase the signal level of downstream bars as mentioned earlier. As a result, the light in the downstream bars is always augmented. The first bar (A) is the only one having a signal strength the same as in the single bar scenario (excluding the effect of the electronic crosstalk from the adjacent bar 2B). Note a weaker signal amplitude of the 2D bar compared to the one of the 2C bar. We presume this is due to lower signal contribution from adjacent pixels (charge sharing between pixels) - the 2D-bar pixel has only one adjacent pixel within the train. However, this effect was not studied in more detail (the leakage effect between pixels was addressed in [5], Fig. 5).

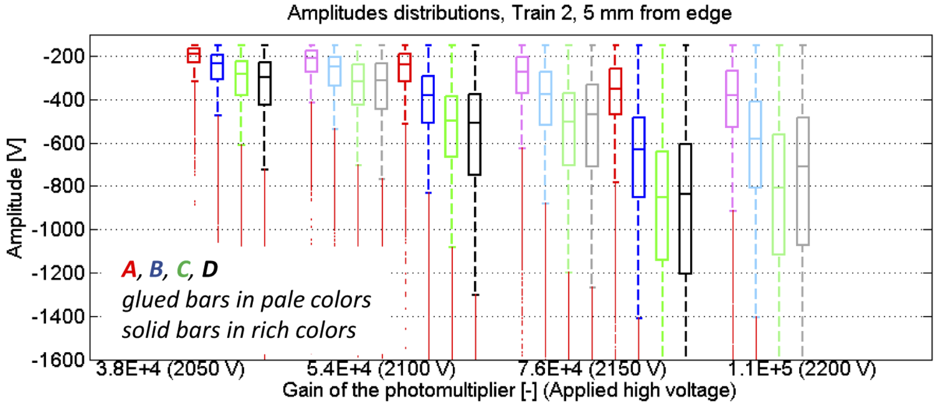

Fig. 7. Signal strength of bars installed in the train measured at a distance of 5 mm from the edge of the ToF for various gains of the photomultiplier.

The signal strength of the train is closely related to the efficiency of the train which is an important performance characteristic. We directly measured the efficiency with respect to the SiPM trigger during the measurement campaign. We evaluated the train efficiency for the cases (called majority trigger cases) in which either all four bars ('=4'), at least three bars ('>=3'), at least two bars ('>=2'), or at least one bar ('>=1') generated a valid signal with the amplitude larger than the signal-to-pedestal threshold of -150 mV. The '=4' case and the '>=3' case were of the main interest (due to better train resolution, see below). The results are summarized in Table 2. The values obtained at the preferred gains are highlighted. The efficiency of the '=4' case is affected by a lower signal strength of the bar 2A with respect to other bars in the train (there is no enrichment by photons from upstream bars). As the signal level of the solid bar 2A is much higher (by a factor of 1.6, as seen above), the solid train has significantly higher efficiency as compared to its glued counterpart for the '=4' case. See the Discussion section below for further discussion of this result.

4.2. Timing resolution

Concerning the timing resolution, we measured the resolution of single bars and that of full trains. The measurements of the timing resolution of the bars and the whole trains were performed with respect to the first SiPM detector acting as a trigger. We preprocessed the output signal by the CFD module. The timestamp of leading edge was treated as the arrival time of a signal pulse. The arrival time of a signal pulse from a PMT pixel was determined relative to the arrival time of

Table 2. Efficiency of the ToF measured with respect to the SiPM trigger for the amplitude threshold of -150 mV at the distance of 5 mm from the edge.

		Glued bars				Solid bars			
		Number of bars with detectable signal				Number of bars with detectable signal			
HV [V]	Gain [-]	=4	>=3	>=2	>=1	=4	>=3	>=2	>=1
2050	$3.8 \cdot 10^4$	-	-	-	-	20%	68%	90%	94%
2100	$5.4 \cdot 10^4$	28%	68%	89%	94%	**67%**	**91%**	**93%**	**95%**
2150	$7.6 \cdot 10^4$	**66%**	**90%**	**93%**	**95%**	89%	93%	94%	95%
2200	$1.1 \cdot 10^5$	86%	93%	94%	96%	-	-	-	-

the trigger (the time difference). In the following, we express the timing resolution by the sigma parameter of the Gaussian fit of the timestamp distributions [5].

Results are summarized in Table 3 (with uncertainty of ±2 ps) for single bars at the distance of 5 mm from the edge. Here, the values of measured timing resolutions stand for the bars after subtraction of the trigger contribution of 13 ± 1 ps. The values obtained for the proposed gains are highlighted. Data were filtered out with the signal amplitude larger than the threshold -150 mV. Note that the timing resolution of the photomultiplier pixels varies, and this variation notably contributes to the results. Concerning the other distances from the edge, the timing resolutions at the edge were better by 5 ± 2 ps on average and the ones at the 9 mm distance from the edge were slightly better by 1 ps on average with respect to the 5 mm distance case.

Table 3. Timing resolution of single bars in [ps] (uncertainty ±2 ps) for the amplitude threshold of -150 mV at a distance of 5 mm from the edge.

Bar	Glued bars			Solid bars		
	Gain $5.4 \cdot 10^4$ (HV 2100 V)	Gain $7.6 \cdot 10^4$ (HV 2150 V)	Gain $1.1 \cdot 10^5$ (HV 2200 V)	Gain $3.8 \cdot 10^4$ (HV 2050 V)	Gain $5.4 \cdot 10^4$ (HV 2100 V)	Gain $7.6 \cdot 10^4$ (HV 2150 V)
2A	40	**39**	35	49	**46**	42
2B	40	**38**	36	47	**43**	40
2C	39	**36**	32	45	**43**	40
2D	38	**36**	34	44	**41**	38

For the same gain of the photomultiplier, the solid bars gave worse resolution by 3 ± 2 ps on average (for all scanned distances from the edge). However, the difference grew to 6 ± 2 ps comparing the timing resolutions for the optimal gains, i.e. $7.6 \cdot 10^4$ for glued bars and $5.4 \cdot 10^4$ for solid bars. This additional worsening of the timing resolution was due to lower gain of the photomultiplier in the case of the solid bars. Nevertheless, the worse resolution of the solid bars for the same gain was a surprising finding in the light of the significant improvement in the light throughput resulting in a higher number of photoelectrons in the photomultiplier.

The timing resolution of the whole Train 2 was measured with all bars of the train installed on the photomultiplier. It was calculated from a distribution of arithmetic averages of timestamps given by individual bars in the train which produced a valid signal (they were triggering). For the case of all four bars triggered ('=4'), the train resolution is theoretically expected to be ½ of the timing resolution of a single bar in the train provided all four bars have the same resolution and no correlation exists between them. In practice, however, the correlation of timestamps among the bars is non-negligible due to electronic crosstalk (the optical crosstalk has no effect here as discussed in [5]). This results in a worsening of the timing resolution of the train. The timing resolution of a train depends on the number of triggering bars. Fewer triggering bars leads to a worse resolution. The timing resolutions given by our measurements are summarized in Table 4 (with uncertainty of ±2 ps) for all assumed majority trigger cases measured at the 5 mm distance of from the edge. The resolution contribution 13 ps from the SiPM trigger was subtracted. The highlighted values stand for the preferred gain levels of the PMT as were mentioned before.

Table 4. Timing resolution of Train 2 in [ps] (uncertainty ±2 ps) for different majority trigger cases (the amplitude threshold of -150 mV, at the distance of 5 mm from the edge).

	Glued bars			Solid bars		
Case	Gain $5.4 \cdot 10^4$ (HV 2100 V)	Gain $7.6 \cdot 10^4$ (HV 2150 V)	Gain $1.1 \cdot 10^5$ (HV 2200 V)	Gain $3.8 \cdot 10^4$ (HV 2050 V)	Gain $5.4 \cdot 10^4$ (HV 2100 V)	Gain $7.6 \cdot 10^4$ (HV 2150 V)
>=1	30	**28**	30	30	**28**	30
>=2	27	**28**	28	29	**28**	29
>=3	27	**27**	27	27	**28**	27
=4	26	**28**	28	27	**27**	28

At the first sight, the timing resolution of both trains were worse by about 10 ps with respect to the output from measurements on the SPS beam [4,5]. This issue is caused by the beam itself. Nevertheless, the timing resolution was the same for both the glued and the solid trains, regardless of the applied majority trigger. There is also no distinction between the majority trigger cases although the train resolution deteriorates with a lower number of triggering bars. This is due to high relative occurrence of cases with three and four bars involved in the arrival time measurement. This is indicated in Table 5 where results for individual number of triggering bars are plotted (exactly a one bar triggered etc.) together with their relative occurrence in the dataset. They are labeled as the 'equal' cases. At the first sight, the '=1' and '=2' cases are almost suppressed. Note the worse timing resolution values for the '=1' case with respect to the values for single bars in Table 3. This is assumed to be due to the electronic crosstalk from the other channels (even when they did not pass the trigger threshold) which affect the clarity of the signal (there is no electronic crosstalk in the single bar case). See the next section for further discussion of the results.

Table 5. Timing resolution of the Train 2 in [ps] for different 'equal' cases of triggering bars (the amplitude threshold of -150 mV, at the distance of 5 mm from the edge) together with their relative occurrence in measured data.

	Glued bars						Solid bars					
	Gain $5.4 \cdot 10^4$ (HV 2100 V)		Gain $7.6 \cdot 10^4$ (HV 2150 V)		Gain $1.1 \cdot 10^5$ (HV 2200 V)		Gain $3.8 \cdot 10^4$ (HV 2050 V)		Gain $5.4 \cdot 10^4$ (HV 2100 V)		Gain $7.6 \cdot 10^4$ (HV 2150 V)	
Case	σ [ps]	occ.	σ [ps]	occ.	σ [ps]	occ.	σ [ps]	occ.	σ [ps]	occ.	σ [ps]	occ.
=1	54 ± 5	5%	44 ± 5	2%	38 ± 5	2%	53 ± 5	4%	44 ± 5	1%	45 ± 5	1%
=2	30 ± 2	21%	29 ± 2	4%	27 ± 5	2%	32 ± 5	21%	27 ± 5	2%	41 ± 5	1%
=3	26 ± 2	41%	25 ± 2	24%	25 ± 2	7%	26 ± 2	48%	26 ± 2	24%	24 ± 5	4%
=4	26 ± 2	28%	28 ± 2	66%	28 ± 2	86%	27 ± 2	20%	27 ± 2	67%	28 ± 2	89%

5. Discussion

The main message from these measurements is the improvement by a factor of at least 1.6 of the signals produced with the single solid bars compared to their glued counterparts. This is in good agreement with simulations (Fig. 4, bar 2A) which predicted the wavelength cut of the glue at 235 nm removes more than one third of the useful Cherenkov light. However, the simulation underestimated the amplitude improvement of the 2D bar in the full train (a factor of 1.5 in simulation). We assume this is due to the fact our model does not comprise additional interaction between bar channels at the photomultiplier level (namely charge sharing) and the response of the photomultiplier overall. In the simulation, the photodetection efficiency (PDE) of the photomultiplier model was extrapolated down to 160 nm as a constant function of the wavelength with the value of 16% taken from the lowest known value at the wavelength of 200 nm. The good agreement between data and the simulation proved that the PDE of the used photomultiplier is significant below 200 nm despite being unknown in the deep UV region.

For proper operation, a good separation of the signal from the pedestal is required. In the setup, a threshold of -150 mV was the optimum value. The required mean signal amplitude is then -300 mV or bigger. The corresponding optimum gain for the glued bars was $7.6 \cdot 10^4$, and $5.4 \cdot 10^4$ for the solid bars.

The rate of our beam test events at DESY (and at the SPS in the past) was of order of kHz, a rate that does not affect the performance of the photomultiplier. In such conditions, the efficiency of the ToF with the solid bars was substantially higher compared to the glued counterpart for the same gain, see Table 2. This is especially true for the '=4' trigger condition in which we require all bars in the train to produce a valid signal (surpassing the signal-to-pedestal threshold of -150 mV). However, if we reduce the gain from $7.6 \cdot 10^4$ to $5.4 \cdot 10^4$ for solid bars we end up with the same efficiency as for glued bars at a gain of $7.6 \cdot 10^4$ (keeping in mind we operate in a low-rate regime).

The timing resolution is the main performance characteristic of the ToF detector. Although the timing resolution of the train is the decisive parameter, we also focused on the timing performance of the single bars. According to the Table 3, the solid bars gave worse resolution by 3 ± 1 ps in average for the same gain. This was surprising. We expected a slightly better resolution due to higher number of photons on the photomultiplier photocathode despite the fact there is a saturation of the timing resolution of photomultipliers with the increasing number of photoelectrons as reported in [15]. We tried to explain this deterioration as the effect of the Cherenkov light dispersion. As the solid bars miss the glue layer, the wavelength range of accepted photons spreads down to 160 nm where the index of refraction of the fused silica (and of dielectrics in general) quickly rises. However, our simulation did not reveal any significant change of the time distribution of photons hit counts on the PMT photocathode. On the other hand, these distinctions disappeared when all bars were installed in the train and we studied the timing performance of the whole train. When a train average time is determined, the difference of 3 ps present in the timing resolution of single bars (solid vs. glued) is suppressed. Theoretically, the resolution of the train is half of the single bar resolution. Thus, the difference is 1.5 ps in case of the full train which is comparable with our uncertainty of measurement.

It is interesting that the train timing resolution did not change (within the uncertainty of ±2 ps) among the applied majority triggers. Thus the '>=1' case gave the same timing performance as the '>=3' or '=4' cases. The explanation is found in Table 5. The relative occurrence of the '=1' case (exactly only one of bars triggered) or the '=2' case was below 5%. Actually, most frequently all four bars triggered (66% or 67%), followed by the case in which at least three bars were triggering (24%). The best timing resolution was obtained for the case '=3'. The '=4' case suffered somewhat from the poorer timing performance of the first bar as no photon enrichment is present from the upstream bars. Adding a fake bar in front of the first bar would solve this issue. However, there is lack of space for such modifications. From these results we can deduce which of the majority trigger cases to use for the ToF operation based on the timing resolution and the efficiency. The selection criterion based on the '>=3' case is optimal.

It is known that the real gain of MCP photomultipliers decreases for high rates of incoming light pulses [9,16]. This is related to a growth of the average charge collected on the photomultiplier's anode and the speed of its drainage. This effect plays a critical role in the deployment of the ToF detector in the LHC collider with the 40 MHz bunch crossing rates. The expected frequency of pulses is 20 MHz per train for the forthcoming pile-up mode of the collider. Figure 8 plots rate characteristics of the used PMT for the gains of $5.4 \cdot 10^4$ and $7.6 \cdot 10^4$ and various output amplitudes at the low frequency of 10 kHz (the reference amplitudes). These measurements were performed on a picosecond laser at the wavelength of 402 nm, see [10] for details concerning the measurement setup. The whole PMT was uniformly illuminated and only the channel (pixel) 22 was measured (no Cherenkov bars were installed). Output signals were amplified with the same preamplifiers as used in the DESY beam tests. Measurements were performed in the range of 10 kHz to 50 MHz or less where the strip current exceeded the safe value of 500 μA (the black and purple curves, see below). For each scan, the relative amplitude was calculated as the ratio of the measured mean output amplitude to the one measured at 10 kHz, see Fig. 8(b). Note that the level of the noise does not depend on the pulse rates.

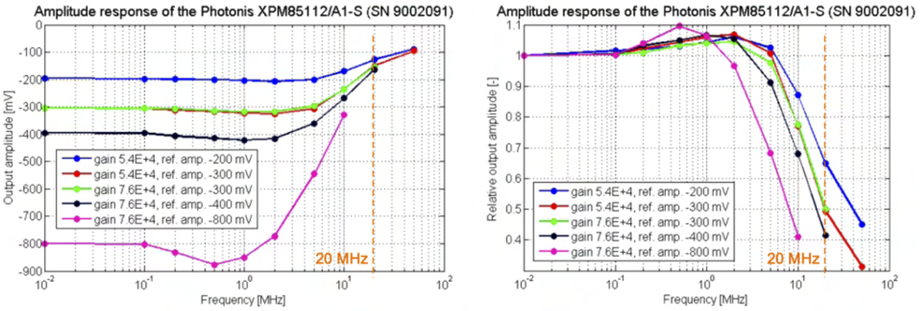

(a) (b)

Fig. 8. Results of the rate scans of the PMT Photonis XPM85112/A1-S (a) in terms of measured output amplitudes, (b) in terms of relative amplitudes with respect to the one at 10 kHz (the lowest frequency).

In Fig. 8, the configuration with gain $5.4 \cdot 10^4$ and reference amplitude -200 mV (blue curve) corresponds to a single glued bar, at that gain, from the DESY test (Fig. 6). It provided the lowest attenuation at increased input rate, likely due to the lowest generated charge on the MCP-PMT. Similarly, the configuration with gain $5.4 \cdot 10^4$ and reference amplitude -300 mV (red curve) corresponds to a single solid bar from the same test. The configuration with gain $7.6 \cdot 10^4$ and reference amplitude -300 mV (green curve) corresponds to a single glued bar at that gain. Both red and green configurations had similar rate characteristics as they produced the same charge in the multi-channel plate.

The configuration with gain $7.6 \cdot 10^4$ and reference amplitude -400 mV (black curve) corresponds to a single solid bar at that gain. The last configuration with gain $7.6 \cdot 10^4$ and reference amplitude -800 mV (purple curve) corresponds to the full installed train, at that gain, from the DESY test (Fig. 7). The last case had the worst rate performance due to relatively high level of charge generated on the PMT anode.

At the rate of 20 MHz, all configurations (except the purple one) provide similar amplitudes of approximately -150 mV. This is related to the fact that there is a limited charge available in the PMT for the electron multiplication in its MCP plates. However, this amplitude is also the level of the pedestal separation in our ToF setup. In other words, the efficiency of detection using ToF with the photomultiplier as used is very low at the expected operating rate of 20 MHz. One can overcome this issue by decreasing of the PMT gain by for example the factor of 5 and add an extra amplification stage to compensate and get back to the optimal level for the CFD operation. But the timing resolution deteriorates due to worse signal-to-noise ratio. As indicated in [10], the timing resolution then gets worse by a factor of 2-3. Then, an additional noise level reduction is required.

6. Conclusion

We designed and tested new type of optical bars of the ToF detector for the AFP project. To obtain the required L-shape, the bars were previously made by gluing together two separately produced arms of the bar. This resulted in a degradation of their optical throughput. Recently a new production technique was developed allowing for a production of a glueless (solid) version of the bars. We successfully tested these during the June 2019 campaign at DESY in a 5 GeV electron beam. The results presented here confirmed our expectations concerning the strength of the signal produced by the ToF detector and its measurement efficiency. However, the timing resolution remained unchanged because of limitations on the photomultiplier side. Theoretically, there is still a room for further improvements on the optical system (a fake front bar or radiator). On the other hand, the photomultiplier is the most limiting element due to its behavior in the regime of high rates of incoming relativistic particles.

Funding

Ministerstvo Školství, Mládeže a Tělovýchovy (LM2015056, LM2018104); European Regional Development Fund (CZ.02.1.01/0.0/0.0/16_013/0001403, CZ.02.1.01/0.0/0.0/16_019/0000754, CZ.02.1.01/0.0/0.0/17_049/0008422); Univerzita Palackého v Olomouci (IGA_Prf_2020_007).

Acknowledgments

The measurements leading to these results have been performed at the Test Beam Facility at DESY Hamburg (Germany), a member of the Helmholtz Association (HGF).

Disclosures

The authors declare no conflicts of interest.

References

1. A. B. Kaidalov, V. A. Khoze, A. D. Martin, and M. G. Ryskin, “Extending the study of the higgs sector at the lhc by proton tagging,” Eur. Phys. J. C **33**(2), 261–271 (2004).
2. FP420 Collaboration, “The FP420 R&D project: Higgs and New Physics with forward protons at the LHC,” Nucl. Instrum. Methods Phys. Res., Sect. A **4**(10), T10001 (2009).
3. L. Nozka, A. Brandt, M. Rijssenbeek, T. Sykora, T. Hoffman, J. Griffiths, J. Steffens, P. Hamal, L. Chytka, and M. Hrabovsky, “Design of cherenkov bars for the optical part of the time-of-flight detector in geant4,” Opt. Express **22**(23), 28984–28996 (2014).
4. L. Nozka, L. Adamczyk, G. Avoni, A. Brandt, P. Buglewicz, E. Cavallaro, G. Chiodini, L. Chytka, K. Ciesla, P. M. Davis, M. Dyndal, S. Grinstein, P. Hamal, M. Hrabovsky, K. Janas, K. Jirakova, M. Kocian, T. Komarek, K. Korcyl, J. Lange, D. Mandat, V. Michalek, I. L. Paz, D. Northacker, M. Rijssenbeek, L. Seabra, P. Schovanek, R. Staszewski, P. Swierska, and T. Sykora, “Construction of the optical part of a time-of-flight detector prototype for the AFP detector,” Opt. Express **24**(24), 27951–27960 (2016).
5. L. Chytka, G. Avoni, A. Brandt, E. Cavallaro, P. M. Davis, F. Foerster, M. Hrabovsky, Y. Huang, K. Jirakova, M. Kocian, T. Komarek, K. Korcyl, J. Lange, V. Michalek, L. Nozka, I. L. Paz, M. Rijssenbeek, P. Schovanek, T. Sykora, and V. Urbasek, “Timing resolution studies of the optical part of the AFP time-of-flight detector,” Opt. Express **26**(7), 8028–8039 (2018).
6. J. Lange, E. Cavallaro, S. Grinstein, and I. L. Paz, “3D silicon pixel detectors for the ATLAS Forward Physics experiment,” Nucl. Instrum. Methods Phys. Res., Sect. A **10**(03), C03031 (2015).
7. L. Adamczyk, E. Banas, A. Brandt, M. Bruschi, S. Grinstein, J. Lange, M. Rijssenbeek, P. Sicho, R. Staszewski, T. Sykora, M. Trzebinski, J. Chwastowski, and K. Korcyl, “Technical Design Report for the ATLAS Forward Proton Detector,” (2015) Technical Report CERN-LHCC-2015-009. ATLAS-TDR-024.
8. F. Krizek, J. Ferencei, T. Matlocha, J. Pospisil, P. Pribeli, V. Raskina, A. Isakov, J. Stursa, T. Vanat, and K. Vysoka, “Irradiation setup at the U-120M cyclotron facility,” Nucl. Instrum. Methods Phys. Res., Sect. A **894**, 87–95 (2018).
9. A. Tremsin, J. Pearson, G. Fraser, W. Feller, and P. White, “Microchannel plate operation at high count rates: new results,” Nucl. Instrum. Methods Phys. Res., Sect. A **379**(1), 139–151 (1996).
10. T. Komarek, A. Brandt, V. Chirayath, L. Chytka, M. Hrabovsky, L. Nozka, M. Rijssenbeek, T. Sykora, and V. Urbasek, “Timing resolution and rate capability of Photonis miniPlanacon XPM85212/A1-S MCP-PMT,” *In review process* (2020).

11. Geant4 Collaboration, “Recent developments in Geant4,” Nucl. Instrum. Methods Phys. Res., Sect. A **835**, 186–225 (2016).
12. R. Diener, J. Dreyling-Eschweiler, H. Ehrlichmann, I. M. Gregor, U. Kotz, U. Kramer, N. Meyners, N. Potylitsina-Kube, A. Schutz, P. Schutze, and M. Stanitzki, “The DESY II test beam facility,” Nucl. Instrum. Methods Phys. Res., Sect. A **922**, 265–286 (2019).
13. M. Albrow, H. Kim, S. Los, M. Mazzillo, E. Ramberg, A. Ronzhin, V. Samoylenko, H. Wenzel, and A. Zatserklyaniy, “Quartz Cherenkov Counters for Fast Timing: QUARTIC,” Nucl. Instrum. Methods Phys. Res., Sect. A **7**(10), P10027 (2012).
14. M. Bonesini, T. Cervi, A. Menegolli, M. C. Prata, G. L. Raselli, M. Rossella, M. N. Spanu, and M. Torti, “Detection of vacuum ultraviolet light by means of SiPM for high energy physics experiments,” Nucl. Instrum. Methods Phys. Res., Sect. A **912**, 235–237 (2018).
15. J. Vavra, D. W. G. S. Leith, B. Ratcliff, E. Ramberg, M. Albrow, A. Ronzhin, C. Ertley, T. Natoli, E. May, and K. Byrum, “Beam test of a time-of-flight detector prototype,” Nucl. Instrum. Methods Phys. Res., Sect. A **606**(3), 404–410 (2009).
16. F. Uhlig, A. Britting, W. Eyrich, A. Lehmann, C. Schwarz, and J. Schwiening, “Performance studies of microchannel plate pmts,” Nucl. Instrum. Methods Phys. Res., Sect. A **695**, 68–70 (2012).

178.22.113.33 {ts '2020-06-19 12:32:34'}

Research Article Vol. 31, No. 3 / 30 Jan 2023 / *Optics Express* 3998

Optics EXPRESS

Upgraded Cherenkov time-of-flight detector for the AFP project

Libor Nozka,[1,*] **Giulio Avoni,**[2] **Elzbieta Banas,**[3] **Andrew Brandt,**[4] **Karel Cerny,**[1] **Paul M. Davis,**[5] **Serge Duarte Pinto,**[6] **Vjaceslav Georgiev,**[7] **Miroslav Hrabovsky,**[1] **Tomas Komarek,**[1] **Krzysztof Korcyl,**[3] **Ivan Lopez-Paz,**[8] **Marko Milovanovic,**[9] **Goran Mladenovic,**[10] **Dmitry A. Orlov,**[6] **Michael Rijssenbeek,**[11] **Petr Schovanek,**[12] **Tomas Sykora,**[13] **Maciej Trzebinski,**[3] **Vladimir Urbasek,**[12] **and Jan Zich**[7]

[1] *Joint Laboratory of Optics of Palacky University and Institute of Physics AS CR, Faculty of Science, Palacký University, 17. listopadu 12, 771 46 Olomouc, Czech Republic*
[2] *INFN Bologna and Universita di Bologna, Dipartimento di Fisica, viale C. Berti Pichat, 6/2, IT – 40127 Bologna, Italy*
[3] *Institute of Nuclear Physics Polish Academy of Sciences, Cracow, Poland*
[4] *The University of Texas at Arlington, Department of Physics, Box 19059, Arlington, TX 76019, USA*
[5] *Centre for Particle Physics, Department of Physics, University of Alberta, Edmonton, AB T6G 2G7, Canada*
[6] *Photonis Defense Inc., 1000 New Holland Ave., Lancaster, PA 17601, USA*
[7] *University of West Bohemia, Dept. of Applied Electronics and Telecommunications, Univerzitni 26, Pilsen, 30100, Czech Republic*
[8] *Institut de Física d'Altes Energies (IFAE), The Barcelona Institute of Science and Technology (BIST), Campus UAB, 08193 Bellaterra (Barcelona), Spain*
[9] *DESY, Platanenallee 6 D-15738 Zeuthen, Germany*
[10] *University of Belgrade - Faculty of Mechanical Engineering, Kraljice Marije 16, Belgrade, Serbia*
[11] *Stony Brook University, Dept. of Physics and Astronomy, Nicolls Road, Stony Brook, NY 11794-3800, USA*
[12] *Institute of Physics of the Academy of Sciences of the Czech Republic, Na Slovance 2, Prague, Czech Republic*
[13] *Charles University, Faculty of Mathematics and Physics, Institute of Particle and Nuclear Physics, V Holesovickach 2, CZ - 18000 Praha 8, Czech Republic*
[*] *libor.nozka@upol.cz*

Abstract: We present the results of our performance studies of the upgraded Cherenkov time-of-flight (ToF) detector for the AFP (ATLAS Forward Proton) project. The latest version consists of solid L-shaped fused silica bars, new customized ALD-coated micro-channel plate photomultipliers (MCP-PMTs) miniPlanacon XPM85112-S-R2D2 with an extended lifetime which operate at low gains (order of 10^3), and an updated construction. The improvements were aimed to increase the efficiency, the lifetime as well as the radiation hardness of the detector which has been designed to operate in high radiation areas (above 400 kGy/year). The detector was finally tested at the CERN-SPS test-beam facility (120 GeV π^+ particles) in August 2021 prior to its installation at the Large Hadron Collider (LHC) at CERN. Measurements proved the detector kept its inner timing resolution of 20 ps despite the rather low gain of its photodetector and reduced optical throughput caused by inevitable changes in the detector geometry.

Published by Optica Publishing Group under the terms of the Creative Commons Attribution 4.0 License. Further distribution of this work must maintain attribution to the author(s) and the published article's title, journal citation, and DOI.

#480624 https://doi.org/10.1364/OE.480624
Journal © 2023 Received 11 Nov 2022; revised 16 Dec 2022; accepted 27 Dec 2022; published 19 Jan 2023

1. Introduction

The design and the physics motivation needed for the time-of-flight (ToF) subdetector for the ATLAS-AFP project itself has already been described thoroughly in our previous papers: the physics concept in [1–3] performance studies in [4]; simulation benchmark studies in [5]; details of the optics in [6]; and timing studies in [6,7]. The ToF detector has been designed as a part of the proton tagging detector AFP to decrease the background to central exclusive production processes $p + p \longrightarrow p + X + p$ where X stands for the centrally produced system, which could consist of a pair of jets, a pair of intermediate vector bosons (W^+W^-), or a Higgs boson H. It operates at high radiation levels above 400 kGy/year or $4 \cdot 10^{15}$ n_{eq}/cm^2 (the n_{eq} stands for a neutron equivalent dose of an energy of 1 MeV) at 5 mm from the beam centre.

For clarity, the geometry of the ToF detector is depicted in Fig. 1. The ToF assemblage consists of a 4×4 matrix of L-shaped bars made of fused silica (SK-1300 by O'Hara, optical constants in [5]). The outer dimensions of the matrix are a height of 73.3 mm, a width of 65.5 mm (in the direction of radiators), and a depth of 25.2 mm. The dimensions of each bar are reported in [6]. Each bar serves both as a Cherenkov radiator and a light guide towards a fast multichannel-plate photomultiplier (MCP-PMT) device (the sensor plane in Fig. 1). There is a thin mirror optical layer on the 45° cut surface in the bar elbow.

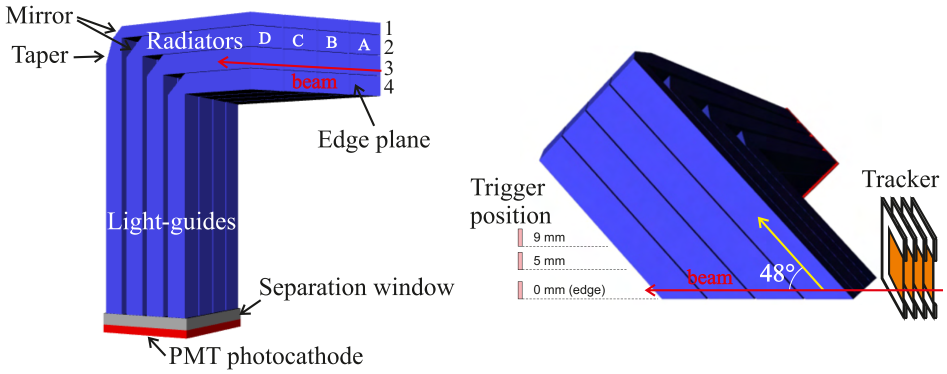

(a) (b)

Fig. 1. Optical part of the ToF subdetector made for test measurements: (a) side view with (b) top view together with position of the tracker and three positions of the SiPM trigger used during test measurements. The trigger position is measured relatively to the edge plane which is common for all the bars.

Besides this, the bars of the Train 1 are equipped with an extra polished surface, called taper, to further enhance their optical throughput [5]. The rows of four bars along the beam direction are called trains and are labeled with a number. The bars in each train are labeled with the letters A, B, C, and D along the direction of the incoming particles. In this way, the bars in the Train 1 are labeled 1A, 1B, 1C, and 1D and so on for the other trains. The acceptance area of the AFP detector is 16.8×20.0 mm^2, given by the dimensions of a tracker module at the front [8] and its tilt as illustrated in the Fig. 1. In the past, L-shaped bars were constructed so that the two arms of a bar were produced separately and then glued together [6]. For the ToF upgrade, we decided to make the bars solid (without glue) which made the production more complex. The glue-free solution improved the optical throughput of the optical system by 18%, see also Fig. 4 in [6], and the radiation hardness [9].

In our previous design, both the optics (bars) and the photomultiplier were placed inside the Roman Pot which was evacuated to a rotary vacuum (5-50 mbar). It was necessary to treat the photomultiplier and its high-voltage cables in a special way to avoid any accidental discharge spikes (we operated at the bottom part of the Paschen curve here). To remove this problem, the upgraded ToF detector introduced a separation of the photomultiplier from the vacuum side, see Fig. 2. The evacuated area is inside a Roman Pot covered by a detector flange on its open side. Both ToF and tracker detectors are installed here, except for the ToF's photomultiplier which is inserted in a movable tube going through a hole in the detector's flange. A 2.9 mm thick window separates the photomultiplier from the vacuum side. The window is made of the same material as bars (fused silica, SK-1300). It was coded by a simple anti-reflection layer made of 35 nm thick MgF_2 and annealed at 300°C. It is an additional optical element on the Cherenkov pulse path towards the photodetector resulting in a decrease of the total throughput of the ToF optics. The movable tube allows for the easy and precise alignment of the whole ToF detector with respect to the tracker thanks to a set of four precision screws mounted in the far end of the tube, see Fig. 2. The vacuum tightness around the tube is achieved by means of a custom-made bellows (by Mewasa AG, Switzerland).

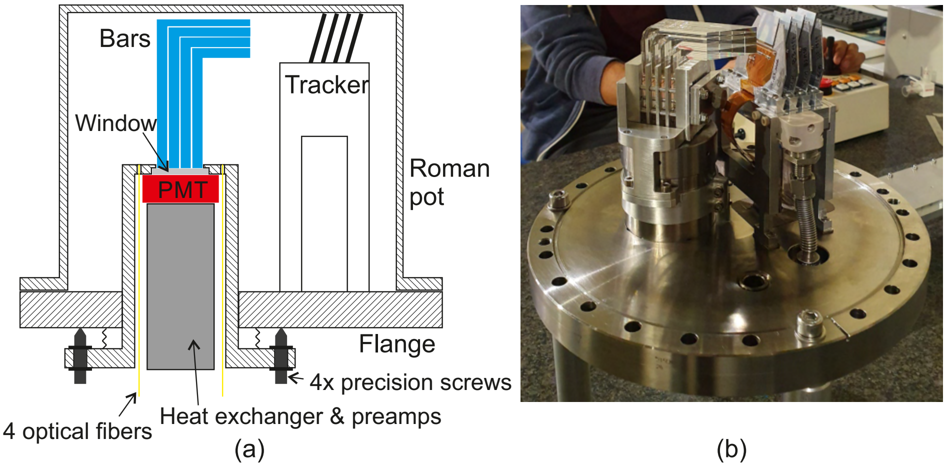

(a) (b)

Fig. 2. AFP detector with the upgraded ToF detector: (a) schematic view inside the Roman pot – area inside the Roman pot is evacuated, (b) real view on the assembly (without the pot).

Photonis produced four new photomultipliers miniPlanacon XPM85112-S-R2D2 for us: S/N 9002196 (labelled as #2196, MCP resistance 44 MΩ); 9002199 (#2199, 35 MΩ); 9002200 (#2200, 27 MΩ); and 9002201(#2201, 55 MΩ). They have a fused silica entrance window and a Bialkali photocathode. Their two-stage multi-channel plate (MCP) was ALD-coated (resistive and secondary emissive layers) by Arradiance to achieve an extended lifetime above 10 C/cm^2. The PMTs #2196 and #2199 have a standard anode gap of 2.9 mm. The PMTs #2200 and #2201 have a reduced anode gap of 0.6 mm. The backend electronic circuits of all photomultipliers were redesigned to reduce electronic crosstalk between anode pads (pixels) and to adapt to the new preamplifiers of the first stage [10]. Like the original design by Photonis, the back-end electronics were realized by two printed circuit boards (PCBs): the bias PCB and the anode PCB, each with a size of 32×32 mm^2, see Figs. 3(a) and 3(b). In the bias PCB, the original MCP-OUT bias resistor was removed because it caused crosstalk between the anode pads and it had no meaning for separate readouts of pixels. We also optimized wires lengths to make the same propagations delays among the channels. We enlarged auxiliary connecting Nickel strips to reduce parasitic impedances as well. The default output pinout on the anode PCB (pin header) was replaced by an equally spaced grid of 50 Ω RF MMCX female connectors, Fig. 3(c), to connect the new coaxial one-channel preamplifiers PA-a, Fig. 3(d). Having lower MCP resistance, the PMTs #2199 and #2200 were candidates for installation to the ToF and here we report mostly on the results of using these devices. The #2196 was used as a backup and for future test measurements. The #2201 PMT was considered for radiation hardness tests.

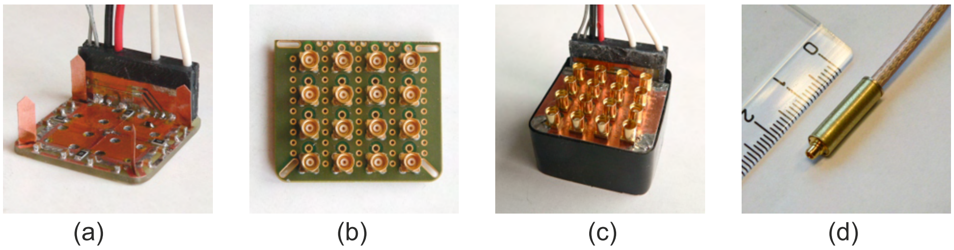

Fig. 3. Snapshots from the construction of a prototype of the modified version of the photomultiplier XPM85112: (a) the bias PCB equipped with a black HV input block and four Nickel strips for grounding connection with the anode PCB; (b) the anode PCB with MMCX female connectors; (c) assembled prototype with both PCBs; (d) coaxial one-channel preamplifier stage with MMCX connectors (Pa-a).

The PA-a preamplifiers are current-to-voltage converters with the conversion constant of 25 mV/mA and a voltage amplification of 20 dB (10×). They are equipped with MMCX male connectors on the PMT side and a 1.7 m long coaxial cable with the same MMCX ending on the other side. This solution ensures better protection against outside electromagnetic interference, an easier replacement of a damaged PA-a, and improved heat removal through the body of the detector. The PA-as are supplied from next voltage-to-voltage preamplifiers - PA-b modules. PA-bs are in the form of NIM modules. Each NIM module consists of a control motherboard and eight one-channel daughter boards with two stages of voltage-to-voltage preamplifiers with the total gain of 39 dB with available attenuation by 31.5 dB. Note that the gain varies among individual channels with an uncertainty range of ±1dB (±10%). Each channel is provided with a low-pass analog filter with a cut-off frequency of 1.4 GHz for noise rejection (LFCG-1400+ by Mini-Circuits).

This latest version of the ToF detector was subject to several performance measurements. It is known that the gain of the MCP photomultipliers decreases with increased repetition frequency (rates) of incoming light pulses [11] depending on the initial gain (at low kHz rates). We plan to use our photomultipliers on the gain of around 2000 based on our preliminary tests (it is ten times less than in our previous ToF detector). We refer to this gain as the DC gain because it was measured by a producer in a so-called DC mode [12]. Such low gain allows us to suppress the negative effect of high rates on the actual gain of the photomultiplier at the cost of a worse timing resolution. As the ToF detector will run in the LHC with an expected event rate of 20 MHz per train, we needed to address the behavior of the photomultipliers at high rates. These rate measurements were done in our laboratory on a setup with a pulsed picosecond laser. The results are reported in [10]. We found out that there was no significant gain deterioration of the PMTs #2199 and #2200 at the rate of 20 MHz and their timing resolution was 23 ps and 16 ps respectively (for 25 photoelectrons). The gain of the #2196 dropped by 42% at a 20 MHz rate and its timing resolution got worse: from 23 ps to 40 ps.

The timing performance of the whole ToF detector was the goal of the measurements made at the CERN-SPS test-beam facility (120 GeV π^+ particles) in August 2021 prior to its installation at the Large Hadron Collider (LHC) at CERN. Our first measurements with solid (glue-free) bars were performed in 2019 in DESY (Hamburg, Germany) in an electron beam with the energy of 5 GeV [9]. But the characteristics of such a beam are rather different from that of an LHC proton beam. We therefore focused on measurements with the 120 GeV π^+ beam which had very similar effects on our detector as the LHC proton beam (mainly a high production of secondary particles on the DESY beam).

2. Simulation studies

The overall optical throughput of the upgraded ToF optical part changed if compared to the previous version. Removing the glue from the bars resulted in an increase of their optical throughput by at least 23% due to an additional increase of the wavelength region from 165 to 235 nm [9]. On the other hand, the separation window introduces extra losses due to its attenuation and the additional two optical interfaces of glass-air (authors are not aware of an optical grease suitable at high radiation levels of 400 kGy or more). The performance predictions of the new optics on the SPS beam were simulated in the Geant4 simulation framework [13]. The transverse geometrical profile of the passing pion beam was a square 3×3 mm^2 (particle positions randomly scattered in it) to mimic the acceptance window given by the size of the trigger used in the beam test measurements, see Fig. 1(b) and the next section. The ToF model embodies all optical parts and a model of the photocathode of the photomultiplier using experimental values of its quantum efficiency (QE) [14]. The spectral range of Cherenkov light was restricted to the range from 160 nm to 650 nm. The lower limit was due to the absorption edge of the glass SK-1300 and the upper limit due to a low QE of the photocathode above 650 nm. As there are no known values of QE below 200 nm, we assigned the value 0.16 at the lowest known wavelength of 200 nm to the region down to 160 nm. The collection efficiency η of the photomultiplier was set to 0.6 (set by producer). A model of the separation window was used in the simulation which included the anti-reflection layers on both sides of the window.

As the measurements were focused on the Train 2, results for the Bar 2A (the first one) and 2D (the last one) were investigated in the simulation studies. Hereafter, when we speak of a bar performance, we mean the whole channel including the bar, the photocathode, and a corresponding pixel of the photomultiplier. The results of the simulation showed that the presence of the separation window decreased the total optical throughput by 16%. This is caused by attenuation in the window itself, but it is mainly due to Fresnel losses at additional air/vacuum-glass optical interfaces.

Regarding the comparison of glued and solid bars, Table 1 summarizes the number of photoelectrons produced on the photomultiplier's photocathode for the glued and the solid bars of the Train 2. The results presented are valid for the trigger position at the edge, 5 mm, and 9 mm from the edge, see Fig. 1(b). The following observations can be made:

- Solid bars benefit from the presence of deep UV photons. For all types of bars (A-D), the solid bars produced more photoelectrons than their glued counterparts by a factor of 1.7-1.8.
- Among solid bars, the Bar 2D produced more photoelectrons than 2A by a factor of 1.2. The multiplication factor was the same among the glued bars.
- Bars A always produced fewer photoelectrons than Bars B, C, and D because the bars upstream the beam receive the part of the Cherenkov light leaking from the downstream bars [7]. However, this effect depends on the distance of the passing particle from the edge. It is pronounced for large distances from the edge as seen on ratios 2X/2A in the table.

Note the relatively high standard deviations which correspond to the low number of photoelectrons with high fluctuations produced in general. The Cherenkov pulse is generated within 27 ps by a passing relativistic pion in a bar (or proton in the case the LHC). The pulse stretches out on its way to the photocathode due to the geometry of the bar and a significant dispersion of its refractive index in the ultraviolet region. Figure 4(a) shows how wavelengths of incoming photons are distributed in time on the sensor for the solid Bar 2D (but relevant for all solid bars without glue). The pulse length is 500 ps in the case of the solid bars. The glued bars suppress the light below 235 nm resulting in the final pulse length of 250 ps. The time distribution of produced photoelectrons on a photocathode is in Fig. 4(b) where photoelectrons are counted in 25 ps wide time slices. A small spread of produced photoelectrons in time results in a better shape of the falling edge and a higher amplitude (in absolute value) of the output signal from the photomultiplier. This has a positive impact on the timing performance in general. From this point of view, the light dispersion in bars affects the timing resolution rather negatively. It is assumed that the falling edge of the signal is mostly formed by photoelectrons produced in the first 250-300 ps. From this point of view, photons from the low ultraviolet end of the wavelength spectra do not contribute to the final timing performance of the detector. In the first 300 ps however, the solid bars still produce 1.7 times more photoelectrons than their glued counterparts.

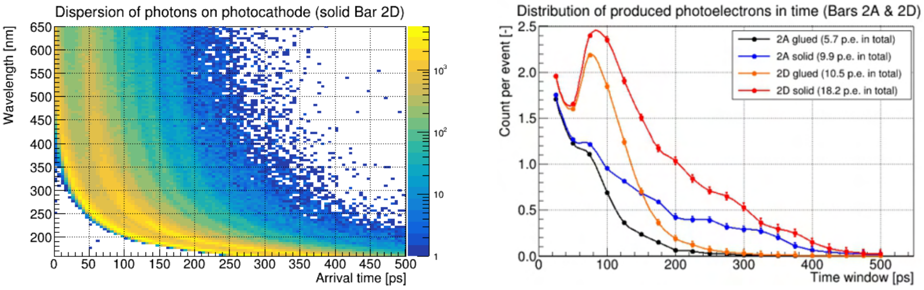

(a) (b)

Fig. 4. (a) Simulated time dispersion of the Cherenkov pulse for the solid Bar 2D, and (b) time spread of produced photoelectrons in the Bars 2A and 2D, solid and glued, calculated in 25 ps wide time slices (results valid for the beam π^+ 120 GeV, QE in [14], η=0.6, presence of the separation window, and trigger position at 5 mm from the edge).

Table 1. Number of photoelectrons produced in the Train 2 with glued or solid bars. The parameter S/G stands for the ratio solid/glued of number of photoelectrons (results valid for the beam π^+ 120 GeV, QE in [14], η=0.6, and installed separation window).

	Edge			5 mm			9 mm		
Bar	Glued	Solid	S/G	Glued	Solid	S/G	Glued	Solid	S/G
2A	9 ± 3	16 ± 4	1.8 ± 0.7	6 ± 2	10 ± 3	1.7 ± 0.7	6 ± 2	10 ± 3	1.7 ± 0.7
2B	11 ± 3	19 ± 4	1.7 ± 0.6	9 ± 3	15 ± 4	1.7 ± 0.7	6 ± 2	10 ± 3	1.7 ± 0.7
2C	11 ± 3	19 ± 4	1.7 ± 0.6	10 ± 3	18 ± 4	1.8 ± 0.7	9 ± 3	16 ± 4	1.8 ± 0.7
2D	11 ± 3	19 ± 4	1.7 ± 0.6	10 ± 3	18 ± 4	1.8 ± 0.7	10 ± 3	17 ± 4	1.7 ± 0.6
ratios									
2B/2A	1.2 ± 0.5	1.2 ± 0.4		1.5 ± 0.7	1.5 ± 0.6		1.0 ± 0.5	1.0 ± 0.4	
2C/2A	1.2 ± 0.5	1.2 ± 0.4		1.7 ± 0.7	1.8 ± 0.7		1.5 ± 0.7	1.6 ± 0.6	
2D/2A	1.2 ± 0.5	1.2 ± 0.4		1.7 ± 0.7	1.8 ± 0.7		1.7 ± 0.7	1.7 ± 0.6	

Estimation of the signal characteristics Photoelectrons produced in the PMT's photocathode and accepted in the first multi-channel plate (MCP) are then multiplied in both multichannel plates of the PMT. As mentioned above, the DC gain G of the PMT embodies its collection efficiency of η. For simulation purposes, one needs to use a gain valid for a single-photoelectron input which is not affected by η. Here, it is called the single-photoelectron gain G_{SPE} (it is labeled as G_{PHD} in [12]). Roughly, $G \cong \eta G_{SPE}$ where $\eta \approx 0.6$ (given by the producer). All used photomultipliers (#2196, #2199, and #2200) were operated on the high voltage of 1545 V. The G values of the photomultipliers were: 1800 (#2196), 2300 (#2199), and 2100 (#2200) with an uncertainty range of ±15%. The charge generated at the MCP output is then drained away through the backend electronics of the PMT and is then measured as a voltage drop on an anode resistor in the first amplification stage. The preamplifier thus serves as a current-to-voltage (A/V) converter. An equivalent electrical circuit of our photomultipliers is shown in Fig. 5 together with the input part of the first stage amplifier (PA-a). It includes impedances of real components as well as parasitic impedances (in gray). The frequency response (transfer function) of this description is shown in Fig. 6(a). The circuit acts as a low-pass filter with a cut-off frequency of 2.2 GHz (#2200 with a reduced anode gap of 0.6 mm) or 2.5 GHz (#2196 and #2199 with a regular anode gap of 2.9 mm). The current-to-voltage conversion is realized by the 50 Ω anode resistor R_a. However, its parallel wiring to the input impedance Z_i (50 Ω) of the preamplifier represents a total load impedance Z_L of 25 Ω. The input impedance Z_i of the PA-a preamplifier depends on the frequency. Its precise estimation for frequency content of our typical signal shape is outside the scope of this paper. Here, its mean value is expected to lie in an uncertainty range of ±5% around its nominal value.

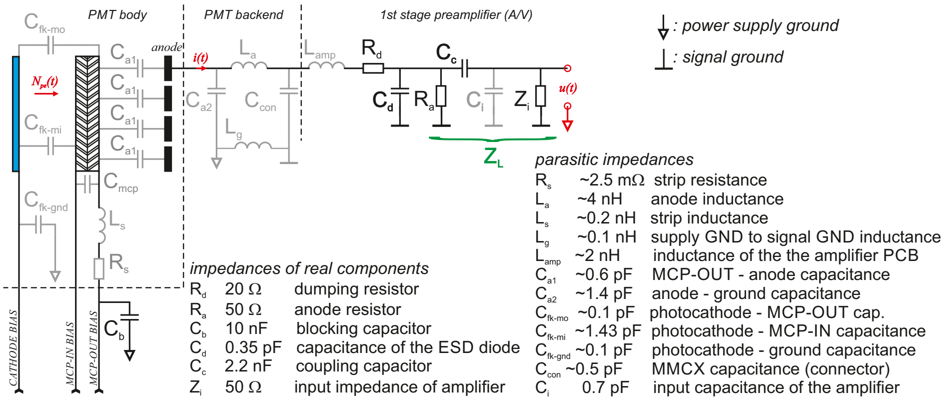

impedances of real components

R_d	20 Ω	dumping resistor
R_a	50 Ω	anode resistor
C_b	10 nF	blocking capacitor
C_d	0.35 pF	capacitance of the ESD diode
C_c	2.2 nF	coupling capacitor
Z_i	50 Ω	input impedance of amplifier

parasitic impedances

R_s	~2.5 mΩ	strip resistance
L_a	~4 nH	anode inductance
L_s	~0.2 nH	strip inductance
L_g	~0.1 nH	supply GND to signal GND inductance
L_{amp}	~2 nH	inductance of the the amplifier PCB
C_{a1}	~0.6 pF	MCP-OUT - anode capacitance
C_{a2}	~1.4 pF	anode - ground capacitance
$C_{fk\text{-}mo}$	~0.1 pF	photocathode - MCP-OUT cap.
$C_{fk\text{-}mi}$	~1.43 pF	photocathode - MCP-IN capacitance
$C_{fk\text{-}gnd}$	~0.1 pF	photocathode - ground capacitance
C_{con}	~0.5 pF	MMCX capacitance (connector)
C_i	0.7 pF	input capacitance of the amplifier

Fig. 5. Equivalent electrical circuit of the miniPlanacon XPM85112-S-R2D2 (one channel) designed by our group and implemented by the producer Photonis, together with the input part of the first-stage preamplifier (parasitic impedances in gray color). Z_L is the total load impedance.

The values of the parasitic impedances were estimated by direct calculations based on the corresponding geometrical and material specifications. Those of them having reductions measurable on the signal strength are listed in Table 2 with their (estimated) nominal value, range of realistically possible values, and effects on the signal shape. The rest of the parasitic impedances in the model have a negligible effect on the resulting amplitude as they are not directly part of the signal path. Note the parasitic anode inductance L_a has a positive effect on the signal amplitude at the expense of the steepness of the pulse. This is because its higher values shift the cut-off frequency of the back-end electronics towards lower frequencies. The strip inductance L_s affects the crosstalk among the pixels. Its higher value increases the strength of the signal on the common MCP-OUT wire causing higher crosstalk. The crosstalk signal behaves opposite the pulse causing a distortion of the pulse edge when added to a proper signal pulse generated at anode pads.

Using this model in the LtSPICE [15] simulation toolkit, the goal was to estimate a signal shape at the impedance load Z_L produced by a bunch of generated photoelectrons N_{pe} in pulse (pe or p.e. stands for photoelectron(s)). The MCP was simulated as a current source producing

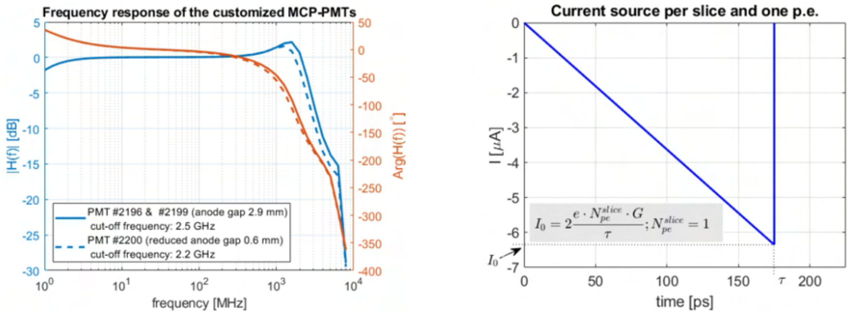

(a) (b)

Fig. 6. (a) Frequency response of the customized MCP-PMTs (acting as a low-pass filters), (b) triangular current pulse generated by the MCP from one photoelectron used for calculations of output signal waveforms (example plot valid for PMT #2200).

Table 2. Parasitic impedances, their estimated nominal values, and ranges of possible values (other parasitic impedances in Fig. 5 are taken as known with a nominal value). Correlation (positive) and anti-correlation (negative) effect of an impedance on the amplitude means that its growth causes an increase and decrease of the amplitude (in its absolute value) respectively.

Impedance	Nominal value	Lower limit	Upper limit	Effect on signal amplitude
C_{a1}	0.1 pF (2.9 mm)[a] 0.5 pF (0.6 mm)[a]	– –	– –	anti-correlates, decrease by 8% when changing from 0.1 to 0.5 pF
C_i	0.7 pF	0.3pF	2.1 pF	anti-correlates, 7%[b]
C_{con}	0.9 pF	0.2 pF	1 pF	anti-correlates, 3%[b]
L_a	2.5 nH	1.5 nH	9.5 nH	correlates, 3%[b]
L_s	0.2 nH	0.05 nH	1.25 nH	correlates, 6%[b]
L_{amp}	2 nH	0.5 nH	3 nH	correlates, 0.3%[b]
L_g	0.1 nH	0.05 nH	1.3 nH	correlates, 1%[b]

[a] Value of C_{a1} depends on the size of the anode gap (2.9 mm for PMTs #2196 and #2199, 0.6 for PMT #2200),
[b] Relative change of the amplitude when changing the impedance from the lower to upper limit.

current impulses in time. Time profiles of the N_{pe} was extracted from the Geant4 simulation for the solid Bar 2D and the glued Bar 2A (the highest number of produced photoelectrons vs. the lowest amount) in the form of 25 ps wide time slices according to the profiles in Fig. 4(b). For each slice in time, a simple current source was proposed generating a triangle pulse according to the shape in Fig. 6(b). The current amplitude I_0 was set to $2eN_{pe}^{slice}G_{SPE}/\tau$ where e is the elementary charge, N_{pe}^{slice} is the number of accepted photoelectrons in a given time slice, G_{SPE} is the single-photoelectron gain of the photomultiplier and $\tau = 175$ ps is the estimated rise time of the current pulse in the MCP [16].

In summary, there was a set of impulse current sources with various strengths defined by a given N_{pe}^{slice} distributed in time according to the time distribution of the photoelectrons produced, as seen in Fig. 7(a) for the PMT #2200. The total current profile was saw-toothed, but the discrete changes lay in the frequency range of tens of GHz and were effectively smeared out by the electronics of the photomultiplier (a low-pass filter as mentioned above). The output signal based on this input is in Fig. 7(b) for both the glued and solid bars geometries.

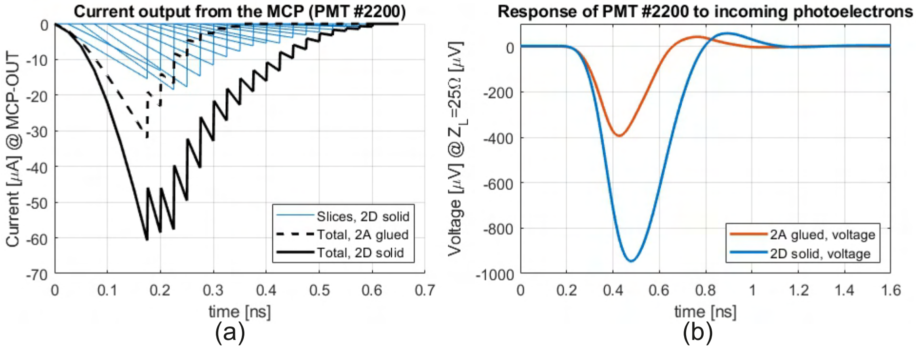

Fig. 7. Simulation of the PMT #2200 response: (a) electric current at the output of the MCP as a sum of contributions by photoelectrons arriving in 25 ps wide time slices for Bars 2A glued and 2D solid at 5 mm from the edge, (b) corresponding output voltage on the total impedance load Z_L.

By definition, the pulse voltage area A_u^L (more precisely the pulse integral) measured at the load resistance is directly related to the generated charge Q:

$$Q = \int_0^\infty i(t) \cdot dt = \frac{1}{Z_L} \int_0^\infty u(t) \cdot dt = \frac{1}{Z_L} A_u^L \tag{1}$$

where $i(t)$ is the current draining the charge through the Z_L and $u(t)$ is the corresponding voltage at the load impedance. The total charge generated on the anode pad is $Q = -eN_{pe}G_{spe}$ where e is the elementary charge, N_{pe} is the number of photoelectrons accepted in the MCP of the photomultiplier, and G_{spe} is the single-photoelectron gain of the MCP. Adding to the Eq. (1), the pulse area is linked to the N_{pe} as follows:

$$A_u^L = -e \cdot G_{SPE} \cdot Z_L \cdot N_{pe} \equiv p \cdot N_{pe} \tag{2}$$

Assuming Z_L constant, the parameter p depends only on the used gain of the photomultiplier. It is in units of [V·s/p.e.] or [Wb/p.e.] (although not intuitive, the unit V·s is actually the unit of magnetic flux Wb (Weber)).

The signal area A_u^L at the load impedance is highly correlated to its amplitude a_u^L through $A_u^L = k_s a_u^L$. The constant k_s is a time constant. It is the width of an equivalent rectangular pulse with the amplitude of the original one and the same charge content. Adding to Eq. (2), we get:

$$a_u^L = \frac{e \cdot Z_L \cdot G_{spe}}{k_s} N_{pe} \equiv k \cdot N_{pe} \tag{3}$$

where k is an amplitude yield per one photoelectron in units of [V/p.e.].

By definition, $p = k_s k$. The k_s is a function of the pulse shape. As the signal is amplified in the amplification chain, the pulse is extended in time in such a way that its amplitude decreases keeping its area constant. Thus consequently, k_s increases. Unless an appropriate backward correction is applied, one should rather focus on the pulse area because this quantity is minimally distorted on the signal pathway.

Table 3 summarizes the calculated values of k_s, k, and p for all used photomultipliers at a given gain. These values were obtained directly from an analysis of the simulated output pulse shapes as discussed above assuming the results presented in Fig. 4(b) and Fig. 7. They are in agreement with Eqs. (1–3) which means the presented mathematical description is consistent with the ltSPICE model.

Table 3. Parasitic impedances, their estimated nominal values, and ranges of possible values (other parasitic impedances in Fig. 5 are taken as known with a nominal value).

PMT	G [-]	k_s [ps]	k [μV/p.e.]	p [fWb/p.e.]
#2196	1800	232	−43	−10
#2199	2300	232	−55	−13
#2200	2100	252	−45	−12

Note that the values of k_s and k in Table 3 are valid only at the impedance load. The signal pulse is smeared in the amplification chain due to losses in coaxial cables and mostly in the low-pass filter in the PA-b unit. Their values differ from ones calculated from amplified signal characteristics $a_u = g \cdot a_u^L$ and $A_u = g \cdot A_u^L$ (where g is the amplification of the preamplifiers). The smearing affects also the pulse rising edge. In the example shown in Fig. 7(b), the measured value of k_s is 507 ps which is about twice higher than that in the impedance load predicted by the simulation. The p is preserved by definition (Eq. (2)) which is equivalent to the assumption of preserving the pulse area (after dividing by the amplification gain).

3. Experimental setup

The experimental measurements were done on the H6 beamline of the SPS North Area at CERN [17] in the middle of August 2021. The facility provided a π^+ beam of the energy 120 GeV with rates of tens of kHz. The experimental setup was like the one used in our previous measurements in DESY [9]. The only change was to use the Roman pot with the upgraded ToF. The scheme of the measurement setup is shown in Fig. 8 together with a picture of the typical arrangement of the experimental setup.

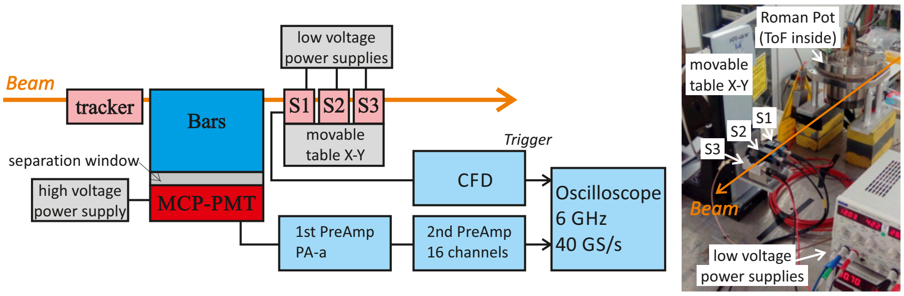

(a) (b)

Fig. 8. (a) Scheme of the experimental setup, (b) typical arrangement of the measurement setup on beam test measurements.

There were used the new MCP photomultipliers #2199, #2196, and #2200 (XPM85112-S-R2D2) by Photonis described above. The photomultipliers were operated at 1545V using a HV divider with a ratio of 1:10:1 (500 kΩ : 5 MΩ : 500 kΩ) providing the gain 1800 (#2196), 2300 (#2199), or 2100 (#2200). The Train 2 with the full complement of 4 bars (solid or glued) was installed on top of the separation window and aligned to its pixelization [6]. The output signal from each pixel (channel) was amplified by the PA-a and PA-b preamplifiers mentioned above providing the total amplification gain of 1000. This value includes the attenuation of the 1.7 m long cable being part of the PA-a amplifier. The amplified signal was collected by means of a fast LeCroy WaveMaster 806Zi-B oscilloscope (bandwidth of 6 GHz, sampling of 40 GS/s).

The oscilloscope was triggered by the signal from one of three detectors S1, S2, and S3 downstream of the beam. Each trigger detector consisted of a 15 mm long fused silica bar of 3×3 mm^2 cross-section coupled to a silicon photomultiplier (SiPM) manufactured by ST Microelectronics (S1, S2, type: NRD09_1 with 3.5×3.5 mm^2 and 58 μm cell size) [18,19] or by SensL (S3) [20] that detected Cherenkov radiation. They were placed on a two-axis movable stage (remotely controlled) in the beam-transverse plane to select a specific area of the ToF detector for study. The first detector S1 (the closest to the ToF) was mostly used as a trigger. The others were used for the measurement of their mutual resolution and, in turn, the resolution of the S1. The signal from the S1 detector was preprocessed by a CFD (Constant Fraction Discriminator) unit to minimize its time-walk (with a threshold value of −400 mV). A custom software CFD was implemented in the offline analysis of raw signals from the photomultiplier to extract arrival times of generated pulses with respect to the trigger.

4. Measurements and results

There were three main goals: (1) the timing resolution of the detector using solid bars and comparisons to the glued counterparts, (2) the validation of the ToF model including modelling the MCP-PMT using analysis of raw signal waveforms, and (3) the timing resolution at a higher gain. The aim of the last goal was to compare the detector performance at gain levels used in the past ([7]). The last goal is mentioned in the Discussion section only because of its lower priority. Measurements were focused on the Train 2 which had been our reference train across all test measurements. Except the first train with a taper, other trains behave in a similar way. Mutual comparisons were investigated in the past [7]. During all measurements, the trigger S1 was positioned to have a coincidence with the following ToF areas in the beam: 0 mm from the edge (in short the edge), 5 mm, and 9 mm from the edge, see also Fig. 1(b). First, the timing resolution of the trigger (S1) was determined by means of a comparative timing resolution measurement among all SiPM detectors. The timing resolution of the trigger S1 detector was found to be 11 ± 1 ps. The photomultiplier #2199 was used for the main comparative measurements of glued and solid bars for three positions of the trigger. The #2200 was used for high gain studies. The different photomultipliers were compared in the framework of a configuration at 5 mm from the edge with solid bars and the normal operational gain (2000) of the PMTs.

4.1. Raw signal analysis

In this analysis, the focus was on the signal strength of glued and solid bars in the Train 2 as well as a comparison of bars within the train. This analysis was done in terms of the pulse area at the impedance load A_u^L and the number of photoelectrons N_{pe} which was calculated from the area using Eq. (2). After rearrangement and assuming the statistical behavior of the experimental data, the number of photoelectrons was estimated as follows:

$$\langle N_{pe} \rangle = -\frac{1}{e \cdot Z_L \cdot G_{SPE}} \langle A_u^L \rangle = -\frac{\eta}{e \cdot g \cdot Z_L \cdot G} \langle A_u \rangle = \frac{1}{g \cdot p} \langle A_u \rangle \tag{4}$$

where $\langle N_{pe} \rangle$ is a mean number of photoelectrons evaluated from a mean value of the pulse area $\langle A_u \rangle$ calculated from a set of events for the same conditions (number of events was 50 000 in our measurements); $g = 1000$ is the total gain of the preamplifiers; G is the (DC) gain of the photomultiplier; $\eta = 0.6$ is the collection efficiency; and the value of p is in Table 3.

Figure 9(a) shows a typical histogram of amplitudes for the solid Bar 2C with a good separation from the pedestal at −100 mV. Figure 9(b) demonstrates linearity between the amplitude and the area of the signal which is in turn proportional to the total charge (and the number of photoelectrons N_{pe}) generated within the photomultiplier. In this example, $k_s = 0.507$ ns.

Figure 10 shows the signal strength (signal areas at the load impedance) of the bars in the Train 2 for both the solid (in rich colors) and the glued (in pale colors) versions measured at

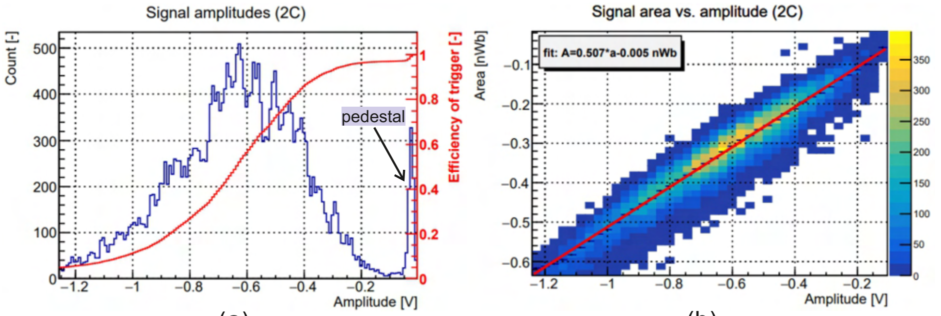

(a) (b)

Fig. 9. Example of the raw signal analysis of the measurement of the solid Train 2 using the PMT #2199 at the DC gain of 2300 and the trigger position at 5 mm from the edge: (a) histogram of amplitudes taken from waveforms produced in the channel of the solid Bar 2C, (b) mutual dependency between the signal amplitude and its area (which is proportional to the total charge in pulse generated by the photomultiplier).

all specified distances from the edge of the bars (the trigger positions, see Fig. 1(b)). These values were obtained by dividing the measured signal areas by the amplification gain of 1000. The height of each box is equal to the span between quantiles 0.25 and 0.75 of the distribution of the areas given and the position of the black line in each box indicates its mean value. The corresponding ratios of pulse areas (solid bars vs. glued counterparts and among bars in the train) are summarized in Table 4. Here, S/G denotes the solid-to-glued ratio. The ratios 2B/2A, 2C/2A and 2D/2A are briefly denoted in summary as 2X/2A in the next text.

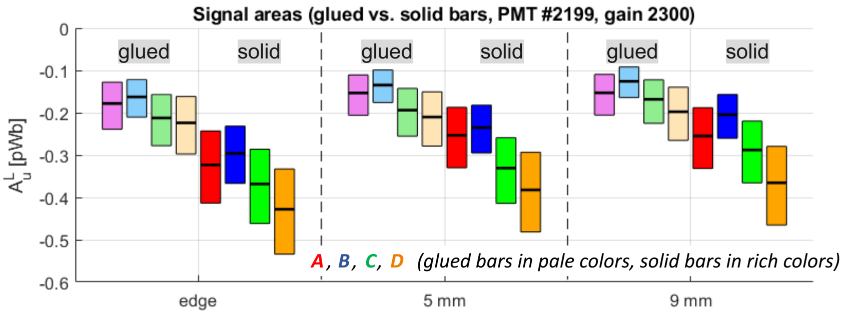

Fig. 10. Signal strength at the load impedance of bars in the Train 2 measured at various distance from the edge of the ToF for the (DC) gain of 2300 of the photomultiplier #2199.

On the one hand, the results revealed a discrepancy with regard to expectations in the case ratios between bars. The simulations predicted an augmentation of the signal in the channels 2B-2D compared to the first (upstream) Bar 2A by a factor of 1.2-1.7 based on the trigger position, see Table 1. Instead, the signal strength of the bar 2B was lower by approximately 10%. The Bars 2C and 2D produced stronger signals than the Bar 2A by a factor of 1.2-1.3 (at the edge) or 1.3-1.4 (5 mm and 9 mm) which was less than expected. This would mean that the channel of the Bar 2A has a higher amplification in the back-end side of the PMT electronics. On the other hand, S/G ratios are in an agreement with the simulations, see Fig. 11(a). This indicates the simulation satisfactorily predicted the number of photoelectrons generated in the deep UV region. See the Discussion section for a detailed analysis of this result.

Table 4. Measured mean pulse areas A_U^L in [pWb] of the bars in the Train 2 (solid and glued) using the PMT #2199. The parameter S/G stands for the ratio solid/glued of mean areas.

	Edge			5 mm			9 mm		
Bar	Glued	Solid	S/G	Glued	Solid	S/G	Glued	Solid	S/G
2A	−0.178	−0.323	1.8±0.7	−0.153	−0.256	1.7±0.7	−0.153	−255	1.7±0.7
2B	−0.163	−0.296	1.8±0.6	−0.135	−0.240	1.8±0.7	−0.126	−205	1.6±0.6
2C	−0.212	−0.368	1.7±0.6	−0.194	−0.331	1.7±0.6	−0.168	−288	1.7±0.7
2D	−0.224	−0.428	1.9±0.7	−0.210	−0.375	1.8±0.7	−0.198	−365	1.8±0.8
ratios									
2B/2A	0.9±0.4	0.9±0.3		0.9±0.4	0.9±0.3		0.8±0.3	0.8±0.3	
2C/2A	1.2±0.5	1.1±0.4		1.3±0.5	1.3±0.5		1.2±0.5	1.3±0.5	
2D/2A	1.3±0.5	1.3±0.5		1.4±0.6	1.5±0.5		1.2±0.5	1.4±0.5	

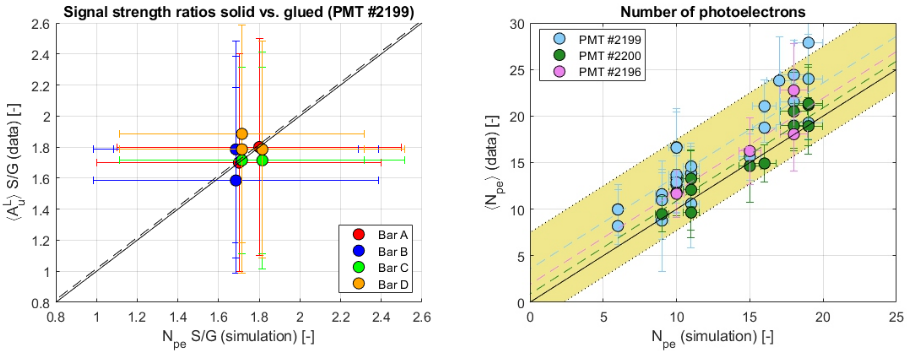

(a) (b)

Fig. 11. Comparison of experimental data (CERN SPS, π^+, 120 GeV) with simulation for the Train 2: (a) ratios of pulse areas between solid bars and glued counterparts (Table 1) with corresponding ratios between the number of photoelectrons given by simulation (Table 4) using PMT #2199, (b) estimated number of photoelectrons. The yellow shaded area represents uncertainty of N_{pe} by data due to errors in determinations of the PMT gain, preamplifiers gain, and the impedance load. The solid black line denotes positions of the perfect match between data and simulation and the dashed lines indicate the mean shift of measured values from simulation results.

The plot in Fig. 11(b) summarizes how the simulation agrees with data in terms of an estimation of the number of photoelectrons generated and accepted by the photomultipliers according to Eq. (4). Each point represents a specific case of a bar type (A-D, solid or glued) and a trigger position. The solid black line denotes positions of the perfect match between data and simulation. For each photomultiplier, the dashed line represents a mean deviation from the simulation. The estimation of N_{pe} from data was affected with uncertainties in determination of the PMTs gains (±15%), fluctuations of the gain of preamplifiers across channels (±1 dB, ±10%), and the input impedance Z_i (±5%) of the PA-a preamplifiers (as noted earlier in the text). This uncertainty is a rather high ±6 p.e. and is visually depicted by the shaded yellow band in the figure. At first sight, the model slightly underestimates the number of photoelectrons compared to data by 2.6 p.e. on average.

4.2. Timing performance

Timing resolution is the main characteristics of the ToF detector. By design, a crossing particle hits one of four trains triggering (possibly) all bars in the train. Thus, the resolution is given by timing resolutions of the individual trains. The timing resolution of a train was calculated as an amplitude-weighted average of arrival times measured in each bar of the train. This weighted sum approach gives a higher importance to those signal outputs with higher amplitudes in the average. It could happen that only three or two bars or even one bar triggers. The timing resolution is affected correspondingly. The timing performance was analyzed for all trigger cases in which all bars or at least given number of bars triggered. It showed that all four bars triggered together in most cases (94%). Thus in the following, only the case was considered in which all four bars in a train triggered.

Figure 12(a) shows results from the analysis of the timing resolution of the glued and the solid bars. For each trigger position, solid bars exhibited a better resolution by 4 ps on average. The timing resolution of the whole solid Train 2 improved as well by 3 ps on average. Its resolution was: 20 ± 2 ps at the edge, 22 ± 2 ps at 5 mm, and 24 ± 2 ps at 9 mm from the edge. Figure 12(b) summarizes these results for solid bars only with all photomultipliers in various trigger positions. As expected, there were no significant differences in the timing resolution among the photomultipliers. There is a worse timing resolution of the PMT #2196 at the channel of the Bar 2A which could be attributed to the lower strength of the signal output at this channel (probably due to a worse response of the PMT pixel). The timing resolution of the full Train 2 at 5 mm was: 24 ± 2 ps for the #2196, 23 ± 2 ps for the #2199, and 21 ± 2 ps for the #2200. At the edge, the timing resolution for the setup with the PMTs #2199 and the #2200 was 20 ± 2 ps and 19 ± 2 ps respectively. The only #2199 was used or measurements at 9 mm from the edge giving 24 ± 2 ps.

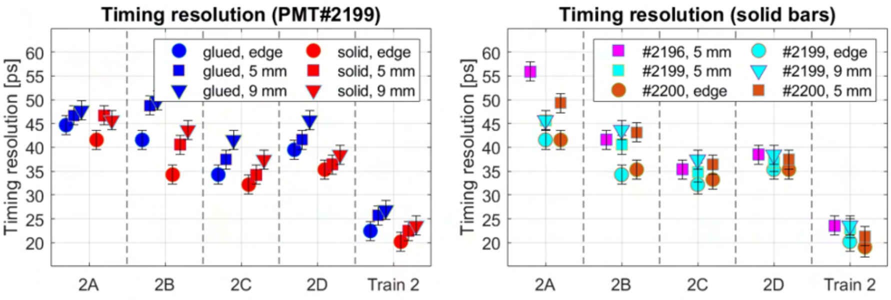

(a) (b)

Fig. 12. Results of timing resolution measurements: (a) comparison of glued and solid bars of the Train 2 using the PMT #2199, (b) results for solid bars and all photomultipliers. Photomultipliers were operated at 1545V (HV divider ratio 1:10:1) providing the gain 1800 (#2196), 2300 (#2199), or 2100 (#2200).

5. Discussion

The timing performance is the main characteristics of the ToF detector. Its recent upgrade addressed all shortcomings of the original ToF version while maintaining its proven radiation hardness which is critical in conditions of the LHC environment (total expected dose of 400 kGy/year at a distance of 5 mm from the beam centre). There were worried that changes in its construction (the additional separation window) and its low PMT operational gain (down to 2000) would significantly deteriorate the timing resolution. Values measured in the vicinity of 20 ps are acceptable for the AFP project. The PMTs #2200 and #2199 particularly gave promising results. Based on the results of rate measurements [10], both devices were chosen for installation in the LHC environment.

Solid bars helped a lot to maintain the timing resolution at around 20 ps. All the mentioned results of the timing resolution were valid for low rates of passing particles per train (tens of kHz). In the LHC, the rate will be 20 MHz per train. In general, the performance of photomultipliers decreases at these rates due to limits in the speed of charge replenishing of the MCP. This causes a drop of its actual (effective) gain [10,11]. As mentioned in the Introduction, laser measurements showed that there was no gain drop of the PMT #2199 and #2200 at 20 MHz and at the gain of 2000. Thus, these two PMTs should operate with the same performance in the LHC tunnel at that gain. The arrival time of a whole train was calculated as a (weighted) arithmetic average of the arrival time of each bar. Looking at Fig. 12, the mean resolution of each bar in the Train 2 was roughly $\sigma_b = 38$ ps (across all the PMTs, trigger at 5 mm from the edge). This theoretically corresponds to the train resolution $\sigma_t = 19$ ps applying the rule $\sigma_t = \sigma_b/\sqrt{N}$, where $N = 4$ is number of bars in the train. This rule is valid if there is no crosstalk among the bars. The mean measured timing resolution of the Train 2 was about 21 ps, close to $\widetilde{\sigma_t}$. This indicates that the crosstalk was small which was one of the goals of the suggested changes in the backend electronics of the photomultipliers.

It is common that pixels behave non-uniformly across a MCP-PMT due to space inhomogeneities both of the photocathode QE and the emissive layer in the MCP as well as due to amplification variations of the amplifiers across channels (approximately ±10%). Thus, there is no reason to compare the experimental data with the simulation in terms of pulse area ratios among bars in train (like 2X/2A in Table 4). Comparisons between solid and glued bar counterparts are however not affected by this issue. As seen in Fig. 11(a), there is a good agreement between the simulation and the experimental data in this way. One drawback of the simulation was the unknown quantum efficiency of the MCP-PMT photocathode at wavelengths below 200 nm (in deep UV). We simply assigned the value of 0.16 at the lowest known wavelength of 200 nm to the region down to 160 nm. By nature, the production of Cherenkov photons grows rapidly with lower wavelengths and any significant changes of QE below 200 nm would cause a serious deviation of the real response from that of the model. An analysis of the S/G ratios (Fig. 11(a)) indicates the simulation satisfactorily predicted the number of photoelectrons generated in the deep UV region when taking into consideration that the glued bars effectively work down to 233 nm due to the glue cut-off point and solid bars work down to 160 nm [9]. Thus, the QE is around 0.16 on average below 200 nm.

Measurements at high gains ($10^4 - 10^5$) with the PMT #2200 during the beam test measurements were performed to see what timing resolution we could expect at normal operational gains. We reached a timing resolution of down to 15 ps at the DC gain of $3.5 \cdot 10^4$ and at the edge which is comparable with our results in the past with the simpler geometry of the ToF [6,7]. However, the conditions at the LHC don't allow the ToF operation at those gain levels without a significant loss of efficiency.

We also tried to predict the output signal strength from the photomultipliers by means of an equivalent electrical circuit, see Fig. 5. The credibility of such a model depends both on its complexity and a correct estimation of each component, in particular parasitic impedances. The model was successfully verified in the past on data from laser measurements comparing amplitudes on one-photoelectron levels at the light wavelength of 405 nm. The comparison with beam test data presented here was more difficult due to its higher complexity - especially the wide spectral range of incoming Cherenkov light (from 160 nm to 600 nm) associated with a spread distribution of photoelectrons in time, and the complex geometry of the optical part.

6. Conclusion

Last two years, the ToF detector for the AFP project underwent significant design changes to remove various construction shortcomings. The throughput of its optical system was affected by the extra quartz window in the light path. Beside this, there was the requirement of operating the photomultiplier at lower gains close to 2000 to compensate for the signal attenuation at high pulse rates of 20 MHz. A new backend electronics of MCP-PMTs was designed in cooperation with Photonis, Inc. to suppress the electronic crosstalk among channels, to adapt to our changes in the ToF design, and to improve protection against external electromagnetic interference.

Based on these modifications, Photonis produced four new ALD coated miniPlanacon XPM85112-S-R2D2 photomultipliers for us: S/N 9002196 (MCP resistance of 44 MΩ), 9002199 (35 MΩ), 9002200 (27 MΩ), and 9002201 (55 MΩ). We proposed their equivalent electrical model. We used it also to extend our simulations of the ToF detector by calculations of the output signal waveforms based on simulated time distributions of the initial Cherenkov pulse done in Geant4. The beam test measurements at the CERN SPS beam proved the credibility of such a model, although improvements are still needed. Namely, a model of QE in deep UV region must be better specified (need to measure). There is also a plan to measure irradiated bars from the LHC environment in the SPS beamtest facility to better understand the effect of the radiation damage.

The measurements confirmed the detector kept its timing resolution of 20 ps at low gain levels of its photomultiplier (order of 10^3). Without gain constrains, we reached the limit of 15 ps at a gain of $3.5 \cdot 10^4$. The detector is now installed in the LHC tunnel and is ready for running in the Run 3 campaign of the LHC.

Funding. Narodowe Centrum Nauki (UMO-2019/34/E/ST2/00393); Ministerstwo Edukacji i Nauki (2022/WK/08); Ministarstvo Prosvete, Nauke i Tehnološkog Razvoja (451-03-68/2022-14/200105); Univerzita Palackého v Olomouci (IGA_PrF_2022_004); European Regional Development Fund (CZ.02.1.01/0.0/0.0/16_019/0000754); Ministerstvo Školství, Mládeže a Tělovýchovy (LM2018104, LTT 17018).

Acknowledgments. The measurements leading to these results have been performed at the H6 beamline of the SPS North Area at CERN.

Disclosures. The authors declare no conflicts of interest.

Data availability. Data underlying the results presented in this paper are not publicly available at this time but may be obtained from the authors upon reasonable request.

References

1. A. B. Kaidalov, V. A. Khoze, A. D. Martin, and M. G. Ryskin, "Extending the study of the higgs sector at the lhc by proton tagging," Eur. Phys. J. C **33**(2), 261–271 (2004).
2. FP420 Collaboration, "The FP420 R&D project: Higgs and New Physics with forward protons at the LHC," J. Instrum. **4**(10), T10001 (2009).
3. L. Adamczyk, E. Banas, A. Brandt, M. Bruschi, S. Grinstein, J. Lange, M. Rijssenbeek, P. Sicho, R. Staszewski, T. Sykora, M. Trzebinski, J. Chwastowski, and K. Korcyl, "Technical Design Report for the ATLAS Forward Proton Detector," (2015). Technical Report CERN-LHCC-2015-009. ATLAS-TDR-024.
4. K. Cerny, T. Sykora, M. Tasevsky, and R. Zlebcik, "Performance studies of Time-of-Flight detectors at LHC," J. Instrum. **16**(01), P01030 (2021).
5. L. Nozka, A. Brandt, M. Rijssenbeek, T. Sykora, T. Hoffman, J. Griffiths, J. Steffens, P. Hamal, L. Chytka, and M. Hrabovsky, "Design of cherenkov bars for the optical part of the time-of-flight detector in geant4," Opt. Express **22**(23), 28984–28996 (2014).
6. L. Nozka, L. Adamczyk, G. Avoni, A. Brandt, P. Buglewicz, E. Cavallaro, G. Chiodini, L. Chytka, K. Ciesla, P. M. Davis, M. Dyndal, S. Grinstein, P. Hamal, M. Hrabovsky, K. Janas, K. Jirakova, M. Kocian, T. Komarek, K. Korcyl, J. Lange, D. Mandat, V. Michalek, I. L. Paz, D. Northacker, M. Rijssenbeek, L. Seabra, P. Schovanek, R. Staszewski, P. Swierska, and T. Sykora, "Construction of the optical part of a time-of-flight detector prototype for the AFP detector," Opt. Express **24**(24), 27951–27960 (2016).
7. L. Chytka, G. Avoni, A. Brandt, E. Cavallaro, P. M. Davis, F. Foerster, M. Hrabovsky, Y. Huang, K. Jirakova, M. Kocian, T. Komarek, K. Korcyl, J. Lange, V. Michalek, L. Nozka, I. L. Paz, M. Rijssenbeek, P. Schovanek, T. Sykora, and V. Urbasek, "Timing resolution studies of the optical part of the AFP time-of-flight detector," Opt. Express **26**(7), 8028–8039 (2018).

8. J. Lange, E. Cavallaro, S. Grinstein, and I. L. Paz, "3D silicon pixel detectors for the ATLAS Forward Physics experiment," J. Instrum. **10**(03), C03031 (2015).
9. L. Nozka, A. Brandt, K. Cerny, M. Hrabovsky, T. Komarek, F. Krizek, D. Mandat, M. Milovanovic, M. Rijssenbeek, P. Schovanek, T. Sykora, V. Urbášek, and J. Zatloukal, "Performance studies of new optics for the time-of-flight detector of the AFP project," Opt. Express **28**(13), 19783–19796 (2020).
10. T. Komarek, V. Urbasek, A. Brandt, K. Cerny, J. DeFazio, V. Georgiev, M. Hrabovsky, Z. Kubik, L. Nozka, D. Orlov, S. D. Pinto, M. Rijssebeek, T. Sykora, and J. Zich, "Characterization of the miniPlanacon XPM85112-S-R2D2 MCP-PMT with a custom modified backend electronics," Nucl. Instrum. Methods Phys. Res., Sect. A **1041**, 167330 (2022).
11. T. Komarek, A. Brandt, V. Chirayath, L. Chytka, M. Hrabovsky, L. Nozka, M. Rijssenbeek, T. Sykora, and V. Urbasek, "Timing resolution and rate capability of Photonis miniPlanacon XPM85212/A1-S MCP-PMT," Nucl. Instrum. Methods Phys. Res., Sect. A **985**, 164705 (2021).
12. D. Orlov, T. Ruardij, S. D. Pinto, R. Glazenborg, and E. Kernen, "High collection efficiency MCPs for photon counting detectors," J. Instrum. **13**(01), C01047 (2018).
13. Geant4 Collaboration, "Recent developments in Geant4," Nucl. Instrum. Methods Phys. Res., Sect. A **835**, 186–225 (2016).
14. P. M. Duarte, "Quartic: An ultra-fast time-of-flight counter," Ph.D. thesis, The University of Texas, Arlington (2007).
15. G. Brocard, "The LTspice IV Simulator: Manual, Methods and Applications," Swiridoff Verlag, Wurth (2013).
16. F. Tang, "Modeling for MCP-PMT Output Signal," presentation in frame of LAPPD project (2008).
17. J. Lange, L. Adamczyk, G. Avoni, E. Banas, A. Brandt, M. Bruschi, P. Buglewicz, E. Cavallaro, D. Caforio, G. Chiodini, L. Chytka, K. Ciesla, P. M. Davis, M. Dyndal, S. Grinstein, K. Janas, K. Jirakova, M. Kocian, K. Korcyl, I. L. Paz, D. Northacker, L. Nozka, M. Rijssenbeek, L. Seabra, R. Staszewski, P. Swierska, and T. Sykora, "Beam tests of an integrated prototype of the ATLAS forward proton detector," J. Instrum. **11**(09), P09005 (2016).
18. M. Albrow, H. Kim, S. Los, M. Mazzillo, E. Ramberg, A. Ronzhin, V. Samoylenko, H. Wenzel, and A. Zatserklyaniy, "Quartz Cherenkov Counters for Fast Timing: QUARTIC," J. Instrum. **7**(10), P10027 (2012).
19. L. Chytka, M. Hrabovsky, T. Komarek, V. Michalek, L. Nozka, T. Sykora, and V. Urbasek, "Time resolution of the SiPM-NUV3S," Nucl. Instrum. Methods Phys. Res., Sect. A **935**, 51–55 (2019).
20. M. Bonesini, T. Cervi, A. Menegolli, M. C. Prata, G. L. Raselli, M. Rossella, M. N. Spanu, and M. Torti, "Detection of vacuum ultraviolet light by means of SiPM for high energy physics experiments," Nucl. Instrum. Methods Phys. Res., Sect. A **912**, 235–237 (2018).

147.231.27.222 {ts '2023-01-23 07:22:24'}

Nuclear Inst. and Methods in Physics Research, A 1041 (2022) 167330

Contents lists available at ScienceDirect

Nuclear Inst. and Methods in Physics Research, A

journal homepage: www.elsevier.com/locate/nima

Characterization of the miniPlanacon XPM85112-S-R2D2 MCP-PMT with custom modified backend electronics

T. Komárek [a,*], V. Urbášek [b], A. Brandt [c], K. Černý [a], V.A. Chirayath [c], J. DeFazio [d], V. Georgiev [e], S. Hail [c], M. Hrabovský [a], Z. Kubík [e], L. Nožka [a], D. Orlov [f], S. Duarte Pinto [f], M. Rijssenbeek [g], T. Sýkora [h], F. Yang [c], J. Zich [e]

[a] *Joint Laboratory of Optics, Palacky University, 17. listopadu 50A, Olomouc, 77207, Czech Republic*
[b] *Institute of Physics of the Academy of Science of the Czech Republic, Na Slovance 2, Prague 8, 18221, Czech Republic*
[c] *The University of Texas at Arlington, Department of Physics, 701 S. Nedderman Drive, Arlington, 76019, TX, USA*
[d] *Photonis Defense Inc., 1000 New Holland Ave, Lancaster, 17601, PA, USA*
[e] *University of West Bohemia, Department of Electronics and Informatics, Univerzitní 26, Pilsen, 30100, Czech Republic*
[f] *Photonis Netherlands B.V., Dwazziewegen 2, Roden, 9301 ZR, Netherlands*
[g] *Stony Brook University, Department of Physics and Astronomy, Nicolls Road, Stony Brook, 11794, NY, USA*
[h] *Charles University, Faculty of Mathematics and Physics, Ke Karlovu 3, Prague, 12116, Czech Republic*

ARTICLE INFO

Keywords:
Micro-channel plate photo-multiplier tubes
Time-of-flight
Fast timing
Cherenkov radiation

ABSTRACT

We report the results of the measurements of three pieces of the new Photonis miniPLANACON microchannel-plate photomultipliers (MCP-PMTs) intended for use in the demanding environment of the Large Hadron Collider (LHC) beamline as a part of the AFP Time-of-Flight detector. These photomultipliers were modified in cooperation with the manufacturer by using a custom backend and were subjected to numerous tests, with the focus on the rate capability and crosstalk behaviour. We determined that the two of them with a lower MCP resistance are able to operate without significant saturation at an anode current density of 1 μA/cm^2. These two are, therefore, suitable for the intended use and are currently installed as part of the AFP detector packages.

1. Introduction

Photomultiplier tubes (PMTs) are widely used in particle and astroparticle physics experiments for the detection of low photon fluxes. Among them, microchannel-plate photomultipliers (MCP-PMTs) are preferred in many fields of application because they have these main advantages: (1) A fast response in tens of picoseconds (in terms of transit-time spread) thanks to the short distances the electrons have to travel and its high electric field (tens of kV/cm); (2) Insensitivity to magnetic fields even above 1 T [1] thanks to the same reasons; and (3) High spatial resolution thanks to the granularity of the microchannel plates allowing for pixelization through the use of multiple anode pads.

MCP-PMTs, however, also have some disadvantages. They cannot operate at gains higher than 10^7 due to limitations of the pulse charge capacity per channel [2] and, until recently, a limited lifetime. The lifetime is affected by the large total surface of a microchannel plate which makes it difficult to outgas the channels completely. Internal electron bombardment, therefore, generates ions through electron stimulated desorption. These bombard the cathode backwards with a kinetic energy at the order of keV(s) (depending on MCP bias voltage) and reduce its quantum efficiency [3,4]. Furthermore, as the cumulative charge handled by the MCP plane increases, the gain decreases. Both effects limit the useful lifetime of MCP-PMTs without proper MCP modifications to an integrated (or cumulative) anode charge (IAC) of about 0.5 C/cm^2.

A novel MCP technology using glass microcapillary array substrates functionalized by the application of resistive and secondary emissive layers using atomic layer deposition (ALD) significantly improved the quality of MCP plates. Photomultipliers with the ALD coating of the MCP plates are characterized by an excellent lifetime reaching 5 C/cm^2 or even higher as reported by the Lehmann group [4].

The time-of-flight (ToF) detectors of the AFP (ATLAS Forward Proton) project [5] use photomultipliers of the miniPlanacon family made by Photonis with two MCP plates, one PMT per ToF detector. They are equipped with a matrix of 4 × 4 anode pads with a pixel size of $5.8 \times 5.8\,\mathrm{mm}^2$. Each pixel corresponds to one of sixteen L-shaped fused silica bars forming the optical part of the detector. The detection of passing protons (originating from proton–proton collisions at the LHC) is based on Cherenkov light production in the bars. A typical diffractive

---

[*] Corresponding author.
E-mail address: tomas.komarek@cern.ch (T. Komárek).

https://doi.org/10.1016/j.nima.2022.167330
Received 11 May 2022; Received in revised form 7 July 2022; Accepted 19 July 2022
Available online 6 August 2022
0168-9002/© 2022 Published by Elsevier B.V.

proton normally passes four bars in one of four rows of the detector. Each row is called a train. Until 2018, a yield of 15–20 photoelectrons (P_e) was achieved per pixel (60–80 photoelectrons in total per proton in a train) [6]. Since then the yield has increased by a factor of 1.6 [7] due to technological improvements in the production of the bars.

As the anode pads share the same MCP, parasitic crosstalk among the pads affects their output signals. It consists of the electronic crosstalk discussed in the next section and the charge sharing which we briefly describe here. A Cherenkov light pulse emitted in a bar of the ToF detector is almost uniformly distributed across an area of $6 \times 5\ \mathrm{mm}^2$ at the output of the bar on the photomultiplier window [7]. The correspondingly generated charge cloud leaving the MCP pores partly hits anode pads in adjacent pixels at the same time. This effect is known as the charge sharing crosstalk. The charge sharing is less pronounced in tubes with a shorter distance between the anode pads and the MCP output plane [4]. As mentioned above, one proton hits four bars in a train of the ToF resulting in the uniform illumination of one row of four photomultiplier pixels. The charge sharing among pixels in that row is not an issue because it does not cause a loss of timing resolution (the signal arrives at the same time for all four channels due to detector geometry) and any pulses due to the charge sharing towards pixels in adjacent rows can easily be rejected. This form of crosstalk can be controlled primarily by two mechanisms: restricting the channel area that the light can hit and by the reduction of the anode gap by the manufacturer.

Two non-ALD XPM85112 tubes with two MCP plates in each, utilizing $10\ \mu\mathrm{m}$ pores, were used for Run 2 of the LHC (Large Hadron Collider) at CERN in 2017. The first one had an MCP resistance of $48\,\mathrm{M\Omega}$ and a reduced anode gap of $0.6\,\mathrm{mm}$. The latter one was equipped with MCP plates with a total resistance of $17\,\mathrm{M\Omega}$ and a standard anode gap of $2.9\,\mathrm{mm}$. The ToF detectors were each exposed to the rate of $4\,\mathrm{MHz}$ of the signal protons per train (per four pixels) resulting in a total proton flux through each ToF detector of $4.8 \cdot 10^{13}$ during the entire 2017 operation. Both photomultipliers reached an IAC of approximately $2.4\,\mathrm{C/cm}^2$ during this period. This resulted in the degradation of their quantum efficiencies and a drop in the overall performance [8]. Besides this, the PMT gain decline due to high rates of incoming protons negatively affected the performance of the detector [9].

This behaviour was measured in laboratory laser tests and reported in [10]. As stated there, the maximum effective rate estimate (above which the gain declines) is inversely proportional to the MCP resistance, the intrinsic gain (at low kHz rates), and the number of photoelectrons produced by the photocathode. If the last two parameters increase, the amount of the generated charge increases whilst the higher MCP resistance impedes its fast charge draining. Thus, the lower MCP resistance helps achieve better rate capability. The same holds for the lower number of photoelectrons and lower gain, but such PMT rate behaviour improvement is at the expense of the deterioration of its timing resolution [10].

These facts led us to require the following from the MCP-PMTs intended for Run 3 of the LHC (in which the expected proton rate will be $20\,\mathrm{MHz}$ per train): an MCP resistance below $30\,\mathrm{M\Omega}$; a proper ALD coating to extend the lifetime of the tube above $10\,\mathrm{C/cm}^2$; and the ability to work at low intrinsic gains at the order of 10^3 so as to shift the maximum light pulse rate above $20\,\mathrm{MHz}$ without a significant decline of the operational gain and timing performance due to saturation. Photonis produced the three miniPlanacon XPM85112-S-R2D2 PMTs for us. We modified the backend electronics of the tubes in cooperation with Photonis to suppress the electronic crosstalk among pixels. The next section describes the three photomultipliers and the backend modifications.

2. Tested devices and their modifications

Based on our experience from Run 2 of the LHC we decided to use new MCP-PMTs for Run 3 of the LHC (in which the expected proton rate will be $20\,\mathrm{MHz}$ per train). The three miniPlanacon XPM85112-S-R2D2 PMTs produced by Photonis for us are: S/N 9002196 (an MCP resistance of $44\,\mathrm{M\Omega}$), 9002199 ($35\,\mathrm{M\Omega}$), and 9002200 ($27\,\mathrm{M\Omega}$). Later in the paper we often identify them using the last four digits of the S/N only. The spread and deflection of the MCP resistances from the $< 30\,\mathrm{M\Omega}$ requirement are probably due to difficulties in keeping to this parameter during production, particularly with regard to the ALD coating made by Arradiance LLC. They have a fused silica entrance window and a Bialkali photocathode. Their two-stage MCP is ALD-coated (resistive and secondary emissive layers) by Arradiance LLC to achieve an extended lifetime above $10\,\mathrm{C/cm}^2$. We intend to operate them at a low intrinsic gain of $2 \cdot 10^3$ to shift the maximum proton rate (at which timing does not yet deteriorate) above $20\,\mathrm{MHz}$. All these photomultipliers are produced with a matrix of 4×4 pixels defined by square anode pads with a size of $5.8 \times 5.8\,\mathrm{mm}^2$ and a spacing gap of 0.6 mm between them. We decided to modify the back end electronics of the PMTs to fit into the new design of the AFP detector and to suppress negative electronic crosstalk. Furthermore, one of the PMTs (9002200) featured a reduced anode gap of $0.6\,\mathrm{mm}$ (which is much lower than the standard gap of $2.9\,\mathrm{mm}$ present in the other two pieces) in an attempt to reduce charge sharing among the anode pads. We will evaluate this later in the paper.

Standard XPM85112 photomultipliers are equipped with two 16-pin arrays of signal output connectors, each consisting of eight signal-ground pairs of pins. In the past, we developed an eight-channel first stage pre-amplifier (called PA-a) designed to directly connect with the block (see Fig. 1a). Such a configuration, however, was a concentrated source of heat. For the new Run 3, the compact PA-a modules were replaced with a set of in-line one-channel preamplifiers equipped with MMCX male connectors on the end towards the PMT and a 1.7 m long coaxial cable with the same MMCX ending on the other side (see Fig. 1b). This solution allows for better protection against outside electromagnetic interference, easier replacement of any damaged PA-a, and better heat removal through the large overall surface area. For this reason, we needed to modify the layout of the output pins of the new PMTs and add MMCX female connectors to them.

The electronic crosstalk among the anode pads is present mostly due to the shared MCP output electrode (MCP-OUT) and existing capacitance between the MCP output plane and the anode pads. This distorts the shape of the signal rising edge and deteriorates the timing performance of the PMT. Fig. 2a shows an equivalent circuit of the original photomultiplier design by Photonis. The real electronic components are in a black colour, while the parasitic impedances are indicated in grey. Note the MCP-OUT BIAS part is realized by four parallel branches on the PMT backend (one per each side), whereas only one of them is shown in the scheme. The yellow rectangle represents a nickel strip (50 um thick and 2 mm wide) which connects MCP-OUT BIAS on the backend side with the MCP-OUT electrode plane. The bias resistor R_b and the capacitor C_b form the high-frequency grounding of the MCP-OUT plane together with the intrinsic impedance L_s of the strip. The intrinsic resistance of the strip is negligible with respect to the R_b and it is omitted here. When a developing charge cloud propagates to the MCP-OUT plane, a parasitic crosstalk voltage arises on this grounding part. Its magnitude heavily grows with the value R_b of the bias resistor. The parasitic voltage is shared among all the anodes of the PMT through the capacitances C_{a1}. The bias resistor R_b is a load resistor for the MCP-OUT electrode and it is meant for the readout of the whole MCP output signal. It has no function with regard to a separate readout of individual pixels. Removing the bias resistor is one way of reducing the crosstalk as was done in the ALICE experiment [11]. Moreover, ALICE halved the anode capacitance (C_{a2}) through the optimization of wire lengths and the ground location. This further led to a decrease in the undesirable crosstalk between adjacent anode pads [11]. Segmentation of the MCP-OUT plane is another way to suppress the electronic crosstalk. This approach was taken in the Hamamatsu photomultiplier SL10 in the frame of the Super-KEKB project [12].

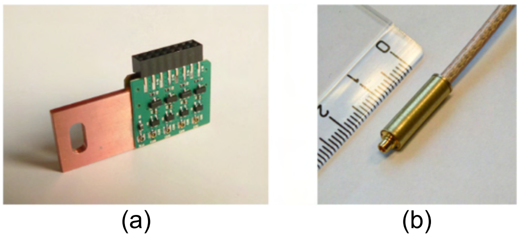

Fig. 1. (a) Eight-channel PA-a module with a copper chiller to be connected to the original design of the PMT and its holder, (b) in-line one-channel version with MMCX connector for the new design of the ToF detector.

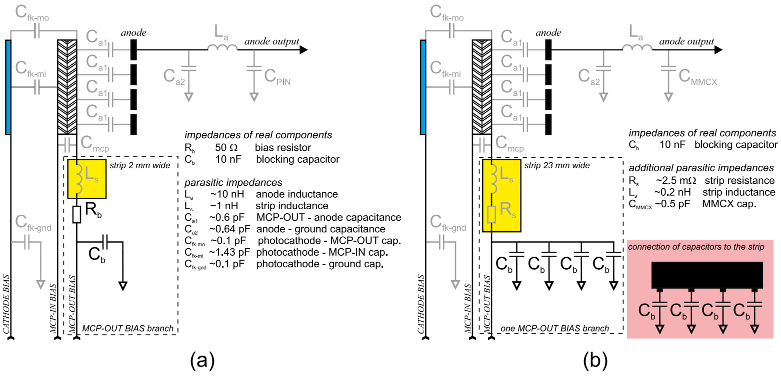

Fig. 2. Semi-realistic electronical circuit of (a) the original MCP-PMT XPM85112 by Photonis, (b) the modified design. Real electronic components are in black and parasitic impedances are in grey. The pink inset shows how capacitors are connected to the extended strip.

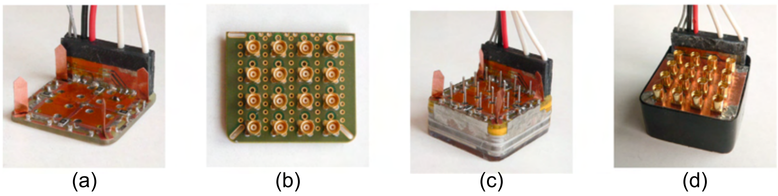

Fig. 3. Snapshots from the construction of a prototype of the modified version of the photomultiplier XPM85112: (a) the bias PCB equipped with a black HV input block and four Nickel strips for a grounding connection with the anode PCB, (b) the anode PCB with MMCX female connectors, (c) the prototype after installation of the bias PCB and without the anode PCB, (d) the assembled prototype with both PCBs.

We were inspired by the approach used in the ALICE experiment and proposed a similar solution without the bias resistor and with various additional modifications aimed to decrease the unwanted capacitances and inductances (see Fig. 2b). All these modifications were done in cooperation with Photonis. In Fig. 2b, the bias resistors are missing and only a parasitic resistance R_s of the strip is included in each MCP-OUT BIAS branch. The width of the Nickel strips is now 23 mm on three of the four branches. The last one, close to a high-voltage connector, contains a Nickel strip 12 mm wide due to the spatial limitations (see Fig. 3a). Besides this, each branch is equipped with four or two (on the branch with the shorter strip) parallel 4.7 nF capacitors C_b distributed equally across the Nickel strip (see the pink inset in Fig. 2b). In this design, the high-frequency grounding is formed by these capacitors and the strip impedance (given by R_s and L_s) which is low. Thus, the crosstalk strength is lower with this design.

Like the original design by Photonis, the back end electronics consists of two printed circuit boards (PCBs): the bias PCB and the anode PCB, each with a size of 32×32 mm^2 (see Figs. 3a and 3b). The bias PCB has four layers. It contains all the above-mentioned modifications, and it is additionally equipped with an NTC (Negative Temperature Coefficient) thermistor for monitoring the PMT temperature. A black HV input block is bonded to the bias PCB. It includes high-voltage input cables from a high-voltage divider as well as the signal cables of the thermistor. The anode PCB is designed for equal wiring of all the output anode signals and to mount the MMCX female connectors (see Fig. 3b). The distribution of the connectors follows the original spatial distribution of the anodes output pins. In the original design, the distance between both PCBs is around 5 mm. The distance is shortened to 2 mm in the modified design. The original ground connections between PCBs of four 1 mm wide Nickel strips on their corners were replaced by 4 mm wide strips as seen in Fig. 3c. Fig. 3d shows an assembled prototype of a modified XPM85112.

3. Measurement setup

A scheme of the setup can be seen in Fig. 4. The measurements were performed using the Hamamatsu M10303-29 laser system. The laser

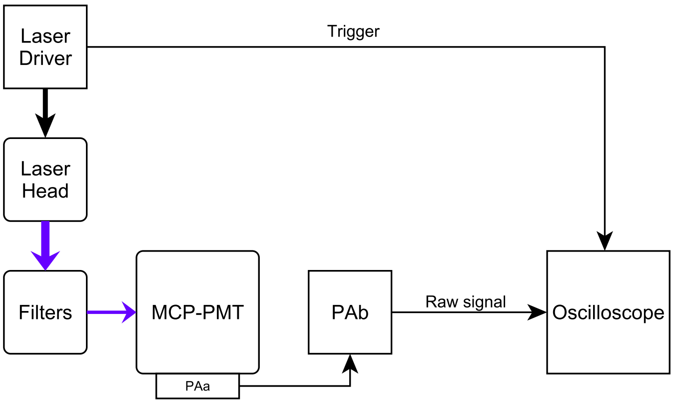

Fig. 4. The measurement setup scheme. In some cases, the amplifiers were left out to get a single photoelectron reference charge for the PMT gain measurements.

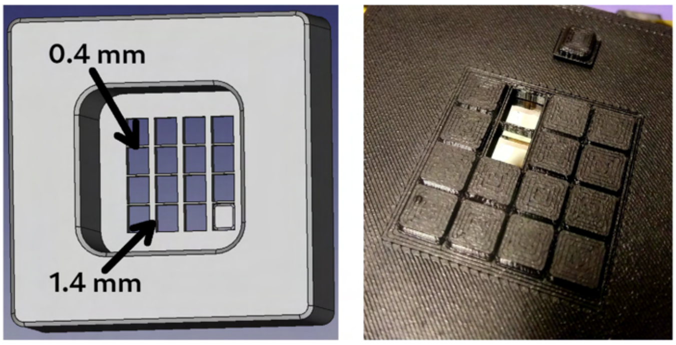

Fig. 5. The mask used to select the active channels using individual plugs. The dead space gap sizes at the channel boundaries are marked on the left.

head in use had a wavelength of 405.6 nm and 64.9 ps long pulses. The light from this laser was routed through neutral density filters (OD 0-8) and towards the PMT using two optical fibres with a solarized 200 μm core and an overall length of 2 m. The second fibre was either directly attached to the PMT front face through a fixed collimator to illuminate only the centre part of the channel (in the case of gain measurements, where we aim to eliminate any losses to neighbouring channels due to charge sharing) or routed to an adjustable focus collimator to expand the beam in a dark box over a distance of ∼ 50 cm to illuminate the PMT in a uniform fashion. A 3D printed custom mask (Fig. 5) was used to select the desired channels for illumination, leaving the rest covered. The mask replicated the shape and layout of the fused silica cherenkov bars used in the AFP ToF system (5×6 mm rectangles, centred over the PMT channels). A single channel or an entire column of four channels was used in the measurements, depending on what the goal was. The full column scenario represented the typical response of the AFP ToF system, where a series of four bars is hit by each passing particle.

The PMT body was wrapped with electromagnetic shielding tape and placed in an aluminium dark box to improve its shielding from outside interference. The signal pulse from the PMT was typically amplified using the custom broadband amplifiers with two stages (PAa+PAb) mentioned earlier and read out by an oscilloscope (LeCroy WavePro 806Zi-B with a 6 GHz bandwidth and a 40 GS/s sampling rate), which was triggered by the laser driver sync out signal.

4. Measurement design and results

4.1. Gain curves

Each PMT was subjected to several different measurements. The first one of those was always the gain curve measurement using the pulse charge method. This method is based on integrating the current from the PMT channel being tested when struck by a single photon. For signal to be produced at all, the photon needs to be converted to a photoelectron which in turn has to be accepted and multiplied by an MCP pore, therefore, passing both quantum and collection efficiencies. The charge is obtained by integrating the voltage waveform and dividing it by the known load of 50 Ω. Doing this with no amplifiers and with single photon events at high gain, we can divide the integrated charge by the elementary charge e to get the absolute gain. This is then repeated with amplifiers to get their precise gain. The amplifiers then allow us to measure at a lower PMT gain without losing the signal peak in noise. When the amplified single-photon pulse becomes too weak at around 1750 V, we continue with stronger light pulses of about 5 Pe detected, stitching the measurements together at that point (which is measured at both light levels). This stitching is done a second time at around 1600 V, switching to ∼ 50 P_e pulses that are observable even at gain as low as 10^3. The resulting gain curves are shown in Fig. 6.

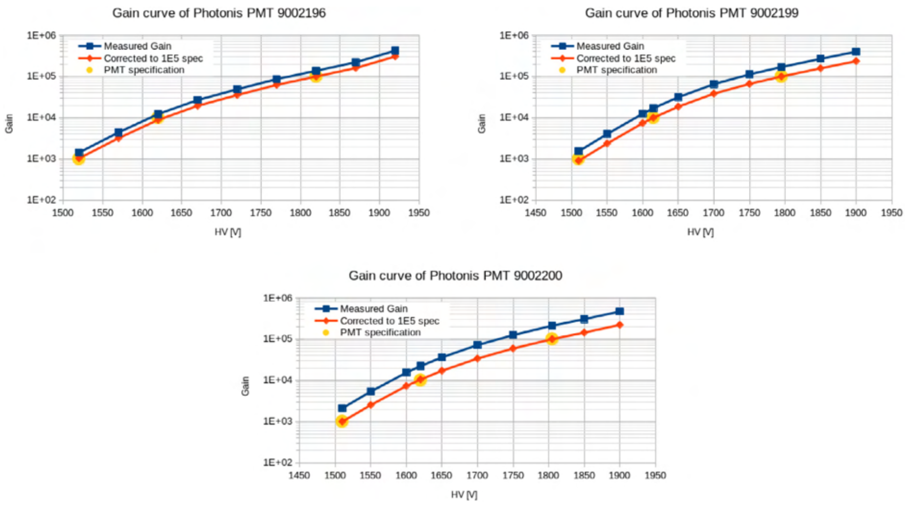

Fig. 6. Gain curves of the three PMTs subject to our tests. Yellow points come from the manufacturer's specification. The blue curve is our result with reference to the single-photon charge we measured; the red curve is that curve corrected to match the 10^5 gain point from the PMT specification.

The difference in the gain curves measured (blue) as compared to the specification points (yellow) can be attributed to different measurement methods (pulse charge vs current method used by the manufacturer) and the typical slightly changing gain of individual PMT channels. When the gain curve is corrected by a fixed factor to match the 10^5 gain point from the specification, it hits the other specification points with an error of only $1-4\,\%$ (red curve). This tells us the gain measurement was performed correctly and the differences can really be attributed to the measurement method. In particular, our pulse method excludes collection efficiency and takes into account only electrons which are collected and multiplied by the MCP. In contrast, the current method using constant illumination through which the specification was determined includes the collection efficiency in the results. In essence, the ratio between the two curves is a rough measurement of the collection efficiency, which is typically $\sim 50\,\%$ in this type of MCP-PMTs [13].

When the obtained gain curves are later used to determine the number of photoelectrons, only the ratio between the gains at two points on the curve is important and, therefore, the original and corrected curves yield the same results. However, one has to be careful which curve is used when setting up the gain of the PMT itself.

4.2. Timing resolution (TTS)

The timing resolution of the devices being tested was determined by measuring the transit time spread (TTS), the single photoelectron timing resolution. The highest gain data from gain curve measurement, where only single photons were typically detected, were used for this. All of the PMTs tested here have TTS of $38.8 \pm 0.5\,\text{ps}$ (measured as $42 \pm 0.5\,\text{ps}$ before laser pulse width subtraction). An example plot and the fit can be seen in Fig. 7.

4.3. Gain behaviour after high rate PMT saturation

As previously reported in [10], the earlier generation of single layer ALD treated long-life MCP-PMTs suffered from extended gain deterioration after being saturated by a high photon flux, which only slowly recovered to the original values. The tubes evaluated here use a double ALD layer (denoted as R2D2) and were subject to the same test which showed a completely different behaviour pattern. As can be seen in Fig. 8, the gain actually increases by up to $20\,\%$ when returning to low rates ($10\,\text{Hz}$) after a saturated state ($20\,\text{MHz}$ of $25\,\text{P}_\text{e}$ pulses for 1 min).

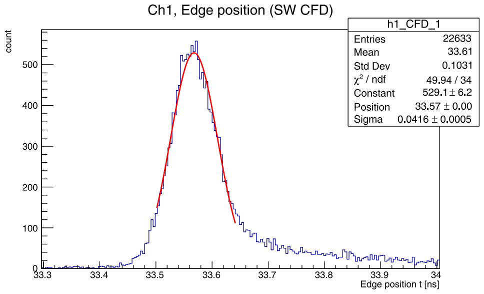

Fig. 7. TTS of PMT 2196 at 1920 V. The tail on the right of the peak is caused by photoelectrons that bounce from the MCP front face and are accepted by a pore later [14]. When the histogram range is extended to cover the whole tail (spanning $\sim 2.5\,\text{ns}$), the RMS rises to $0.29\,\text{ns}$.

The recovery does not reach the original value within the 30-minute test and seems instead to stabilize at $110\,\%$ according to the fit parameters. However, when the PMT is not powered, the recovery is accelerated compared to this measurement and gain reaches the original value under half an hour (deviation of less than $1\,\%$ from the pre-saturation level). This information was utilized when preparing the measurement protocol for the rate capability tests (inserting waiting periods of 30 min) in order to prevent the influence of previous high-rate measurements on the baseline gain.

4.4. Rate capability

The rate capability of the PMT is of the utmost importance in our ToF system. The rates of incoming protons passing the detector may reach $20\,\text{MHz}$ in Run 3 of the LHC as the luminosity at interaction points is increased. Thus, we need to show that the PMTs can operate under these conditions without losing too much gain (manifesting as

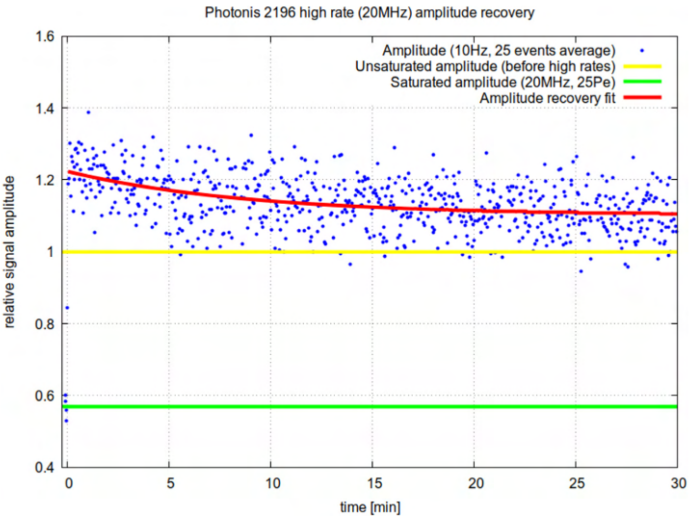

Fig. 8. Gain behaviour of PMT 2196 when recovering from saturation, seen as changes in mean amplitude. The 25 P_e pulse rates were reduced from 20 MHz ($\sim 1\ \mu A/cm^2$) to 10 Hz at $t = 0$. Each blue dot represents the average amplitude of 25 pulses for better plot clarity. The point near $t = 0$ at ~ 0.85 contains partially high and low rate data and is, therefore, an artefact of the switch to low rates.

a lower efficiency of our ToF system) or timing resolution. To aid the rate capability, we use a low PMT gain of 2000 (with respect to the red, current method gain curves in Fig. 6, corresponding to ∼ 4000 pulse gain, which excludes collection efficiency). With the expected number of photoelectrons of 20−30 per proton in each channel hit and a 20 MHz detection rate, the required rate capability is $\sim 1\ \mu A/cm^2$ in terms of anode current density.

As four channels in a row are hit in a typical detection event, we set up our channel mask accordingly to open a single row of channels across the PMT. This has the most impact on the timing measurement by allowing for the averaging of the four channels, but it has only a marginal impact on the rate limit [10], as the charge per area is the same as if a single channel had been opened only.

The number of photoelectrons (P_es) in the measured channels was determined as the ratio of the median area under waveform as compared to a single P_e measurement, using the gain curve to correct for the PMT gain difference (single P_e measurements require high gain $\geq 10^5$). We aimed to obtain data at P_e of 25 and 50, with some small variations across the PMTs due to setup (filter) limitations.

The rate scans were performed from 10 kHz up, with this lowest rate point serving as a reference for the relative gain determination. The gain ratio was calculated using the median area under waveform values. If, however, a simple amplitude was used instead, the results would have been essentially identical.

Fig. 9 shows the relative gain dependence on the pulse rate, where the gain starts to deteriorate at several MHz, varying across the PMT pieces and the number of $P_e s$ in the pulse. We can easily see that at comparable P_e, the MCP resistance has a significant influence on the rate limit, with the lower values allowing for higher rates without the gain suffering. A comparison of the gain behaviour and the timing resolution can be found in Table 1.

The timing resolution results originate from the same measurement set and, therefore, the same considerations about P_es apply. The arrival time of the pulse is determined through a software CFD (constant fraction discriminator), thus removing time walk by triggering at 42 % of the pulse height, which was previously determined to yield the best results. A minimum amplitude cut of 12 mV was used as a cut-off threshold for the events, resulting in > 99 % efficiency at sufficient light levels of $\sim 20 P_e$ or more.

Table 1
Train (4 channel average) timing resolution and relative gain of each PMT when subjected to 10 kHz and 20 MHz pulses of $\sim 25\,P_e$ ($\sim 0.5\,nA/cm^2$ and $\sim 1\ \mu A/cm^2$).

PMT	MCP R	σ_t (10 kHz)	σ_t (20 MHz)	Gain ratio (20 MHz/10 kHz)
2196	44 MΩ	22.5 ps	39.5 ps	0.58
2199	35 MΩ	22.8 ps	22.8 ps	1.07
2200	27 MΩ	14.8 ps	16.3 ps	0.99

The timing resolution strongly depends on the number of P_es, as can be seen in Fig. 10. The train combination (average of arrival times of the four channels forming a train) improves the timing significantly, as expected. In all cases, the timing starts to deteriorate at roughly the same rates as the gain, which can be seen by comparing Figs. 9 and 10.

4.5. *Crosstalk*

As we mentioned in the Introduction, we have studied electronic crosstalk and the crosstalk by charge sharing as separate effects. Whilst the electronic crosstalk from a channel affects all the others approximately to the same extent, the charge sharing takes place only in the immediate vicinity. As the footprint of the ToF bars on the PMT and, therefore, also of the mask openings are asymmetric, we expect to see less charge sharing in the direction where there is a larger width covered/not illuminated (dead area) at the channel boundaries (1.4 mm) as compared to the smaller width (0.4 mm). The smaller anode gap is then expected to give the electrons leaving the MCP less room to spread, reducing the charge sharing in all directions.

The crosstalk measurements were again performed using the channel mask, but with only a single channel open. Four channels were still monitored with the oscilloscope: the open channel, one of its direct neighbours in either direction (where charge sharing and electronic crosstalk mix) and one channel far away (influenced only by electronic crosstalk). A schematic illustration of the channel layout can be seen in Fig. 11.

The results match the expectations, as can be seen in Fig. 12 and Table 2. Both the reduced anode gap and a wider channel boundary dead area contribute to reducing the crosstalk. In our specific case, the

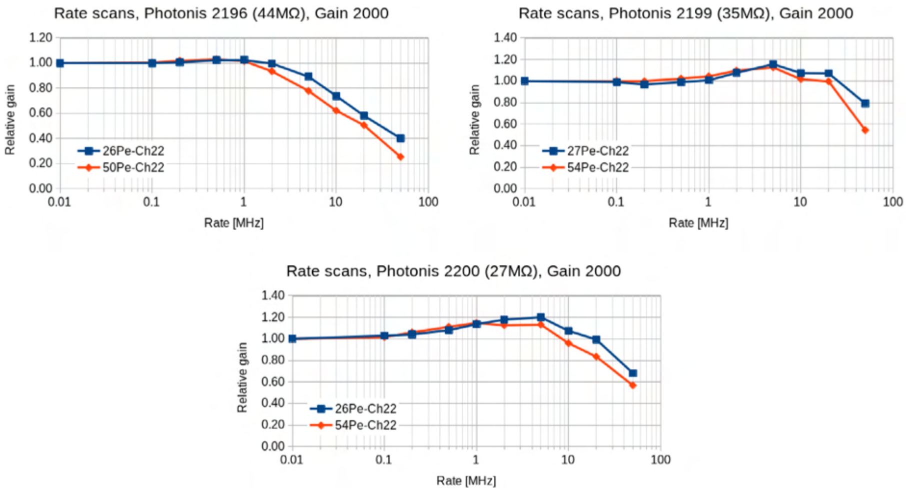

Fig. 9. Relative gain during rate scans. Relative gain values at 20 MHz are in Table 1. 20 MHz rate of ∼ 25 P_e pulses corresponds to anode current of ∼ 1 μA/cm^2.

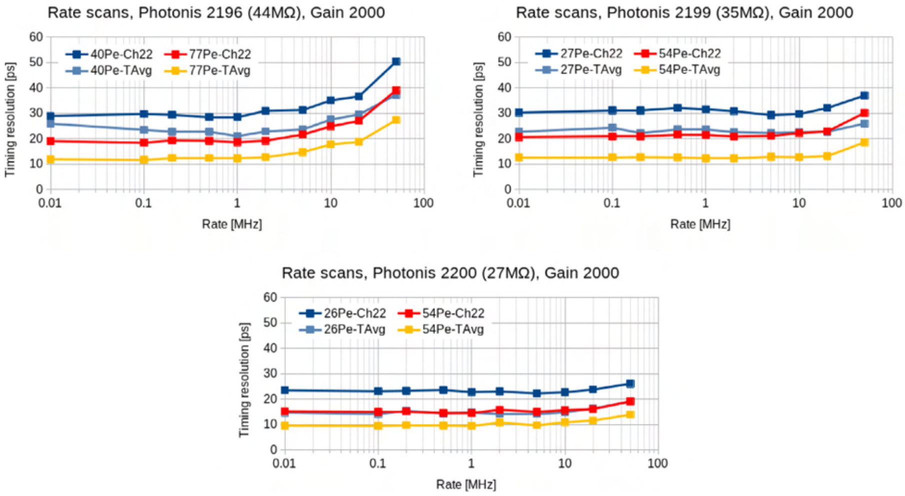

Fig. 10. Timing resolution of the detector during rate scans. The TAvg timing is determined as a train (4 channels in a row) average, relevant to our use case. Actual values at 10 kHz and 20 MHz are in Table 1. 20 MHz rate of ∼ 25 P_e pulses corresponds to anode current of ∼ 1 μA/cm^2.

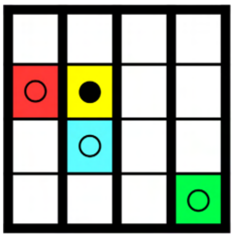

Fig. 11. The layout of observed channels during crosstalk measurements. All the channels that are observed are marked with a circle. The sole channel which is illuminated as well as monitored is marked with a filled circle. The colours correspond to the colour coding in Fig. 12.

Table 2
Charge sharing strength as compared to the primary channel signal.

Channel spacing	Standard anode gap	Reduced anode gap
In train (0.4 mm)	7.5 %	5.5 %
Next train (1.4 mm)	5.0 %	3.0 %

narrow gaps between the ToF bars are along the train, which means the channels are hit together by a single event. As the ToF optical part is designed in such a way that the light from these channels reaches the PMT at the same time, any charge sharing does not present an issue. In the direction across trains, the dead area is wider, limiting the possible charge sharing magnitude and thus producing fewer fake triggers in trains that are neighbours to the one really hit with a proton.

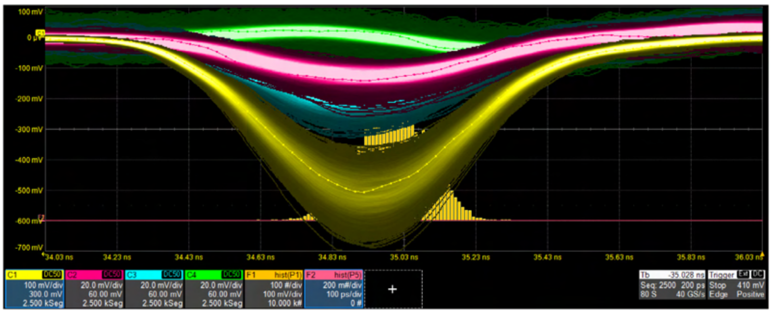

Fig. 12. An example of waveforms during the crosstalk measurement of PMT 2199. The yellow waveform (C1) is the illuminated channel; red (C2) is the neighbour across trains; and blue (C3) the neighbour in the same train (charge sharing is the dominant source of crosstalk in C2 and C3). Green (C4) is a channel far away from the one with light, exhibiting the electronic crosstalk only. The colouring scheme follows Fig. 11. Note the different vertical scale on C1 (illuminated channel), shrunk by a factor of 5 compared to the crosstalk channels.

The green (C4) waveform in Fig. 12 is the aforementioned electronic crosstalk which manifests as a weak pulse with reversed polarity. This is caused by the inherently imperfect grounding of the shared ground, which is then briefly influenced by the fast signal. Such crosstalk is present in all channels at a similar magnitude of 1.5 % of the signal pulse, but is inseparable from the signal where some crosstalk is present, while influencing its edge and amplitude. For this reason, the proportion of charge sharing is in reality slightly higher than in Table 2, but with respect to the threshold tuning and real detector operation, the values in the table are more relevant than the ones with such correction in place would be.

5. Discussion

Gain curves were determined using the pulse charge method and when corrected for a small, fixed factor difference due to different methods used, they match the gain points specified by the manufacturer very well (a deviation of 1–4 %). These gain curves were later used to determine the proper HV for target gain and to calculate the average number of photoelectrons in each measurement.

The single photoelectron timing resolution (TTS) was determined to be 38.8 ± 0.5 ps in all three pieces. This is about 10 ps worse than most of the devices we tested so far, which were typically just below 30 ps [10,14].

When comparing tubes with a similar MCP R, the rate capability of these PMTs slightly exceeds the XPM85212/A1-S performance we reported on in [10] There a 36 MΩ tube exhibited a 20 % gain drop already at 1.38 $\mu A/cm^2$, whereas the 2199 tested here with an almost equivalent MCP R of 35 MΩ MCP exhibits the same gain drop at 2.5 $\mu A/cm^2$. The rate capability again depends strongly on the resistance of the MCP (ones with lower R are handling higher rates better), as expected. At 20 MHz with ∼ 25 photoelectrons (∼ $1 \mu A/cm^2$), the two PMTs with the lower resistance (27 MΩ, 35 MΩ) have only a negligible loss of gain whereas the third one (44 MΩ) has a loss of gain that is not detrimental to its overall performance. The timing resolution is noticeably impacted only at rates where the gain is starting to be impacted as well. The PMTs can work well at these high rates, particularly thanks to the low gain operation, which draws less charge per pulse from the MCP.

The PMTs do not exhibit the prolonged gain drop as those evaluated in [10]. On the contrary, after being subject to high rates, the gain is actually temporarily increased. This phenomenon can also explain the gain rise in rate capability plots in Fig. 9. The PMT 2196, which is not able to perform at high rates so well, exhibits a different type of behaviour — the gain bump is not explicitly visible in the rate plots, but it contributes instead only to a less steep initial gain decline, since the bump probably occurs at similar rates for all PMTs while keeping the gain equivalent. In order to remove the impact of this gain change effect induced by high rate saturation, all measurements were done with waiting periods of 30 min between them.

The crosstalk between the channels was measured as two separate effects. One part is electronic, originating in the capacitive couplings between channels and ground rebound. This has the same impact on all channels within the PMT and is proportional to the primary pulse amplitude (∼ 1.5 %). The second effect is charge sharing within the PMT, where parts of the generated electron spray hit adjacent anode pads. This strongly depends on the geometry, specifically how close to the channel boundary photons are allowed to land, and also on the anode gap size (a shorter gap means less spreading of the electrons leaving the MCP and less charge sharing).

6. Conclusion

Three pieces of miniPlanacon XPM85112-S-R2D2 MCP-PMTs with modified backend electronics were tested. The tests were performed using a picosecond laser setup, with the focus on timing resolution, while rate capability and crosstalk, gain curves were also determined.

The rate capability of each PMT strongly depends on its MCP resistance, as expected. Low PMT gain operation also allows them to reach a high rate capability, while more focus has to be directed towards proper shielding from interference to maintain a reasonable signal-to-noise ratio. When the PMTs are saturated with too much light, gain starts to drop, and the timing resolution is negatively impacted as well. Recovery from the PMT saturation happens through temporarily increased gain which returns to normal in under half an hour if the PMT is not powered.

Crosstalk between the channels was determined to consist of two types: one with influence over the whole PMT (ground rebound) and the other with influence only on its direct neighbours (charge sharing). The latter is heavily influenced by the anode gap size (a smaller gap allows for less electron spread) and the geometry of the illuminated area of each channel.

Funding

The authors gratefully acknowledge the support from the Operational Programme Research Development and Education – European Regional Development Fund, project no. CZ.02.1.01/0.0/0.0/16_019/0000754 of the Ministry of Education, Youth and Sports of the Czech Republic (MSMT); Research Infrastructure for experiments at CERN

LM 2018104 (MSMT); Getting new knowledge of the microworld using the CERN infrastructure LTT17018 (MSMT); Palacky University IGA_PrF_2022_004; and the U.S. Department of Energy DE-SC0011686.

Declaration of competing interest

The authors declare that they have no known competing financial interests or personal relationships that could have appeared to influence the work reported in this paper.

Data availability

Data will be made available on request.

References

[1] A. Lehmann, M. Böhm, A. Britting, W. Eyrich, M. Pfaffinger, F. Uhlig, A. Belias, R. Dzhygadlo, A. Gerhardt, K. Götzen, G. Kalicy, M. Krebs, D. Lehmann, F. Nerling, M. Patsyuk, K. Peters, G. Schepers, L. Schmitt, C. Schwarz, J. Schwiening, M. Traxler, M. Zühlsdorf, M. Düren, E. Etzelmüller, K. Föhl, A. Hayrapetyan, B. Kröck, O. Merle, J. Rieke, M. Schmidt, T. Wasem, E. Cowie, T. Keri, P. Achenbach, M. Cardinali, M. Hoek, W. Lauth, S. Schlimme, C. Sfienti, M. Thiel, Recent developments with microchannel-plate PMTs, Nucl. Instrum. Methods A 876 (2017) 42–47.

[2] P. Inc., Photomultiplier Tubes: Principles and Applications, Photonis, Brive, France, 2002.

[3] C. Ertley, O. Siegmund, T. Cremer, C. Craven, M. Minot, J. Elam, A. Mane, Performance studies of atomic layer deposited microchannel plate electron multipliers, Nucl. Instrum. Methods A 912 (2018) 75–77.

[4] A. Lehmann, M. Böhm, W. Eyrich, D. Miehling, M. Pfaffinger, S. Stelter, F. Uhlig, A. Ali, A. Belias, R. Dzhygadlo, A. Gerhardt, K. Götzen, G. Kalicy, M. Krebs, D. Lehmann, F. Nerling, M. Patsyuk, K. Peters, G. Schepers, L. Schmitt, C. Schwarz, J. Schwiening, M. Traxler, M. Düren, E. Etzelmüller, K. Föhl, A. Hayrapetyan, K. Kreutzfeld, O. Merle, J. Rieke, M. Schmidt, T. Wasem, P. Achenbach, M. Cardinali, M. Hoek, W. Lauth, S. Schlimme, C. Sfienti, M. Thiel, Lifetime of MCP-PMTs and other performance features, J. Instrum. 13 (2018) C02010.

[5] J. Lange, L. Adamczyk, G. Avoni, E. Banas, A. Brandt, M. Bruschi, P. Buglewicz, E. Cavallaro, D. Caforio, G. Chiodini, L. Chytka, K. Ciesla, P. Davis, M. Dyndal, S. Grinstein, K. Janas, K. Jirakova, M. Kocian, K. Korcyl, I. Paz, D. Northacker, L. Nozka, M. Rijssenbeek, L. Seabra, R. Staszewski, P. Swierska, T. Sykora, Beam tests of an integrated prototype of the ATLAS forward proton detector, J. Instrum. 11 (2016) P09005.

[6] L. Nozka, A. Brandt, M. Rijssenbeek, T. Sykora, T. Hoffman, J. Griffiths, J. Steffens, P. Hamal, L. Chytka, M. Hrabovsky, Design of Cherenkov bars for the optical part of the time-of-flight detector in Geant4, Opt. Express 22 (2014) 28984–28996.

[7] L. Nozka, A. Brandt, K. Cerny, M. Hrabovsky, T. Komarek, F. Krizek, D. Mandat, M. Milovanovic, M. Rijssenbeek, P. Schovanek, T. Sykora, V. Urbasek, J. Zatloukal, Performance studies of new optics for the time-of-flight detector of the AFP project, Opt. Express 28 (2020) 19783–19796.

[8] K. Cerny on behalf of the ATLAS Collaboration, Performance study of the ATLAS forward proton time-of-flight detector system, in: The 28th International Workshop on Vertex Detectors 2020, 2020, p. 055.

[9] T. Sykora on behalf of the ATLAS Collaboration, ATLAS forward proton time-of-flight detector: LHC Run2 performance and experiences, J. Instrum. 15 (2020) C10004.

[10] T. Komarek, V. Urbasek, A. Brandt, V.A. Chirayath, V. Chytka, M. Hrabovsky, L. Nozka, M. Rijssenbeek, T. Sykora, Timing resolution and rate capability of photonis miniplanacon XPM85212/A1-S MCP-PMT, Nucl. Instrum. Methods A 985 (2021) 164705.

[11] Yu.A. Melikyan on behalf of ALICE Collaboration, Performance of Planacon MCP-PMT photosensors under extreme working conditions, Nucl. Instrum. Methods A 952 (2020) 161689.

[12] K. Inami, T. Mori, T. Matsumura, S. Kurimoto, Y. Suzuki, T. Murase, Y. Yurikusa, M. Akatsu, Y. Enari, T. Hokuue, A. Tomita, N. Kishimoto, T. Ohshima, T. Ihara, H. Nishizawa, Cross-talk suppressed multi-anode MCP-PMT, Nucl. Instrum. Methods A 592 (2020) 247–253.

[13] D. Orlov, T. Ruardij, S.D. Pinto, R. Glazenborg, E. Kernen, High collection efficiency MCPs for photon counting detectors, J. Instrum. 13 (01) (2018) C01047, http://dx.doi.org/10.1088/1748-0221/13/01/c01047, URL https://doi.org/10.1088/1748-0221/13/01/c01047.

[14] A.G. Brandt, Development of a 10 Picosecond Time-of-Flight Counter, Tech. Rep., Univ. of Texas, Arlington, TX (United States), 2010, http://dx.doi.org/10.2172/973786, URL https://www.osti.gov/biblio/973786.

Nuclear Inst. and Methods in Physics Research, A 935 (2019) 51–55

Contents lists available at ScienceDirect

Nuclear Inst. and Methods in Physics Research, A

journal homepage: www.elsevier.com/locate/nima

Time resolution of the SiPM-NUV3S

Ladislav Chytka [a,*], Miroslav Hrabovský [a], Tomáš Komárek [a], Václav Michálek [a], Libor Nožka [a], Tomáš Sýkora [b], Vladimír Urbášek [a]

[a] *Palacky University, Faculty of Science, RCPTM, Joint Laboratory of Optics of Palacký University and Institute of Physics of the Academy of Sciences of the Czech Republic, 17. listopadu 12, 771 46, Olomouc, Czech Republic*

[b] *Charles University in Prague, Faculty of Mathematics and Physics, Institute of Particle and Nuclear Physics, V Holesovickach 2, CZ — 18000 Praha 8, Czech Republic*

ARTICLE INFO

Keywords:
Silicon photomultiplier (SiPM)
Multi pixel photon counter (MPPC)
Cherenkov time-of-flight
Femtosecond laser pulse

ABSTRACT

Silicon photomultipliers (SiPMs) have become an interesting alternative to conventional and micro-channel plate photomultipliers, proving to be a very good option for Cherenkov light based time-of-flight detectors. The important characteristic for this application is the intrinsic time resolution for a wide range of wavelengths (from below 250 nm up to about 600 nm).

We present a study of the time resolution of two SiPMs: a 3×3 mm^2 FBK SiPM-NUV3S and a 3.5×3.5 mm^2 STMicroelectronics prototype SiPM. The measurement was performed for two representative wavelengths (280 nm and 420 nm) under the variation of SiPM overvoltage and light intensity.

The measured transition time spread (TTS) of the devices was (285 ± 9) ps (FBK) and (154 ± 20) ps (STM). The time resolution dropped with increasing mean number of photoelectrons (N_{pe}) as $\sigma_{\mathrm{TTS}} N_{\mathrm{pe}}^{-\frac{1}{2}}$ with saturation observed for high N_{pe}. The obtained best time resolutions were (8 ± 1) ps and (4 ± 1) ps for the FBK and STM SiPM respectively at N_{pe} of the order of 10^6 for 420 nm photons. The results for the two wavelengths were comparable, with 280 nm photons providing worse results at very high illumination.

1. Introduction

Silicon photomultipliers – matrices of avalanche photodiodes connected in parallel – have proved to be a very good option for Cherenkov time-of-flight (ToF) detectors [1,2]. Such a detector consists of a photosensor coupled to a radiator bar with high refraction index, transparent to ultraviolet light, in which Cherenkov photons are produced when a charged relativistic particle traverses it. In this application, it is the intrinsic timing resolution of the SiPM that, together with the light yield of the radiator, determines the timing properties of the detector as a whole.

During the development of the ToF system of the ATLAS Forward Proton (AFP) detector [3], currently installed at the Large Hadron Collider at CERN, a 3.5×3.5 mm^2 SiPM produced by STMicroelectronics (NRD09_1, 58 $\times$58 μm cell size) was utilized. It was coupled with a 3 cm long quartz Cherenkov radiator and served as a timing reference. It reached a time resolution of 11 ps [2].

Since the STM NRD09_1 is no longer produced, we were examining a possible replacement. Taking into account their performance in the MEG II scintillation detector [4] and low price, we measured the properties of a 3×3 mm^2 SiPM manufactured by FBK (SiPM-NUV3S [5], 40 $\times$40 μm cell size), capable of detecting light in near ultra-violet spectrum, with a focus on the time resolution under variation of the light intensity, overvoltage and light wavelength. Time resolutions were compared to those of the STM NRD09_1.

Cherenkov radiators produce light of wavelengths from below 250 nm and the light yield increases with decreasing wavelength down to a limit given by the radiator material [6]. Therefore, it is important to know the timing properties not only near the peak efficiency (420 nm for the FBK SiPM-NUV3S) but also for the deeper UV region. Here we present a comparison of timing properties of the SiPMs for 420 nm and 280 nm wavelengths.

2. Methods

2.1. Measurement setup

We used a Coherent Mira 9000 laser system with 2nd (420 nm) and 3rd (280 nm) harmonic generation with the pulse width of 150 fs as light source. The laser beam was coupled into an optical fiber splitter (Y) cable. Coupling was adjusted such that the two outputs of the fiber splitter had an equal intensity (with observed deviation within 10% of the output power). One output was fed into a reference SiPM (another STM NRD09_1) which was used as the trigger. The other output was attenuated by a set of neutral density (ND) filters and detected by the

---

[*] Corresponding author.
E-mail address: ladislav.chytka@upol.cz (L. Chytka).

https://doi.org/10.1016/j.nima.2019.04.082
Received 13 June 2018; Received in revised form 18 April 2019; Accepted 23 April 2019
Available online 9 May 2019
0168-9002/© 2019 Elsevier B.V. All rights reserved.

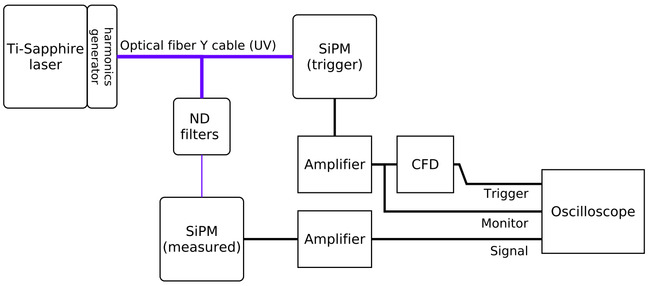

Fig. 1. The scheme of the measurement setup. Boxes with round corners represent optical components and SiPMs, rectangles stand for electronic devices.

SiPM under test. A circular area with 3 mm diameter was illuminated for both SiPMs. The scheme of the setup is illustrated in Fig. 1.

The outputs from both the measured and the triggering SiPMs were amplified by two-stage 32 dB low-noise broadband pre-amplifiers.[1] A third amplifier with the amplification of 16 dB was added for the measured STM SiPM. The amplified signal from the triggering SiPM was split. One output was used for a direct monitoring and the other was processed by a constant fraction discriminator (CFD) made by University of Alberta [7] to reduce the trigger jitter. The constant fraction was set to 42% tuned to minimum jitter. The data acquisition was handled by LeCroy WavePro 7200 A oscilloscope with 2 GHz bandwidth and 10 GS/s sampling frequency. The SiPMs were powered by TTi QL564TP power supply.

The second output of the triggering SiPM was used to ensure a stable laser output: the amplitude of the monitoring signal was kept constant between measurements and the shape of the monitoring signal was observed for a possible laser instability. The trigger jitter, including the readout of the reference SiPM, was determined to be $(4 \pm 1)\,\mathrm{ps}$ for the 420 nm photons and $(8 \pm 1)\,\mathrm{ps}$ for the 280 nm photons.

Measurements were performed in an air-conditioned laboratory at the temperature of 23 °C stabilized within 1 °C. The SiPMs were not thermally stabilized to keep the detector simple. Each SiPM was encapsulated in an aluminum box connected by an aluminum bracket to an optical breadboard, and the SiPMs were placed in a dark box with feedthroughs for cables and optical fibers.

2.2. Estimation of the number of photoelectrons

The mean number of photoelectrons (N_{pe}) produced in an illuminated SiPM was estimated from the Poissonian probability of pedestal events with subtraction of dark pulses [8] as

$$N_{\mathrm{pe}} = -\ln \frac{N_{\mathrm{ped}}}{N_{\mathrm{tot}}} + \ln \frac{N_{\mathrm{ped}}^{\mathrm{dark}}}{N_{\mathrm{tot}}^{\mathrm{dark}}}, \tag{1}$$

where N_{ped} is the number of recorded events without a pulse (i.e. pedestal events), N_{tot} is the total number of collected events and $N_{\mathrm{i}}^{\mathrm{dark}}$ expresses the corresponding numbers for the case without illumination of the SiPM.

The pedestal threshold was set to 0.5 photoelectron level, determined from the dark pulse amplitude for each bias voltage applied to the measured SiPM.

Eq. (1) is usable up to $N_{\mathrm{pe}} \approx 10$ due to the acquired total number of events from 10^4 to $3 \cdot 10^4$. For higher light intensities, we extrapolated the N_{pe} estimate based on the optical density value of the used ND filters: first, the number of photons before the ND filters was estimated[2] ($N_i = N_{\mathrm{pe},i} \cdot 10^{d_i}$, where d_i is the ith filter optical density value and $N_{\mathrm{pe},i}$ is the corresponding N_{pe} value determined from Eq. (1)) for each filter value for which it was possible to estimate N_{pe} using Eq. (1) and average $\bar{N}$ was calculated; then N_{pe} estimate for a filter optical density d was calculated from $N_{\mathrm{pe}} = \bar{N} \cdot 10^{-d}$. The procedure was applied separately for each SiPM and each wavelength.

2.3. Time resolution analysis

We used broadband amplifiers to preserve pulse shapes and the amplified pulses were captured as the full waveforms using the oscilloscope.

The acquired waveforms were preprocessed to obtain an optimal timing performance and to minimize the electronic jitter contribution. First, a low-pass filter was applied to cut off high frequency interferences. Then, the 0.5 photoelectron threshold was applied to remove pedestal events.

After the preprocessing, we used a constant fraction discriminator algorithm implemented in the analysis software (with the constant fraction set to 42% corresponding to the hardware CFD) to determine the time of the pulse detection with respect to the time of the trigger. The time resolution was obtained from a Gaussian fit to the signal time distribution.

Examples of time distributions are shown in Fig. 2. It is evident that, for the single photoelectron case, there are pronounced tails caused by delayed photoelectrons, uniformly distributed dark pulses and electronic noise fluctuations superimposed to the time distribution of the photoelectrons generated by the laser. The Gaussian fit was performed iteratively around the central part of the distribution to measure the time resolution without the influence of delayed photoelectrons and dark pulses. This influence decreased with increasing number of photoelectrons, as can be seen in the right part of Fig. 2.

The contribution of the trigger and the electronics jitter to the time resolution is subtracted in quadrature in the values and plots that follow.

The low-pass filter cut-off frequency was optimized for each SiPM to obtain the best time resolution. The optimal value was found to be 900 MHz for the FBK SiPM and 1400 MHz for the STM device. In the text below, we quote an overvoltage (OV) value $V_{\mathrm{OV}} = V_{\mathrm{bias}} - V_{\mathrm{BD}}$, where V_{bias} is the voltage applied to the SiPM and the breakdown voltage V_{BD} was measured to be 28.1 V for the STM SiPM and 26.6 V for the FBK device.

The time resolution is expected to behave as $\sigma_{\mathrm{TTS}} N_{\mathrm{pe}}^{-\frac{1}{2}}$ [9], where TTS stands for Transit Time Spread, i.e. the time spread of transition of single photoelectrons, with saturation at high N_{pe} values. The saturation originates from an internal electronic jitter (labeled σ_{const} in the formula below) of an SiPM, which needs to be added in quadrature to describe the measured points as a function of N_{pe}. Therefore, we fit the distribution of time resolution vs. N_{pe} with

$$\frac{\sigma_{\mathrm{TTS}}}{\sqrt{N_{\mathrm{pe}}}} \oplus \sigma_{\mathrm{const}} \equiv \sqrt{\frac{\sigma_{\mathrm{TTS}}^2}{N_{\mathrm{pe}}} + \sigma_{\mathrm{const}}^2}. \tag{2}$$

---

[1] produced by Stony Brook University [7].

[2] The photodetection efficiency was neglected, as it is assumed not to change under varying illumination.

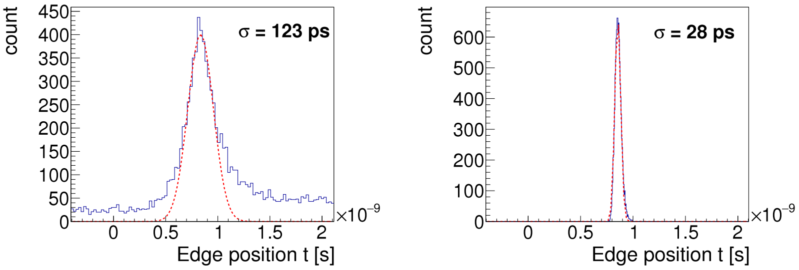

Fig. 2. A typical time distribution for a single photoelectron (left) and a high number of photoelectrons (right). Histograms show time distributions for STM SiPM operated at 2.9 V overvoltage and illuminated by 420 nm laser light for $N_{\mathrm{pe}} = 1.2$ (left) and $N_{\mathrm{pe}} = 270$ (right). The Gaussian fits from which the time resolution was extracted are represented by the dashed red line.

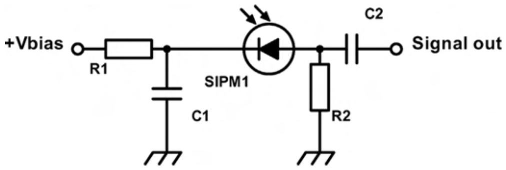

Fig. 3. Circuit diagram of the SiPM connection.

2.4. Time resolution uncertainty estimate

We found that the influence of the electronic noise originating from electronic components in the SiPM connection (Fig. 3) cannot be neglected, especially for the single photoelectron illumination. The main source of the noise is the 1 kΩ load resistor (R2 in Fig. 3) due to the Johnson–Nyquist noise. This influence is the main contribution to the systematic uncertainty.

We evaluated the noise contribution using simulated pulses superimposed to the measured noise. We generated a set of samples with different mean pulse amplitudes. All the pulses were generated at a fixed time with zero time smearing. The noise sample acquired for the SiPM was then superimposed to each Monte Carlo sample and the time uncertainty was determined for each case. The uncertainty was found to be inversely proportional to the mean pulse amplitude A (in V) according to $\frac{6.8\pm0.2}{A} + (1.5 \pm 0.2)$ ps.

The systematic uncertainty is included in the following values and plots.

3. Results

3.1. Time resolution

Fig. 4 plots the dependence of the time resolution on N_{pe} and V_{OV}. The time resolutions of both SiPMs follow very well the $\sigma_{\mathrm{TTS}} N_{\mathrm{pe}}^{-\frac{1}{2}} \oplus \sigma_{\mathrm{const}}$ law (the lines in the figure show the fit results). Both SiPMs show a similar behavior for the two wavelengths.

To determine the best possible resolution with the available illumination, we removed the ND filters and subsequently obtained N_{pe} of the order 10^6 for 420 nm photons with corresponding time resolutions of (8 ± 1) ps and (4 ± 1) ps for the FBK and STM SiPM, respectively. For 280 nm photons, N_{pe} was of the order 10^4 and we obtained the resolutions of (27 ± 1) ps (FBK) and (8 ± 1) ps (STM). The SiPMs were operated just below the V_{BD} for this measurement.

The right part of Fig. 4 shows the dependence of the time resolution on the increasing V_{OV}. The STM photosensor resolution decreases up to $V_{\mathrm{OV}} = 2.9$ V and then levels off. The maximum values of 68 ps and 75 ps for 280 nm photons and 420 nm photons, respectively, decrease down to 36 ps (280 nm photons) and 52 ps (420 nm photons). The FBK device shows significant changes for different V_{OV} values, but there is no clear monotonic trend. For 280 nm photons the minimum time resolution is 60 ps and the maximum is 69 ps. For 420 nm photons the minimum time resolution is 73 ps and the maximum is 83 ps. The results are not directly comparable between wavelengths, as the N_{pe} estimate varies.

To justify the usage of Gaussian widths σ to quantify time resolutions, Fig. 5 plots the correlation between the time resolution expressed in σ obtained from the Gaussian fit and the full width at half-maximum (FWHM) value of the time distribution. For the ideal Gaussian, the linear fit $\mathrm{FWHM} = K \cdot \sigma$ should yield $K \approx 2.35$. The values are lower for both SiPM types, but the deviation is small (below 5%). The deviation is caused by the tails of the time distributions, as can be seen in Fig. 2, the tails slightly broaden the fit even in case of abundant photoelectrons (the peak of the distribution is visible above the fit line).

3.2. Single photon response

Single photon measurements were performed for $N_{\mathrm{pe}} \approx 1$ in order to estimate σ_{TTS}. However, the level of the electronic noise was close to 0.5 photoelectron level of the SiPM signal and induced significant smearing of the pulse amplitude as well as the time jitter. Therefore, it was not possible to select only 1 photoelectron events based on the signal amplitude. The time jitter was included as a systematic uncertainty based on the simulation described above.

Fig. 6 plots measured single photon time resolution as a function of V_{OV}. The results show very similar values for both wavelengths with minimal TTS of (223 ± 92) ps for FBK SiPM and (123 ± 30) ps for the STM one. The two SiPMs show a different dependence on V_{OV}: while the STM TTS is slightly improving up to $V_{OV} = 2.9$ V, the TTS of FBK SiPM is increasing. In all cases, the decreasing size of the error bars illustrates mainly the increasing signal-to-noise ratio as the 1 photoelectron amplitude increases, although a contribution from increasing photodetection efficiency is also observed in the decreasing statistical uncertainty.

4. Discussion

As seen in Fig. 4, the time resolutions follow the law $\sigma_{\mathrm{TTS}} N_{\mathrm{pe}}^{-\frac{1}{2}} \oplus \sigma_{\mathrm{const}}$. For the σ_{TTS}, however, all measured points for $N_{\mathrm{pe}} \approx 1$ fall lower than the fit parameters suggest. This is because these points underestimate σ_{TTS}, since the time resolution for $N_{\mathrm{pe}} \approx 1$ comprises also contributions from events with more photoelectrons with probability given by the Poisson distribution with mean value of 1. Due to the noise influence, it was not feasible to decrease the light intensity. Even though the difference in TTS is within uncertainties of the fit and measured values, the fit values provide more reliable measurement of σ_{TTS}.

The measurements with a very large N_{pe} (10^4–10^6) provide estimate of the σ_{const} in Eq. (2), as the first term of Eq. (2) is negligible for

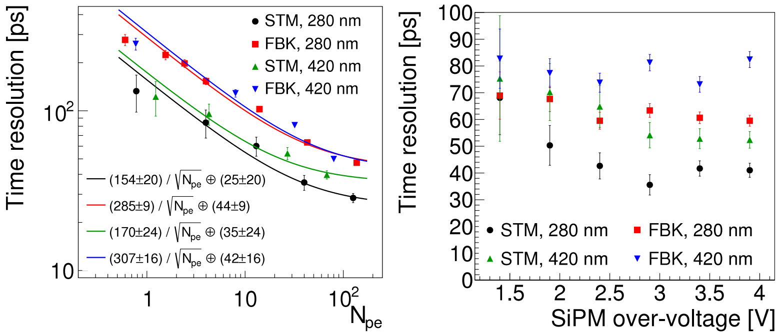

Fig. 4. Time resolution dependence on N_{pe} for the $V_{\mathrm{OV}} = 2.9\,\mathrm{V}$ (left); the resolution as a function of V_{OV} for N_{pe} in range 20–30 for 420 nm photons and 35–45 for 280 nm photons (right). N_{pe} calculation changes at $N_{\mathrm{pe}} \approx 10$, as described in Section 2.2.

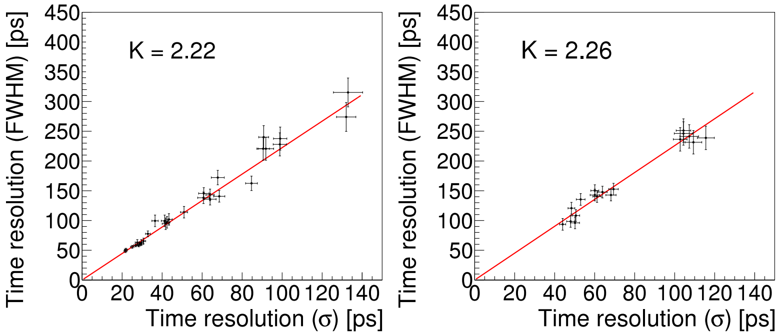

Fig. 5. Correlation between the time resolution expressed in σ obtained from the Gaussian fit and the full width at half-maximum (FWHM) value of the time distribution. The values are fitted by $\mathrm{FWHM} = K\sigma$. The fit is represented by the red line. Left: STM SiPM; right: FBK SiPM.

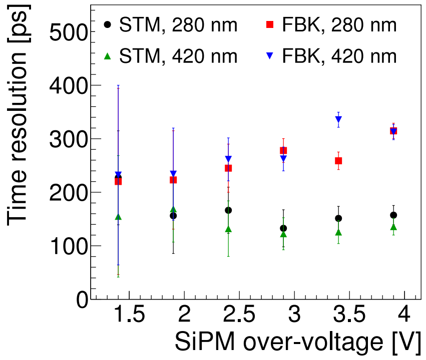

Fig. 6. Time resolution dependence on the V_{OV} for $N_{\mathrm{pe}} \approx 1$.

large N_{pe} and what remains is the constant term originating from an electronic jitter within the SiPM. The main contribution to the jitter is assumed to be of thermal noise origin, which is not directly dependent on V_{OV}. Considering also shot noise contribution, which will increase with the V_{OV} due to the increased current, the measured values (below the V_{BD}) provide lower bounds for a given SiPM and wavelength. The dark counts contribution to the jitter (that would also increase with the V_{OV}) can be neglected as the $N_{\mathrm{pe}} = 10^4$–10^6.

Overall, the FBK SiPM performance was consistently worse than that of the STM SiPM with time resolution 2–3 times worse. Considering the 11 ps resolution achieved with STM SiPM during the beam test campaigns, the expected beam test time resolution for the FBK device would be 20–35 ps. This is not adequate for their use as time reference in beam tests of the AFP ToF system, as such resolution is at best comparable to the ToF system under test.

5. Conclusion

We measured the timing properties of SiPMs from FBK and STM. The devices manifested TTS of $(285 \pm 9)\,\mathrm{ps}$ (FBK) and $(154 \pm 20)\,\mathrm{ps}$ (STM). The time resolution decreased with increasing N_{pe} as $\sigma_{\mathrm{TTS}} N_{\mathrm{pe}}^{-\frac{1}{2}} \oplus \sigma_{\mathrm{const}}$ with the best time resolutions, achieved for N_{pe} of the order 10^6 for 420 nm photons, of $(8 \pm 1)\,\mathrm{ps}$ and $(4 \pm 1)\,\mathrm{ps}$ for the FBK and STM SiPM, respectively.

The results for the two wavelengths were comparable, with 280 nm photons providing worse results at very high illumination: $(27 \pm 1)\,\mathrm{ps}$ (FBK) and $(8 \pm 1)\,\mathrm{ps}$ (STM) at N_{pe} of the order 10^4.

The STM SiPM has already proved to be a great photosensor for Cherenkov time-of-flight systems, reaching 11 ps when combined with a 3 cm quartz radiator [2]. However, the FBK device was found to provide worse resolution by a factor of 2–3.

Based on our findings, we are still facing the challenge of finding a suitable backup photosensor for upcoming beam tests.

Acknowledgments

The authors gratefully acknowledge the support from projects of MSMT of Czech Republic (LM 2015058) and of Palacky University, Czech Republic IGA_PrF_2019_008.

The authors gratefully acknowledge the support received from the Operational Programme Research Development and Education-European Regional Development Fund, projects no. CZ.02.1.01/0.0/0.0/17_049/0008422, CZ.02.1.01/0.0/0.0/16_019/0000754 and CZ.02.1.01/0.0/0.0/16_013/0001403 of the Ministry of Education, Youth and Sports of the Czech Republic.

References

[1] A. Ronzhin, M. Albrow, K. Byrum, M. Demarteau, S. Los, E. May, E. Ramberg, J. Vávra, A. Zatserklyaniy, Tests of timing properties of silicon photomultipliers, Nucl. Instrum. Methods Phys. Res. A 616 (1) (2010) 38–44.

[2] J. Lange, L. Adamczyk, G. Avoni, E. Banas, A. Brandt, M. Bruschi, P. Buglewicz, E. Cavallaro, D. Caforio, G. Chiodini, L. Chytka, K. Ciela, P. Davis, M. Dyndal, S. Grinstein, K. Janas, K. Jirakova, M. Kocian, K. Korcyl, I.L. Paz, D. Northacker, L. Nozka, M. Rijssenbeek, L. Seabra, R. Staszewski, P. Swierska, T. Sykora, Beam tests of an integrated prototype of the ATLAS forward proton, detector, J. Instrum. 11 (09) (2016) P09005.

[3] L. Adamczyk, E. Bana, A. Brandt, M. Bruschi, S. Grinstein, J. Lange, M. Rijssenbeek, P. Sicho, R. Staszewski, T. Sykora, M. Trzebiski, J. Chwastowski, K. Korcyl, Technical Design Report for the ATLAS forward proton detector, Technical Report CERN-LHCC-2015-009. ATLAS-TDR-024, 2015.

[4] P.W. Cattaneo, M. De Gerone, F. Gatti, M. Nishimura, W. Ootani, M. Rossella, Y. Uchiyama, Development of high precision timing counter based on plastic scintillator with SiPM readout, IEEE Trans. Nucl. Sci. 61 (5) (2014) 2657–2666.

[5] Near Ultraviolet (NUV) SiPMs, (SiPM-NUV1S) First Sensor, 2015, Available from http://www.first-sensor.com/cms/upload/datasheets/SiPM-NUV_501628.pdf.

[6] L. Nozka, L. Adamczyk, G. Avoni, A. Brandt, P. Buglewicz, E. Cavallaro, G. Chiodini, L. Chytka, K. Ciesla, P. Davis, M. Dyndal, S. Grinstein, P. Hamal, M. Hrabovsky, K. Janas, K. Jirakova, M. Kocian, T. Komarek, K. Korcyl, J. Lange, D. Mandat, V. Michalek, I.L. Paz, D. Northacker, M. Rijssenbeek, L. Seabra, P. Schovanek, R. Staszewski, P. Swierska, T. Sykora, Construction of the optical part of a time-of-flight detector prototype for the AFP detector, Opt. Express 24 (24) (2016) 27951–27960.

[7] AFP Collaboration, ATLAS forward proton detectors: Time-of-flight electronics, Acta Phys. Polon. B 7 (2014).

[8] P. Eckert, R. Stamen, H.-C. Schultz-Coulon, Study of the response and photon-counting resolution of silicon photomultipliers using a generic simulation framework, J. Instrum. 7 (08) (2012) P08011.

[9] S. Gundacker, E. Auffray, N.D. Vara, B. Frisch, H. Hillemanns, P. Jarron, B. Lang, T. Meyer, S. Mosquera-Vazquez, E. Vauthey, P. Lecoq, SiPM time resolution: From single photon to saturation, Nucl. Instrum. Methods Phys. Res. A 718 (2013) 569–572, Proceedings of the 12th Pisa Meeting on Advanced Detectors.

Published by IOP Publishing for Sissa Medialab

Received: *July 4, 2016*
Accepted: *September 5, 2016*
Published: *September 19, 2016*

Beam tests of an integrated prototype of the ATLAS Forward Proton detector

J. Lange,[a,1] **L. Adamczyk,**[b] **G. Avoni,**[c] **E. Banas,**[d] **A. Brandt,**[e] **M. Bruschi,**[c] **P. Buglewicz,**[d,f] **E. Cavallaro,**[a] **D. Caforio,**[g] **G. Chiodini,**[h] **L. Chytka,**[i] **K. Cieśla,**[d,f] **P.M. Davis,**[j] **M. Dyndal,**[b] **S. Grinstein,**[a,k] **K. Janas,**[b] **K. Jirakova,**[i] **M. Kocian,**[l] **K. Korcyl,**[d] **I. Lopez Paz,**[a] **D. Northacker,**[m] **L. Nozka,**[i] **M. Rijssenbeek,**[m,n] **L. Seabra,**[o] **R. Staszewski,**[d] **P. Świerska**[d,f] **and T. Sykora**[p]

[a] *Institut de Física d'Altes Energies (IFAE), The Barcelona Institute of Science and Technology (BIST),*
08193 Bellaterra (Barcelona), Spain

[b] *AGH University of Science and Technology, Faculty of Physics and Applied Computer Science,*
al. Mickiewicza 30, PL-30059 Cracow, Poland

[c] *INFN Bologna and Università di Bologna, Dipartimento di Fisica,*
viale C. Berti Pichat, 6/2, IT - 40127 Bologna, Italy

[d] *Institute of Nuclear Physics, Polish Academy of Sciences,*
Radzikowskiego 152, PL-31342 Kraków, Poland

[e] *The University of Texas at Arlington, Department of Physics,*
Box 19059, Arlington, TX 76019, U.S.A.

[f] *Cracow University of Technology,*
Warszwaska 24, PL-31155 Kraków, Poland

[g] *Czech Technical University in Prague,*
Zikova 4, CZ - 166 35 Praha 6, Czech Republic

[h] *INFN Lecce and Università del Salento, Dipartimento di Fisica,*
Via Arnesano IT - 73100 Lecce, Italy

[i] *Joint Laboratory of Optics, RCPTM, Palacký University,*
17. listopadu 50A, 77207 Olomouc, Czech Republic

[j] *Centre for Particle Physics, Department of Physics, University of Alberta,*
11335 Saskatchewan Drive NW, Edmonton, Canada

[k] *ICREA,*
Pg. Lluís Companys 23, 08010 Barcelona, Spain

[l] *SLAC National Accelerator Laboratory,*
2575 Sand Hill Rd, Menlo Park, U.S.A.

[m] *Stony Brook University, Dept. of Physics and Astronomy,*
Nicolls Road, Stony Brook, NY 11794-3800, U.S.A.

---

[1] Corresponding author.

© CERN 2016, published under the terms of the Creative Commons Attribution 3.0 License by IOP Publishing Ltd and Sissa Medialab srl. Any further distribution of this work must maintain attribution to the author(s) and the published article's title, journal citation and DOI.

doi:10.1088/1748-0221/11/09/P09005

[n] *European Laboratory for Particle Physics (CERN),*
Rte. de Meyrin, CH-1211 Geneva 23, Switzerland
[o] *Laboratório de Instrumentação e Física Experimental de Partículas, LIP,*
Av. Elias Garcia 14, Lisbon, Portugal
[p] *Charles University in Prague, Faculty of Mathematics and Physics,*
Institute of Particle and Nuclear Physics,
V Holesovickach 2, CZ - 18000 Praha 8, Czech Republic

E-mail: joern.lange@cern.ch

Abstract: The ATLAS Forward Proton (AFP) detector is intended to measure protons scattered at small angles from the ATLAS interaction point. To this end, a combination of 3D Silicon pixel tracking modules and Quartz-Cherenkov time-of-flight (ToF) detectors is installed 210 m away from the interaction point at both sides of ATLAS. Beam tests with an AFP prototype detector combining tracking and timing sub-detectors and a common readout have been performed at the CERN-SPS test-beam facility in November 2014 and September 2015 to complete the system integration and to study the detector performance. The successful tracking-timing integration was demonstrated. Good tracker hit efficiencies above 99.9% at a sensor tilt of 14°, as foreseen for AFP, were observed. Spatial resolutions in the short pixel direction with 50 μm pitch of 5.5 ± 0.5 μm per pixel plane and of 2.8 ± 0.5 μm for the full four-plane tracker at 14° were found, largely surpassing the AFP requirement of 10 μm. The timing detector showed also good hit efficiencies above 99%, and a full-system time resolution of 35 ± 6 ps was found for the ToF prototype detector with two Quartz bars in-line (half the final AFP size) without dedicated optimisation, fulfilling the requirements for initial low-luminosity AFP runs.

Keywords: Large detector systems for particle and astroparticle physics; Particle tracking detectors; Performance of High Energy Physics Detectors; Timing detectors

ArXiv ePrint: 1608.01485

Contents

1 Introduction

The ATLAS collaboration [1] at the Large Hadron Collider (LHC) at the European Laboratory for Particle Physics (CERN) is installing the ATLAS Forward Proton (AFP) detector to measure very forward protons (p) scattered at small angles from the ATLAS interaction point (IP) [2]. To this end, a combination of high-resolution pixel tracking modules for fractional-energy loss and momentum measurements and fast time-of-flight (ToF) detectors for event pile-up removal is placed at about 210 m from the IP at both sides of ATLAS and only 2–3 mm away from the outgoing Large Hadron Collider (LHC) beam. Roman pots are used as the beam interface. The approved AFP scenario foresees an initial low-luminosity operation with a low pile-up (number of interactions per bunch crossing $\mu \lesssim 1$) during short dedicated LHC runs. At a later stage, the system might be also operated at standard LHC luminosities during a large part of the regular LHC runs if a safe operation under these conditions has been demonstrated. The installation is performed in two stages: an AFP tracking system at one side ("one-arm") of the IP was already installed during the end-of-year 2015-2016 shutdown. The full two-arm system with both tracking and timing detectors at both sides of the IP is planned to be completed during the extended end-of-year 2016-2017 shutdown.

Parts of the individual AFP detector components and sub-systems have been tested in the past. However, it is critical to demonstrate that the separate detector components can be operated together as an integrated system. To this end, a first unified AFP prototype has been developed, which combines tracking and ToF prototype detectors and a common trigger and readout (excluding the Roman-pot housing at this stage). To verify its operability and measure its performance, beam tests have been carried out at the CERN-Super Proton Synchrotron (SPS) with 120 GeV pions in November 2014 and September 2015.

In section 2 a short overview on the design of the AFP detector, its components and readout is given, as well as a description of the AFP prototype and the beam-test setup. Section 3 describes the operation during beam tests including calibration, triggering and data taking. The beam-test results including the measured performance of the tracking and ToF detectors are presented in section 4. Summary and conclusions are given in section 5.

2 The AFP detector and the beam-test prototype

In this section, the design of the final AFP detector is briefly described, as well as the AFP beam-test prototype and setup. More details of the final design can be found in the AFP Technical Design Report [2].

The final AFP detector will consist of two Roman-pot stations at each side of the ATLAS IP, at 205 and 217 m away from it, as sketched in figure 1 (top). The station closer to the IP will include a tracker of four pixel planes. The station further away (shown in figure 1, bottom) will comprise an identical tracker and in addition a time-of-flight (ToF) detector of four trains of four L-shaped Cherenkov-radiating Quartz bars (LQbars) each (only two LQbars per train are shown in the sketch).

2016 JINST 11 P09005

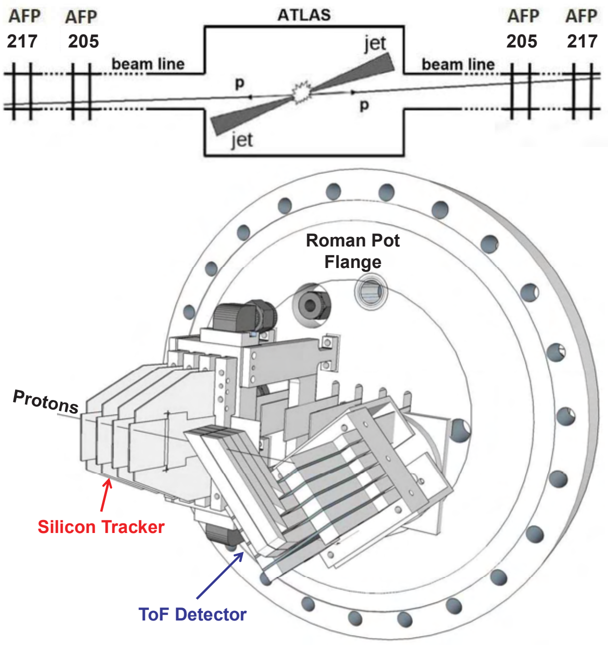

Figure 1. Top: layout of the AFP stations at both sides of the ATLAS IP at 205 and 217 m. Bottom: Design of the 217 m AFP detector including tracking and time-of-flight systems (only two LQbars per train are shown as used in the beam test; the final version will comprise four LQbars per train).

The AFP prototype for the beam tests is shown in figure 2. It was designed to be similar to the final AFP layout, but exhibited some differences explained in the following. It was built of five pixel planes and a ToF system of four trains of two LQbars each (i.e. half of the final AFP ToF system).

Note that the coordinate system during these beam tests differs from the standard AFP convention used in ref. [2]. In the beam tests, the short pixel direction with 50 μm pitch was oriented along the y direction and the long pixel direction with 250 μm pitch in the x direction (see figures 2 and 3). The beam axis was in z direction. The coordinate origin was placed in the centre of tracker plane 0. This coordinate system will be used in this paper unless noted otherwise.

2.1 Tracking system

2.1.1 AFP design and requirements

The purpose of the AFP tracker is the measurement of the position and angle of the scattered protons, which in combination with the LHC magnet system between the IP and AFP will allow the determination of their fractional energy loss and momentum. The tracker is required to exhibit a position resolution of 10 μm per four-plane station in the direction horizontal to the LHC tunnel floor and 30 μm in the vertical one. Furthermore, its proximity to the beam implies the need for slim edges of about 100–200 μm to minimise dead material, and it has to be able to withstand a

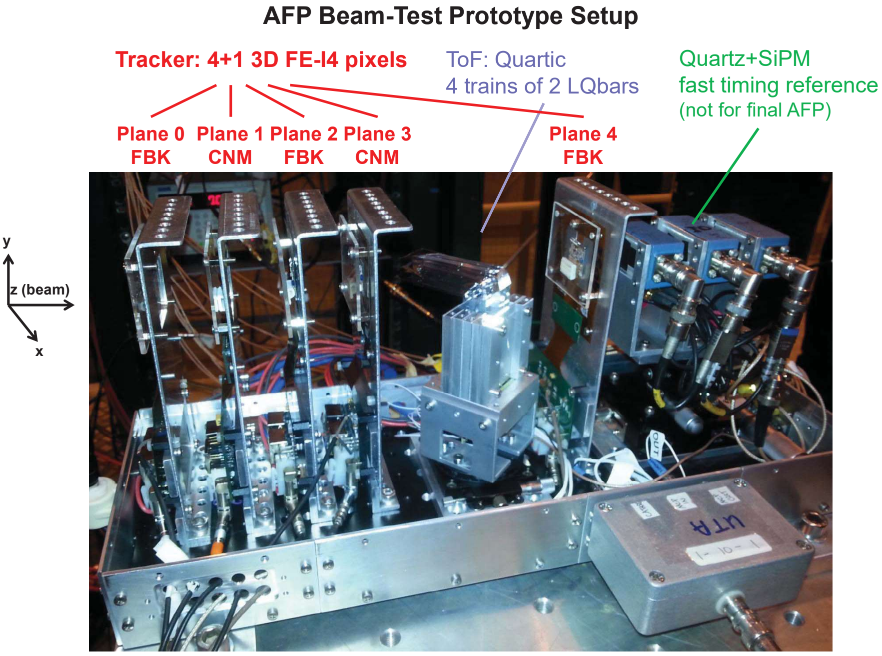

Figure 2. The integrated AFP beam-test prototype with tracking planes at perpendicular incidence.

highly non-uniform irradiation (with expected maximum fluence levels of about $3 \times 10^{15}\, n_{\mathrm{eq}}/\mathrm{cm}^2$ for 100 fb^{-1} integrated luminosity if AFP is operated in its measurement position close to the beam). Each AFP tracking station comprises four pixel modules, each made of a 3D silicon pixel sensor interconnected to an FE-I4 front-end chip [3]. The modules are placed with a pitch of 9 mm as shown in figure 1 (bottom). The pixels have a size of 50 and 250 μm in the horizontal and vertical directions, respectively. In the horizontal (short pixel) direction, the tracker is oriented with a small tilt of 14° between the sensor normal and the beam to enhance the hit efficiency and horizontal resolution, whereas in the vertical (long pixel) direction, a staggering of about 60 μm between successive planes is planned to improve the vertical resolution.

Silicon pixel sensors based on the 3D technology [4], in which the electrodes penetrate the sensor bulk as columns perpendicular to the surface, are chosen for AFP due to an excellent radiation hardness together with a low depletion voltage and their maturity proven by successful production runs for the ATLAS Insertable B-Layer (IBL) [5]. The vendors include FBK (Fondazione Bruno Kessler, Trento, Italy) [6] and CNM (Centro Nacional de Microelectronica, Barcelona, Spain) [7]. The sensors of both vendors are produced on a 230 μm thick p-type substrate, but FBK sensors have 3D columns fully passing through, whereas CNM 3D columns stop about 20 μm before reaching the other side. For edge termination, FBK uses a 3D guard fence of ohmic columns, whereas CNM in addition implements a 3D guard ring. For the first stage of AFP, CNM produced already a dedicated run of 3D sensors with 180 μm slim edge [8].

The read-out is performed by the FE-I4 front-end chip (version FE-I4B) with 336 × 80 pixels with a pixel size of $50 \times 250\,\mu\text{m}^2$, comprising a total active area of $1.68 \times 2.00\,\text{cm}^2$. It operates with a clock at 40 MHz consistent with the nominal LHC bunch crossing rate. The chip contains pre-amplifiers and a discriminator for each pixel with adjustable signal threshold (typically in the range of 1.5–3 ke^-) and time-over-threshold (ToT). The ToT is recorded with a resolution of 4 bits in units of clock cycles (25 ns) and is related to the measured charge. The tuning of threshold and ToT as well as the calibration of the ToT-to-charge relation is performed with a charge-injection circuit using an injection capacitor and an adjustable voltage step pulse. The FE-I4 chip provides a so-called HitOr output signal if at least one pixel fires, which is the logical OR of the discriminator signals of all pixels and can be used for triggering.

During the IBL development and qualification, 3D FE-I4 pixel modules have demonstrated a hit efficiency above 97% after uniform proton irradiation to $5 \times 10^{15}\, n_{\text{eq}}/\text{cm}^2$ [9]. The efficiency was observed to be about 1% higher in case of a sensor tilt of about 15° as low-field and dead regions from the 3D columns lose their impact when a particle does not traverse perpendicularly. The spatial resolution depends on a number of different parameters such as the beam incidence angle in combination with the sensor thickness (determining the degree of charge sharing between neighbouring pixels), the operational parameters (voltage, tuning points), the charge or ToT resolution and the cluster-centre algorithm. For perpendicular incidence, the spatial resolution was found to be 12 μm in the short pixel direction for the 98% of the events with pixel-cluster size 1 and 2 (degrading to 15 μm including all cluster sizes due to delta rays) [10]. In the long direction, the overall resolution was measured to be 73 μm. As demonstrated in the AFP beam tests of this study, for sensors tilted by 14° with respect to the short pixel direction, as planned for AFP, the resolution in that direction improves to about 6 μm for cluster size 1 and 2 due to enhanced charge sharing and interpolation (see section 4.4.1). Furthermore, for a full AFP station of four pixel modules, an improvement of position resolution over the single module is expected as discussed further in section 4.4.1.

In view of the application of 3D pixel modules in AFP, it was verified in dedicated studies that slim edges with a remaining insensitive width of only 15–200 μm can be produced without affecting the current, noise and edge efficiency and that the modules can withstand a highly non-uniform irradiation up to fluences expected after running for $100\,\text{fb}^{-1}$ at standard LHC luminosity [11, 12].

2.1.2 Prototype tracking system

For the AFP beam tests, the pixel modules used consisted of spare 3D sensors from the IBL production (three by FBK, two by CNM) bump-bonded to the FE-I4B readout chip and assembled on an IBL-type flexible circuit board (flex) as shown in figure 3. All sensors except plane 3 had already AFP-compatible slim edges. To protect the modules, especially the wirebonds, a 2 mm thick plastic cover was used with a distance of 5 mm to the sensor. In the 2014 beam test, the plastic cover extended over the full sensor area, whereas in 2015 holes covered with Kapton tape were made over the upper part of the sensor to minimise material in front of the sensor (see section 4.3). The modules were mounted on Aluminium frames with a thickness of 0.5 mm under the sensor. The frames were placed on a base plate in two different configurations:

1. Facing the beam under normal incidence (0° between the sensor normal and the beam axis). Because of the easy mounting of the pixel modules, this was the standard beam-test

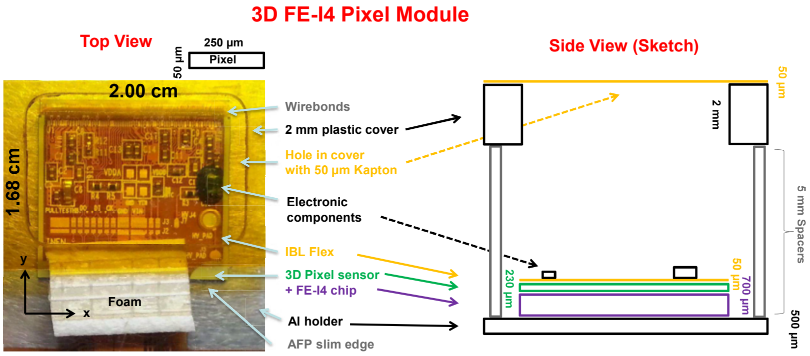

Figure 3. The 3D FE-I4 pixel-module prototype in top view (left) and a side-view sketch (right).

configuration for the AFP integration tests and measuring the performance of the ToF detector (see figure 2). Four modules (number 0 to 3) were placed with a pitch of 3.75 cm in front of the timing system (similarly to the final AFP configuration). An additional module (number 4) was placed behind the timing system with a distance of 13.75 cm to module 3 to improve the reconstructed-track precision at the position of the ToF detector and to allow a monitoring of particle interactions in the Quartz material.

2. With a tilt of 14° between the sensor normal and the beam axis with respect to the short pixel direction (y coordinate in the beam test). This configuration was used to study the tracker performance under more realistic AFP conditions. In this case, all five planes were placed with an equidistant pitch of 5 cm. The ToF system was not included.

2.2 Time-of-flight system

2.2.1 AFP design and requirements

In the final two-arm AFP detector, the ToF system is designed to reject combinatoric background from pile-up by precisely measuring the arrival times of the two protons to determine if they both come from the primary vertex as identified by the central tracker. For the initial low-luminosity runs with a low pile-up of $\mu \lesssim 1$, a time resolution of about 30 ps is required, whereas for runs at standard LHC luminosity with more than 50 pile-up events 10 ps are envisaged in order to give a primary-vertex constraint of 2 mm for sufficient background rejection.

As timing detectors in the 217 m stations, a system based on a set of L-shaped Cherenkov-radiating Quartz or fused silica bars (LQbar) is foreseen [2], a Roman-pot-compatible modification of the original Quartic detector [13–15]. The baseline consists of 16 LQbars organised into four rows (called trains) of four LQbars each (see also figure 4 for the half-size prototype version). The Cherenkov radiator bars are oriented with the Cherenkov angle of 48° with respect to the beam axis. Thus, the created Cherenkov light passes along the long direction of the radiators to the 90° bend, where the light is reflected so that it continues along the perpendicular light-guide bars to a

2016 JINST 11 P09005

multi-pixel Micro-Channel-Plate Photomultiplier (MCP-PMT). The output signals of all MCP-PMT channels are amplified with a low-noise preamplifier (PreAmp) and discriminated using Constant Fraction Discriminators (CFD). The CFDs apply two types of thresholds: a fixed threshold that determines the minimum level for the signal amplitude to be accepted; and a fractional threshold, set to a certain fraction of the signal amplitude, which determines the starting and end time of the CFD output signal, thereby compensating time-walk effects. Finally, the time of the rising edge of the CFD output is digitised with a 12-channel High-Precision Time-to-Digital Converter (HPTDC) board, which includes three HPTDC chips [15–17]. The finest time bin of the HPTDC chip is 24.4 ps. Laboratory tests indicate an intrinsic HPTDC time resolution of about 13 ps.

Previous beam tests were primarily focused on the performance of straight bar (Qbar) detectors with various bar configurations and dimensions. Single-Qbar + MCP-PMT combinations were measured with a 6 GHz LeCroy oscilloscope (without the HPTDC) and determined to have a resolution of about 20 ps for bar heights ranging from 2 to 5 mm. Multiple-Qbar configurations showed that each additional bar in the train improves the measurement despite non-trivial correlations between the bars. For example at a previous beam test, a six-Qbar train was measured to have a resolution of about 14 ps including the HPTDC resolution, closing in on the 10 ps target. The morphing of the straight bar into the LQbar was studied and shows that the LQbar-based detector could match or even exceed the Qbar detector with careful optimisation [18].

2.2.2 Prototype time-of-flight system

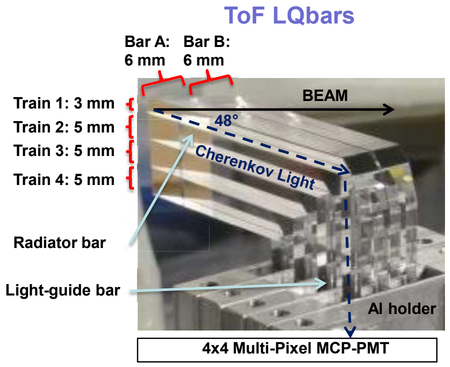

Figure 4. The LQbar ToF prototype detector with four trains of two LQbars each (half of the final number of LQbars per train).

The AFP beam-test prototype ToF system consisted of four rows (trains 1–4) of two LQbars (A and B) as shown in figures 2 and 4, oriented with the Cherenkov angle to the beam (half the number of LQbars per train with respect to the baseline design). The radiators of the upper train were 3 mm high in y, those of the lower three trains 5 mm. The length of the radiator bars in the short horizontal direction was 6 mm, the length in the long horizontal direction ranged from 35 to 57 mm. At the side opposite to the kink, the radiators were cut such that this edge was parallel to the beam, giving an effective edge length of about 8 mm. The LQbars were mounted in an Aluminium

2016 JINST 11 P09005

holder with 1 mm thick isolation plates between the light-guide bars of different trains and 125 μm thin spacer wires between those of the same train. At the radiator level, the different trains were optically isolated using mylar foils. The ends of the LQbars were brought into contact (without the use of optical grease) with a 10 μm-pore mini-Planacon MCP-PMT by Photonis with 4×4 anode pixels of $6 \times 6\,\text{mm}^2$ size with a space of 0.25 mm between adjacent pixels.

In addition to the LQbar timing system, three fast timing reference detectors consisting of straight Quartz bars ($3 \times 3\,\text{mm}^2$ cross section, 3 cm long in beam direction) coupled to Silicon Photomultipliers (SiPMs) by STMicroelectronics (Catania, Italy) were used [14]. They were placed under perpendicular beam incidence (i.e. not oriented with the Cherenkov angle) behind the AFP prototype for testing purposes.

The signals of all timing detectors were amplified, discriminated with CFDs and digitised with the HPTDC board as described above.

In the 2015 beam test, also other LQbar types and configurations were tested, such as single bars, matt bars, spatial gaps between bars of the same train, the addition of optical grease, as well as different types of MCP-PMTs. However, the analysis of these different ToF configurations is still on-going. In this paper, only the above-described standard configuration will be covered. A publication with a more detailed description of the production and properties of the AFP ToF detector is in preparation.

2.3 Readout and trigger

2.3.1 AFP design and requirements

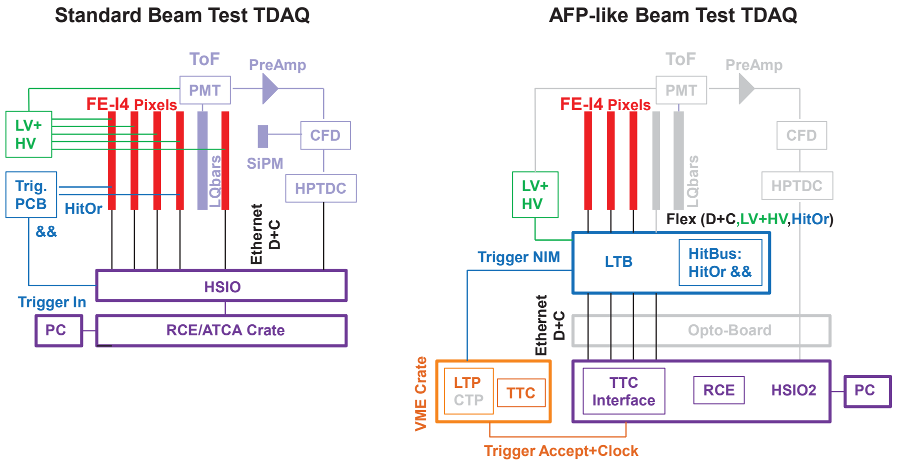

Figure 5. The readout and TDAQ schematics for most of the runs (left) and for special runs to test a TDAQ system close to the final AFP one (right); grey components were not included in these special runs.

For the readout of both tracking and ToF modules, the Reconfigurable Cluster Elements (RCE) system [19] is used, which is based on an Advanced Telecommunications Computing Architecture (ATCA) [20] standard. It consists of the RCE boards that generate commands and receive data

2016 JINST 11 P09005

(C+D), the Cluster Interconnect Modules (CIM) that work as control units and communication interfaces, as well as of the High-Speed Input-Output (HSIO) board that interfaces to the pixel front-ends and HPTDC chips and is responsible for data decoding, buffering and routing. The data and commands between the RCE system on the one hand and the FE-I4 and HPTDC chips on the other hand are sent via optical fiber using an opto-board close to the detectors as a converter between electrical and optical signals.

In the initial one-arm AFP phase, the trigger is taken from the coincidence of several tracking planes using the FE-I4 HitOr signal (see section 2.1.1). The logical processing of the HitOr trigger signals from different pixel planes is performed on the HitBus chip [21]. For the full AFP detector including the ToF system, the trigger is planned to be extracted from a coincidence of LQbar signals in one train to reduce the trigger dead time (the HitOr dead time is discussed in section 3.2) and to include a coarse position information by distinguishing which train is hit.

The trigger signals are then converted to the Nuclear Instrumentation Module (NIM) logic standard and sent to the ATLAS Central Trigger Processor (CTP) [22] for combining it with trigger signals from other ATLAS sub detectors. The signal from the ATLAS central trigger informing that an event is accepted, as well as the ATLAS central clock, are distributed to the AFP RCE system via the Timing, Trigger and Control (TTC) unit [22]. The readout is sketched in figure 5 (right).

2.3.2 Prototype readout and trigger

Different versions of the RCE system were used in the beam tests: in 2014, the first version with the HSIO1 board connected via optical fiber to an RCE ATCA crate outside the beam area; and in 2015 the second version with the HSIO2 board which includes already an RCE component on-board, making an external crate unnecessary. Whereas the operation of the RCE system with the FE-I4 chip had been extensively proven already before, e.g. in the IBL stave integration [23], its operation with the HPTDC system still had to be implemented and optimised before and during the November 2014 beam test.

The trigger of the combined system was given by signals from the tracking system as planned for the initial one-arm AFP phase. Two different configurations were used (see figure 5 left and right):

1. During large parts of both beam tests (for tracking-timing integration and detector performance studies), a custom-made electronic circuit board was used to combine several FE-I4 HitOr signals from different planes to form a coincidence trigger signal in the Transistor-Transistor-Logic (TTL) format. This trigger signal was then directly fed into the RCE HSIO board to trigger the readout of the FE-I4 pixel devices and the HPTDC. The data and commands between the FE-I4 pixel devices or the HPTDC and the RCE HSIO were sent electrically via shielded Ethernet cables. The clock was provided internally by the RCE system. Low and high voltage (LV/HV) was provided separately and directly for each pixel module.

2. In dedicated tests, a configuration more similar to the final AFP Trigger and Data Acquisition (TDAQ) system was studied. Three FE-I4 pixel modules were connected via a flexible cable to a Local Trigger Board (LTB) that provided low and high voltage for each module, as well as the data and command interface to the RCE HSIO2 board via Ethernet cables. This board included also the HitBus chip for different trigger logic processing of the HitOr signals from up to three

2016 JINST 11 P09005

FE-I4 pixel modules. The HitBus trigger output was an LVDS signal that was converted into NIM standard and sent to a Local Trigger Processor (LTP) in an external Versa Module Eurocard bus (VMEbus) crate, which was used to locally test the compatibility with the ATLAS CTP system. The LTP created a trigger-accept signal, which was then sent via a TTC system in the same VMEbus crate and optical fiber cable to the TTC interface board on the RCE HSIO2 board. Also the clock was externally provided by the TTC module to the RCE HSIO2 board.

In addition to the full HPTDC-RCE readout system, for testing purposes and specific time-resolution studies without the HPTDC contributions, the ToF signals were also recorded with a LeCroy SDA760ZI oscilloscope.

3 Beam test operation

The AFP beam tests took place at the H6B and H6A beam lines of the CERN-SPS with 120 GeV pions for one week in November 2014 and two weeks in September 2015, respectively.

3.1 Operational parameters and calibration

Before the data taking, the operational parameters were set and the pixel devices and the HPTDC calibrated.

By default, bias voltages of 10 V were applied to the 3D pixel sensors. Each FE-I4 pixel was tuned to a threshold of 2 ke$^-$ (3 ke$^-$ in 2014) and a ToT of 10 (in units of 25 ns clock cycles) at an injected charge Q of 20 ke$^-$ (referred to as 10@20 ke$^-$ in the following). For this, the internal charge-injection mechanism was used with the same calibration parameters (such as injection capacitance) assumed for all five pixel planes (in reality, the charge-injection calibration parameters have a chip-to-chip spread of 15% [24], but the exact values were not known for the IBL spare devices used in these beam tests).

The MCP-PMT voltage, which determines the gain, was set to 1900 V by default (corresponding to a gain of 2×10^5), the SiPM voltage to 30.7 V. The CFD fixed threshold was set to 100 mV, the fractional threshold to 24% of the signal amplitude.

In dedicated runs also the following variations of the values of some of these parameters were studied (default values marked in **bold**):

- Pixel sensor bias voltage [V]: 1, 2, 4, 7, **10**, 20
- Pixel threshold [ke$^-$]: 1.5, **2.0**, 2.5, 3.0
- Pixel ToT: 10@16 ke$^-$, **10@20 ke$^-$**, 5@20 ke$^-$
- MCP-PMT voltage [V] (gain): 1750 (0.7×10^5), 1800 (1.0×10^5), 1850 (1.7×10^5), **1900** (2.0×10^5)

The ToT-to-charge relation of the pixel devices can in principle be obtained for each device and each pixel separately by scanning the injected charge per pixel and measuring the ToT response [24].

This was, however, not possible with the setup during the beam test. Instead, as a rough approximation, a global relation was obtained previously in stand-alone studies from the average over all pixels of a similar pixel device. The relation is approximately parabolic with a fit giving

$$Q[\mathrm{e}^-] = 1909 + 363 \times (ToT - 1) + 141 \times (ToT - 1)^2 \tag{3.1}$$

for the standard tuning.[1] In addition, a global charge calibration factor of 1.4 was applied as obtained from the measurement of the gamma lines of Am-241 and Cd-109 sources, consistent with earlier observations [24].

The calibration of the HPTDC is primarily to characterise the non-linearities in the timing measurement due to variations of the time-bin size. Uncorrected these non-linearities can introduce a timing error up to 150 ps. Calibration requires an input uncorrelated to the reference clock, usually a free-running oscillator. A normalised histogram of these events over the number of TDC bins gives a measurement of the size of each bin allowing a look-up table to be generated to correct for the accumulation of the error in bin size. This calibration can then either be applied online or offline. Once calibrated, measurements remain fairly stable although degradation with aging, radiation damage, and temperature variation is expected requiring periodic re-calibration. Variation in absolute timing vs. temperature is measured at 2.5 ps/K. Chip temperatures vary little during operation and each is instrumented with a thermistor to monitor this.

2016 JINST 11 P09005

3.2 Trigger and data taking

As mentioned in section 2.3.2, for most of the runs, a custom-made PCB was used to provide the trigger from the hit coincidence of several tracking planes. In 2014, planes 0, 3 and 4 were used for triggering, in 2015 only planes 0 and 3. In dedicated runs, the more realistic TDAQ system with the HitBus chip, LTP and TTC was successfully tested. In those runs, the first three planes were included in the HitBus-chip trigger logic, which was configured with the RCE system to give a trigger signal if all three planes fire or, alternatively, if two out of the three planes fire.

Of special interest for the integration of the AFP trigger into the ATLAS TDAQ system are the latency (i.e. the delay of the arrival of the trigger signal after the particle crossing) and the duration of the trigger signal, which were measured with the oscilloscope (using the SiPM signals as fast timing reference). The latency including the FE-I4 HitOr processing, the HitBus-chip processing, as well as the NIM conversion was found to be about 100 ns, i.e. 4 nominal LHC bunch-crossing spacings of 25 ns, which can be accommodated into the AFP trigger-latency requirements. The duration of the NIM trigger signal was found to be about 200 ns with a significant spread of about 50 ns for the standard operational parameters and at perpendicular beam incidence. This can be explained with the HitOr signal being the logical OR of the discriminator signals of all pixels in a chip, i.e. its duration is typically the ToT of the pixel with the highest signal in an event (referred to as *maximum hit ToT* in the following). This distribution is shown in figure 6. For a most probable deposited charge of about 17 ke$^-$ in 230 μm silicon at perpendicular incidence and a standard ToT tuning of 10@20 ke$^-$, this leads to a peak of 8 clock cycles of 25 ns with a significant spread due to Landau fluctuations and charge sharing. The AND between the HitOr signal of different planes in the HitBus chip is then dominated by the shortest HitOr signal among all planes.

---

[1] Here and in all following plots, *ToT* is the decoded ToT information from the front-end chip in units of 25 ns clock cycles, ranging from 1 for events just above the threshold to 14 as overflow bin.

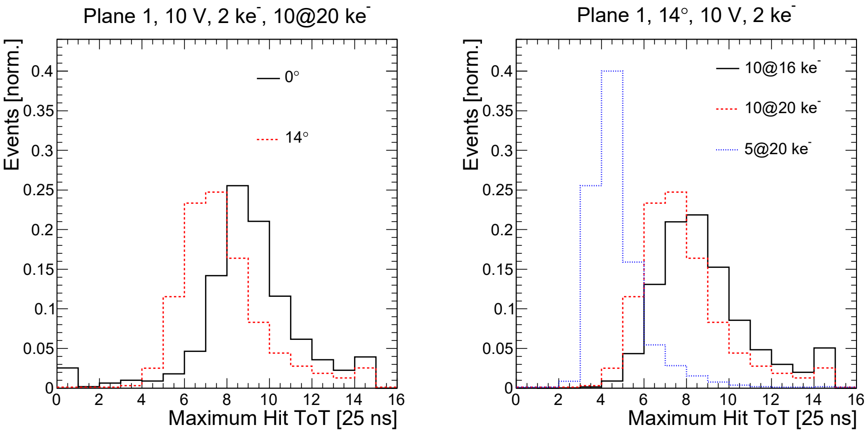

Figure 6. Distribution of the maximum hit ToT in an event in plane 1 (indicative for the HitOr duration) for different angles (left) and ToT tunings (right) at otherwise standard operational parameters. The bin at 14 includes entries for ToT≥14 (overflow).

The large duration of the HitOr trigger signal has two consequences. Firstly, the ATLAS CTP would assign triggers for each bunch crossing for which the trigger signal is high, although a particle might have crossed the detector only during the first bunch crossing. Hence for the final AFP TDAQ system, the trigger-signal duration will be reduced to 25 ns before being fed into the CTP. Secondly, it implies a trigger dead time since no new trigger can be given while the HitOr signal is still high from a previous hit. It will depend on the run conditions whether this has significant implications on the trigger efficiency. It is possible that the first dedicated low-luminosity AFP runs will be operated not with the nominal LHC bunch-crossing spacing of 25 ns, but at e.g. 100 ns. In addition, the AFP detector occupancy per minimum-bias interaction is expected to be only about 2–4% [2]. Hence, for low-pile up conditions with e.g. only one interaction per bunch crossing, a 200 ns trigger dead time in combination with 100 (25) ns bunch-crossing spacing will lead to trigger efficiencies of 96 (85)% in case of 2% occupancy per interaction or 92 (72)% in case of 4% occupancy. It should be noted, however, that this is only a rough calculation neglecting beam-related backgrounds (which are not yet known precisely) and the exact distribution of pile-up multiplicity and of the trigger dead time.

In any case, in order to reduce the trigger dead time and improve the efficiency, the dependence of the maximum-hit-ToT distribution (as indication of the HitOr duration) was studied for different angles and tunings. Figure 6 shows that the maximum hit ToT is reduced for the AFP tilt of 14° (due to enhanced charge sharing) and for a ToT tuning of 5@20 ke$^-$. Tuning to even lower ToT values at 20 ke$^-$ was not successful during the beam test but might be achieved with more care. However, reducing the ToT for a given charge compromises the position resolution for charge-interpolating algorithms, as discussed in section 4.4.1. A compromise could be to tune two of the four AFP planes to e.g. 5@20 ke$^-$ for efficient triggering, and the remaining two to e.g. 10@20 ke$^-$ for improved position resolution. No strong dependence of the maximum hit ToT on bias voltage and threshold tuning was observed.

2016 JINST 11 P09005

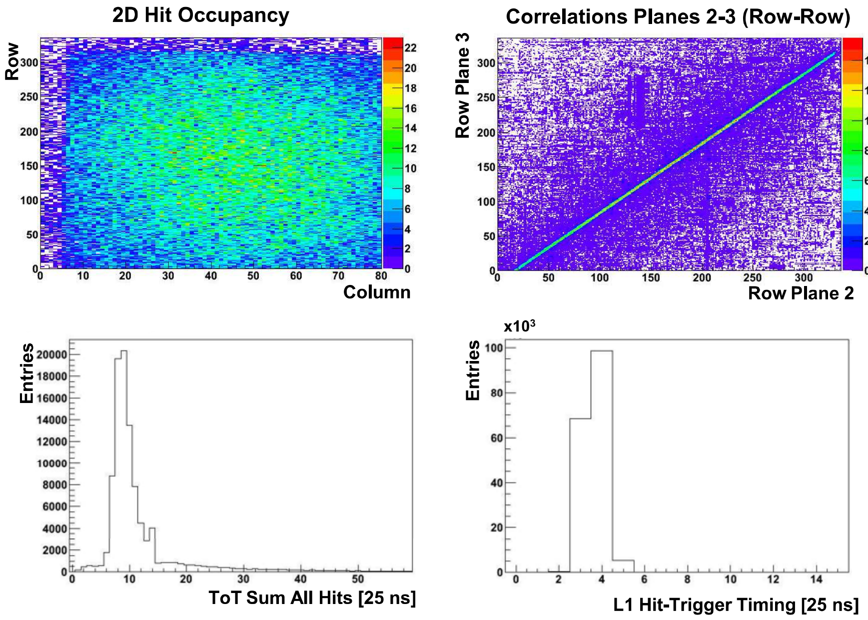

Figure 7. Online-monitoring distributions. Top left: the 2D hit occupancy map of one pixel sensor. Top right: the correlation between the rows of two consecutive pixel planes. Bottom left: the ToT sum of all hits in the event (simple cluster-charge distribution). Bottom right: the timing of the recorded hits with respect to the trigger signal (Level 1 or L1 distribution).

After triggering, the signals of the pixel detectors, i.e. the addresses and ToTs of the pixels above threshold, were recorded for typically 16 (5) consecutive clock cycles in 2014 (2015). The timing distribution of the recorded hits with respect to the trigger signal (so-called Level 1 distribution, in units of 25 ns clock cycles) is shown in figure 7, bottom right. The clear peak indicates low noise levels and a good synchronisation between the recorded hits and the trigger.

The system operation during data taking was stable, e.g. half-day runs without user interaction were possible. Altogether, 38 M events were collected in 2014 and 210 M events in 2015, at typical average rates of a few hundred Hz.

Many parameters of the tracking system could be monitored at the online level (see figure 7 for examples). In addition to the Level-1 distribution already discussed, the 2D hit occupancy maps for each tracking plane were monitored and used for performing the alignment of the beam with respect to the detectors. Good correlations between the hit column (and row) numbers of two consecutive pixel planes, respectively, indicated that real tracks were recorded and that the inter-plane alignment precision was at the mm level. Moreover, the ToT sum of all hits (roughly indicating the cluster charge) was monitored online and behaved as expected.

4 Data analysis and detector performance

The data taken including the tracker and ToF hit information were stored in a common data format and analysed offline.

4.1 Tracker reconstruction

The offline pixel-hit clustering and track reconstruction were performed with the software framework *Judith* [25].

4.1.1 Pixel hit clustering

Neighbouring hit pixels were grouped into hit clusters. The cluster-centre position for each coordinate (x, y) was determined either with a ToT-weighted or charge-weighted (i.e. after the ToT-to-charge conversion explained in section 3.1) mean of the single-pixel centres. As default, the ToT-weighted mean was taken since this is a simple algorithm using direct measurement information with a position resolution similar to the charge-weighted mean. More discussion on the resolution and its dependence on the different cluster-position algorithms can be found in section 4.4.1.

Figure 8 shows a collection of important pixel-hit and cluster distributions for plane 1 (a CNM device like in the final AFP detector, which was not included in triggering and hence unbiased) at standard operational parameters, compared for 0° and 14° tilt: cluster multiplicity, cluster size in both directions (i.e. over how many pixels a cluster extends in x, y), hit ToT (including all hit pixels before clustering) and cluster charge Q after ToT-to-charge conversion and clustering. For the cluster size y and the hit ToT, the dependence on voltage, threshold and ToT tuning at 14° tilt is presented in figure 9. All these distributions are shown for the minimal-material region defined in section 4.3.

More than 90% of all events have only one cluster per pixel plane, similar for all operational parameters. Larger cluster multiplicities are mainly from material interactions as discussed in section 4.3 and possibly from noise; as shown in section 4.1.2, events with more than one reconstructed track are only about 2%. The fact that at 14° almost no events have no clusters (increasing to 3% at 0°) indicates already the excellent hit efficiency as presented in section 4.3.

The cluster size is an important parameter for the position resolution as discussed in section 4.4.1. The situation is sketched in figure 10. In the long pixel direction (x), charge sharing is minimal and most of the clusters (about 97%) extend only over one pixel, similar for all operational parameters and angles in y. A higher degree of charge sharing takes place in the short pixel direction (y). At standard operational parameters (figure 8) and 0°, 81% of the clusters still have a cluster size y of 1, but in 17% of the cases charge is shared between 2 pixels; a cluster size y of more than 2 happens for 2% of the clusters and must be due to delta rays and noise since this is geometrically not possible at 0°. Charge sharing in y is strongly enhanced at 14° tilt since the particles travel over 57 μm in that direction (at a pixel pitch of 50 μm) and hence pass through mostly 2 pixels (measured for 81% of the clusters) and sometimes 3 (measured for 4% of the clusters). However, due to the threshold occasionally one pixel does not fire, so that for 14% of the clusters the cluster size y is found to be 1. From figure 9 it can be seen that at 14°, charge sharing in plane 1 is increasing with voltage since this is a CNM sensor with non-fully-through-passing columns, which is not yet depleted throughout its whole depth at low voltages. FBK devices with fully-through-passing

2016 JINST 11 P09005

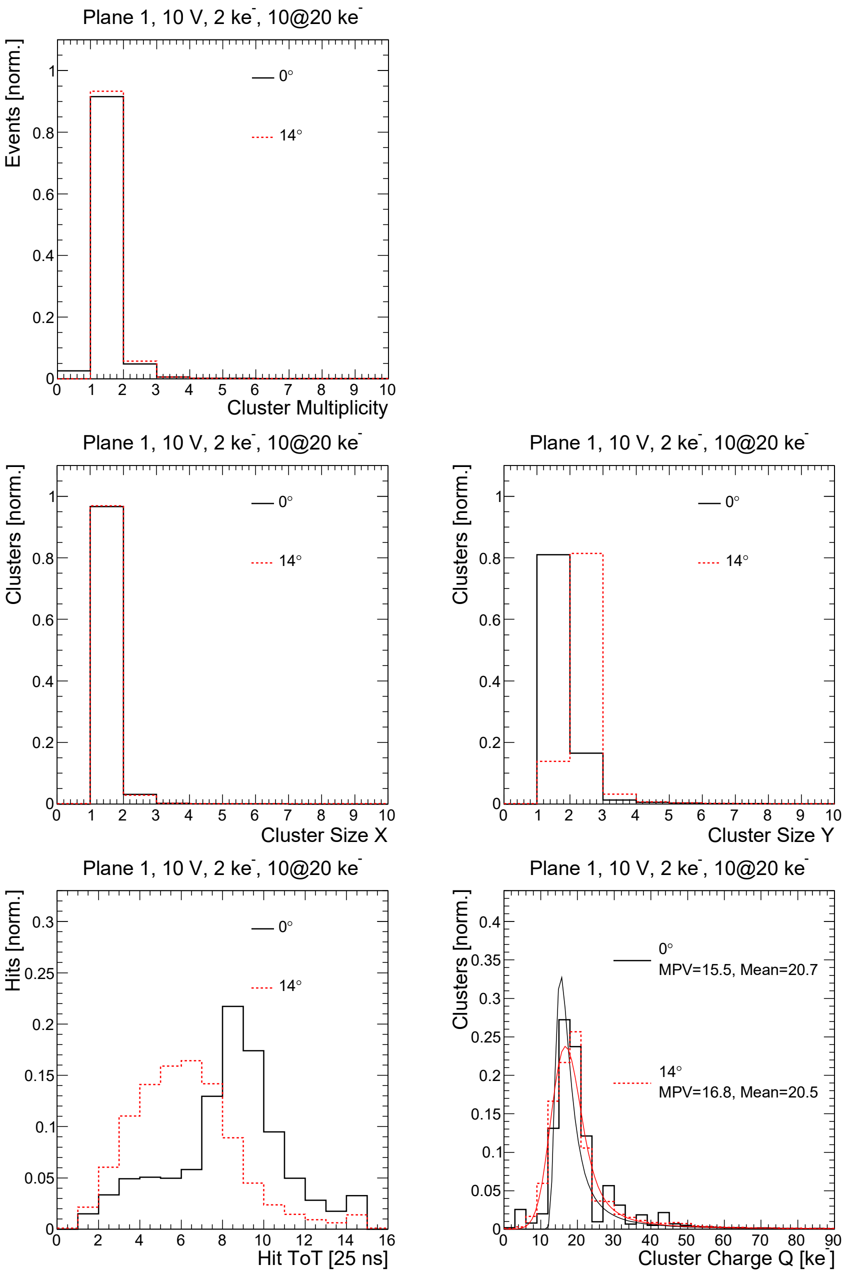

Figure 8. Hit and cluster properties for plane 1 (CNM) at 0 and 14 degrees at standard operational parameters.

2016 JINST 11 P09005

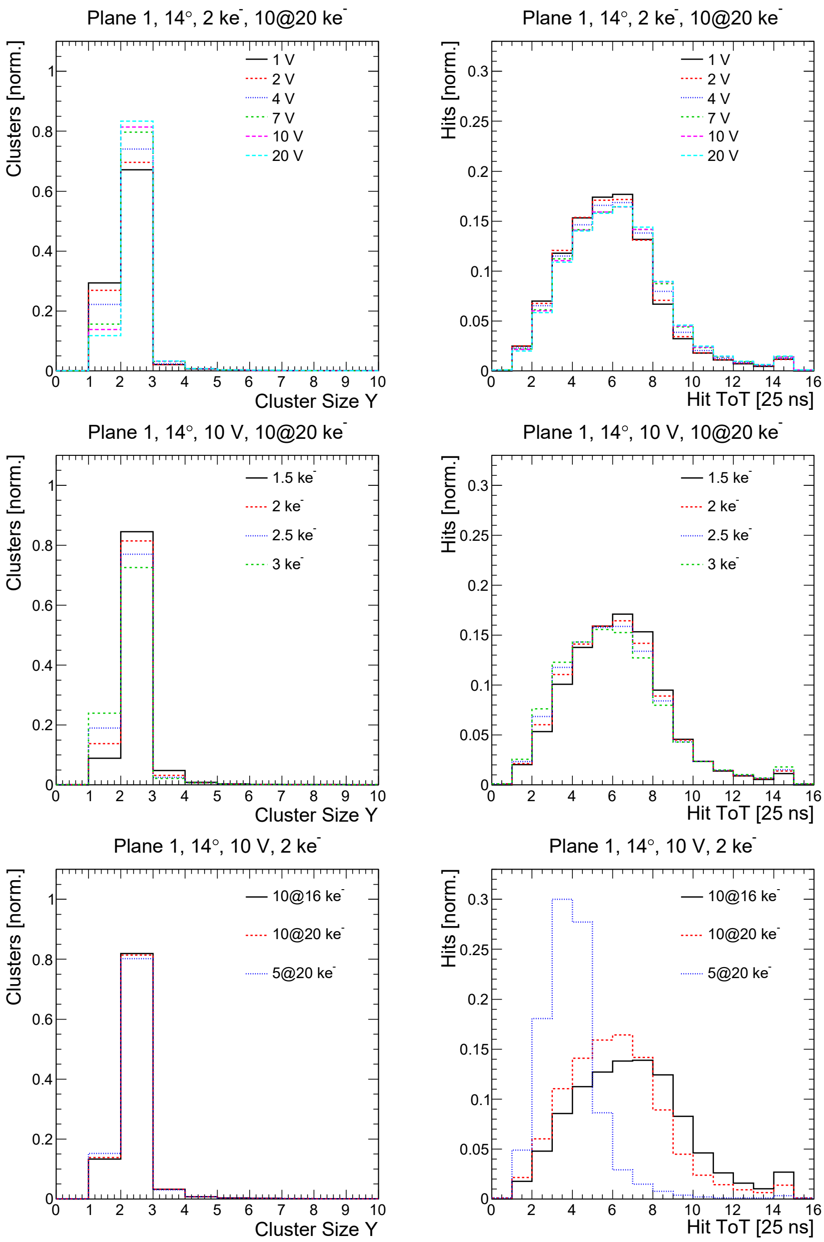

Figure 9. Cluster size in y direction (left) and hit ToT (right) distribution for plane 1 (CNM) at different operational parameters: bias voltage dependence (top), threshold dependence (centre) and ToT tuning dependence (bottom).

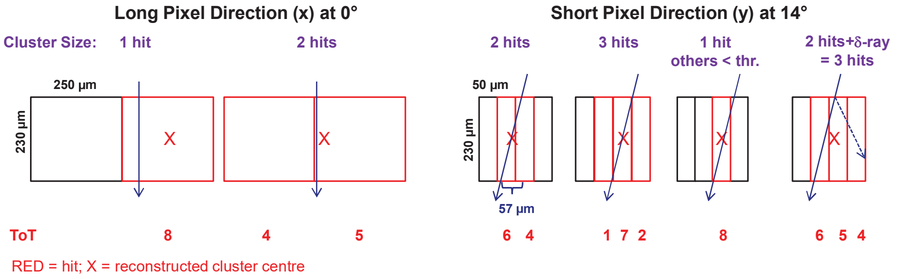

Figure 10. Sketch of pixel hits and clusters for the long pixel direction x at 0° (left) and the short pixel direction y at 14° (right). The ToT values are examples.

columns, on the contrary, show hardly any voltage dependence for the cluster size. When increasing the threshold, the events with a cluster size y of 1 are increasing, as expected. No strong dependence on the ToT tuning is observed.

At standard operational parameters (figure 8), the distribution of the hit ToT peaks at 8 for 0°, which is consistent with the expectation of 17 ke$^-$ most probable deposited charge and no charge sharing. For 14° the ToT distribution is shifted to lower values with a peak at 6 due to enhanced charge sharing. After the ToT-to-charge conversion, the cluster charge (the sum of all pixels hit) is roughly consistent between 0° (most probable value MPV = 15.5 ke$^-$) and 14° with an MPV of 16.8 ke$^-$ (from geometry one would expect 3% more charge at 14° than at 0°) and expectations. It should be noted that the 4-bit ToT resolution and the non-linearity between ToT and charge (see equation (3.1)) are not ideal for precision charge measurements, which is not the aim of these devices. From figure 9 it can be seen that the hit ToT slightly increases with voltage in plane 1 (due to more efficient charge collection and more complete depletion for the CNM device) and decreasing threshold (mainly an effect of the re-definition of the ToT-to-charge relation since e.g. ToT=1 is by definition close to the threshold and hence moves when changing it). Obviously, when changing the ToT tuning, the ToT distribution is highly affected and can be shifted to much lower values for 5@20 ke$^-$, as discussed already in section 3.2 for the maximum hit ToT in the event.

The distributions for the other planes are consistent with plane 1 when considering the chip-to-chip charge-calibration spread of 15%, except for the fact that the FBK sensors are fully depleted already at 1 V and hence show almost no voltage dependence.

4.1.2 Track reconstruction

Subsequently, tracks were reconstructed from the clusters by fitting a linear function for each direction (x and y) after applying a simple track-cluster-finding algorithm. At least three planes are required to have a hit included in the track. As input resolutions for the weights in the χ^2 fit, the resolutions individually measured for different cluster sizes (from section 4.4.1) were used. Alignment was performed in two steps: first a coarse alignment based on the inter-plane correlations between two consecutive pixel layers (see figure 7, top right) was applied; subsequently a fine alignment was performed based on the track residual distributions (i.e. the difference between the projected track position on each layer and the cluster position). Shifts in x and y and rotations around the z axis were corrected for. For more details see reference [25].

Track reconstruction of the AFP-prototype test-beam data has been performed for different scenarios:

1. The *all-plane scenario* includes all five planes into the track fit, which is mostly used for the analysis of the ToF detector as it gives the best precision at the ToF-detector position.

2. The *first-four-plane (AFP-like) scenario* takes only the first four equidistant planes into account, thereby being the most realistic with respect to the final AFP configuration.

3. In the *DUT scenarios*, specific planes are excluded from the track fitting and thus treated as independent, unbiased devices-under-test (DUT) for efficiency or resolution studies.

The performance of track reconstruction is found to be similar for all scenarios (the following plots and numbers refer to the AFP-like first-four-plane scenario): for about 97% of the events exactly one track is reconstructed as seen from figure 11 (left). Events with no reconstructed tracks are at the percent level and mostly originate from tracks at the edges of the tracker where due to misalignment not enough planes were hit by the particle. Events with more than one reconstructed track are found in only 2% of the cases. Figure 11 (right) shows the number of planes included in the track. Due to the excellent hit efficiency at 14° (see section 4.4.2), almost all tracks include all four planes (in the central detector region). At 0°, about 5% of the tracks include only three planes, consistent with the two unbiased planes having an efficiency of 97.5% (the two triggering planes have naturally an efficiency of 100%). The reconstructed tracks are found to be parallel to the beam axis with an average angle in x and y of about 0.1°.

For the analyses presented here, event cleaning cuts have been applied unless stated otherwise. Events with exactly one track and one cluster per plane have been selected to reduce combinatorial background and events with material interactions.

4.2 Spatial correlation between tracking and timing detector

The main objective of the 2014 beam test was the integration of the tracking and timing subsystems with a common trigger and readout. To verify that this integration worked and that the recorded tracking and timing data were inter-related with each other, the spatial tracking-timing correlation was studied. Figure 12 shows the number of events as a function of the track position extrapolated to the timing detector (using the all-plane track-reconstruction scenario with cleaning cuts as described in section 4.1.2) and the firing timing channel (the eight LQbars).

It can be seen that the track position and timing channels that give a signal are clearly correlated with each other in space. In the y direction, the four trains piled on top of each other can be clearly seen. Even a small misalignment between bar A and B of train 1 is visible, which has been confirmed by optical inspection. Train 4 is only partly visible due to the limited pixel-detector and trigger acceptance below −7 mm. In the x direction it can be seen that the overlap between LQbars and the pixel detectors ranges from −6 mm (the LQbar cut edge parallel to the beam) to the end of the pixel detector at about 10 mm.

These correlation distributions were also used for offline alignment between the timing channels and the tracking detector for the following analyses.

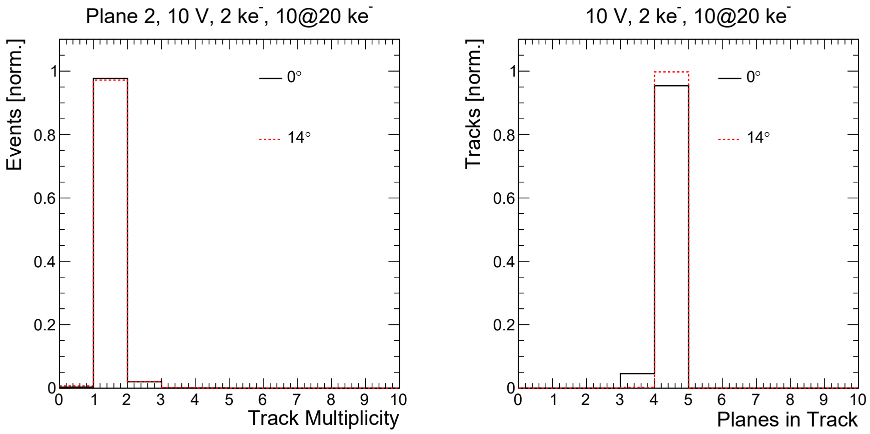

Figure 11. Track properties for a track reconstruction from the first four planes (AFP-like scenario) at 0 and 14°: track multiplicity (left) and number of pixel planes included in the track (right) for a central region.

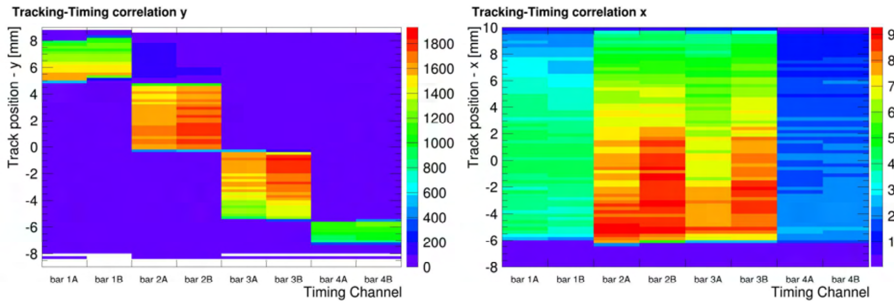

Figure 12. The spatial correlation between reconstructed-track position and ToF channels in the y (left) and x (right) direction at $V_{\text{MCP-PMT}} = 1800\,\text{V}$ for the tracker at 0°. For the bar arrangement and naming scheme see figure 4.

4.3 Material interactions

It is important to understand particle interactions in the detector material such as multiple scattering, nuclear interactions and delta rays since they could degrade the performance. Table 1 gives an overview on the detector material in terms of nuclear-interaction and radiation length and the corresponding expected multiple-scattering parameters. This is compared for the beam-test setup (with only two LQbars per train, with a flex on top of the pixel sensor, and with and without plastic cover) and the final AFP detector (with four LQbars per train and no flex or cover).

The tracker material in terms of radiation length X_0 is 1.7% (2.3%) per tracker plane for the beam-test setup without (with) the plastic cover. This implies a mean multiple-scattering angle $\theta_{0,\text{MS}}$ of 12.4 (14.6) μrad for 120 GeV particles, which leads to a mean offset of 0.6 (0.7) μm at the next tracker plane for the setup with 14° tilt with a plane pitch of 5 cm. This is an important

Table 1. Overview on material interactions, compared for the beam-test setup with and without 2 mm plastic cover (930 μm Si + 500 μm Al + 500 μm Kapton flex, 1.6 cm LQbars, 120 GeV particles) and the final AFP detector (930 μm Si + 500 μm Al, 3.2 cm LQbars, 6.5 TeV particles): the detector material in terms of nuclear interaction length λ_I (ToF and tracker) and radiation length X_0 (tracker), the mean multiple-scattering angle $\theta_{0,\mathrm{MS}}$ and the corresponding offset d_{MS} at the next tracking plane (5 cm pitch for the beam test, 9 mm for the final AFP detector). The material constants and formulas are from reference [26].

	ToF	Tracker (per Plane)			
Setup	x/λ_I [%]	x/λ_I [%]	x/X_0 [%]	$\theta_{0,\mathrm{MS}}$ [μrad]	d_{MS} [μm]
Beam Test (no Cover)	3.6	0.4	1.7	12.4	0.6
Beam Test (Cover)	3.6	0.7	2.3	14.6	0.7
Final AFP	7.3	0.3	1.5	0.2	2×10^{-3}

parameter for the resolution measurements in section 4.4.1. For the final AFP detector without the flex, the material budget in terms of radiation length is reduced to 1.5%. Together with the high proton momentum of close to 6.5 TeV, the multiple-scattering effects are negligible with only 0.2 μrad scattering angle and a mean offset of 2×10^{-3} μm at the next tracking plane with a distance of 9 mm.

Nuclear interactions in the Quartz material of the ToF detector could give rise to secondary particles that might affect the time resolution. These additional particles should be measurable in the last tracking plane 4 behind the ToF detector as additional hits and charge deposition. From the nuclear interaction length of $\lambda_I = 44$ cm for Quartz, one would roughly expect an interaction for 3.6% of the events for a two-LQbar train of 1.6 cm depth along the beam. For the final AFP detector with four LQbars per plane, this would increase to 7.0%. On the contrary, for each tracking plane one would expect a nuclear interaction in only 0.4% of the events. This increases to 0.7% if the sensor is covered by the 2 mm plastic protection and decreases to 0.3% for the final AFP detector without the flex on the sensor.

In the 2014 data, no signs of Quartz material interactions were found from the average cluster multiplicity and deposited charge of plane 4 [2]. It was suspected that the 2 mm thick plastic cover in front of each pixel sensor absorbed part of the secondaries from upstream material, as well as produced new secondary particles, in particular delta rays, that presented a large background for the upstream secondaries. Hence, in 2015 a hole in the plastic cover was made over most of the sensitive pixel area (see section 2.1.2, in particular figure 3).

Figure 13 shows the pixel map for the average cluster multiplicity for planes 0 and 4 for a 2015 run in which only the two lower trains 3+4 of the ToF detector were included. One can clearly distinguish the different regions. The cluster multiplicity is significantly higher for the region covered by plastic. However, also in the region without cover, one can clearly identify localised material interactions from the electronic components of the flexible circuit board (cf. figure 3). Since those will not be on top of the sensor for the final AFP pixel modules, a so-called *minimal-material region* is defined avoiding the largest of these components as well as the plastic cover. For plane 4 one can now clearly distinguish the region with the interactions in the LQbars from the region without. Figure 13 (bottom left) shows the full cluster-multiplicity distribution for the different regions of plane 4, namely the minimal-material, LQbar and LQbar+cover region. The LQbar

2016 JINST 11 P09005

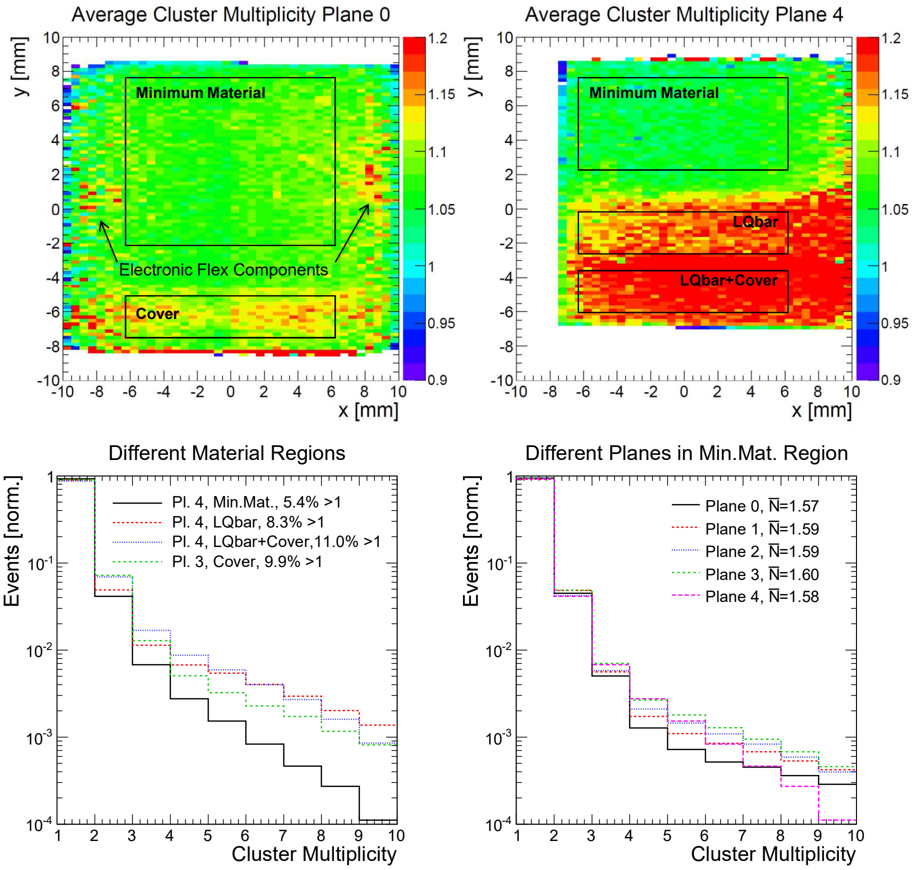

Figure 13. Top: average cluster-multiplicity map for planes 0 and 4 as a function of track position at 0° tilt. Indicated are the different selected material regions of interest (the total areas covered by the plastic or the LQbars are larger). Bottom: the cluster-multiplicity distribution for different regions of planes 4 and 3 (left) and for different planes in the minimal-material region (right).

region has a significantly higher cluster multiplicity (8.3% of the events have > 1 cluster) than the minimal-material region (5.4% of the events have > 1 cluster). This is roughly consistent with the expected 3.6% of the events with nuclear interactions in the LQbars. Adding the plastic cover to the LQbar region increases the number of events with > 1 cluster to 11.0%, probably mostly due to delta rays. It is interesting to note that the fraction of events with multiplicities between 2–5 increases (consistent with delta rays that are usually produced with low multiplicity), whereas the multiplicities above 5 decrease, probably due to absorption of secondaries from the LQbars in the plastic cover. The cover region of plane 3 is also added to the figure in order to show that it has a roughly similar multiplicity distribution as the LQbar+cover region of plane 4, which explains why no clear signs of Quartz material interactions were seen in the 2014 data with the plastic cover everywhere.

2016 JINST 11 P09005

For the tracker, it is also important to know whether the upstream planes influence the downstream ones. Figure 13 (bottom right) shows the cluster-multiplicity distribution for the minimal-material region compared for all planes. The average cluster multiplicity $\bar{N}$ does not seem to increase systematically from one plane to the other. This is mainly because the number of events with 2 clusters (which is dominating over events with higher multiplicities) is similar for all planes. These events are probably dominated by low-energetic delta rays that are immediately absorbed in one plane. However, the number of events with larger multiplicities, which probably mostly stem from nuclear interactions, does increase with plane number since those secondaries can pass through several planes and can hence accumulate and multiply. Only the last plane, 4, does not follow this trend, possibly due to secondaries with an angle that miss the last plane because of the much larger distance to the previous planes. In any case, these events with high multiplicities still stay at the sub-percent level.

The impact of the tracker material interactions is expected to be slightly different for the final AFP detector with different tracker holders, the Roman pot outside, no flex with electronic components on top of the sensor and a reduced pitch of 9 mm between the planes. Hence, these studies will be repeated for the final detector in the next beam test in 2016. For a better understanding of the nature of the interactions, simulations will need to be performed and compared to the data.

In order to minimise the influence of material interactions in these analyses, the tracker studies are typically performed for events with tracks in the minimal-material region, and for most tracker and ToF studies a cluster multiplicity of maximally 1 in each plane is required.

4.4 Performance of the tracking system

4.4.1 Spatial resolution

General spatial-resolution considerations The spatial resolution of each pixel plane as well as of the whole AFP tracker system is a crucial performance parameter. Each AFP station acts as a beam telescope of four planes and can provide a full track (position and angle). However, to measure the angle of the forward proton tracks precisely, the two AFP stations on each side of the IP, separated by 12 m, are combined, which is not studied here. The most important track-performance parameter for each station individually is the combined position resolution of the four-plane system, which is best in the centre of the four equidistant planes as discussed below.

It has to be distinguished between qualitatively different situations in the short and long pixel direction:

1. *Digital/binary/discrete* situation in the long (250 μm) pixel direction (beam test x/AFP vertical coordinate):

   If only one pixel is hit in a certain direction, as is the case in 98% of the events in the long pixel direction (see figure 8 centre left), the measured hit-cluster position only assumes discrete values, namely the pixel centre as sketched in figures 10 and 14. In such a case, the digital or binary resolution of pitch/$\sqrt{12}$, i.e. 72 μm for a pitch of 250 μm, is obtained, as confirmed in previous beam tests (see section 2.1.1).

   In such a discrete situation, the combined tracker resolution of several pixel planes highly depends on the offset of the planes with respect to each other as shown in figure 14: e.g. in case

2016 JINST 11 P09005

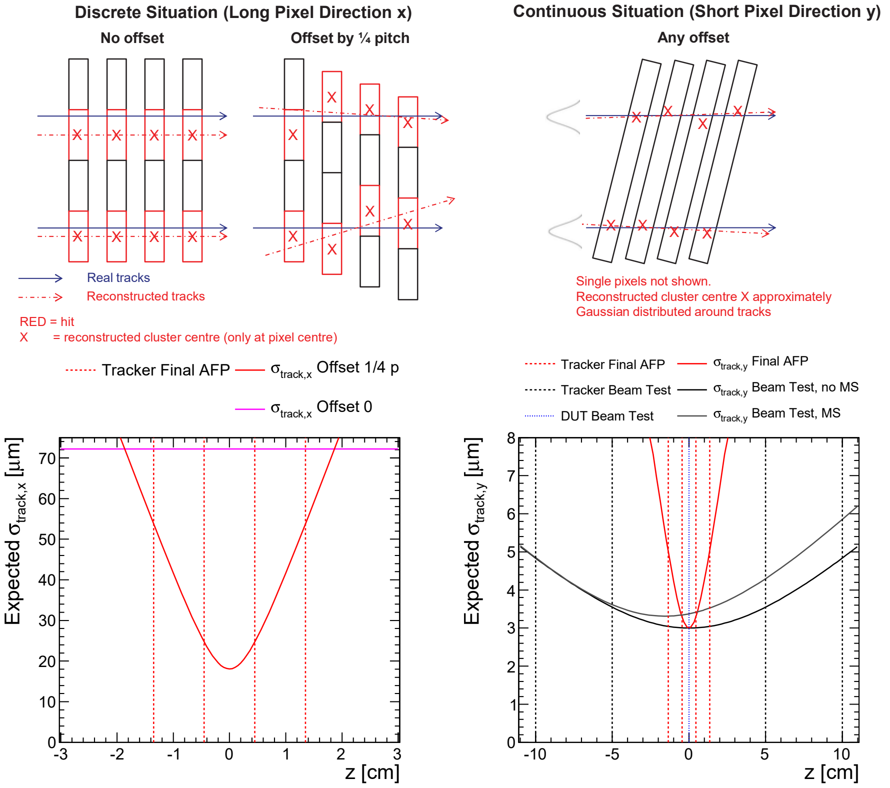

Figure 14. Top: sketches of the track reconstruction for the discrete situation in the long pixel direction (left), where most of the clusters have only one hit, so that its position is almost always assigned to the pixel centre (this is shown for different staggering scenarios with an offset of 0 or 1/4 pitch between successive planes); and for the continuous situation in the short pixel direction (right), where the reconstructed cluster position approximately follows a Gaussian distribution around the track. Bottom: the corresponding expected track resolution as a function of z in the long pixel direction (left) for different staggering scenarios for the final AFP tracker; and in the short pixel direction (right) at 14° tilt with 6 μm input resolution per plane for the final AFP tracker, as well as for the plane-2-as-DUT track-reconstruction scenario in the beam test, with and without MS effects from the beam-test tracker planes.

of perfect alignment (no offset of planes), no improvement over the single-plane resolution is achieved for perpendicular tracks since each pixel plane gives a redundant measurement. In the case of staggering the modules by 1/4 of a pitch, as planned for the final AFP detector, the track resolution for four pixel planes is improved to 1/4 of the binary resolution, i.e. 18 μm. However, the actual staggering present in this beam test was random since no precision alignment was available. Moreover, the resolution cannot be measured reliably with a setup of a few identical planes in the discrete regime (e.g. in case of no offset of planes, the difference in hit position between successive planes is always 0). Hence, a resolution measurement in the long pixel

2016 JINST 11 P09005

direction is not pursued here but needs to be performed with the final AFP detector including the actual staggering achieved with an external precision telescope in future beam tests.

2. *Analog/continuous* situation in the short (50 μm) pixel direction at 14° tilt (beam test y/AFP horizontal coordinate):

   In the short pixel direction at 14° tilt, due to charge sharing between pixels, the hit position can be interpolated using the ToT or charge information, giving a measurement with approximately continuous values. As explained in section 2.1.2, such a situation was studied in special runs with all five pixel planes at 14° tilt with an equidistant pitch of 5 cm without the ToF detector.

   In this case, neglecting multiple scattering, the track resolution $\sigma_{\text{track},y}$ as a function of z can be predicted from the uncertainties of the straight-line parameters of the fit (slope s_y and offset b_y) and their covariance cov_y as

   $$\sigma_y^2(z) = \sigma_{b_y}^2 + z^2 \cdot \sigma_{s_y}^2 + 2z \cdot cov_y. \tag{4.1}$$

   This is shown in figure 14 with an input resolution of 6 μm per plane (as measured below) for the track-reconstruction scenario with the central plane 2 excluded as DUT from the track fitting. This is compared to the final AFP configuration with four planes with 9 mm pitch. In both cases the track uncertainty is symmetric around its minimum in the centre of the four tracking planes. The minimum track uncertainty is the same in both cases, namely half of the input resolution per plane, i.e. 3 μm as it scales with $1/\sqrt{N_{\text{planes}}}$. In the continuous case, the resolution can be measured with a setup of a few identical planes like the one in this beam test.

   The effect of multiple scattering on the track resolution has been assessed in a simple Monte-Carlo simulation, which introduces a Gaussian-distributed multiple-scattering angle $\theta_{0,\text{MS}}$ at each plane (see section 4.3) as well as a Gaussian smearing of the hits around the true particle position according to the resolution. Then the simulated hits are fitted with a straight line and compared to the true track position (in the absence of multiple scattering). The expected degradation of track resolution due to multiple scattering in the tracker centre is found to be 0.4 μm for the beam test with 120 GeV particles, as shown in figure 14. For the final AFP detector with 6.5 TeV protons, the effect is found to be negligible.

3. *Mixed* situation in the short pixel direction at perpendicular incidence:

   for the short pixel direction at 0°, there is a mixed situation of cluster size 1 in about 85% of the cases (digital) and cluster size 2 in about 12% of the cases (to which analog algorithms can be applied). However, since this configuration is well studied in previous beam tests and has no relevance for the final AFP detector at 14° tilt, this will not be covered here.

In the following, the resolution in the short pixel direction y at 14° tilt (analog/continuous case) will be studied.

Spatial-resolution determination methods The resolution is determined with two different methods, namely with the triplet method, which gives the average single-plane resolution for three successive planes, and with the track-DUT method, which gives the convoluted resolution of a four-plane track and a single DUT plane.

1. Average Single-Plane Resolution with the Triplet Method:

   One method to measure the average per-plane resolution of three identical planes without a track fit (only using the alignment constants from a previous track fit) is the *triplet* technique. It defines a residual variable res_{trip} from the hit position x_i of three successive equidistant planes (e.g. $i = 1, 2, 3$) as

   $$res_{\text{trip}} = \frac{x_1 + x_3}{2} - x_2.$$

   An effective average single-plane (SP) resolution can be obtained from the spread (RMS or σ of a Gaussian fit) as $\sigma_{\text{SP,trip}} = \sqrt{2/3} \cdot \sigma_{\text{trip}}$ assuming the resolutions of all planes are equal and neglecting possible misalignment or multiple-scattering effects. In the simulation mentioned above, the effect of multiple-scattering has been assessed to be less than 0.1 μm, which is conservatively included as systematic uncertainty.

2. Convoluted Track and Single-Plane Resolution with the Track-DUT method:

   another method to determine the resolution is to exclude one plane (DUT) from the track fit and calculate the residual $res_{\text{track-DUT}}$ as the difference between the DUT cluster centre and the track position extrapolated to the DUT. The spread ($RMS_{\text{track-DUT}}$ or $\sigma_{\text{track-DUT}}$) gives the convolution of the DUT single-plane resolution $\sigma_{\text{SP,DUT}}$ and the track resolution σ_{track} at the position of the DUT plane. Neglecting multiple-scattering and assuming the equality of all planes, both contributions can be disentangled by using eq. 4.1 as illustrated in figure 14, e.g. using the relation that in the centre of a four-plane system the track resolution is expected to be half of the single-plane resolution.

   As mentioned above, it was found in simulations that for the beam-test conditions with 120 GeV particles, multiple scattering would degrade the track resolution for a straight-line fit by about 0.4 μm with respect to conditions without scattering. Hence, to calculate the track resolution for the beam-test conditions, one would need to correct for this. However, in the end the parameter of interest is the track resolution of the final AFP tracker for 6.5 TeV particles with negligible multiple scattering. In the simulation, it was found that the convoluted $\sigma_{\text{track-DUT}}$ is hardly affected by multiple scattering in the beam test, namely by less than 0.05 μm. This can be explained by the fact that the position displacement due to scattering builds up successively from one plane to the next, so that the displacement at the DUT is correlated to the one at other planes, and the effect largely cancels out in the difference between the DUT hit position and the track position extrapolated to the DUT. Hence, the bias for σ_{track} under AFP conditions introduced by neglecting scattering in the analysis should be small. Nevertheless, for a conservative estimate of the systematic uncertainty due to multiple scattering, the full 0.4 μm difference was taken.

Spatial-resolution results

Figure 15 shows the residual distributions for the triplet method involving planes 1, 2 and 3 (top) and for the track-DUT method with the central plane 2 as DUT (bottom). Default operational parameters (10 V, 2 ke$^-$, 10@20 ke$^-$) and the charge-weighted cluster centre were taken here. Only events with one track and one cluster per plane were taken into account to eliminate combinatorial background. Each distribution is shown both including all cluster sizes and restricted to cluster

2016 JINST 11 P09005

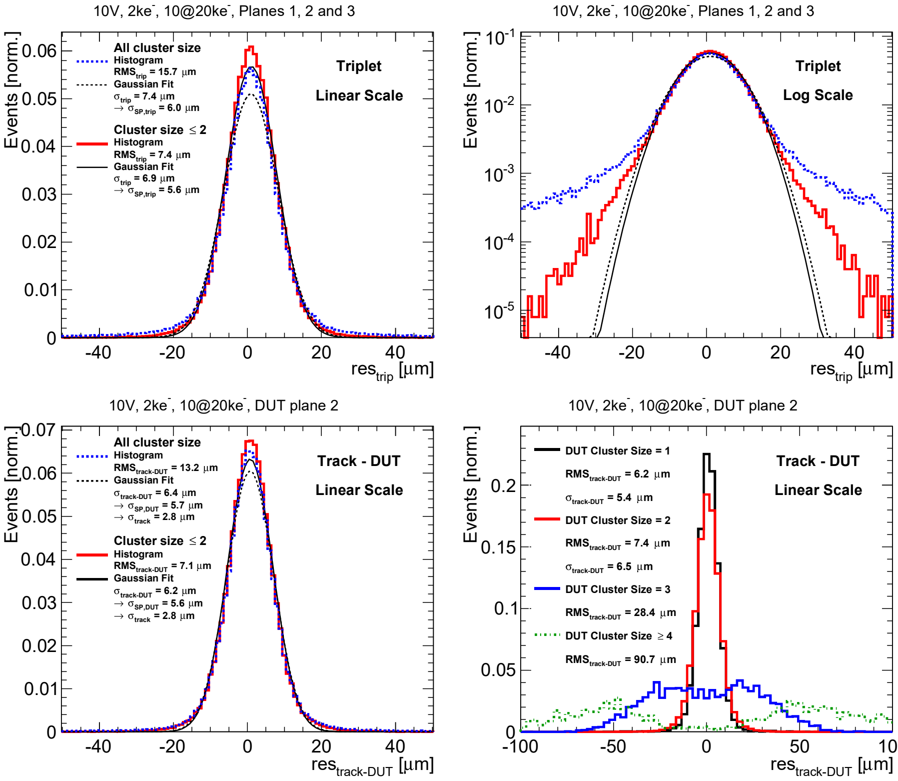

Figure 15. The residual distributions to determine the spatial resolution. Top: the triplet residual res_{trip} using planes 1, 2 and 3, for all cluster sizes and cluster size ≤ 2, in linear (left) and logarithmic (right) scale. Bottom: the track-DUT residual $res_{\mathrm{track\text{-}DUT}}$ for plane 2 as a DUT, for all cluster sizes and cluster size ≤ 2 of both tracking and DUT planes (left); and for different DUT cluster sizes, whereas the tracking-plane cluster sizes were not restricted (right). All distributions are normalised to unit area. In all cases the standard operational parameters and charge-weighted algorithm were used.

sizes of ≤ 2 (96% of all clusters). It can be seen that including all cluster sizes, non-Gaussian tails are present with an RMS significantly larger than the σ of a Gaussian fit. However, these tails are significantly reduced for cluster sizes of ≤ 2 and the RMS approaches the σ within maximally 0.9 μm. In contrast, the Gaussian σ is not strongly affected by the restriction to cluster sizes of ≤ 2.

More details of this effect can be seen in figure 15 (bottom right) that shows the track-DUT residual distribution separately for different cluster sizes in the DUT (whereas the cluster size of the planes included in the track fit is not restricted). The residuals of DUT cluster size 1 and 2 have a narrow, almost Gaussian peak, whereas for 3 and ≥ 4 a broad double-peak structure is obtained. As discussed in section 4.1.1, a cluster size of 3 is in fact geometrically possible at 14° (although suppressed by the threshold effect). But on the one hand probably the charge-weighted cluster

2016 JINST 11 P09005

centre is not ideal in this case, and on the other hand the sample of cluster size 3 is expected to also contain events with originally lower cluster size, but with delta rays that travel inside the sensor from one pixel to another and artificially enlarge the cluster size and shift the centre of the cluster (as illustrated in figure 10 right). In fact clusters with a size of at least 4 are geometrically not possible at 14° and are hence expected to be completely dominated by this effect.

Since 96% of the clusters in one plane have cluster sizes of ≤ 2, it is simple and efficient to either reject events with larger cluster sizes or to down-weight them in the track fit. Hence, the σ of cluster sizes of ≤ 2 will be taken as the figure of merit for the resolution in the following.

For the standard tuning and the charge-weighted cluster-centre algorithm, a single-plane resolution of $\sigma_{\text{SP,trip}} = 5.6 \pm 0.5\,\mu\text{m}$ was obtained for the triplet of planes 1, 2 and 3. The results for other possible combinations of planes (0, 1, 2 and 2, 3, 4) agreed within $0.5\,\mu$m. Hence, any difference in resolution between different planes was not much larger than this level. The statistical uncertainties were $0.03\,\mu$m only; conservative systematic uncertainties assigned include the $0.5\,\mu$m difference between triplets, $0.1\,\mu$m from a variation of fit ranges (full range vs. restriction to $\pm 3\sigma$) and the $0.1\,\mu$m multiple-scattering effect estimated from simulation as discussed above.

The convoluted track-DUT resolution for the central plane 2 as DUT was found to be $\sigma_{\text{track-DUT}} = 6.2 \pm 0.6\,\mu\text{m}$. Disentangling both as described above (assuming the resolution of the four-plane system to be half of the single plane) gives $\sigma_{\text{SP,DUT}} = 5.6 \pm 0.5\,\mu\text{m}$ (consistent with $\sigma_{\text{SP,trip}}$ from the triplet method) and $\sigma_{\text{track}} = 2.8 \pm 0.5\,\mu\text{m}$. Again, the statistical uncertainties were maximally $0.03\,\mu$m only. For $\sigma_{\text{SP,DUT}}$, the systematic uncertainty to account for plane-to-plane variations was taken from the triplet method above (such plane-to-plane variations could not be tested directly for the track-DUT method since taking another, i.e. non-central, plane as DUT would change the relation between the single-plane and the track resolution). This was then propagated as well to the systematic uncertainties of $\sigma_{\text{track-DUT}}$ and σ_{track}. The latter includes in addition the conservative $0.4\,\mu$m systematic uncertainty for multiple-scattering effects as explained above.

The resolution is compared in table 2 for different cluster-centre algorithms, voltages, thresholds and ToT tunings.

The ToT-weighted algorithm was found to only slightly degrade the resolution by about 5%. Hence, due to its simplicity and the lack of the ToT-to-charge calibration for some of the tunings under study, the ToT-weighted algorithm was taken as default without compromising the resolution significantly. However, it should be noted again that the ToT-to-charge calibration was only obtained from a similar device and averaged for all pixels. In the future it is planned to do this for each device and pixel separately, which might improve the performance of the charge-weighted algorithm.

No strong dependence on voltage and threshold was found. The resolutions at 10@16 ke$^-$ and 10@20 ke$^-$ ToT tuning points are similar and degrade by about 15% for 5@20 ke$^-$ as expected due to the degrading charge/ToT resolution. Hence, tuning at 5@20 ke$^-$, which improves the dead time of the HitOr trigger signal as discussed in section 3.2, has a measurable but moderate effect on the resolution, keeping the value well within the AFP requirements.

To conclude, even for the simplest cluster-centre and track-fit algorithms without optimisation, a track resolution of $2.8 \pm 0.5\,\mu$m was found for the short pixel direction, largely surpassing the AFP requirement of $10\,\mu$m. In the future, this might be even further improved by a more careful ToT-to-charge calibration, more optimised cluster-centre algorithms such as involving the η correction or neural networks [27] as it is done for the ATLAS pixel detector, and more advanced track-fit and

Table 2. The spatial resolutions: the measured convolution of track and DUT resolution ($\sigma_{\text{track-DUT}}$); after disentangling the track and single-plane DUT contributions σ_{track} and $\sigma_{\text{SP,DUT}}$ assuming σ_{track} to be half of $\sigma_{\text{SP,DUT}}$; and the single-plane resolution $\sigma_{\text{SP,trip}}$ obtained from the triplet of planes 1, 2 and 3. The uncertainties are dominated by systematic effects like plane-to-plane variations and multiple scattering as explained in the text. The resolution is compared for different algorithms, voltages and tuning points. If not stated otherwise, the ToT-weighted algorithm and standard operational parameters were used. The values are for cluster size ≤ 2.

	Resolution [μm]			
Variation	$\sigma_{\text{track-DUT}}$	σ_{track}	$\sigma_{\text{SP,DUT}}$	$\sigma_{\text{SP,trip}}$
Different Algorithms				
Charge-weighted	6.2 ± 0.6	2.8 ± 0.5	5.6 ± 0.5	5.6 ± 0.5
ToT-weighted	6.5 ± 0.6	2.9 ± 0.5	5.8 ± 0.5	5.9 ± 0.5
Different Voltages				
1 V	6.7 ± 0.6	3.0 ± 0.5	6.0 ± 0.5	6.0 ± 0.5
2 V	6.6 ± 0.6	2.9 ± 0.5	5.9 ± 0.5	5.9 ± 0.5
4 V	6.5 ± 0.6	2.9 ± 0.5	5.8 ± 0.5	5.8 ± 0.5
7 V	6.5 ± 0.6	2.9 ± 0.5	5.8 ± 0.5	5.9 ± 0.5
10 V	6.5 ± 0.6	2.9 ± 0.5	5.8 ± 0.5	5.9 ± 0.5
20 V	6.5 ± 0.6	2.9 ± 0.5	5.8 ± 0.5	5.9 ± 0.5
Different Thresholds				
1.5 ke$^-$	7.4 ± 0.7	3.3 ± 0.5	6.7 ± 0.6	6.3 ± 0.6
2.0 ke$^-$	6.5 ± 0.6	2.9 ± 0.5	5.8 ± 0.5	5.9 ± 0.5
2.5 ke$^-$	6.3 ± 0.6	2.8 ± 0.5	5.7 ± 0.5	5.8 ± 0.5
3.0 ke$^-$	6.4 ± 0.6	2.9 ± 0.5	5.7 ± 0.5	6.0 ± 0.5
Different ToT Tunings				
10@16 ke$^-$	6.8 ± 0.6	3.0 ± 0.5	6.1 ± 0.5	5.8 ± 0.5
10@20 ke$^-$	6.5 ± 0.6	2.9 ± 0.5	5.8 ± 0.5	5.9 ± 0.5
5@20 ke$^-$	7.5 ± 0.7	3.3 ± 0.5	6.7 ± 0.6	6.9 ± 0.6

alignment methods, e.g. taking into account multiple scattering. In addition, in future AFP tracker versions one might consider to reduce the tilt slightly from 14° to 12–13° in order to enhance the fraction of cluster sizes of ≤ 2 above the present 96% per plane.

4.4.2 Tracker hit efficiency

Using the DUT track-reconstruction scenarios, the per-plane hit efficiencies were determined. This was done for the unbiased pixel planes 1 and 2 that were not used for triggering. The DUT was excluded from the track fit and it was checked for each reconstructed track if a hit in the DUT was found close to the track.

Figure 16 (left) shows the hit efficiencies of planes 1 (CNM) and 2 (FBK) at 0° and 14° beam incidence as a function of bias voltage for the default tuning parameters. At 0°, the CNM device reaches a plateau at 4 V, whereas the FBK device reaches its maximum efficiency already at 1 V. The

2016 JINST 11 P09005

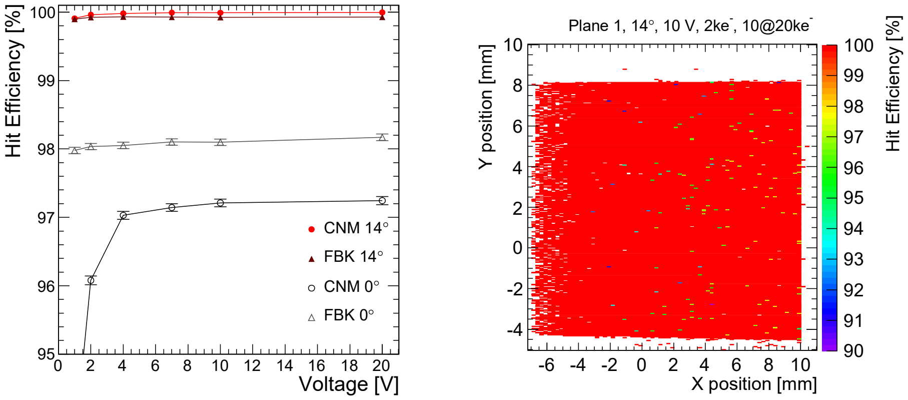

Figure 16. Left: pixel hit efficiencies as a function of bias voltage for planes 1 (CNM) and 2 (FBK) at 0° and 14°. Right: hit efficiency map for plane 1 at 14° and 10 V.

difference is due to the non-passing-through 3D columns in the CNM device, which needs a slightly higher voltage to reach full lateral depletion. The plateau efficiencies of 97–98% are reasonable for an IBL-spare quality device (but are lower than for a good-quality IBL device with > 99% [9]). At the AFP tilt of 14°, however, the efficiencies increase to > 99.9% already from 1 V for both devices, despite the quality class used here. The efficiency improvement for a tilted device is a well-known effect in 3D sensors which exhibit small localised low-efficiency regions at perpendicular incidence due to the insensitivity of the 3D columns and some low-field regions in between [9]. Figure 16 (right) displays the 3D efficiency map for plane 1 at default operational parameters and a tilt of 14°. It can be seen that the high efficiency is uniform over the whole device, apart from single pixels with slightly lower efficiency (white pixels are either masked or regions without entries at the edge due to the beam profile or the lack of overlap with the trigger area). The efficiency results are found to be insensitive to the threshold and ToT tunings within the range studied here.

4.5 Performance of the time-of-flight system

In this section, the performance of the LQbar time-of-flight (ToF) system is presented. The results are from the 2014 data only with the standard setup as described in section 2.2.2. The 2015 data with some setup variations and more detailed studies of the ToF properties are still being analysed.

The common data format of tracking and timing detectors allowed the event-by-event use of track information to predict independently whether a certain LQbar was traversed by a particle, which was crucial for the studies of efficiency, cross talk, noise and time-resolution. For this, well-reconstructed tracks from the all-plane track-reconstruction scenario after cleaning cuts were used as described in section 4.1.2, giving the best track precision at the position of the timing system.

2016 JINST 11 P09005

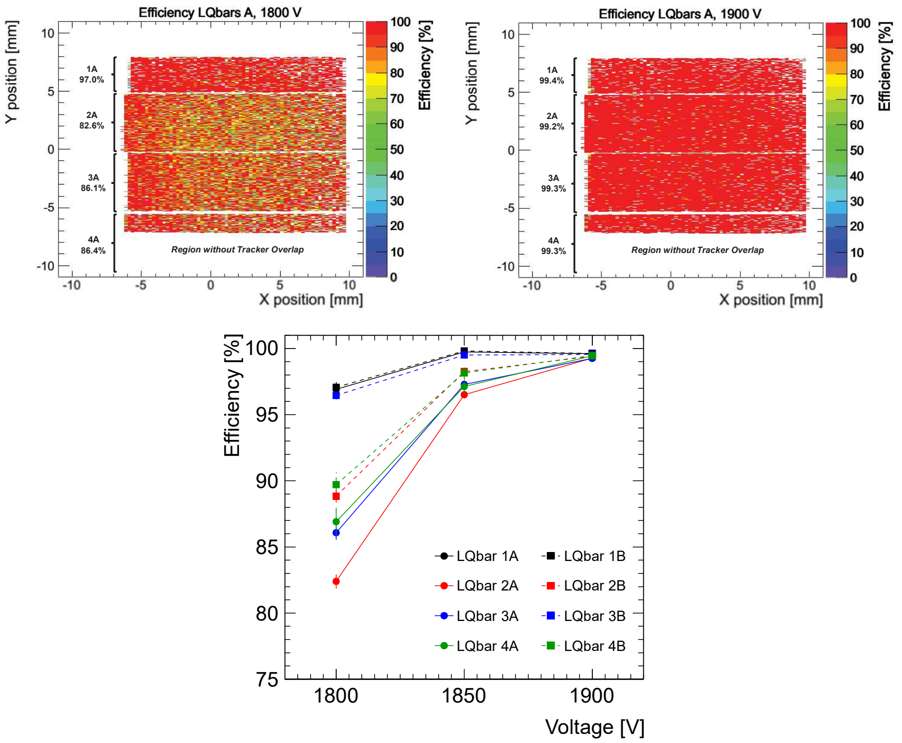

Figure 17. The hit efficiencies of the LQbar ToF channels. Top: the efficiency map as a function of reconstructed track position for the first bar (A) of each train at $V_{\text{MCP-PMT}}$ = 1800 V (left) and 1900 V (right). Bottom: the mean efficiencies as a function of $V_{\text{MCP-PMT}}$ for all eight bars.

4.5.1 LQbar hit efficiency

The hit efficiency of each LQbar was determined using events with tracks passing through the bar of interest and determining the fraction of those events in which this bar gave a signal. Figure 17 (top) shows the two-dimensional hit-efficiency map as a function of reconstructed track position for the first bar (A) of each train at $V_{\text{MCP-PMT}}$ = 1800 V (left) and 1900 V (right), for the fixed CFD threshold of 100 mV. Figure 17 (bottom) displays the corresponding mean efficiencies as a function of $V_{\text{MCP-PMT}}$ for all the bars. It can be seen that the LQbar efficiencies generally increase with $V_{\text{MCP-PMT}}$ as expected as the MCP-PMT gain increases. Whereas at 1800 V, there is a significant spread between the efficiencies of different bars ranging from 83 to 97%, the efficiencies at 1900 V are all above 99%. Another interesting observation at 1800 V is a slightly higher efficiency close to the cut edge near $x = -6$ mm compared to areas further away from it.

This effect was considered in the design, and gives an enhanced light yield, ranging from a few % at 5 mm from the edge of the bar to a factor 2 at the edge of the bar where the whole Cherenkov light cone is detected [18].

2016 JINST 11 P09005

4.5.2 Cross talk between LQbar trains

Another important ToF-detector parameter is the cross talk between bars of different trains. A high level of inter-train cross talk is disadvantageous for the use of the ToF detector as a position-resolved trigger, as well as for the operation at high pile-up and hence occupancies where there might be several trains hit by particles in one bunch crossing. However, for low occupancies like in the beam test, cross talk was found to have no large influence on the time resolution if the bars really hit by the particle can be selected using track information, as demonstrated in section 4.5.4 below.

The cross talk seen by a bar of interest was determined as the fraction of events in which it gives a signal when the track actually passes through a bar in another train (of the same LQbar column A or B).

Figure 18 (top) shows the two-dimensional map of cross talk to LQbar 4A as a function of track position (for tracks passing through other trains) at $V_{\text{MCP-PMT}} = 1800\,\text{V}$ (left) and 1900 V (right), for the fixed CFD threshold of 100 mV. In figure 18 (bottom) the mean cross talk from the first (left) and second neighbours (right) is displayed for all bars as a function of $V_{\text{MCP-PMT}}$. Whereas the cross talk from the first neighbours is at the few-percent level at 1800 V, it increases steeply up to 66–92% at 1900 V. Cross talk from the second neighbour is maximally at the few-percent level up to 1850 V and increases to 8–47% at 1900 V. Cross talk from the third neighbour is not observed. Similar to the efficiency, the cross talk is observed to be higher near the LQbar cut edge at $x = -6\,\text{mm}$.

As the LQbars themselves were optically well isolated between adjacent trains with mylar foils at the radiator level and Aluminium at the light-guide level as explained above, most of the cross talk has to originate from the MCP-PMT level. Possible explanations include optical leakage at or in the photo-cathode window and the lateral spread of the photo electrons in the MCP-PMT. The level of cross talk also depends on the CFD threshold settings. It is believed that it can be significantly reduced with little loss of efficiency by raising the CFD thresholds to somewhat higher than the current 100 mV, as the cross-talk pulse height in a neighbouring LQbar is significantly smaller than the signal pulse height of a hit LQbar. Further studies to understand its origin and to optimise it are envisaged.

4.5.3 LQbar noise

The noise rates of the LQbar channels were measured as their mean signal firing rates in events in which the track missed any LQbar ($x < -7\,\text{mm}$). It was measured to be at the level of 0 to 63 kHz for the fixed CFD threshold of 100 mV, with a large variation between different LQbar channels (which is still under investigation) and increasing with $V_{\text{MCP-PMT}}$ as shown in table 3. This corresponds to noise occupancies in the order of 10^{-4} to 10^{-3} for a 25 ns window.

4.5.4 Time resolution

The HPTDC board digitised the arrival time of the rising edge of the CFD output for each LQbar and SiPM reference channel (only the two SiPMs 1 and 2 were included during these tests). This time information was recorded for each event in the RCE output file. Time resolutions were measured from the spread of the time differences between two timing channels. For this, it was always required that a well-reconstructed track passed through the overlap region of the sensors related to these channels. The $3 \times 3\,\text{mm}^2$ SiPMs were placed between -0.5 to 2.5 mm in x, i.e. their centres

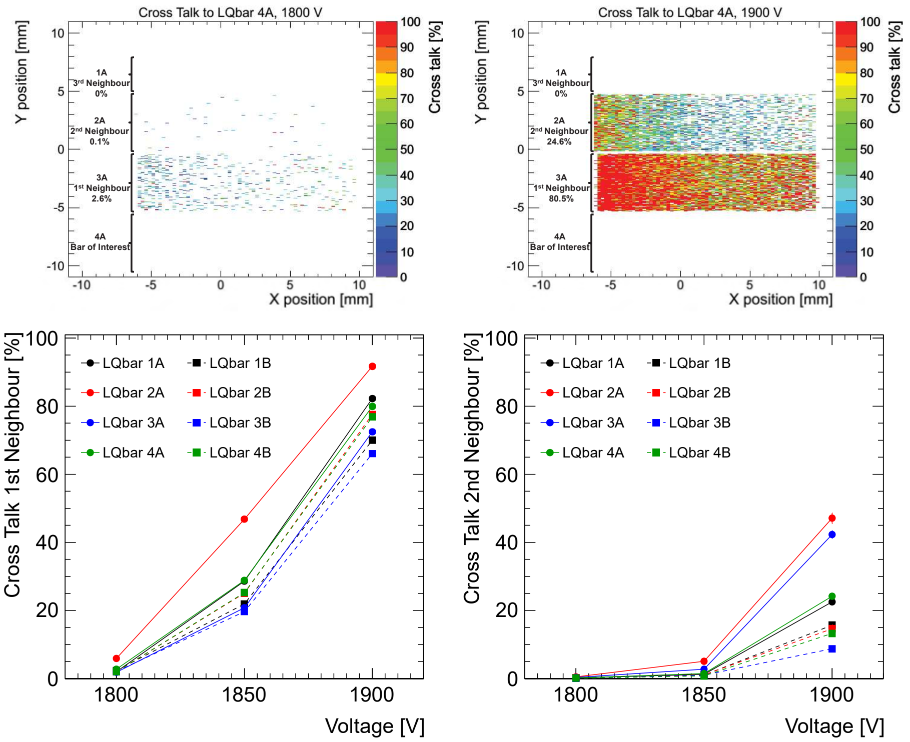

Figure 18. The cross talk between LQbars in neighbouring trains. Top: the map of cross-talk seen by LQbar 4A as a function of track position at $V_{\text{MCP-PMT}}$ = 1800 V (left) and 1900 V (right). Bottom: the mean cross talk from bars in directly neighbouring (left) and next-to-directly-neighbouring trains (right) as a function of $V_{\text{MCP-PMT}}$ for all eight bars.

Table 3. Noise rate per LQbar channel for different voltages.

LQbar Channel	1A	1B	2A	2B	3A	3B	4A	4B
$V_{\text{MCP-PMT}}$	Noise Rate [kHz]							
1800 V	0	3	45	7	10	16	29	28
1850 V	0	14	57	19	22	22	35	35
1900 V	0	20	63	29	47	49	46	47

were about 7 mm away from the LQbar cut edge, and between 3.5 to 6.5 mm in y, i.e. they had an overlap with the LQbar trains 1 and 2 (see figure 12).

The first step is to understand the time resolutions of the SiPM reference devices. Figure 19 (left) shows the time difference between SiPM1 and SiPM2. It is approximately Gaussian distributed and has a total convoluted width of σ_{fit} = 25.1 ps, including the HPTDC contributions of the two SiPM channels, which have been on the same HPTDC chip. This value appeared to be stable for many

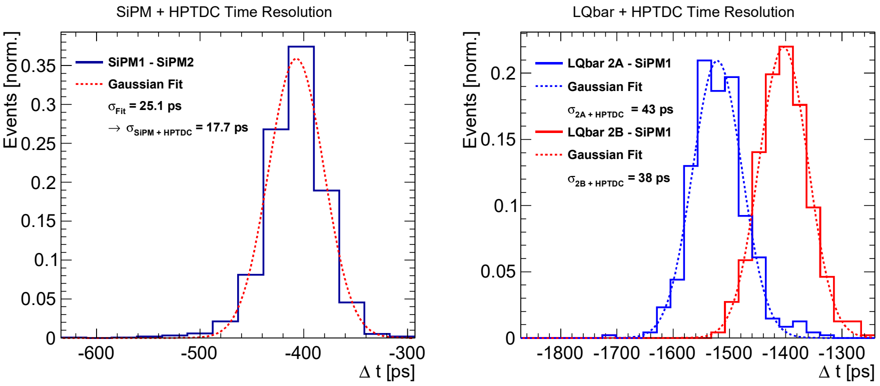

Figure 19. Time differences measured with the HPTDC-RCE readout. Left: the time differences between the two SiPM references with total convoluted resolution σ_{fit} and after dividing by $\sqrt{2}$, $\sigma_{\text{SiPM+HPTDC}}$. Right: the time differences between the LQbars of the second train (2A and 2B) and SiPM1 at $V_{\text{MCP-PMT}}$ = 1900 V; the displayed fitted resolution values here have already the SiPM+HPTDC resolution quadratically subtracted.

Table 4. The time resolutions of different LQbars and the train average for different $V_{\text{MCP-PMT}}$ measured with the HPTDC-RCE readout (i.e. including the HPTDC contribution) with respect to the SiPM reference. $\sigma_{\text{SiPM+HPTDC}}$ was subtracted. The uncertainties include statistical and systematic uncertainties as described in the text.

$V_{\text{MCP-PMT}}$ [V]	1750	1800	1850	1900
LQbar	Time resolution $\sigma_{\text{LQbar+HPTDC}}$ [ps]			
1A	78 ± 5	61 ± 6	52 ± 6	46 ± 5
1B	85 ± 6	60 ± 6	47 ± 6	41 ± 6
Average Train 1	67 ± 7	54 ± 12	44 ± 6	37 ± 6
2A	94 ± 5	80 ± 10	50 ± 6	43 ± 7
2B	94 ± 8	64 ± 5	45 ± 6	38 ± 6
Average Train 2	77 ± 7	63 ± 7	41 ± 6	35 ± 6

different runs within less than 1 ps. Assuming an equal performance of both devices, the resolution of a single SiPM+HPTDC device can be obtained from dividing by $\sqrt{2}$, which gives $\sigma_{\text{SiPM+HPTDC}}$ = 17.7 ps. A similar analysis has been performed with the oscilloscope instead of the HPTDC, which gave a value of σ_{SiPM} = 11.0 ps (the contribution of the oscilloscope is considered to be negligible). Thus, the HPTDC resolution can be estimated from quadratic subtraction as σ_{HPTDC} = 13.9 ps, which is in good agreement with laboratory and previous beam-test measurements. The HPTDC contribution might slightly depend on the exact HPTDC channel combinations, which has not been taken into account at this beam test, but will be studied in the future.

The LQbar time resolutions were measured from the time differences between one bar and one of the SiPM references, respectively. The SiPM and the LQbar channels were connected to different HPTDC chips. This measurement could only be done for the trains 1 and 2 which had an overlap with the SiPMs. The time differences are shown in figure 19 (right) for the LQbars 2A and 2B with respect to SiPM1 at $V_{\text{MCP-PMT}}$ = 1900 V. Measurements using SiPM2 are consistent within a few ps. The resolution values from a Gaussian fit shown there have already the reference resolution $\sigma_{\text{SiPM+HPTDC}} = 17.7$ ps as obtained above quadratically subtracted.

The LQbar resolutions, including the HPTDC contributions, are listed in table 4 for different $V_{\text{MCP-PMT}}$ values. The resolution was found to improve with $V_{\text{MCP-PMT}}$ and at 1900 V it reached values between 38 and 46 ps for the single LQbars. Statistical and fit uncertainties are estimated to be 2 ps, and in addition systematic uncertainties of typically 6 ps have been assigned to account for the differences between the two SiPM references as well as for run-to-run and selection-cut variations.

Also included in table 4 are the results for the resolution of the average time of the two LQbars in one train (A and B). The train average improves the resolution with respect to the best single-bar measurement, e.g. to 35 ± 6 ps for train 2 at 1900 V, consistent with the required design value of 30 ps for initial low-luminosity AFP runs. In general, however, the observed improvement is less than expected for uncorrelated measurements (e.g. for two bars of the same resolution an improvement by $1/\sqrt{2}$ is expected). Correlation between the bars of the same train has been observed before in previous beam tests and can originate in optical leakage at the photo-cathode window or in the lateral spread of the photo electrons in the MCP-PMT, similarly as for the inter-train cross talk.

Further detailed studies of the correlations and of the dependence of the time resolution on the number of LQbars are envisaged, with the aim of optimising the LQbar configurations.

5 Conclusions and outlook

Beam tests with a first unified AFP prototype detector combining pixel tracking and LQbar ToF sub-detectors and a common readout and data format have been performed at the CERN-SPS in November 2014 and September 2015. The successful tracking-timing integration was demonstrated by the spatial correlation of recorded tracking and timing data. A TDAQ system close to the final AFP-ATLAS readout based on a track trigger was successfully tested.

Moreover, the performances of the tracking and ToF systems were studied. The tracker hit efficiency was found to be $> 99.9\%$ per plane at a tilt of 14° like foreseen for the final AFP detector. The spatial resolution in the short 50 μm pixel direction at 14° was found to be 5.5 ± 0.5 μm per pixel plane and 2.8 ± 0.5 μm for the full four-plane tracker in the centre of the four planes. This clearly surpasses the AFP requirement of 10 μm for the horizontal AFP direction by a factor of almost 4. Due to the discrete hit behaviour in the long 250 μm pixel direction (corresponding to the vertical AFP direction), the resolution could not be measured in that direction with the beam-test setup here and in any case will highly depend on the actual staggering achieved in the final AFP detector.

The hit efficiencies of the LQbar ToF detectors were found to increase with MCP-PMT voltage up to more than 99% at 1900 V. However, also the cross talk was observed to increase strongly with voltage for the CFD threshold settings used. The time resolutions of the full LQbar timing detectors including the HPTDC contributions were found to improve with voltage and were measured between 38 ± 6 ps and 46 ± 5 ps per LQbar and 35 ± 6 ps and 37 ± 6 ps per train at 1900 V.

Hence, despite not being fully optimised and including only two LQbars per train, a timing resolution consistent with the low-luminosity target of 30 ps was obtained. Improved time resolutions of 10–20 ps required for high-luminosity operation are believed to be achievable through increasing the number of LQbars per train to the final four (space restrictions in the Roman pot prevent the installation of more), optimising the HPTDC performance, the development of a new HPTDC chip (which is on-going) and a reduction of the mini-Planacon pore size from 10 to 6 μm.

Parts of the ToF data in the 2015 beam test with different LQbar types and configurations are still being analysed. Moreover, in 2016 follow-up beam tests were already performed and more are planned with the final AFP detector and for a further systematic study and optimisation of the LQbar time performance such as cross talk, inter-bar correlations including the dependence of the time resolution on the number of LQbars per train (up to the final four-LQbar-train configuration), and HPTDC contribution. Also, the properties of the track trigger will be investigated further, and the development of an alternative trigger based on the ToF system will be pursued.

In addition, a first arm of the AFP detector with two Roman pots including a tracker each has been successfully installed at one side of the ATLAS IP in the 2015-2016 year-end shutdown, allowing the commissioning and study of the AFP tracker performance and backgrounds with the final detector and the LHC beam.

2016 JINST 11 P09005

Acknowledgments

The authors wish to thank H. Wilkens, S. Vlachos and the CERN SPS and NA teams for valuable support during the beam tests.

The equipment and detectors were provided by the following institutes and people: the CDFs and HPTDC boards by the University of Alberta; the pre-amplifiers and the mechanical setup by Stony Brook University; the MCP-PMT by the University of Texas at Arlington and Photonis; the SiPM reference detectors by M. Albrow; the LQbars by Palacky University Olomouc; the trigger PCB and pixel modules by IFAE Barcelona and INFN Genova; the RCE systems by SLAC; the pixel holders and cables by the ATLAS ITk pixel test-beam group; the LTB by M. Backhaus; the 6 GHz WaveRunner Oscilloscope by LeCroy.

This work was partially funded by: the MINECO, Spanish Government, under grants FPA2013-48308 and SEV-2012-0234 (Severo Ochoa excellence programme); the European Union's Horizon 2020 Research and Innovation programme under Grant Agreement no. 654168; the Polish National Science Centre grant UMO-2012/05/B/ST2/02480; the Czech projects "MSMT INGO II, č. LG15052", "MSMT č. LO1305 (RCPTM-NPU)" and PrF_2016_002 of IGA UP Olomouc; Texas ARP U.S. Dept. of Energy grants (A. Brandt); the U.S. Department of Energy grant DE-SC0007054 and the U.S. National Science Foundation grants PHY1068677 and PHY1119200; CERN/FIS-NUC/0005/2015, OE, FCT from Portugal; previous beam tests by the T-958 Fermilab Test Beam experiment.

References

[1] ATLAS collaboration, *The ATLAS Experiment at the CERN Large Hadron Collider*, 2008 *JINST* **3** S08003.

[2] ATLAS Forward Proton Collaboration, *Technical Design Report for the ATLAS Forward Proton Detector*, Tech. Rep. CERN-LHCC-2015-009 [ATLAS-TDR-024], CERN, Geneva, May, 2015.

[3] M. Garcia-Sciveres et al., *The FE-I4 pixel readout integrated circuit*, *Nucl. Instrum. Meth.* **A 636** (2011) S155.

[4] S.I. Parker, C.J. Kenney and J. Segal, *3-D: A New architecture for solid state radiation detectors*, *Nucl. Instrum. Meth.* **A 395** (1997) 328.

[5] C. Da Via et al., *3D silicon sensors: Design, large area production and quality assurance for the ATLAS IBL pixel detector upgrade*, *Nucl. Instrum. Meth.* **A 694** (2012) 321.

[6] G. Giacomini et al., *Development of double-sided full-passing-column 3D sensors at FBK*, *IEEE Trans. Nucl. Sci.* **60** (2013) 2357.

[7] G. Pellegrini, J.P. Balbuena, D. Bassignana, E. Cabruja, C. Fleta, C. Guardiola et al., 3*D double sided detector fabrication at IMB-CNM*, *Nucl. Instrum. Meth.* **A 699** (2013) 27.

[8] J. Lange, *Recent Progress on* 3D *Silicon Detectors*, `PoS(VERTEX2015)026` [`arXiv:1511.02080`].

[9] ATLAS IBL collaboration, *Prototype ATLAS IBL Modules using the FE-I4A Front-End Readout Chip*, 2012 *JINST* **7** P11010 [`arXiv:1209.1906`].

[10] I. Lopez Paz, E. Cavallaro, S. Grinstein and J. Lange, *Characterization of silicon 3D pixel detectors for the ATLAS Forward Physics experiment*, in proceedings of *Advancements in Nuclear Instrumentation Measurement Methods and their Applications (ANIMMA)*, Lisbon, 20-24 April 2015.

[11] S. Grinstein et al., *Beam Test Studies of* 3D *Pixel Sensors Irradiated Non-Uniformly for the ATLAS Forward Physics Detector*, *Nucl. Instrum. Meth.* **A 730** (2013) 28 [`arXiv:1302.5292`].

[12] J. Lange, E. Cavallaro, S. Grinstein and I. López Paz, 3*D silicon pixel detectors for the ATLAS Forward Physics experiment*, 2015 *JINST* **10** C03031 [`arXiv:1501.02076`].

[13] FP420 R, D collaboration, M.G. Albrow et al., *The FP420 & Project: Higgs and New Physics with forward protons at the LHC*, 2009 *JINST* **4** T10001 [`arXiv:0806.0302`].

[14] M.G. Albrow, H. Kim, S. Los, M. Mazzillo, E. Ramberg, A. Ronzhin et al., *Quartz Cherenkov Counters for Fast Timing: QUARTIC*, 2012 *JINST* **7** P10027 [`arXiv:1207.7248`].

[15] J. Pinfold, *Quartic - The precision Time-of-Flight Counter for the ATLAS Forward Physics Project*, Act. Phys. Pol. B Proc. Suppl. **4** (2011) 71.

[16] M. Rijssenbeek, *ATLAS Forward Proton Detectors: Time-of-Flight Electronics*, *Acta Phys. Pol. B Proc. Suppl.* **7** (2014) 751–758.

[17] M. Mota and J. Christiansen, *A High-Resolution Time Interpolator Based on a Delay Locked Loop and an RC delay line*, *IEEE J. Solid-State Circuits* **34** (1999) 1360–1366 [http://tdc.web.cern.ch/tdc/hptdc/docs/hptdc_manual_ver2.2.pdf].

[18] L. Nozka et al., *Design of Cherenkov bars for the optical part of the time-of-flight detector in Geant4*, *Opt. Express* **22** (2014) 28984–28996.

[19] M. Wittgen et al., *A Reconfigurable Cluster Element (RCE) DAQ Test Stand for the ATLAS Pixel Detector Upgrade*, talk given at *Topical Workshop on Electronics for Particle Physics (TWEPP)*, Aachen, Germany, September 2010.

[20] *AdvancedTCA Overview* http://www.picmg.org/openstandards/advancedtca/.

[21] D. S. Smith, S. Bibyk, K. K. Gan, H. Kagan, R. Kass and J. Dopke, *Development of the hitbus chip platform for the ATLAS DBM detector at CERN*, in proceedings of *IEEE 56th International Midwest Symposium on Circuits and Systems (MWSCAS)*, August 2013, pp. 1204–1207.

[22] S. Ask et al., *The ATLAS central level-1 trigger logic and TTC system*, 2008 *JINST* **3** P08002.

[23] ATLAS collaboration, J. Jentzsch, *Performance tests during the ATLAS IBL Stave Integration*, 2015 *JINST* **10** C04036.

2016 JINST 11 P09005

[24] M. Backhaus, *High bandwidth pixel detector modules for the ATLAS Insertable B-Layer*, PhD thesis, University of Bonn, Germany (2014).

[25] G. McGoldrick, M. Červ and A. Gorišek, *Synchronized analysis of testbeam data with the Judith software*, *Nucl. Instrum. Meth.* **A 765** (2014) 140.

[26] Particle Data Group collaboration, K.A. Olive et al., *Review of Particle Physics*, *Chin. Phys.* **C 38** (2014) 090001.

[27] ATLAS collaboration, *A neural network clustering algorithm for the ATLAS silicon pixel detector*, 2014 *JINST* **9** P09009 [`arXiv:1406.7690`].